From CTA to 3D modelling

A computational framework for morphometrical assessment and biomechanical analysis of atherosclerotic carotid arteries

Lies Quataert
MSc Biomedical Engineering
Faculty of Mechanical, Maritime and Material Engineering
26 April 2023

From CTA to 3D modelling: A computational framework for morphometrical assessment and biomechanical analysis of atherosclerotic carotid arteries

by

Lies Quataert

to obtain the degree of Master of Science in Biomedical Engineering
at the Delft University of Technology,
to be defended publicly on Wednesday April, 26 at 09:30 AM.

Student number:	4436164	
Project duration:	June, 2022 – April, 2023	
Daily supervisor:	PhD ir. A. Tziotziou,	Erasmus MC
Supervisor:	Dr. ir. A. C. Akyildiz,	TU Delft & Erasmus MC
Thesis committee:	Dr. ir. A. C. Akyildiz,	TU Delft & Erasmus MC
	Dr. M. J. Mirzaali Mazandarani,	TU Delft
	Dr. ir. F. J. H. Gijsen,	TU Delft & Erasmus MC

TU Delft Erasmus MC Universitair Medisch Centrum Rotterdam

Summary

Background Ischemic stroke is a major cause of death worldwide. Atherosclerosis in the carotid arteries is an established predictor of these events. Ideally, patient-specific prevention plans can be developed that target advanced plaque development prior to events. Morphometry of advanced calcified plaque phenotypes can be assessed through Computed Tomography Angiography (CTA) but predicting progression on morphometry alone is insufficient as atherosclerosis is nonlinear and heterogeneous. Therefore, it was hypothesized that biomechanical triggers stimulate advanced plaque growth. The biomechanical response can be observed through structural stress and strain in the vessel wall as a response to plaque composition, blood pressure and tethering. So, the research aim of this study is to develop a framework that allows for local and global assessment of structural biomechanical stimuli and morphometrical changes in atherosclerotic carotid arteries

Methods Nine CTA scans paired at baseline and follow-up were selected from the Plaque At RISK study. The carotid bifurcation at the cervical spine was segmented by two independent observers using QAngioCT (Medis Medical Imaging, Leiden, The Netherlands). Contour data was reconstructed into a 3D geometry using a two-phase developed method in which 3D surface was computed first, and the second phase converted this to volumetric parts. Finite Element (FE) models were developed for baseline geometries where Neo-Hookean for calcified and Holzapfel-Gasser-Ogden for non-calcified materials were assigned. For both timepoints, local morphometry was defined in wall thickness (WT), principal curvatures and calcium localization. Contour maps allowed the local association analysis between biomechanics and morphometry. Global plaque progression was computed using the morphometrical parameters and overall plaque burden (PB).

Results This pipeline was successfully run for nine different carotid arteries, which proved overall robustness. The Dice similarity index computed an average segmentation observer similarity of 0.80 (St. Dev. 0.06) and 0.87 (St. Dev. 0.07) for surface reconstruction. Throughout reconstruction, the FE-modeling set the requirements for reconstruction outcome thus the focus was laid on connecting these phases. No patient data was made available during this study, so standardized systolic blood pressure resulted in an average maximum stress of 269.07 kPa and 0.14 strain. Morphometrical analysis detected diseased WT in seven out of nine cases at baseline and all at follow-up. Local principal curvatures uncovered a relation with diseased thickening, indicating its success in detection of irregularities on a surface. Calcified tissue was found in all cases but one at baseline. Average morphometrical change increased 2.71 mm (St. Dev. 7.86 mm) in maximum WT, 0.69 % (St. Dev. 5.75 %) for maximum PB and 12.91 mm^3 (St. Dev. 12.50 mm^3) for calcium. These preliminary results highlighted the importance of multicomponent morphometry analysis. Moreover, correlations between calcium growth and stress (R^2 = 0.33) and WT increase (R^2 = 0.67) indicate that future studies should focus on comprehending atherosclerotic pathways involved in calcified plaque formation.

Conclusion This developed method has laid the groundwork for future research and exposed important relations between analysis methods. The close dependency between reconstruction and FE-modeling, and anatomy and biomechanics emphasize that there is still a lot to discover.

Keywords: Atherosclerosis, Calcium, Carotid arteries, CTA, Finite Element Analysis, Morphometry, Plaque progression, Structural stress, Structural strain

Acknowledgements

With this thesis, I am ending my time as a student at TU Delft. These past years, many people have supported me in various ways and I want to point out the people that helped me get through this last year.

Firstly, I want to thank everybody at the Biomechanics lab in the Biomedical Engineering group at the Cardiology Department of Erasmus Medical Center. I have seen a lot of students come and go in this past year but this group has always welcomed everyone with open arms. Especially my fellow students who, between all the long days of hard work and spontaneous brainstorms over coffee, always made time for sunny lunch breaks outside, pumpkin carving or a drink at Westkop. After studying my first year from home it felt good to spend this time with people in- and outside of the office. The time we spent together has lasted long enough and although I will not miss that old, grey tower, I will wonder about the people that I've met there.

Secondly, I want to thank my supervisors for their support and coaching throughout my internship, literature and thesis this past year. I want to thank Ali for always seeing the positive in a situation and sharing all your valuable knowledge. I also want to thank Katerina for your supervision all this time. Our weekly online and in-person meetings were always a good balance of discussing serious topics and possible future trips to a sunny island somewhere far far away. You both have inspired and motivated me throughout and I hope your enthusiasm sticks with me as I continue my path. You have learned me so much and wish you all the best for your future goals.

Finally, I want to express my gratitude to my parents, my sisters and friends for your never-ending patience, mental support and motivational words all these years. Some have been there from the start and others joined the ride halfway through but I am happy you get to see the end. Thank you for being there during the highs, the lows, and for the many laughs in between.

Lies Quataert
Delft, April 2023

Contents

List of Figures

List of Tables

Nomenclature

Abbreviations

Abbreviation	Definition
.ODB	Abaqus output database file format
.STL	Stereolithography file format
.TEC	Text Encoding Conversion toolkit file format
.TXT	Text file format
2D	2 dimensional
3D	3 dimensional
AHA	American Heart Association
AMC	Academic Medical Center Amsterdam
CCA	Common Carotid Artery
CTA	Computed Tomography Angiography, a noninvasive imaging technique in which the lumen is brightened by the administration of a contrast agent
DC	Dense Calcium, advanced plaque component
DSC	Dice Similarity Coefficient, metric used to compare segmentations and 3D surfaces on similarity
DWT	Diseased Wall Thickness, when wall thickness exceeds 1.50 mm
ECA	External Carotid Artery
EMC	Erasmus Medical Center Rotterdam
FDP	Flow divider point, the region between the ICA and ECA that marks the division of the carotid bifurcation
FE	Finite Element (analysis or modelling), solid continuum mechanics modelling technique to simulate structural biomechanics
FOV	Field of view
FSI	Fluid-Structure Interaction, modelling technique used to obtain wall shear stress
HGO	Holzapfel-Gasser-Ogden hyperelastic material model
HU	Hounsfield Units, greyscales based on tissue density in which air has a low value and dense bonelike structures have a high value
ICA	Internal Carotid Artery
ML	Machine learning algorithm
MRI	Magnetic Resonance Imaging
MUMC	Maastricht University Medical Center
NH	Neo Hookean hyperelastic material model
PARISK	Plaque At RISK study by [1]
PB	Plaque Burden, a relative metric calculated by dividing the plaque area by the total vessel area
PSS	Plaque Structural Stress, reactional force in the vessel wall to tissue tensile blood pressure and tissue tethering
PWSn	Plaque Wall Strain, resultant strain in the vessel wall resulting from structural stresses
VMTK	Vascular Modelling Toolkit (3dslicer.org), software for analyzing arteries
WSS	Wall Shear Stress, a frictional force arising from blood flowing through the artery
WT	Wall Thickness, the distance between the lumen and vessel wall surfaces

1

Introduction

Cardiovascular disease is a leading cause of death worldwide, among which ischemic stroke-related is the most prevailing [2]. This is caused by the rupture of atherosclerotic plaques in the carotid arteries [3, 4]. The presence of atherosclerosis in the carotid arteries is an established predictor for an ischemic event [2, 5].

1.1. Atherosclerosis in carotid arteries

Healthy arteries are built up of three layers, an outer vessel wall, and an inner lumen surface. From the lumen to the vessel wall the layers are tunica intima, tunica media and tunica adventitia. In atherosclerosis lipids accumulate in the intimal layer of the vessel wall, resulting in plaque formation (Figure 1.1). As a result, a sequence of inflammatory responses and cellular differentiation at plaque sites are induced by different triggers. These dynamics change the internal plaque architecture through the development and debris of different types of tissue, characterized as plaque phenotypes [6]. Ultimately, this disease is characterized as a multifactorial systemic and dynamic disease [5].

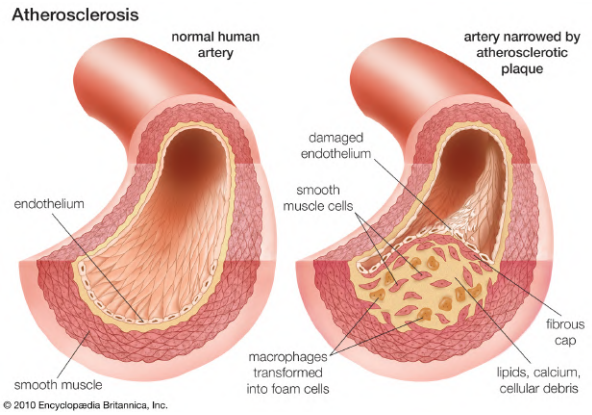

Figure 1.1: Visualization of a healthy human vessel and an atherosclerotic human vessel. In the atherosclerotic vessel, the accumulation of different types of cells are visualized. Figure retrieved from The Brittanica Encyclopedia (2020) [7]

Plaque development is a complex, highly nonlinear process [6]. The American Heart Association (AHA) has characterized plaque growth stages in phenotypes using histology and imaging data. The internal structure and identified tissue types are used to characterize the state of a plaque [2, 8, 9]. Early plaque formation (type I and II) is marked by intimal thickening and a near-normal wall thickness. Type III lesions exhibit small plaque areas with lipid pools and diffuse wall thickening. Stage IV to VIII are considered advanced plaques that have been characterized by the presence of more distinct tissues such as lipid core (IV), collagen fibres (V), haemorrhages (VI), calcifications (VII), or a mixture of fibres and calcium without lipids (VIII) [10]. Although this classification suggests a sequence of growth, all

plaques develop in a different way. Plaque elements that associate with an increased risk of stroke have been deciphered with biomechanical reasoning on plaque rupture. Studies identified that local tissue stiffness in plaque regions is influenced by composition. As a result, a plaque exhibits stronger and weaker regions. The mechanical failure hypothesis states that a plaque will rupture where stresses exceed plaque strength [11]. Of the aforementioned materials, calcified tissue is known to locally impact the strength of a plaque.

Calcium is a marker for an advanced atherosclerotic plaque. It is debris from cellular processes and can change in volume and density over time [12, 13]. Clinical studies have suggested an independent increase in density and volume will positively affect plaque stability. However, the exact relation between calcium volume, plaque growth and disease burden is unclear [12, 14–17]. Calcifications are highly prevalent in carotid arteries which increases with age [18]. In 2021, it was predicted that approximately 21.1% of the world's population has a minor to major atherosclerotic narrowing in the carotid arteries that could later lead to an ischemic event [19].

The carotid arteries play a vital role in the transportation of blood to the inner and outer vasculature of the skull, intra- and extracranial respectively [20]. On each side of the cervical spine, a common carotid artery (CCA) ascends from the aorta and bifurcates at the fourth cervical vertebrae, called the carotid sinus [21]. Upwards, the internal and external carotid artery branches continue (ICA, ECA respectively). These arteries are responsible for blood supply to the intracranial and extracranial parts of the skull (Figure 1.2) [2, 20]. Although the exact point of bifurcation shows intra- and interpatient variability, the carotid sinus has been associated with high-grade atherosclerotic stenoses and a major source for brain embolisms [22–26]. For in vivo inspection of plaques in carotid arteries, imaging modalities are used, preferably noninvasive.

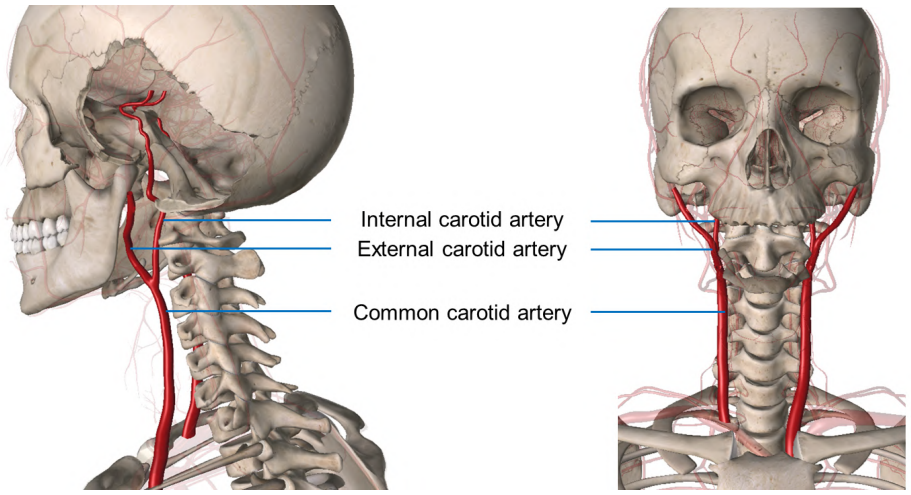

Figure 1.2: Anatomy of the carotid arteries from medial (1.2a) and anterior (1.2b) view. The common, internal and external arteries have been labelled. For better visualization, the temporal bone was removed from the medial view and the mandibula and teeth were removed in the anterior view. This image was created with Essential Anatomy 3.

Computed Tomography Angiography (CTA) is a commonly used noninvasive imaging modality for the assessment of atherosclerotic carotid arteries. This technique enhances the lumen visibility through the administration of a contrast agent. This constructs greyscale pictures with tissue density-dependent colouring. Air is black while more dense tissues like bone are shown in white [27]. The concept of soft tissue identification on CTA has been demonstrated by research, but only after ex vivo histology confirmation. When unravelling plaque morphology using only in vivo data, calcium detection is most reliable [28, 29]. Although CTA is unable to accurately detect soft tissues, it is commonly used in acute stroke settings to identify vessel thrombosis or occlusion, stenosis detection or vascular malformations [30]. Its low level of contraindications, accuracy and speed have made it a common practice in the primary inspection of carotid stenosis in stroke patients [27, 31]. The CTA greyscale has a wider spectrum than what the human eye can perceive. Therefore, computational methods are necessary to gather all the information. Consequently, this data can be used to develop in silico (computational) models for an in-depth analysis of atherosclerotic processes.

1.2. In silico modeling of advanced atherosclerotic carotid plaques

Through in silico modelling, the dynamics of in vivo plaque development can be studied over time without the use of in vitro parameters. Ultimately, these models would be able to predict plaque progression, based on patient-specific characteristics alone. As a result, fitting treatment plans can be created that aim to lessen patients' disease burden and reduce stroke prevalence. The Data - Model - Prediction - Validation - Application approach can be used to achieve this goal [32]. Thus, the primary objective of this study is to establish a foundation for future research by linking data and modelling tools.

Morphometrical and physiological data can be used to generate in silico models. Analysis of vessel morphometry describes *geometrical parameters* in shape and size. Figure 1.3a illustrates these in an idealized 3-dimensional (3D) vessel segment. Here, wall thickness (WT) is the difference between the inner radius (R_i) and outer radius (R_T), and segment length (l) is longitudinally measured. The inner radius will decrease, as WT increases due to plaque formation and progression. Although not depicted in Figure 1.3a, arteries are naturally more curved and the lumen is not perfectly circular as represented in this idealized uniform straight tube. As such, an additional parameter *curvature* κ can be introduced to describe irregularities on the surface. Furthermore, a bifurcation as in the carotid arteries significantly alters its geometrical parameters. The cross-sectional area will increase and wall thickness will decrease closer to the bifurcation, significantly changing its shape [34].

Physiological elements result from blood being pumped through the carotid artery. Figure 1.3b depicts the blood flow (Q) and direction. A longitudinal stretch along the segment length is tethering (T(l)). Blood pressure is exerted perpendicular to the inner luminal surface of the artery[33, 35–37]. The numerous pressure receptors (baroreceptors) in the lumen of the carotid sinus trigger a cellular response to biomechanical pressure and stretch [38]. Pressure-induced baroreceptors are thought to stimulate the inflammatory and growth-promoting cascades that plaques put in motion. Plaque expansion subsequently intensifies stretch-derived tethering, activating the stretch-induced receptors. This forms a self-stimulating cycle of stimuli for plaque-promoting responses [38, 39].

Thus, the susceptibility of the carotid bifurcation for plaque development can be justified by the high concentration of baroreceptors in relation to its changing bifurcation geometry due to plaque growth. This indirect relation could be clarified through biomechanical reasoning.

1.2.1. Biomechanics of atherosclerosis

The use of biomechanical reasoning to elucidate clinical findings on atherosclerosis has been a more recent field of interest. In vascular biomechanics, three parameters can be identified based on the interaction between streaming blood in a solid vessel. In short, *Shear stress* is the frictional force that arises from the differences in material properties between blood, and the luminal surface (Figure 1.4a). Second, *structural stress* can be interpreted from circumferential and longitudinal stresses.

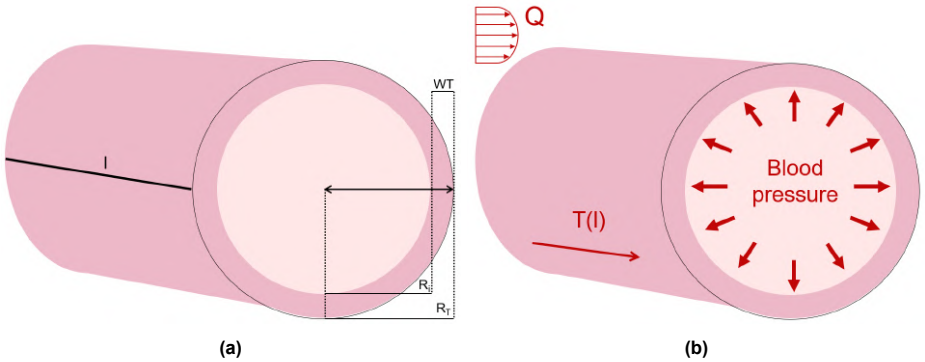

Figure 1.3: Geometrical (1.3a) and physiological (1.3b) parameters in non-stenosed arteries 1.3a: Geometrical wall measurements where l = segment length, R_T = total vessel radius, R_i = inner luminal radius and WT = wall thickness = R_T - R_i. 1.3b: Physiological parameters from blood flowing through the artery where Q = blood flow, T(l) = tissue tethering, stretch along the artery. Phenomena derived from Camasao et al. (2021) [33].

Circumferential stress is a response to the tensile force from blood pressure exerted outward and perpendicular to the lumen surface. Additionally, longitudinal stress arises from tissue tethering and blood pressure. Figure 1.4b shows a 3D illustration of structural stress in an atherosclerotic vessel. Last, *wall strain* is a resultant relative geometrical change and will only be considered in the context of structural stresses.

Wall shear stress

Blood moving along the luminal surface creates a parallel, frictional force, known as wall shear stress (WSS) (Figure 1.4a). The magnitude of WSS increases in smaller lumen diameter, lower blood viscosity or disruption of a uniform blood flow pattern [6, 40–42]. The calculation of WSS is directly dependent on blood viscosity, flow Q and radius R_i according to Camasao et al. (2021) (Figure 1.3a) [33]. Figure 1.4a illustrated the relationship between WSS and morphometrical change due to plaque growth.

The relation between WSS and plaque progression is traced back to the endothelial cell function on the luminal surface. When fluid flows along this cell lining, these cells respond to the friction caused by material differences. In light of plaque initiation and early progression a low WSS profile has been associated with plaque progression [40, 42–44]. This research is modelled through Fluid-Solid Interaction (FSI) methods, where only the lumen surface is required for vessel definition. As the hypothesis on the low-profile WSS and plaque progression only holds in the context of early plaque progression [45, 46]. This leaves unanswered questions on what triggers are involved in advanced plaque progression and calcium development. Therefore, it has been proposed that structural stresses might trigger the progression of advanced plaques.

Structural stress

Plaque structural stresses (PSS) in the vessel wall can be understood through two phenomena (Figures 1.3b and 1.4b). Wall thickness and perpendicular blood pressure cause a circumferential stress component. Longitudinal tension arises from blood pressure, radii sizes and vessel wall tethering [33]. Initially, it was hypothesized that PSS decreases when WT increases, whereas increased blood pressure raises the PSS magnitude. Through a uniform, idealized tube theory, Thubrikar (2007) theorized that the initial lumen stress response is highest with thicker vessel walls. Over the course of this thickness, the stress magnitude decreases [34]. However, in advanced plaques, the PSS response is not only dependent on geometrical and physiological phenomena. Advanced plaques come in a number of phenotypes, each with distinctly different material properties that affect the overall plaque stiffness. Therefore, it is believed that this significantly impacts the local PSS distribution in this diseased vessel wall area [47]

Structural stresses have not been a popular topic of research in the context of plaque progression

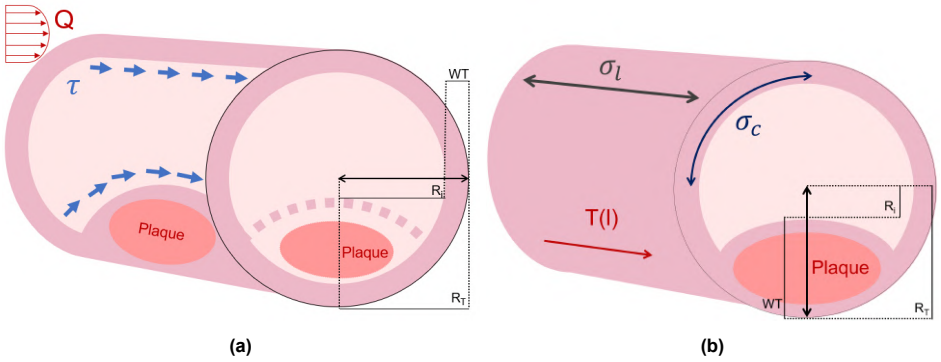

Figure 1.4: Biomechanical principles in atherosclerotic arteries. 1.4a: Principle of wall shear stress (WSS, τ, blue) illustrated. The presence of plaque is obstructive to flow Q (red). Changes in wall thickness measurements R_i and R_T due to plaque presence are shown. Formula: τ = WSS, Q = volumetric flow, μ = blood viscosity. 1.4b: Principle of structural stresses (σ, PSS, blue) and the effect of plaque growth on the change in wall thickness (WT, black). Total structural stress is the sum of circumferential stress (σ_c, dark blue) and longitudinal stress (σ_l, grey). Formulas: σ_l = longitudinal stress, σ_c = circumferential stress, BP = blood pressure, R_i = inner radius, WT = wall thickness including plaque, T(l) = tissue tethering and R_T = total vessel radius. Formulas derived from Camasao et al. (2021) [33].

in carotid arteries. As a result, the pipelines to research this process are limited. A research group at Worcester Polytechnic Institute has spent some years developing a pipeline to model WSS, PSS and plaque progression in carotid and coronary arteries. This combined modelling allows for the interpretation of the biomechanical triggers as well. In short, this group modelled 2D PSS and defined plaque growth in WT increase over time for carotid arteries and has developed this framework since 2008. This pipeline was MRI-based, and often used the same patient sets in different publications. With this pipeline, it has been established that intraplaque haemorrhage increases PSS, and cyclic blood pressure application in the simulation is linearly related to the PSS output [47–50]. Moreover, a negative correlation was found between PSS at baseline and short-term WT increase [51–53]. However, at the second follow-up ($\pm$ 36 months) this correlation did not hold in their population [54]. Subsequently, this research group published a line of papers on the same relation in coronary arteries. On this topic, more independent publications each have reported different correlations and conclusions on the predictive value of PSS for plaque progression [11, 55–58]. This lack of uniform, independently drawn conclusions shows that there is no consensus on the role of PSS in relation to plaque progression and that more research is needed to explore this process.

The importance of plaque phenotyping in computational models is evident. By use of Finite Element (FE) modelling, multiple components can be assembled and assigned fitting material behaviour in one model. The different materials of plaque composites can accurately mimic the material behaviour of the vessel as a whole [13, 16, 47, 59–62]. More studies have recently published an initial framework to evaluate the relationship between PSS and plaque morphology, although a prediction model is yet to come. The inclusion of plaque composition has been reported in the initial model and the simulations regarding 3D geometrical stress results. [45, 63, 64]. As existing frameworks were either developed for plaque rupture, coronary arteries or lacked transparency to reproduce their pipelines, a new framework needs to be designed that integrates FE simulations with the morphometrical assessment of atherosclerotic carotid arteries.

Wall strain

Plaque wall strain (PWSn) represents the relative change in dimensions as a result of the stresses it is exposed to. In the scope of this research, this metric is calculated for the PSS response alone. Due to this relation, PWSn is also directly affected by material stiffness. This strain is known to present a similar distribution as PSS and is therefore closely related to plaque composition as well [65]. It has been presented that soft tissues will increase local PWSn [50]. Although retrieval of this data is a simple addition to the PSS FE modelling, it is hardly reported simultaneously. Given the recent interest in the predictive value of PSS, its direct link with PWSn indicates that this parameter could be of value as well.

1.2.2. Finite Element modeling

Finite Element modelling is a computational method for numerical solving differential equations. In this structural analysis, the carotid geometry is discretized into a finite number of pieces called elements, that are connected to each other through nodes, for which differential equations will be solved. The mesh defines the shape and number of nodes on these elements. Each element is assigned a material model that describes its mechanical behaviour in the simulation. The advantage of FE analysis is that deformations in response to applied loading conditions can be predicted in silico [66].

Material models are used to describe the mechanical response of the elements. In solid continuum mechanics, arteries and atherosclerotic plaques are often modelled as hyperelastic materials as this tissue assembly has experimentally shown highly nonlinear elastic and nearly-incompressible behaviour [67]. This is modelled with the strain energy density function (SEDF, ψ) which describes the stored strain energy due to deformations in relation to neighbouring elements. From this, the resultant stress and strain can be obtained [68, 69]. Equation 1.1 describes the hyperelastic SEDF that is composed of a deviatoric and volumetric component. The deviatoric ψ is further defined by isotropic and anisotropic characteristics of material. The isotropic component represents a non-collageneous matrix reaction whereas the anisotropy describes the fibre-reinforced collageneous component response. The volumetric component depicts the rotating, transforming or stretching material response [67, 70–73].

$$\psi(\tilde{C}) = \psi_{dev} + \psi_{vol} = \psi_{iso}(\overline{C}) + \psi_{ani}(\overline{C}) + \psi_{vol}(J) \tag{1.1}$$

1.3. Research scope and objectives

Only a few frameworks have been published that integrate FE-modeling and morphometrical parameters [45, 54, 63, 64]. With the lack of transparency on method details or aim at coronaries, there is no existing method available for research. So, the aim of this research is to develop a new computational framework that enables local and global assessment of plaque morphometry and structural biomechanics, to answer questions on what the geometric changes in plaques over time are and what their potential biomechanical triggers could be.

The development of this pipeline will be achieved through multiple challenges based on the transition from data to modelling. First, CTA scans of symptomatic patients with calcified atherosclerotic plaque formation in carotid arteries are obtained from the Plaque At RISK (PARISK) study [1]. These are segmented, analyzed and 3D coordinates are extracted. Next, 3D surfaces and volumes are reconstructed of the carotid bifurcation from baseline and follow-up scans. Third, FE-simulations on baseline geometries mimic blood pressure exposure and the structural stress and strain responses are obtained. Simultaneously, morphometrical parameters are also obtained from the reconstructed 3D surfaces. Within the development of this framework, a constant balance is required between computational costs and the level of detail. Due to the 3D reconstruction, the computational costs of this framework are traded off with clinical accuracy and resolution. The robustness of the pipeline is tested by running it for multiple cases, which delivers preliminary results on the topic.

1.3.1. Report outline

This study has two goals: development and demonstration of the pipeline. Figure 1.5 illustrates the structure of this study. Chapters 2 and 3 describe the methodology for segmentation, reconstruction, FE-modeling, morphometry and post-processing. Methods are illustrated with one case. Chapter 4 presents the outcome of the framework and preliminary results from the demonstrations. Finally, Chapter 5 evaluates the pipeline and interprets these results and the study is concluded in Chapter 6.

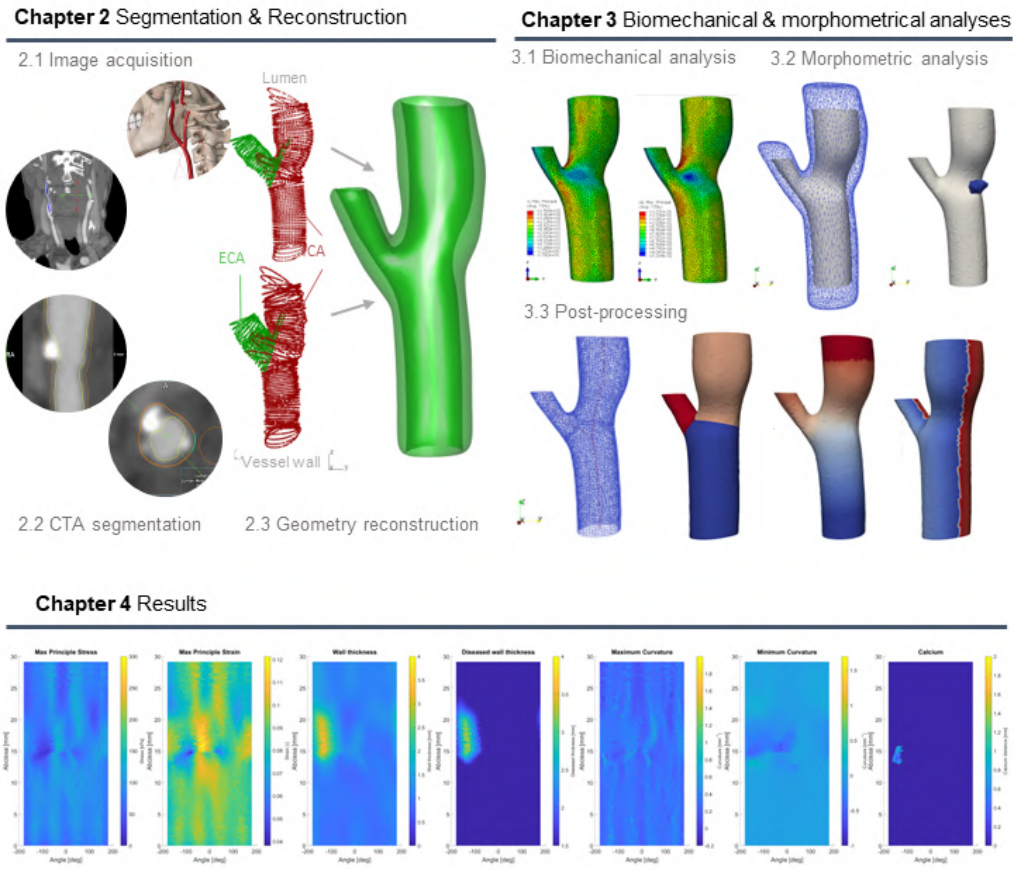

Figure 1.5: Overview of the structure of this study.

2

Segmentation and reconstruction methodology

The first step in researching the relationship between biomechanics and morphometry is to obtain the geometry of the patient-specific carotid arteries. In short, Computed Tomography Angiography (CTA) is segmented and the contours of the lumen and vessel wall are extracted. These are converted into 3D surfaces and assembled with plaque components. Additional data can be found in Appendix A.

2.1. Population description

This study included a random subset of ten carotid arteries from the Plaque At RISK (PARISK) database [1]. This multicenter study included patients that had suffered a transient ischemic attack, amaurosis fugax or a minor stroke with neurological deficits in the anterior circulation. Additionally, patients had an atherosclerotic plaque with < 70 % carotid artery stenosis on the ipsilateral ICA side and were not scheduled for a revascularization procedure. At baseline, clinical data on patient characteristics, medication use and cardiovascular risk factors were collected. Also, a Multidetector-row CTA (MDCTA) was made and blood was drawn at this inclusion point. Over the course of two years, patients were followed up on changes in the clinical data, medication and risk factor affiliation. Based on clinical data, patients were presumed to have an increased risk of recurrent stroke. After two years the MDCTA was repeated [1, 74].

The subset of patients was chosen to best represent the cohort in the PARISK study [1]. CTA scans were chosen from three different centres: two carotids were obtained from Academic Medical Center Amsterdam (AMC), seven arteries were scanned at Erasmus Medical Center Rotterdam (EMC) and one carotid bifurcation at the Maastricht University Medical Center (MUMC) [1]. Additionally, a total of four patient pairs, one single left and one single right carotid were selected. This left a balance of five left and five right carotid arteries. Although patient data was obtained in the original clinical trial, this was not available at the time of this study. Therefore, interpatient variability was accounted for by considering these cases as ten individual vessels [22, 23].

2.1.1. Image acquisition

The CTA scans were taken from the PARISK database [1]. The scanning protocol required a multidetector row contrast-enhanced CTA system (120 kVp, 150-180 mAs, collimation 16 x 0.75 mm, or 64 x 2 x 0.6 mm, pitch < 1 mm). The scan was taken from the ascending aorta to the intracranial circulation (3 cm above the sella turica). Reconstruction of the images was done with a field-of-view (FOV) of 120-160 mm, matrix sized 512 x 512, slice thickness of 1.0 mm, increment 0.6 - 0.7 mm and intermediate reconstruction algorithms were used [1]. All selected scans were reconstructed with the B31f kernel. Following Equation 2.1, this resulted in a voxel size of 0.23 - 0.31 mm^3 [75].

$$voxelsize = pixelsize * slicethickness = \frac{FOV}{matrixsize} * slicethickness \tag{2.1}$$

2.2. Image segmentation

Segmentation is the process of identifying and separating a region of interest from an entire scan [76]. In CTA, the lumen is brightened by the administration of a contrast agent. Here, a 30 mm CCA-ICA centerline was segmented with the carotid bifurcation at the centre [77]. For all cases, baseline and follow-up scans were segmented at both time points. Segmentation of CTA images was performed using the QAngio software package (Medis Medical Imaging, Leiden, The Netherlands). This package consisted of the Medis Suite environment (version 4.0.24.3), QAngio CT RE (version 3.2.0.13), QAngio CT ReportWizard (version 3.2.0.13) and QAngio 3D Workbench (version 1.6.14.2). The first two were used for the segmentation process, the latter two were used for data analysis and extraction.

Segmentation was executed following the workflow from QAngio CT. A semi-automatic seeding method computed a centerline for common and internal carotid artery branches (Figure 2.1a). Following this centerline, contours were automatically drawn in for the lumen and the vessel wall. Per slice, these contours had to be manually adjusted (Figure 2.1b), which formed a 3D set of contours (Figure 2.1d). When contouring was complete, a second centerline was set from the same starting point in the CCA, into the external branch. The process was repeated and the segmentation was completed. The contours represent the inner lumen and outer vessel wall boundaries between which QAngio could perform its composition analysis. Hounsfield units (HUs) are the density-related greyscales in CTA, which can be used to identify different tissue types [29]. Four tissue types were labelled through HU-thresholds in QAngio CT (Table 2.1, Figure 2.1c). QAngio 3D Workbench calculated 3D contour data for the lumen and vessel wall. Moreover, 3D component surfaces were computed for the corresponding labelled HU-voxels.

Table 2.1: Hounsfield Unit (HU) thresholds that were applied during the segmentation process. Values retrieved from De Weert et al. (2006) [29].

Tissue type	HU range
Lumen	300 - 500 HU
Necrotic Core	-250 - 75 HU
Fibrous Fatty Tissue	75 - 200 HU
Fibrous tissue	200 - 600 HU
Dense Calcium	600 - 2048 HU

Interobserver similarity

The segmentation analysis was performed by two independent researchers. In order to quantify the effect of observer training in segmentation and the consequences for geometry reconstruction, the (dis)similarity of contours was examined using the Dice similarity coefficient (DSC). This coefficient considers this overlap between two observations of the same region of interest [78]. The DSC is computed following Equation 2.2. A score of 1 is a perfect overlap between the segmentations [79].

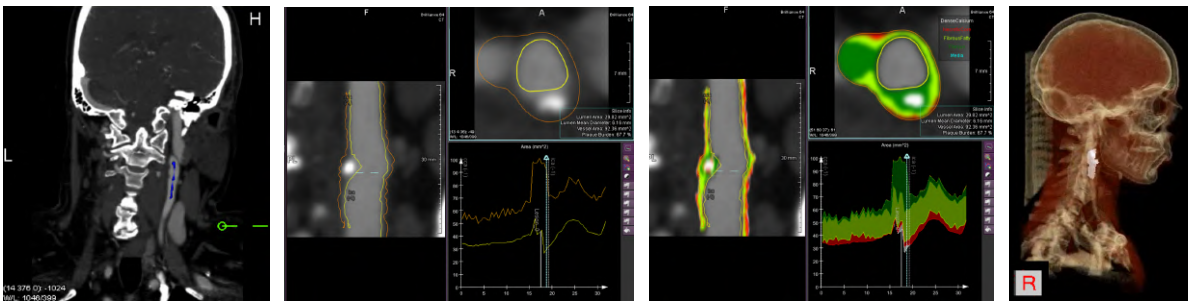

(a) (b) (c) (d)

Figure 2.1: 2.1a: Seeded pathway in blue, segmentation in the anterior CTA plane. 2.1b: Manual contour adjustment during segmentation. Orange = vessel wall, yellow = lumen. 2.1c: Contours with labelled voxels. Dark green = fibrous tissue, light green = Fibrous fatty tissue, red = necrotic core, white = calcium. 2.1d: 3D plane of segmented surface in medial view.

$$DSC = \frac{2 \times |A \cap B|}{|A| + |B|} \tag{2.2}$$

The DSC was calculated for 18 CCA-ICA segments at baseline and follow-up (N = 36) and lumen and vessel wall contours were compared separately. This metric was computed using the SegmentComparison function from the SlicerRT toolbox (3D Slicer version 5.0.3) [80]. Segmentations were performed by two observers. From literature, a DSC of 0.7 was considered an acceptable lower boundary [81].

2.3. Geometry reconstruction

Originally, geometry would be automatically reconstructed in the QAngio post-processing. The QAngio 3D Workbench offered an export of reconstructed lumen and vessel wall in STL-described surfaces. However, two issues arose in this approach. Firstly, lumen and vessel wall surface reconstruction started on a point on the centerline, approaching the contours with hexagonal rings [82], rather than connecting the contour coordinates. As a result, the surface would deviate significantly from the contours, especially around thickened and calcium-rich plaque areas. Secondly, the computation of the lumen, vessel wall and composition surfaces was done independently of each other. So, the lumen and vessel wall surfaces did not match the contours sufficiently, and composition would be detected outside of these surfaces. Moreover, the component surfaces also intersected in regions which caused holes in the assembly and insufficient coherency in the vessel wall definition.

This setback required a new reconstruction method that would start from these contour coordinates rather than estimate these. The greatest challenges arose from the 3D modelling and accurate bifurcation definition. Principles from the 3D-printing and Geomatics communities were closely related to the requirements in geometry description for Finite Element (FE) modelling [83, 84]. Finally, a transparent method was set up to best oversee data transformations and topology definition. The steps are briefly outlined in the following paragraphs, details are described in Appendix A. Data from the segmentations were retrieved in two formats. Lumen and vessel wall contour coordinates were retrieved from QAngio 3D Workbench in text-file. Plaque components were obtained in the surface description in STL-format. The bifurcation surface was reconstructed completely and plaque components were converted to simplify assembly later. Both phases introduced methodological considerations.

2.3.1. Lumen and vessel reconstruction

Surface reconstruction from coordinates was done for the lumen and vessel wall based on an inhouse written Matlab code. The CCA-ICA and CCA-ECA segments were reconstructed separately, and later unified. The step-by-step flow is set out in Figure 2.2. First, the coordinates corresponding to the contours were extracted from the QAngio 3D Workbench extension. In MATLAB 2021R, the coordinates were used to identify a 2-dimensional (2D) mask and transformed into 3D using an isosurface with a Z-axis orientation. This isosurface was smoothed in Vascular Modeling Toolkit (VMTK, 3slicer.org). The smoothed segments were capped and unified to a bifurcation in Grasshopper 3D version 1.0.0007 (Rhinoceros® version 7.24). In Meshmixer both structures were remeshed to smoothen the surface and reduce computational costs [85]. Finally, in Abaqus Unified FEA SIMULIA from Dassault Systèmes (version 2020), the lumen was cut from the vessel wall using a Boolean function. This left a 3D solid carotid bifurcation geometry that could directly be subjected to FE pre-processing.

The reconstruction method and its manual steps involved were assessed using the aforementioned DSC metric (Equation 2.2, Section 2). The initial CCA-ICA isosurface is compared to the final segment before Boolean union with the ECA segment. Baseline, follow-up, lumen and vessel wall segments were compared individually, yielding a sample size of 36 surfaces.

2.3.2. Plaque composition

Plaque component surfaces were reconstructed by QAngio through the marching cubes algorithm [86]. Tissue labels were assigned to the voxels based on HU thresholds (Table 2.1, Figure 2.1c). Two bottlenecks were identified, and not all could be solved. First, complications arose from inconsistent soft tissue voxel labelling. Some voxels were assigned multiple labels and others none. This created

overlapping tissue regions and holes in the composition. Moreover, components that crossed the manually drawn contours were not corrected. As a result, components crossed the inner lumen or outer vessel wall boundaries. This inconsistent tissue labelling could not directly be solved. Secondly, composition reconstruction was thoroughly insufficient. This computed triangulated surfaces with great detail, that computational costs overrode software capacity. This made it impossible to assemble a fully defined vessel structure for further simulation and assessment.

In general, in vivo identification of soft tissues on CTA without validation is a known challenge [28, 29]. Lipids, necrotic cores and intraplaque haemorrhage look similar and validation of at least one other source is required [45, 87]. Additionally, research on the Rotterdam study has presented a correlation between calcified tissues in carotid arteries, and later neurological events [88]. Therefore, this preliminary research was appointed to focus on PARISK patients that presented calcified plaques at the carotid bifurcation, at least on the follow-up scan. Thereby excluding other tissue components. Calcium surfaces were obtained from QAngio and converted to solid entities in Grasshopper. Individual solid bodies were imported and assembled in the vessel geometry in the FE pre-processing in Abaqus.

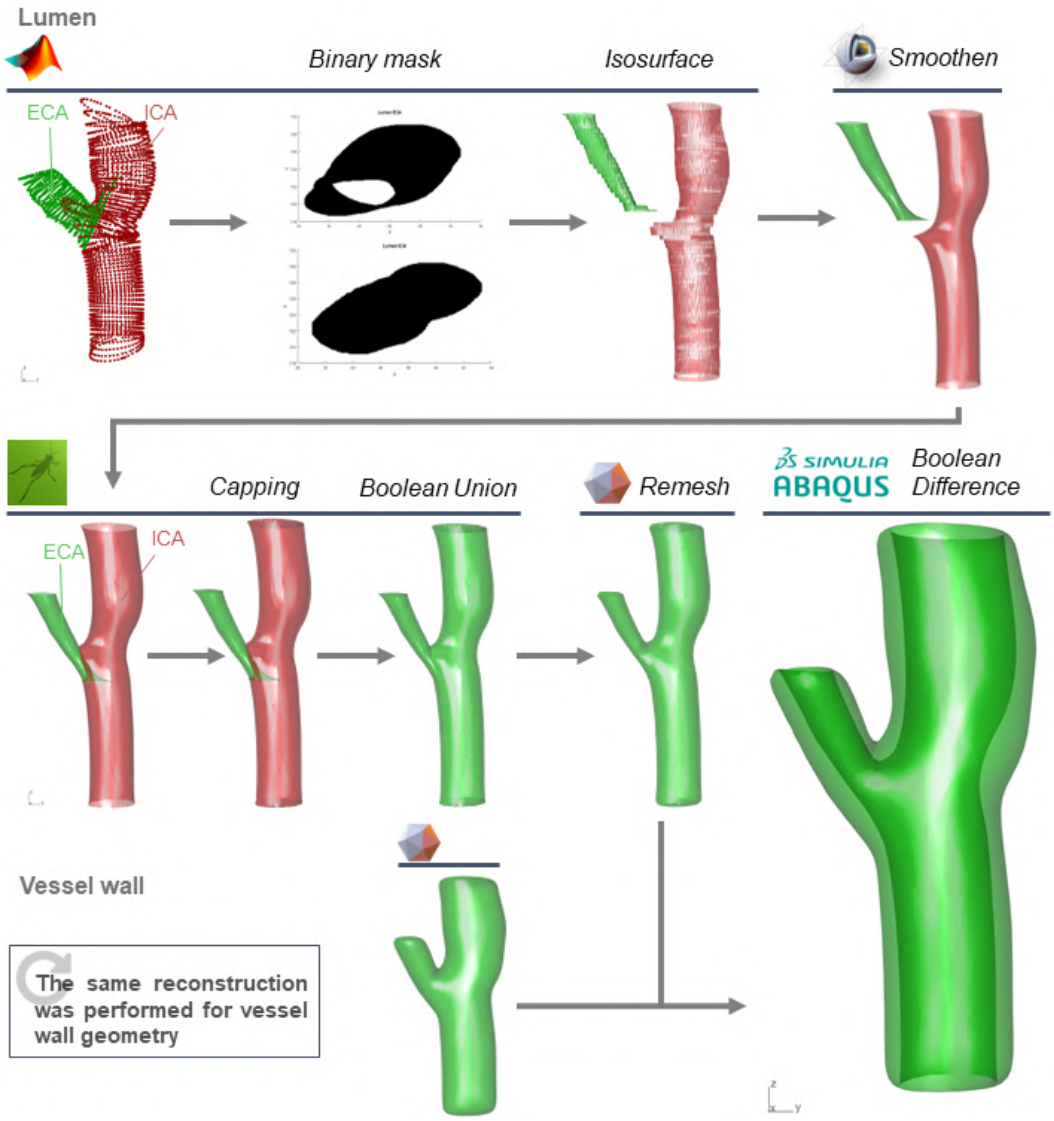

Figure 2.2: Summary of the CTA-based surface reconstruction phase after which the surface was converted to a solid entity. Each step is based on the software that executes it. First, a Matlab code computes an open surface based on the coordinates in each slice. Then, this surface is smoothed in Vascular Modeling Toolkit (3dslicer.org). Next, a Grasshopper function panel closes these surfaces and unifies the ICA and ECA branches. Meshmixer performs a final remeshing to smoothen the bifurcation. Finally, a boolean cut creates hollow vessel geometry in Abaqus.

3

Biomechanics and morphometrical methodology

This chapter outlines the second phase of the methodology comprising the biomechanical, morphometrical and post-processing analyses. Biomechanics is assessed through a structural Finite Element (FE) analysis of the carotid artery geometry. Morphometrics is used to assess the geometry of the carotid and its changes from baseline to follow-up. Finally, both outputs were processed to 2D contour maps which allowed for local correspondence between metrics and a global interpretation of plaque progression.

3.1. Biomechanical modeling

Structural analysis was performed through Finite Element (FE) modeling to obtain the structural stress distribution throughout the carotid geometry. Pre-processing steps include model assembly, material assignment, mesh definition and specifying load application, boundary conditions and the analysis step. All baseline cases followed the same steps and all simulations were performed using Abaqus Unified FEA SIMULIA from Dassault Systèmes (version 2020) [89].

3.1.1. Geometry assembly

The reconstructed carotid bifurcation surface from Chapter 2 was imported to Abaqus as an orphan mesh, and converted to a solid part using a dedicated plug-in (Figure3.1a) [90]. Cases contained one to five calcified bodies, which were imported as individual solid parts (Table C.1, Appendix C). All parts were identified as individual element sets and were merged in the assembly module. In Figure 3.1b the element set for the calcified body is highlighted in red after the parts were assembled.

3.1.2. Material models

Calcified and non-calcified tissue have been identified in this assembly. As such, hyperelastic material models have been used to describe their behaviour. These materials are described through their strain energy density functions (SEDFs). Calcified tissue was assigned the isotropic Neo-Hookean material (NH) and non-calcified tissue behaviour was described through the anisotropic Holzapfel-Gasser-Ogden model (HGO).

The hyperelastic, nearly-incompressible, homogeneous, isotropic NH model is described in the SEDF in Equation 3.1, which is defined in an isotropic and volumetric component. In Equation 3.1, C_{10} is a material constant, $\overline{I}_1$ is the first principal invariant of the right Cauchy-Green deformation tensor, D_1 is the (in)compressibility coefficient and J represents the volume ratio. Coefficients were taken from Heller et al. (2019) (Table 3.1) [91], where calcium was considered nearly incompressible. According to literature, the NH material model is a good fit for calcified tissue's stress response [92, 93].

$$\psi_{NH} = \overbrace{C_{10}(\overline{I}_1 - 3)}^{\psi_{iso}(\overline{C})} + \overbrace{\frac{1}{D_1}(J-1)^2}^{\psi_{vol}(J)} \tag{3.1}$$

Non-calcified tissue in this geometry was the remainder of the 3D solid carotid geometry, minus the calcified bodies. These elements were assumed arterial tissue and were assigned the hyperelastic HGO model. The anisotropic HGO model is known to present the behaviour of different arterial layers through its combination of isotropic hyperelastic extracellular matrix and the anisotropic contribution of local collagen fibre families [67, 72, 73]. Its SEDF is given by Equation 3.2 and 3.3, which is built up of an isotropic, volumetric and anisotropic part. Trivial parameters are the material constant C_{10}, incompressibility coefficient D, k_1 is the relative stiffness of the fibre families for the small strain range, k_2 is a dimensionless stiffness parameter for the large strain range, and κ represents the fibre dispersion. If the κ equals 0, fibres are perfectly aligned. When it is equal to 1/3 the fibres are randomly distributed and present isotropic behaviour [67, 72, 73, 94].

$$\Psi_{HGO} = \overbrace{C_{10}(\overline{I}_1 - 3)}^{\psi_{iso}(\overline{C})} + \overbrace{\frac{1}{D}(\frac{(J^{el})^2 - 1}{2} - ln(J^{el}))}^{\psi_{vol}(J)} - \overbrace{\frac{k_1}{2k_2}\sum_{\alpha=1}^{N} exp[k_2 < \overline{E}_\alpha >^2] - 1}^{\psi_{ani}(\overline{C})} \tag{3.2}$$

$$\overline{E}_\alpha = \kappa(\overline{I}_1 - 3) + (1 - 3\kappa)(\overline{I}_{4\alpha\alpha} - 1) \tag{3.3}$$

As CTA was the only input source of anatomy, no vessel wall layers could be identified nor were collagen fibre family orientations researched. Therefore, global collagen parameters from Swaab et al. (2021) were implemented that assume one fibre family and isotropy (Table 3.1) [94]. Additionally, full incompressibility and homogeneity were also assumed. Table 3.1 shows the implementation of the HGO model.

Table 3.1: Material coefficients for arterial and calcified tissues. The arterial model and the calcified model were taken from literature [91, 94]. HGO = Holzapfel-Gasser Ogden material model, NH = Neo-Hookean material model, [-] = dimensionless coefficient.

Calcified tissue	NH			[91]
	C_{10}	$1.53*10^3$	[kPa]	
	D_1	$1.00*10^-6$	[kPa]	
Arterial tissue	HGO			[94]
	C_{10}	50.00	[kPa]	
	D	0.00	[kPa]	
	k_1	$26.00*10^3$	[kPa]	
	k_2	2.50	[-]	
	κ	$\frac{1}{3}$	[-]	

3.1.3. Mesh definition

A bifurcation is considered a complex geometry, so the part needed smoothening and partitioning for successful mesh generation. Inconsistencies on the surface, sharp angles and small faces could cause the mesh to fail. Therefore, the entire assembly underwent virtual topology. This merged all the surface faces that originated from the orphan mesh input and smoothed the surface. After this, the assembled part was partitioned into smaller segments. This also allowed for a more detailed mesh generation in complex-shaped areas. Moreover, the outlets were partitioned to define a region for boundary conditions and define the border for later data extraction. Figure 3.1c shows an example of this mesh preparation.

The prepared part was meshed using 4-node linear, hybrid tetrahedral elements (C3D4H) (Figure 3.1d) [63, 91]. These elements were most applicable for a complex shape under biomechanical loading with nonlinear material models without further time-consuming preparation of the geometry [63, 95].

Element size was determined through a mesh sensitivity analysis. This yielded between 116 thousand and 444 thousand elements (25 thousand to 81 thousand nodes respectively) for all simulations (Table B.2, Appendix B). Finally, adaptivity jobs were run for all cases on their calcium element sets. This was done to improve overall mesh accuracy and the rules were defined for the final increment step and based the re-meshing on the element energy density.

3.1.4. Simulation conditions

Loading conditions simulated 3D blood pressure on the inner luminal surface. A standardized uniform peak systolic outward pressure of 120 mmHG ($\approx$ 16.00 kPa) was applied (Figure 3.1e) [48, 49, 54]. *Boundary conditions* (BCs) were defined to prevent rigid body motion or rotation in any direction as this geometry represents a segment of the entire carotid artery. Encastered BCs were set at the designated partitioned regions at the CCA, ICA and ECA outlets (Figure 3.1f). *Simulation step* duration was set at 1.00 seconds, with a fixed minimum increment step of 0.005 s. A small time step is required to capture small deformations and ensure model convergence. A larger pressure load will result in larger deformations and for that, a smaller time step must be determined [63]. Nonlinear geometrical deformations were allowed in the analysis and field output requests included principal stresses and strain.

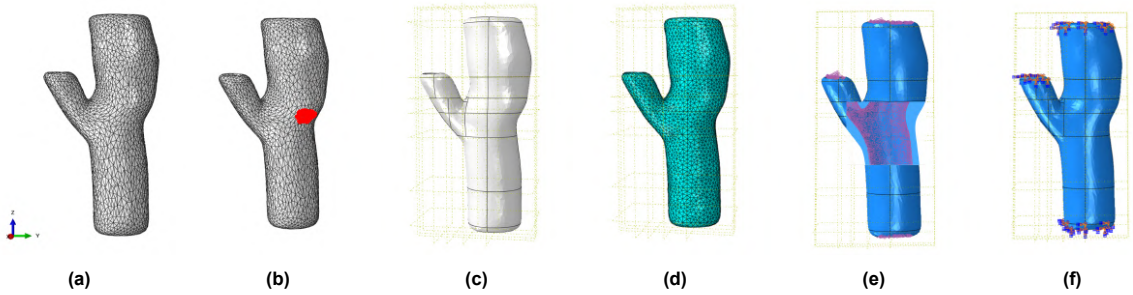

Figure 3.1: Visualization of the FE-method pre-processing steps. 3.1a: Geometry as imported in Abaqus, converted to a solid entity. 3.1b: Assembly of the vessel and calcified tissue element sets. Red = calcium elements. 3.1c: Geometry after merging faces and partitioning of the part. 3.1d: Meshed part. 3.1e: Part showing loading conditions. Cross-section shows lumen as target area. 3.1f: Part showing BCs at the outlets.

3.2. Morphometric analysis

The aim of the morphometric analysis was to assess the atherosclerotic carotid geometry in size and shape at both time points. Subsequently, this morphometrical change over time could be translated into atherosclerotic progression. Morphometrics can be subdivided into local and global parameters. Here, the local analysis is composed of five measures (Figure 3.2). First, wall thickness (WT) was measured and then filtered for diseased thickness (DWT). Next, the shape was assessed for the maximum (k_1) and the minimum (k_2) principal surface curvature. Finally, the presence of calcium was assessed in terms of location and volume (C).

As the follow-up geometry did not match with the baseline, local assessment could only be done for all parameters at one time for each carotid artery. Morphometric progression was defined globally for all aforementioned parameters, and global plaque burden (PB) was computed in the segmentation. All parameters were calculated and analyzed using VMTK and Matlab 2021a.

Wall thickness (WT) was computed using the pointwise minimum distance method from the lumen surface from the FE-analysis and the vessel wall surface as depicted in Figure 3.2a (Figure 2.2, Chapter 2). This parameter was computed for baseline and follow-up geometries. Second, WT data was filtered for values higher than the healthy carotid wall thickness of 1.50 mm [33, 96]. These areas were labelled Diseased wall thickness (DWT). This metric later visualizes the diseased regions on the lumen.

The shape description of the lumen was obtained through the principal curvatures (Figure 3.2b). The 2D metric κ shows how much each point p deviates from a straight line (Figure 3.3a). Equation 3.4

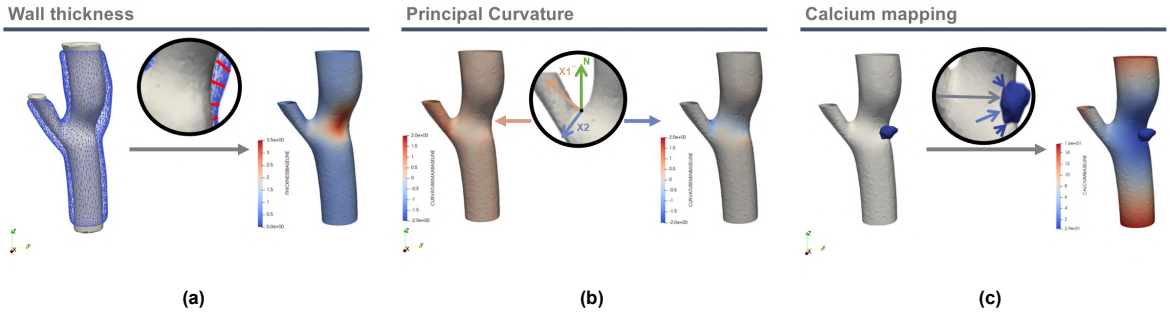

Figure 3.2: Morphometry measurement methods. 3.2a: The pointwise minimum distance computation between lumen and vessel wall surfaces to obtain wall thickness. 3.2b: point-based principal maximum (X1) and minimum (X2) curvature. 3.2c: The pointwise minimum distance computation between lumen and calcium surface. Images created using Paraview 5.9.0 RC1.

shows that this metric depends on the radius of the line or surface in which a greater radius translates to a lower curvature and vice versa. On a 3D surface curvature computation, two tangent vectors X_1 and X_2 can be computed that represent the maximum and minimum principal curvatures, respectively (Figure 3.3b, 3.2b). Surface curvature can be used to locate irregularities on the lumen surface [97].

$$\kappa = |\frac{d\mathbf{T}}{ds}| = \frac{1}{r} \tag{3.4}$$

Third, *Calcium* was analyzed for location relative to the lumen and global assessment. A pointwise minimum distance function computed the distance between each point on the lumen and calcium. Points that were further than 0.8 mm away from calcified tissue were filtered out of localization analysis (Figure 3.2c). The calcium surfaces were obtained from QAngio 3D Workbench along with volumetric data. Volume was computed using the marching cubes algorithm. This was the sum of all pixels labelled as calcified tissue, multiplied by the volume of a pixel (voxel) (Equation 3.5) [86].

$$C = \sum(p_C \times V_p) \tag{3.5}$$

Finally, global *Plaque burden* (PB) was computed in the segmentation analysis in QAngio. This metric has reportedly been correlated with highly prognostic cardiovascular risk factors [98, 99]. In Equation 3.6 the plaque area is the difference between the vessel wall area and lumen area. The plaque area is divided by the total vessel wall area, to obtain the PB. Plaque burden was obtained for the baseline and follow-up geometries in each case.

$$PB = \frac{Area_P}{Area_V} = \frac{Area_V - Area_L}{Area_V} \tag{3.6}$$

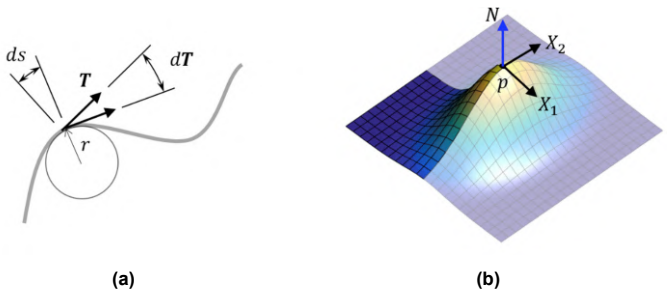

Figure 3.3: Theory of curvature computation explained for 2D (3.3a) and 3D space (3.3b) in relation to Equation 3.4. 3.3a: dT = change in tangent vector T per change in arc length ds. 3.3b: for each point p X_1 = max principal curvature, X_2 = min principal curvature, N = normal vector. Retrieved from Ghasemi et al. (2020) [100].

3.3. Post-processing

The goal of post-processing was to create an output format that allowed for local comparison of the FE output and morphometrical analysis. This could be used to describe the biomechanical behaviour in relation to morphometrical characteristics in each of the cases. The maximum principal stress and strain were obtained from the FE analysis of the baseline geometries and diseased wall thickness, surface irregularities and calcium were localized in the morphometrical analysis at baseline and follow-up. All metrics were computed on the 3D surface. The post-processing method aims to improve interpretability by transforming this data to locally corresponding 2D contour maps for each of these metrics.

Figure 3.4 illustrates the post-processing steps. The foundation is based on an in-house written code and a method described by Antiga et al. (2008) [101]. This MATLAB R2021a code combines VMTK functions and processes the data. First, all data was projected on the respective lumen surface for baseline and follow-up. The computation of a centerline divided this anatomy into three segments: CCA, ICA and ECA. The y-axis (abcissa) and x-axis (angular) coordinates were computed for each of these segments in a 501 x 501 grid. The grids were reduced to a combined CCA-ICA or CCA-ECA segment. The aforementioned projected 3D lumen data was interpolated to this grid using the nearest-neighbours algorithm. Distortions in data may emerge around the bifurcation due to the difference in diameter for the CCA and ICA or ECA.

The location of the geometry at follow-up anatomy did not correspond with the location of the baseline carotids, so no local time-dependent metric was computed. For an impression of change over time, the overall maximum, median and minimum were computed for each of the parameters at baseline and follow-up. Local association analysis was possible within baseline or follow-up parameters. Preliminary results consider the associations between parameters for all cases and were later compared with the literature.

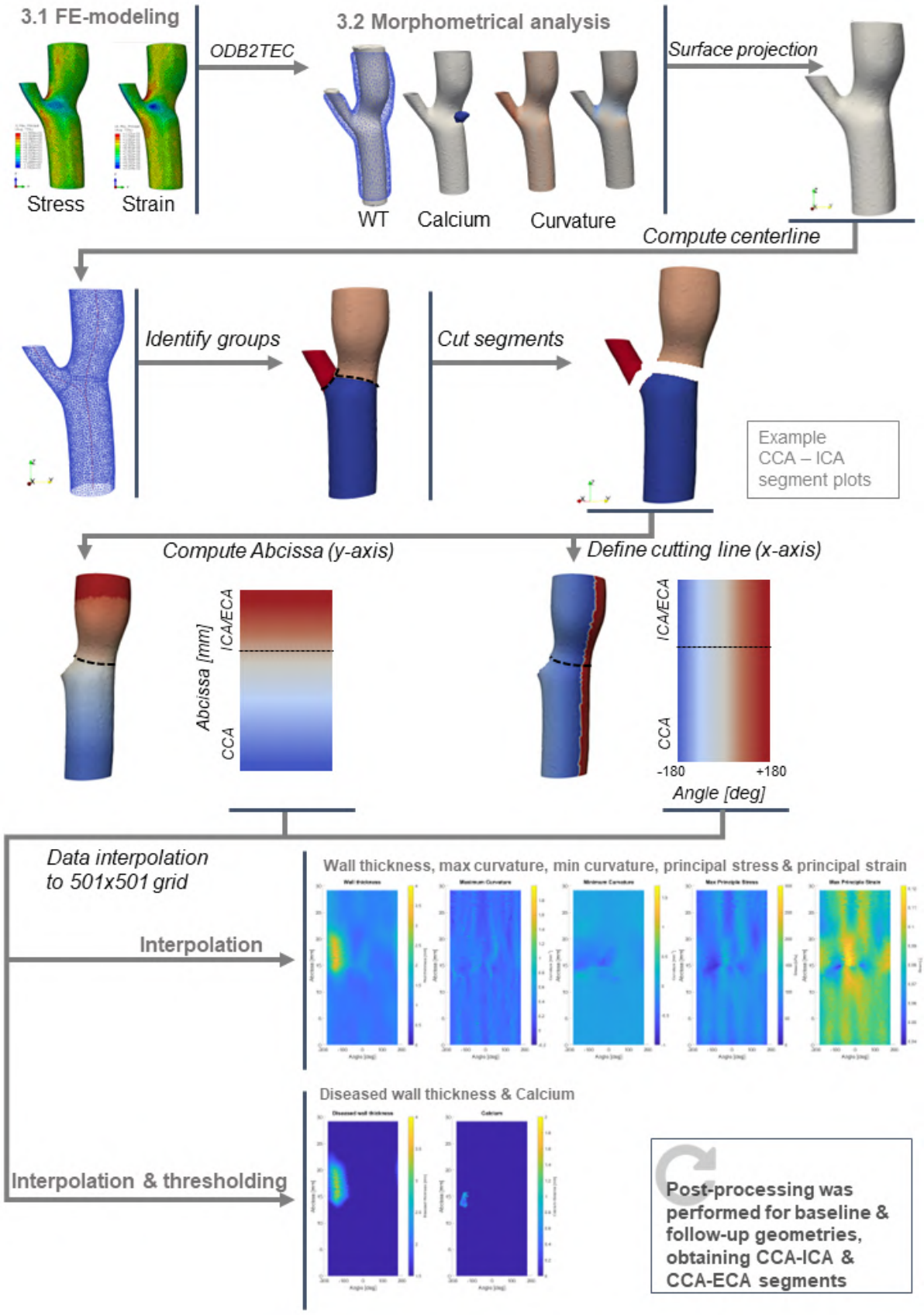

Figure 3.4: Post-processing methodology illustrated for one segment plot in one case. Output from biomechanical modeling was translated to a tec-format and integrated with morphometrical parameters. A centerline was computed to determine three segments, and the structure was split to recombine a CCA-ICA and a CCA-ECA segment. For both segments the abcissa (y-axis) and angular (x-axis) were computed for the contour plot. The 3D computed biomechanical and morphometrical data were interpolated into this grid. Diseased wall thickness and calcium localization were also filtered after interpolation. These steps are repeated for the CCA-ECA segment and the follow-up morphometrical analysis.

4

Framework and preliminary results

This chapter presents the framework and preliminary results. First, data obtained during patient processing in the framework is given. This includes segmentation and reconstruction. Second, the preliminary results obtained from the patient cases are set out. The local analysis, striking observations and global results are shown.

4.1. Framework

4.1.1. Patient exclusion

Originally, ten carotid arteries were segmented at baseline and at follow-up (Figure 4.1). This selection composes of four patient pairs and two individual vessels, and an equal left-right distribution. Over the course of processing, patient 4L was excluded, losing one patient pair. This left nine vessels total of which five were right carotid arteries. Calcified tissue was detected in seventeen out of eighteen carotid arteries.

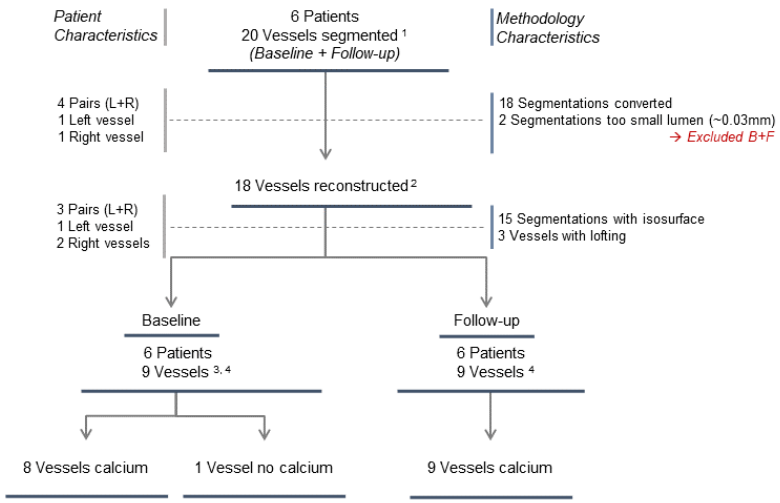

Figure 4.1: Flowchart visualizing the processing of cases throughout the methodology. One vessel was excluded due to reconstruction issues. Ultimately, three pairs, one left and two right carotids were successfully processed. Two reconstruction algorithms were used. [1] = Interobserver similarity was calculated for all segmentations (Section 4). [2] = Reconstruction methods and complications (Section 4). Dice score on reconstruction obtained (Section 4). [3] = Finite Element analysis was performed (Section 4). [4] = Morphometrical analysis performed (Section 4).

4.1.2. Image segmentation similarity

The segmentation methodology in Chapter 2 describes the method of interobserver similarity using the Dice score (DSC). The average DSC of all segmentations combined is 0.80 with a standard deviation of 6.60 %. The scores for lumen and vessel wall contours are shown in Figure 4.2a. Here, the lower boundary of 0.70 is exceeded in only one lumen segmentation. For comparison, Figure 4.2b illustrates the highest lumen Dice score of 0.9 for both observers and Figure 4.2c shows the outlier 0.6 (Figure 4.2c). Differences between observers include the segment length and a shift of the CCA surface. Detailed DSC results are illustrated in Figure A.1 in Appendix A.

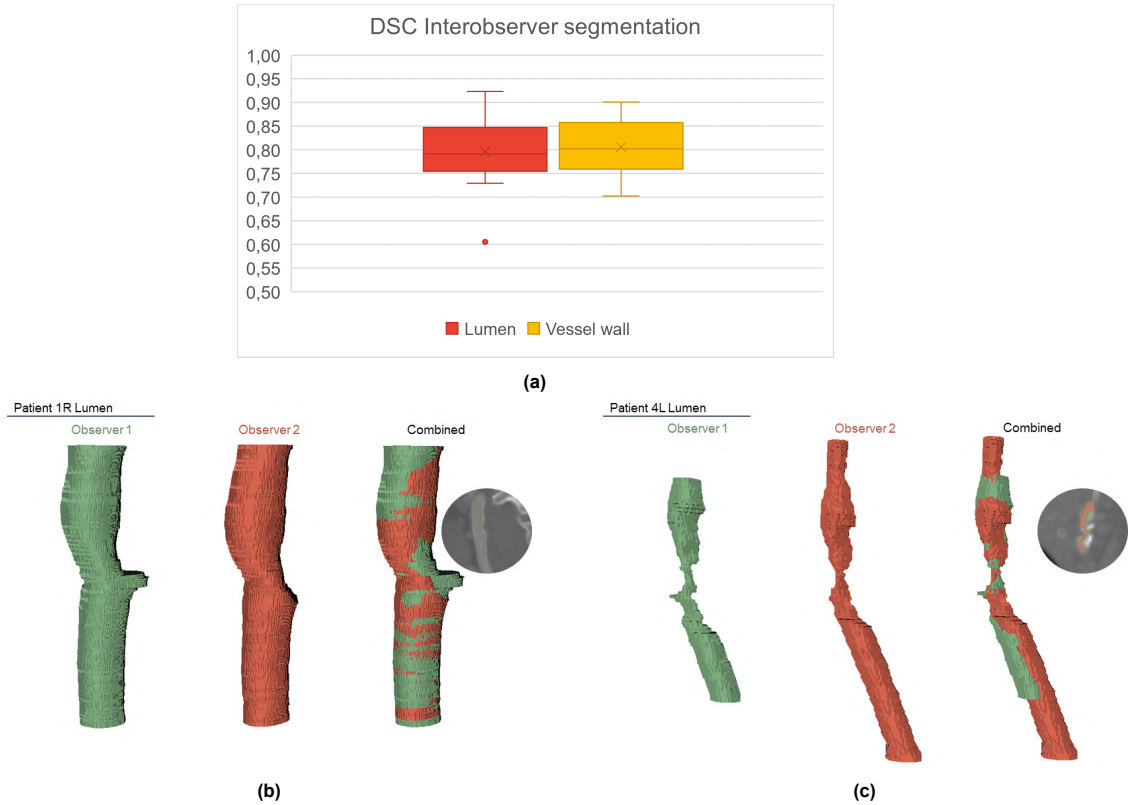

Figure 4.2: 4.2a: Distribution of the Dice similarity coefficient for the lumen and vessel wall segmentation separately. One lumen segmentation fell outside the pattern of the group data. 4.2b: Visualization of the highest lumen score of 0.9 with respect to the anterior CTA view. Red and green represent a different observer's segmentation. 4.2c: Visualization of the outlying lumen score of 0.6 in (a). The anterior CTA also shows the calcifications. Red and green represent different observer's segmentations.

4.1.3. Geometry reconstruction

Reconstruction of the patient-specific anatomy was successful for the nine vessels at baseline and follow-up (Figure 4.1). However, not all vessels were reconstructed using the same function. Three out of twenty reconstructions were performed using an alternative in-house written reconstruction code.

At baseline in cases 2L and 6R, the isosurface function could not compute a connected lumen surface due to the orientation of the segmentation slices. So, to prevent reconstruction from affecting the morphometrical analysis, the follow-up geometry was also intended to be reconstructed with the alternative algorithm. However, in case 6R the follow-up geometry could only be computed with the original method. Therefore, out of nine baseline-follow-up pairs, seven were computed with the method described in Chapter 2, one pair was processed with alternative methods and one pair was reconstructed using both methods. All baseline lumen surfaces are shown in Figure 4.3. The follow-up lumen surfaces can be seen in Figure 4.4.

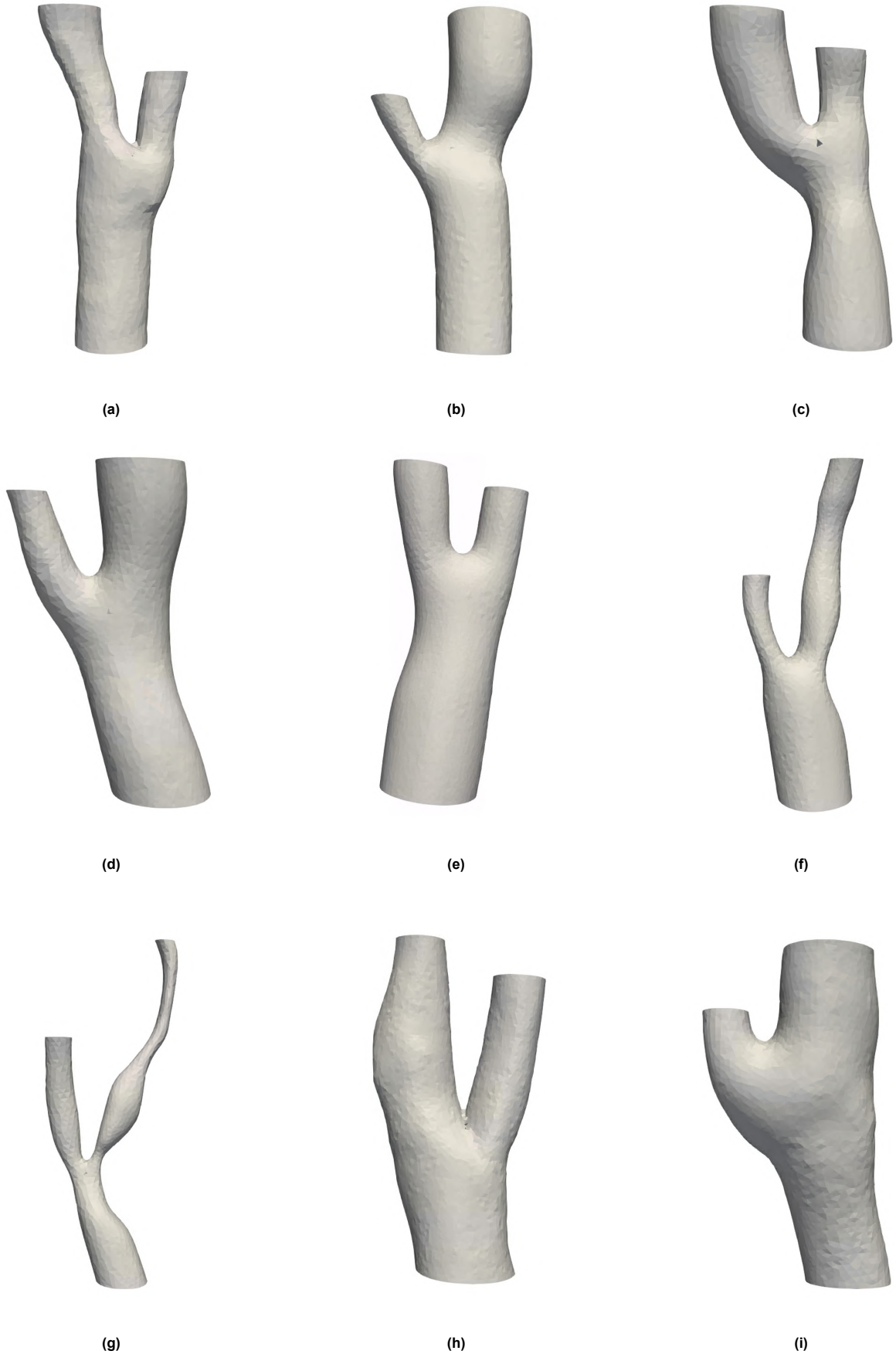

Figure 4.3: Lumen surfaces reconstructed from baseline scans. 4.3a: Patient 1L. 4.3b: Patient 1R. 4.3c: Patient 2L. 4.3d: Patient 2R. 4.3e: Patient 3L. 4.3f: Patient 3R. 4.3g: Patient 4R. 4.3h: Patient 5L. 4.3i: Patient 6R.

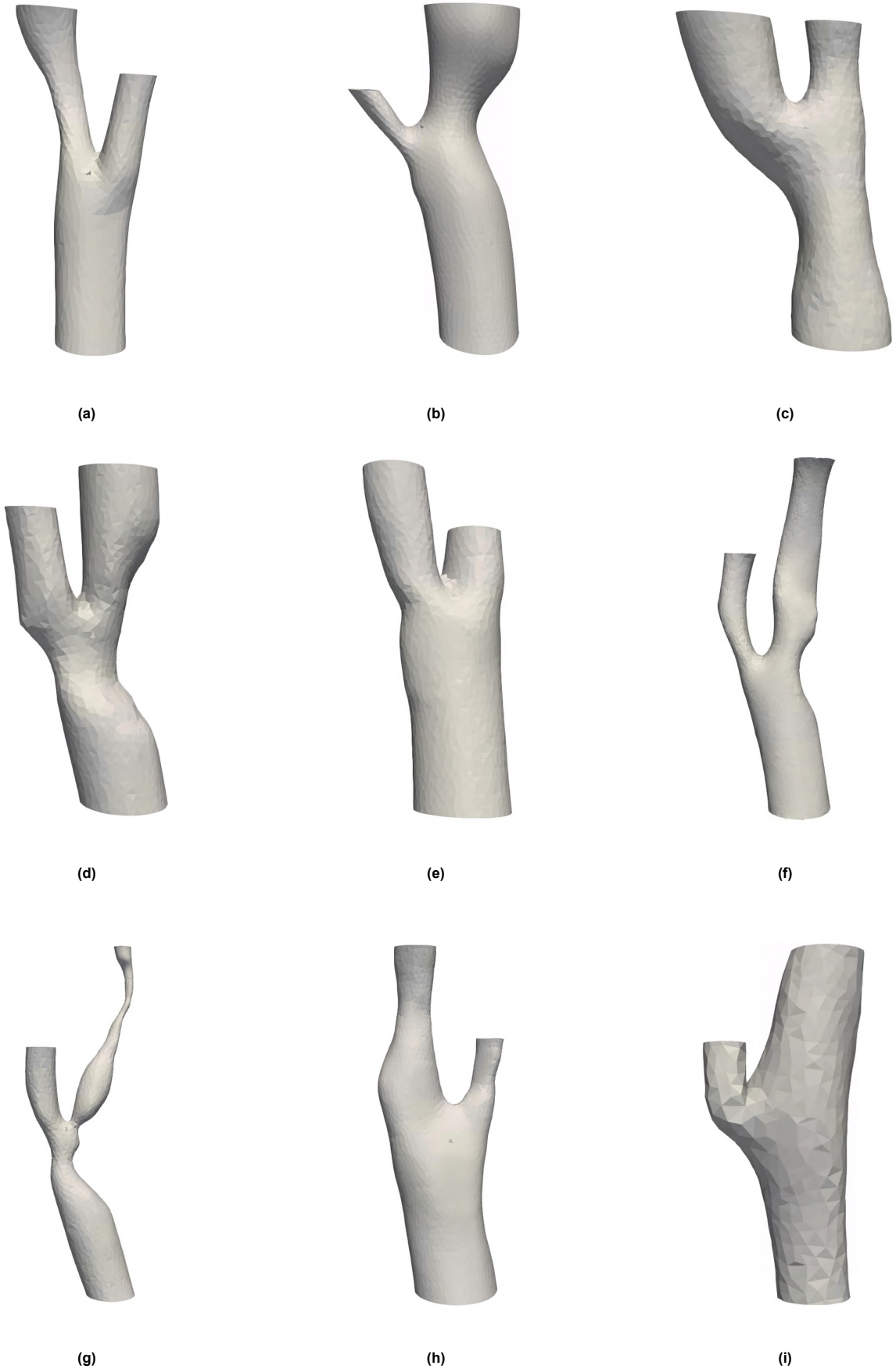

Figure 4.4: Lumen surfaces reconstructed from follow-up scans. 4.4a: Patient 1L. 4.4b: Patient 1R. 4.3c: Patient 2L. 4.4d: Patient 2R. 4.4e: Patient 3L. 4.4f: Patient 3R. 4.4g: Patient 4R. 4.4h: Patient 5L. 4.4i: Patient 6R.

Reconstruction quantification

The reconstruction method described in Chapter 2 is composed of many different steps and types of software. Due to this high conversion rate, the DSC was computed for the CCA-ICA segments of all nine cases at baseline and at follow-up. The initial surface was compared to the final segment, before the ECA-segment was merged (Figure 2.2).

Figure 4.5a shows the results of the Dice calculations. Overall, the mean Dice score was 0.87 (SD: 0.07) similarity between the geometries. More specifically, the lumen score an average 0.88 (SD: 0.06) similarity and the vessel wall was similar for 0.87 (SD: 0.07). In the vessel wall reconstructions, the highest score of 0.94 is shown in Figure 4.5b and the lower outlier of 0.63 is illustrated in Figure 4.5c for comparison. Detailed results per case are illustrated in Figure A.2 in Appendix A.

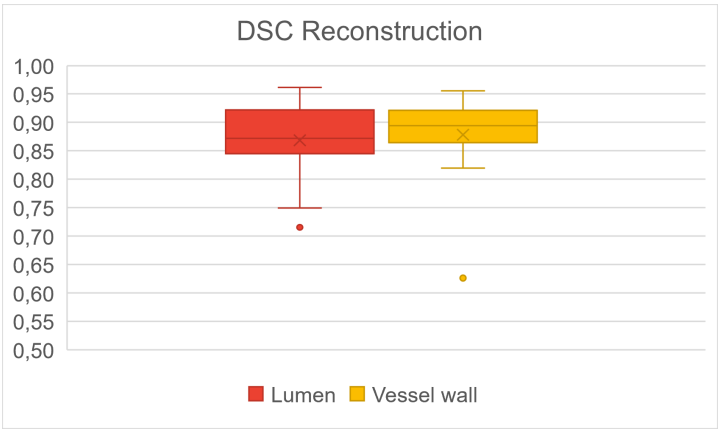

(a)

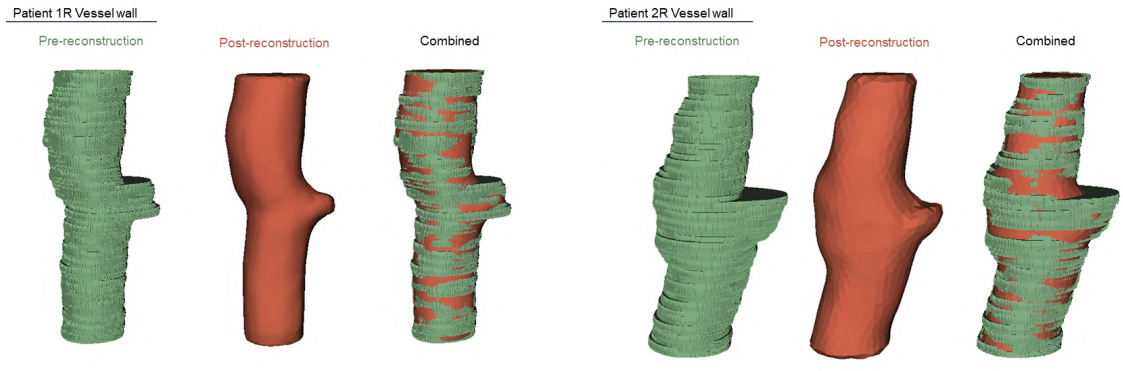

(b) (c)

Figure 4.5: 4.5a: Distribution of the Dice similarity coefficient for the luminal and vessel wall segmentation separately. One lumen segmentation fell outside the pattern of the group data. 4.5b: Visualization of the highest lumen Dice score of 0.9 with respect to the CTA scan (anterior view). Red and green represent a different observer's segmentation. 4.5c: Visualization of the lowest lumen Dice score of 0.6, the outlier in (a). The anterior CTA view also shows the calcifications. Red and green represent different observer segmentations.

4.2. Local biomechanics and morphometry results

All nine cases were successfully post-processed to comparable 2D contour maps. First, an illustrative case will present the local analysis approach and observations. Next, local observations for all nine cases are outlined in trends and striking observations. These results were then processed for global assessment in the next section. All local and global patient-specific results are gathered in Appendices C and D.

4.2.1. Illustrative case: Patient 1R

The analysis and results for case 1R are illustrated in this section. The patient-specific results are composed of 3D, 2D, local and global output parameters. First, Figure 4.6 shows the output from the biomechanical parameters: principal stress and strain in 3D, as obtained from the Abaqus output database (ODB). Second, Figure 4.7 demonstrates the morphometrical analysis of the lumen. Third, Figure 4.8 shows the conversion metrics to interpolate the 3D surface to 2D contour maps. Fourth, Figures 4.9 and 4.10 contain these 2D results. Additionally, global maxima, median and minima are presented with these metrics. Fifth and final, Figure 4.11 includes all global patient-specific output. All metrics regarding biomechanics and morphometry are included.

3D Biomechanical analysis

Figure 4.6 shows the 3D stress and strain directly imaged from the Abaqus ODB. Four different views are presented to give an impression of the 3D structure. This view provides the full bifurcation response and shows how the segments interact (Figure 3.4). The first row shows the maximum principal stress. As the maximum principal strain followed similar patterns, it was decided that the direction of strain would be more of interest. So, the second row shows the maximum principal strain direction. Finally, the third row shows the maximum principal lumen strain relative to the calcified body.

Lower and higher values are found for both stress and strain in the bifurcation. More specifically, the flow divider point (FDP) between the ICA and ECA shows peak maximum values. In post-processing, this region is divided among the ICA and ECA segments. Thus, it was further used as a geometrical landmark in the interpretation of the contour maps.

The bifurcation is also the most complex geometrical area. Along the orientation of the maximum principal strain (second row), there is an overall uniform circumferential direction. However, around the bifurcation and FDP, nonuniform behaviour shows strain at a perpendicular angle away from the lumen.

Finally, the maximum principal strain on the lumen in relation to the calcified body shows similar behaviour as the maximum principal strain. The inclusion of the calcified body shows that this tissue presents a near-zero strain outcome. As this changes the boundary values on the axis, this highlights slightly increased regions of strain that were not observed before.

3D Morphometrical analysis

Secondly, Figure 4.7 exemplifies the shape and size of the lumen surface for baseline and follow-up. This provides a general sense of changes over time. The first row shows the lumen surface in two views for baseline and follow-up. When looking at the orientation of the axes, it can be noted that the baseline and follow-up geometries are rotated relative to each other. The second row shows the relation between the lumen surface and the vessel wall in blue, later expressed in wall thickness. The lumen was originally elongated to later cut through the vessel wall, which can be seen by the extended luminal outlets. Moreover, the change in vessel wall shape over time becomes perceptible. Third and final, is the relation between the lumen and the calcified tissue. Often the calcified tissue is located along the outside of the ICA. Over time, the calcified body also changes in shape, size and location as can be seen here.

3D to 2D Conversion metrics

Third, Figure 4.8 shows the conversion metrics for post-processing 3D results to 2D contour maps for baseline and follow-up. The first column shows the computed centerline (red) inside the surface (blue wireframe). Next in the segment identification, the cutting lines for each of the three segments are shown. This line is set through the FDP, along the bifurcation. In each plot, the CCA segment (blue) is combined with the ICA (beige) or ECA (red). The abcissa metric expresses the height, which is

later translated to the y-axis of the contour plot. The angular metric shows the cutting line that defines the x-axis orientation on these maps. Along this cutting line, a discrepancy can be observed in the transition between segments. This is because the line is re-computed for each segment.

Previous results in Figure 4.7 already indicated a misalignment between baseline and follow-up. The conversion metrics confirm that the baseline and follow-up geometries are translated and rotated relative to each other. As a result, local analysis cannot be extended to a function over time. This was compensated by a global analysis of the parameters over time.

Local analysis results

Next, Figures 4.9 and 4.10 present the contour plots from the 3D output (Figures 4.6, 4.7). Figure 4.9 shows the results for the CCA-ICA segment and Figure 4.10 for the CCA-ECA segment. First, all results from the baseline timepoint were assessed and possible relations among parameters were noted. Second, the follow-up morphometry was analyzed per segment. Third, the baseline metrics for the CCA-ICA and CCA-ECA segments were considered in relation to the follow-up results. Finally, all observations were noted and global values were calculated. This was used for a hypothesis on the association between baseline biomechanics and morphometric progression, which is later discussed.

Figure 4.9 shows the CCA-ICA segment local results. In the first row, the stress and strain maps show similar nonuniform behaviour expressed in regions of increased or decreased magnitude. As mentioned, a peak in both stress and strain is found in the centre middle of the plot that corresponds to the location of the FDP (Figure 4.6). Secondly, baseline morphometrical parameters can be compared, where there is an area in the wall thickness (WT) that is considered diseased WT (DWT). When contrasting this area to other metrics, a respective increase and decrease in maximum and minimum curvature imply a change in shape in these areas. Moreover, the location of the calcified body in this case also corresponds to this DWT area and so the curvature changes. Now, correspondence between biomechanics and baseline morphometrics shows that the calcified DWT region corresponds to a region of decreased stress and strain, just middle-left in the plot. Moreover, lines of increased maximum curvature in the top and bottom segments show correspondence to increased stress and strain stripes. For minimum curvature, no additional patterns were observed in relation to stress and strain.

In Figure 4.9, the follow-up morphometry shows a similar increased area of DWT, at the outer edges of the plot. In this morphometry, there is also correspondence between DWT, maximum and minimum curvature and calcium localization. No specific correspondence was found between curvature metrics and calcium localization.

Next, segment CCA-ECA in Figure 4.10 also shows similar nonuniform behaviour for stress and strain. Again, the FDP corresponds to the peak regions for stress and strain but is split into the middle-left and middle-right sections in this orientation. The DWT area is smaller and is limited to the CCA segment, in the middle-left of the plot. In this segment, this DWT region only corresponds to the location of calcium. The maximum principal curvature shows greater correspondence with other increased stress regions. Decreases in the minimum curvature show stronger correspondence with increases in strain. No new observations were made for the ECA segment specifically. In the follow-up morphometrics, the same pattern for DWT and calcium is found. Additionally, the curvature shows similar patterns of increased stripes in maximum curvature and low spots for minimum curvature.

The global maximum, median and minimum were calculated from the local stress, strain and morphometrical data. For calcium, its volume measurements from the segmentation were included for global analysis.

Global assessment results

Finally, Figure 4.11 shows the global output from the segmentation analysis in QAngio and previously discussed results. A table is made that summarizes the global biomechanical and morphometrical output for each case, expressed in maximum, median and minimum to assess the data distribution. Morphometry here is reduced to WT, plaque burden (PB) and calcium volume.

For case 1R, the maximum and minimum stress and maximum strain magnitudes were found in the CCA-ECA segment. The minimum strain was 0.03 for both segments, implying that this could be in the CCA segment. In baseline WT, the maximum was measured at 3.34 mm and the minimum thickness of 0.38 mm in the CCA-ICA and CCA-ECA segments respectively. At follow-up, the maximum WT of 3.40 mm accounted for in both segments and the lowest 0.46 mm thickness in CCA-ICA. Five out of six

measurements expressed an increase in WT relative to follow-up, with minimum WT in CCA-ICA being the exception. Subsequently, PB was reported for the full carotid artery only. In case 1R the maximum PB decreased over time, but the median and minimum increased over time. Finally, volumetric calcium measurements showed a decrease in volume over time of 1.94 mm^3.

So, over time this case reports a global stress value between 2.72 kPa and 299.80 kPa and the strain rate varied from 0.03 to 0.17 at baseline. Wall thickness ranged between 0.38 mm and 3.34 mm at baseline and 0.46 mm and 3.40 mm at follow-up. The global WT reported an increase for both segments, but not for the minimum WT. Global plaque burden increased in median and minimum, and decreased in the maximum PB. Finally, calcium volume decreased by 1.94 mm^3 over time.

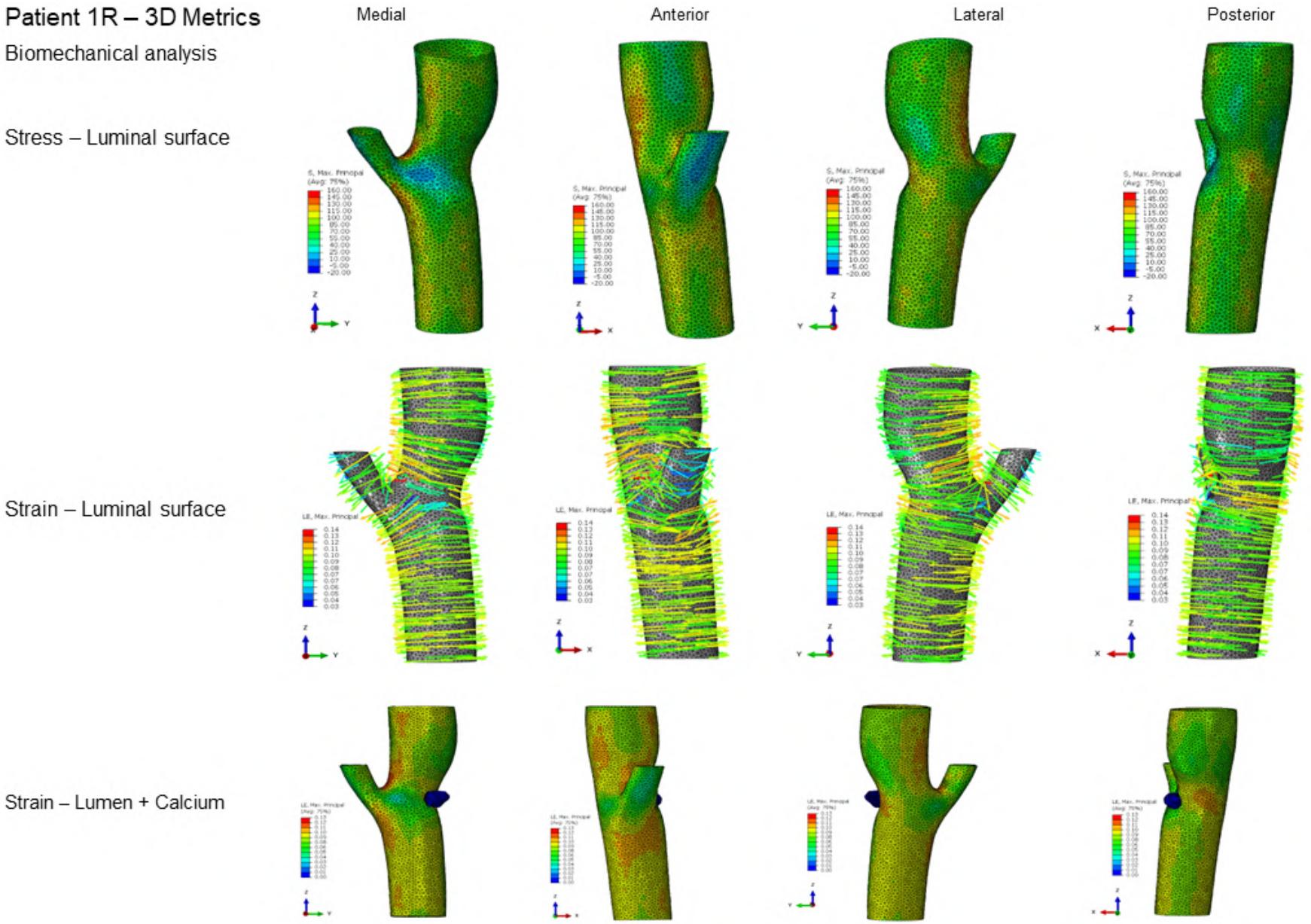

Figure 4.6: 3D results in four views from the Finite Element simulations for patient 1R. Stress and strain are shown for the lumen and strain relative to the calcium is also presented. Medial, anterior, lateral and posterior views are based on basis anatomy, not patient-specifc.

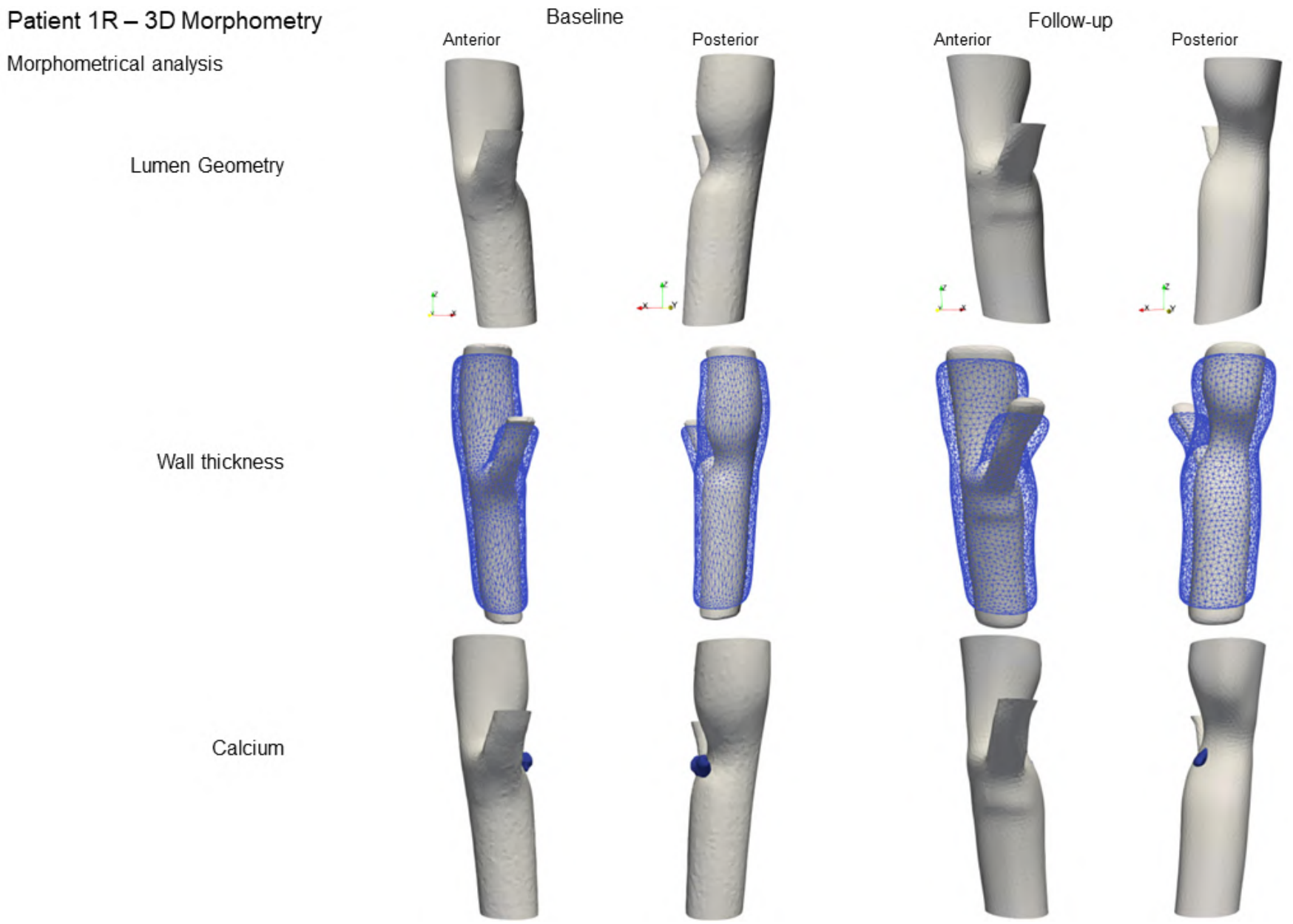

Figure 4.7: 3D results that were used for the morphometrical assessment at baseline and follow-up for patient 1R. Anterior and posterior views show paths of ECA and ICA branches relative to each other.

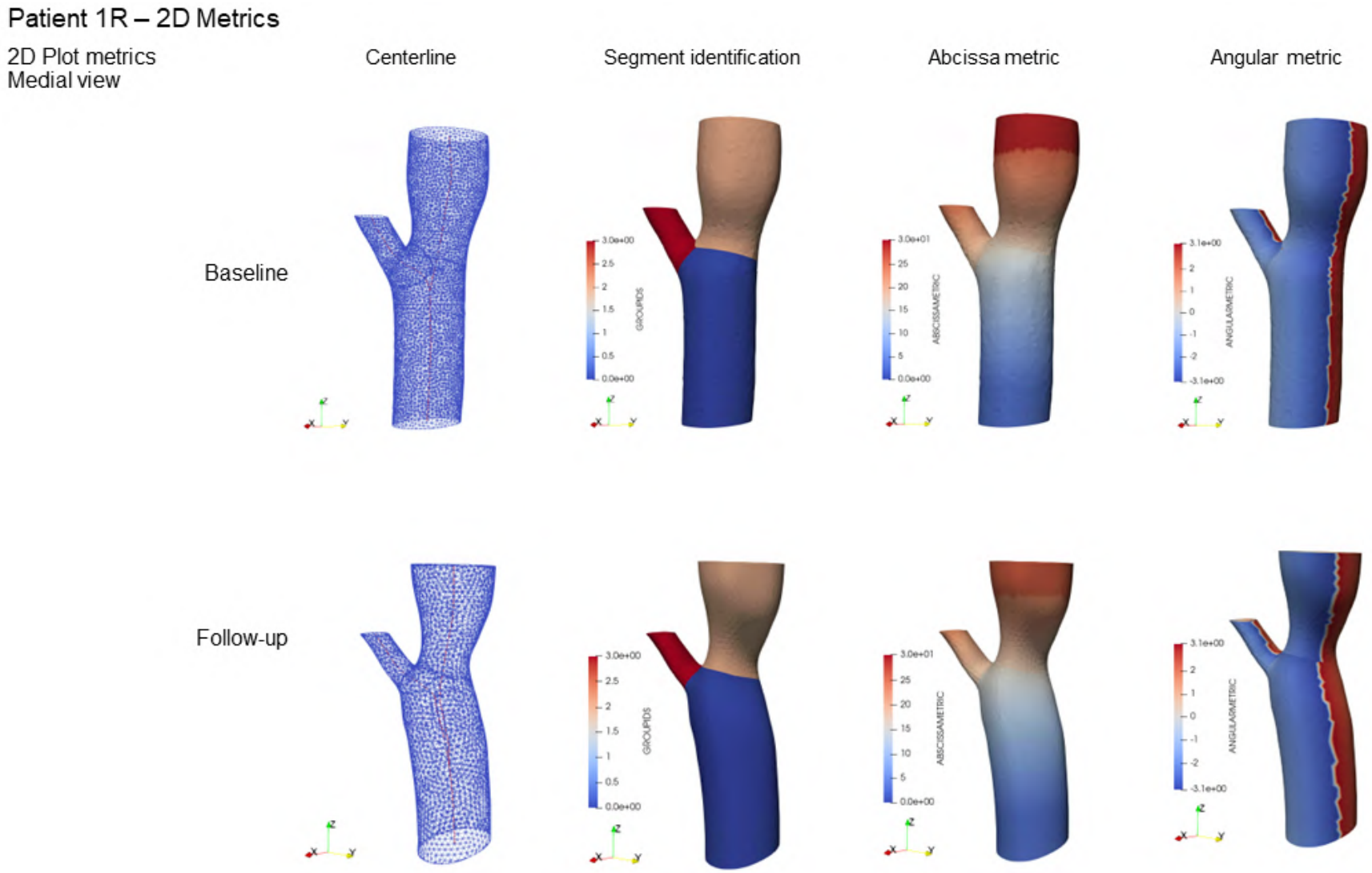

Figure 4.8: Parameters that were used to convert 3D output to 2D for comparison and interpretation of patient 1R.

Patient 1R – 2D CCA-ICA

Biomechanical analysis

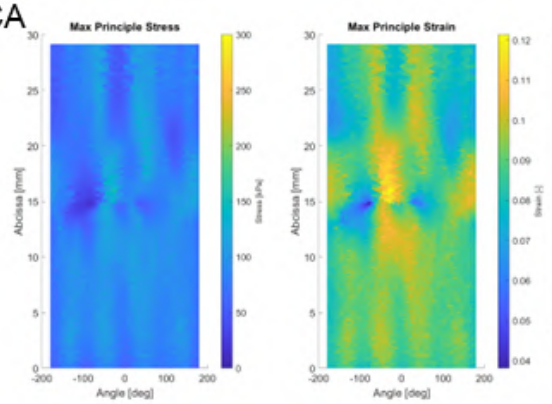

	Stress	Strain	Wall thickness		Max Curvature		Min Curvature	
			Base	*Foll*	*Base*	*Foll*	*Base*	*Foll*
	[kPa]	[-]	[mm]	[mm]	[m^{-1}]	[m^{-1}]	[m^{-1}]	[m^{-1}]
Max	151.91	0.12	3.34	3.40	0.87	0.32	1.58	0.00
Median	85.7	0.09	1.06	1.24	0.30	0.00	0.00	0.00
Min	15.34	0.04	0.79	0.46	0.01	-0.66	0.00	-7.17

Morphometrical analysis

Baseline

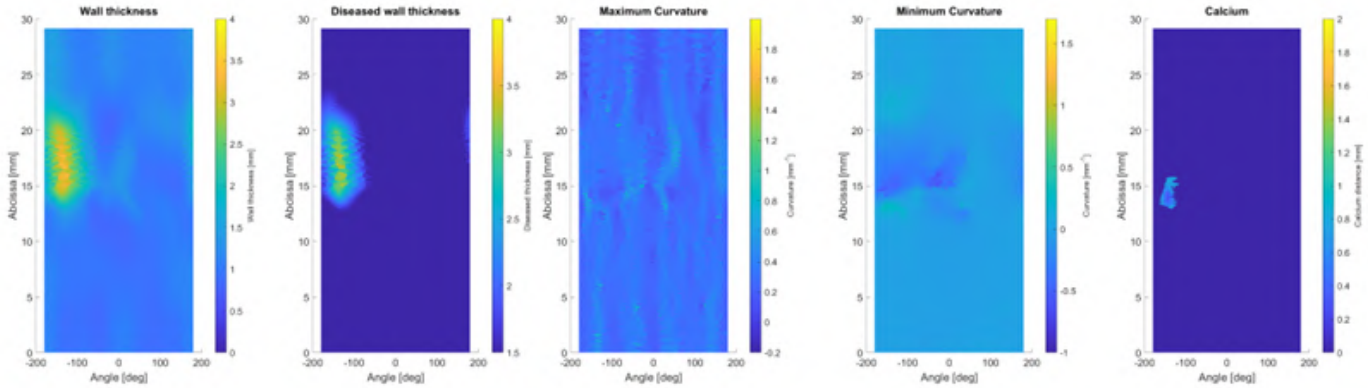

Follow-up

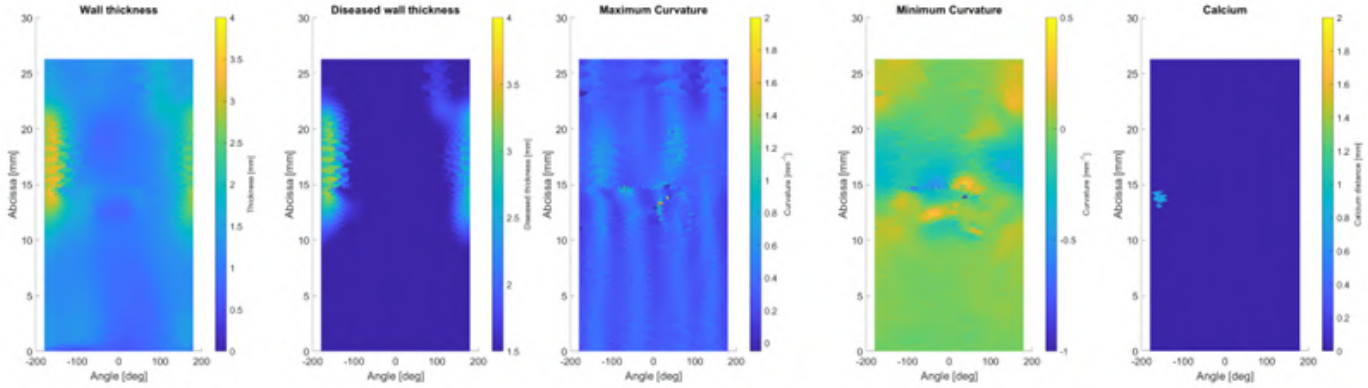

Figure 4.9: 2D biomechanical and morphometrical results for the CCA-ICA segment of patient 1R.

Patient 1R – 2D CCA-ECA

Biomechanical analysis

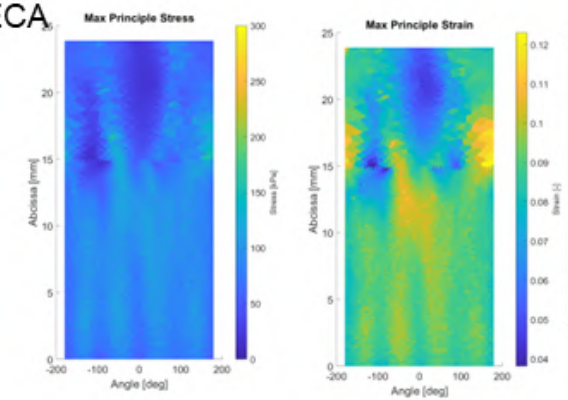

	Stress	Strain	Wall thickness		Max Curvature		Min Curvature	
			Base	*Foll*	*Base*	*Foll*	*Base*	*Foll*
	[kPa]	[-]	[mm]	[mm]	[m^{-1}]	[m^{-1}]	[m^{-1}]	[m^{-1}]
Max	156.78	0.12	3.20	3.40	1.70	1.58	0.32	0.00
Median	85.06	0.09	1.01	1.14	0.33	0.00	0.00	0.00
Min	14.99	0.04	0.38	0.67	0.03	0.00	-2.05	-7.17

Morphometrical analysis

Baseline

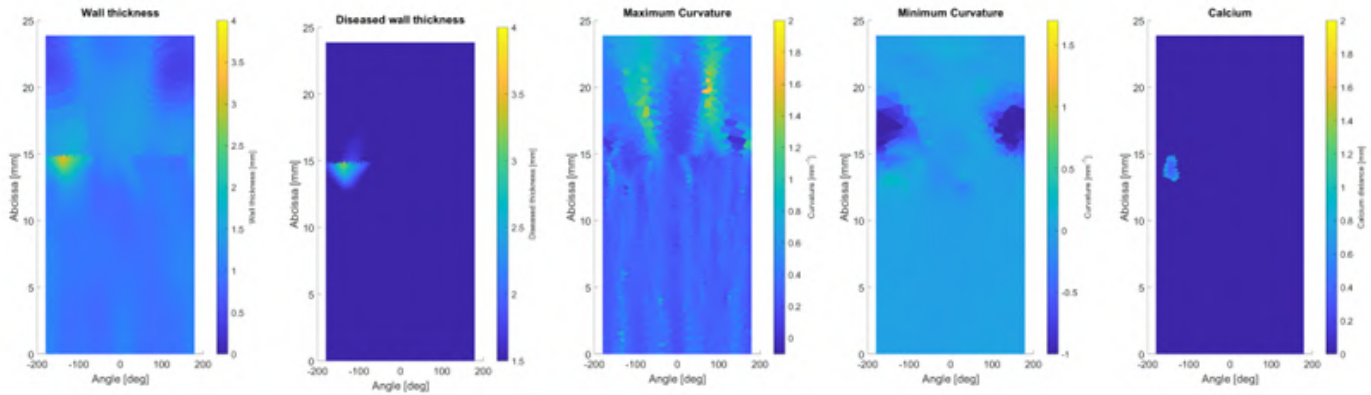

Follow-up

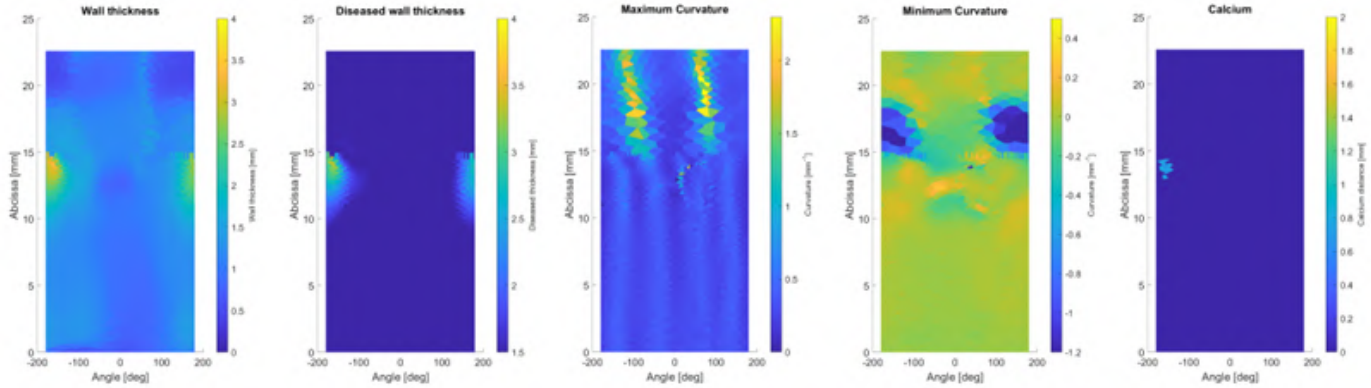

Figure 4.10: 2D biomechanical and morphometrical results for the CCA-ECA segment of patient 1R.

Patient 1R – Metrics

Post-processing metrics			Unit	CCA - ICA	CCA - ECA
Stress	Baseline	Max	[kPa]	151.91	156.78
		Median	[kPa]	85.70	85.06
		Min	[kPa]	15.34	14.99
Strain	Baseline	Max	[-]	0.12	0.12
		Median	[-]	0.09	0.09
		Min	[-]	0.04	0.04
Wall thickness	Baseline	Max	[mm]	5.25	5.25
	Baseline	Median	[mm]	0.98	0.96
	Baseline	Min	[mm]	0.59	0.59
	Follow-up	Max	[mm]	4.96	4.96
	Follow-up	Median	[mm]	1.04	1.04
	Follow-up	Min	[mm]	0.66	0.72
Plaque burden *	Baseline	Max	[%]	72.85	
	Baseline	Median	[%]	40.63	
	Baseline	Min	[%]	34.07	
	Follow-up	Max	[%]	69.76	
	Follow-up	Median	[%]	46.45	
	Follow-up	Min	[%]	35.28	
Calcium *	Baseline		[mm^3]	8.08	
	Follow-up		[mm^3]	6.14	

Figure 4.11: Global results based on the 2D results for patient 1R.

4.2.2. Patient cases

Local results were obtained for all nine cases. As illustrated with case 1R, all metrics were compared for biomechanical behaviour and morphometrical features at baseline, and later contrasted with follow-up geometry through global parameters. The global morphometry is discussed in the next section and has been summarized in Table 4.1. A detailed case-specific table containing all global results is found in Appendix C. All case-specific local output arranged is set out in Appendix D.

Baseline

Biomechanical analysis

In general, the stress and strain maps showed an overall great similarity in behaviour. Areas of maximum stress and strain values were often located around the FDP. This was considered a universal landmark for 2D to 3D conversion in this cohort. Adjacent to this region, an area of decreased strain was often located. Similarly, other areas of decreased stress that were not around the bifurcation, would correspond to an increased strain area. Often, such areas were found in lower in the CCA or higher up in the ICA or ECA.

Wall thickness

Areas of wall thickness (WT) greater than 1.50 mm were labelled and highlighted in the ”Diseased wall thickness” (DWT) plots. Evidently, seven out of nine vessels had reported DWT at baseline. Patient 2R and patient 6R showed no wall thickness exceeding 1.50 mm. Subsequently, patients 1R, 3L and 3R reported no DWT in the ECA segment of the plot where the DWT in the CCA was sliced off at the segment cutting line. Additionally, patient 1L presented no DWT in the CCA, whereas the ICA and ECA did.

The observed thickened areas often crossed the bifurcation along the length of the vessel. Moreover, the thickened regions were most common along the lateral CCA-ICA segment. In the ECA-segment, thickening was more common on the medial side close to the FDP. In relation to *biomechanics*, the maxima of WT, often DWT, matched with regions of decreased stress and strain. The location on the ICA-lateral or ECA-medial side was consistent. Also, the FDP often expressed a maximum in WT as well as a maximum stress and strain.

Curvature

The local principal maximum and minimum curvature showed some correspondence to increased WT regions and indirectly to biomechanics. More specifically, maximum curvature increased in regions adjacent to increased *(D)WT*. Similarly, decreased minimum curvature also corresponded within these areas. Considering the *biomechanics*, the principal minimum curvature showed correspondence with the peak strain locations, and to a lesser degree with stress as well. Decreased minimum curvature is associated with regions of increased strain and stress, especially around the bifurcation. Adjacent to these regions, increased stress and strain were also found, corresponding to increased maximum curvature. The observations on the sole effect of curvature on stress and strain were confirmed in the cases without DWT (2R, 6R). In these cases, a decrease in the minimum curvature was observed in the same location as a peak in stress and strain.

Calcium

Correspondence between calcium maps and the other metrics is influenced by the distance between the lumen and the calcium. The effect of calcified tissue located within 0.5 mm from the lumen could be seen in other maps. Only patient 6R reported no calcium volume at baseline following the segmentation analysis, although the follow-up plot also did not reveal calcified tissue. Moreover, the baseline CCA-ECA segment of patient 5L did not plot calcified tissue, whereas its CCA-ICA segment did. Furthermore, with the exception of case 2R, the location of calcium corresponded with an increased or diseased *wall thickness*. The principal minimum *curvature* showed adjacent decreases around calcium more than the maximum curvature did. Finally, calcified tissue within 0.5 mm of the lumen corresponded to decreased values in *stress and strain* maps. Adjacent to calcified regions the strain showed increased values surrounding these regions.

Follow-up

Similar relations between morphometrical parameters at baseline were observed in the follow-up results. First, a correspondence between thicker *WT* areas and increased *maximum principal curvature* or decreased *minimum principal curvature* was regarded. Second, all cases presented a degree of DWT at follow-up. At the baseline, DWT was observed as a very well-defined region of wall thickening. At follow-up, case 3L, 3R and 5L showed an overall increased wall thickening, not just limited to defined areas. Finally, the follow-up segmentation analysis revealed a *calcium* in all cases, but this could not be localized in every case. To be precise, the follow-up calcium maps for patient 1L did not reveal calcified tissue although previous analyses reported there should be. In the remaining seven cases, the location of calcified tissue corresponded to an increased (D)WT region.

4.3. Global biomechanics and morphometrical change

From the local results presented in the previous section global parameters were calculated, of which the morphometrical change over time is computed. The average of the global parameters for all nine cases is shown in Table 4.1. The extended case-specific version can be found in Appendix C. With these results, a relation was sought between the baseline biomechanics and the morphometrical change over time.

4.3.1. Global morphometrical change

In Table 4.1 the average morphometrical characteristics can be observed for the population. Wall thickness, plaque burden and calcium were selected to define the morphometrical change over time and thereby possibly plaque progression. The average stress ranged between 2.31 kPa and 269.97 kPa and on average strain ranged between 0.03 and 0.14.

The global *curvature* metric was calculated to analyze the shape of the geometries. On average, the median curvature shows a positive maximum curvature at baseline and follow-up. The minimum curvature is near-zero but still positive for baseline and negative for follow-up. The standard deviation of maximum and minimum curvature was high for the average maximum and minimum values. The median values were more consistently spread across the population.

Second, average *wall thickness* at baseline ranged between 0.53 mm and 3.29 mm. At follow-up, WT ranged between 0.29 mm and 5.91 mm. From the standard deviation, a broad range for maximum and a smaller range for the median and minimum WT values is reported. Over time, the average thickness has increased for the maximum and median values, but not in the minimum values. Taking into account the standard deviation, the increase in WT did not apply to all cases. Three CCA-ICA segments reported a negative minimum WT (cases 2L, 2R and 4R). Additionally, the CCA-ICA segment in case 3R reported a wall thickness 39.11 mm, which was a measurement error and therefore disregarded in further analyses. Over time, patient 2L, 3R and 4R reported a negative Δ WT (T) for the median and minimum values. For the minimum Δ WT (T) only patients 1R and 2R demonstrated a positive change over time in one of the segments. Other cases reported a negative minimum Δ WT.

Third, average *plaque burden* at baseline ranged between 37 % and 75 % with a standard deviation of three to ten percent. At follow-up, the average PB exhibited an increase in value and deviation of one percent for the maximum value. On average, Table 4.1 demonstrates an overall plaque burden increase on all three metrics. A decreased maximum Δ PB was reported in cases 2R, 3L, 4R and 6R, of which cases 2R and 6R also reported a decreased minimum Δ PB. Additionally, case 2L reported only a decreased median Δ PB. Other cases posted an increase for the Δ PB parameters.

Finally, *calcium* volume was obtained for the full vessel. On average, cases show an increase in volume over time, with the exception of case 2R. There is a noticeable deviation between calcium volumes in patients. One patient (6R) reported no calcium at baseline, but did at follow-up.

Table 4.1: Global average results for the whole patient cohort (N = 9). For all nine vessels stress, strain, wall thickness (WT), plaque burden (PB) and calcium (C) was averaged (μ) and the standard deviation (ST. Dev. ; SD) was calculated at baseline and follow-up data. Additionally, the average change over time (Δ T) was computed for morphometrics. Stress, strain wall thickness and curvature were obtained in Chapter 3. Plaque burden and calcium were derived from the segmentation in Chapter 2.

Global results				**Average**	**St. Dev.**
N = 9			Unit	μ	SD
Stress	Baseline	Max	[kPa]	269.07	9.66
		Median	[kPa]	61.68	14.98
		Min	[kPa]	2.32	15.30
Strain	Baseline	Max	[-]	0.14	0.03
		Median	[-]	0.07	0.01
		Min	[-]	0.03	0.05
Maximum curvature	Baseline	Max	[m^{-1}]	18.47	42.94
		Median	[m^{-1}]	0.40	0.10
		Min	[m^{-1}]	- 0.66	1.97
	Follow-up	Max	[m^{-1}]	7.10	9.66
		Median	[m^{-1}]	0.28	0.22
		Min	[m^{-1}]	- 45.51	128.44
Minimum curvature	Baseline	Max	[m^{-1}]	15.89	43.56
		Median	[m^{-1}]	0.03	0.11
		Min	[m^{-1}]	- 4.54	7.10
	Follow-up	Max	[m^{-1}]	3.80	7.20
		Median	[m^{-1}]	- 0.01	0.01
		Min	[m^{-1}]	- 12.62	19.69
Wall thickness	Baseline	Max	[mm]	3.20	1.32
		Median	[mm]	1.20	0.47
		Min	[mm]	0.55	0.30
	Follow-up	Max	[mm]	5.91	8.09
		Median	[mm]	1.44	0.35
		Min	[mm]	0.29	0.33
Δ Wall thickness	Δ WT (T)	Max	[mm]	+ 2.71	7.86
		Median	[mm]	+ 0.24	0.38
		Min	[mm]	- 0.26	0.40
Plaque Burden	Baseline	Max	[%]	75.43	9.10
		Median	[%]	49.26	4.06
		Min	[%]	36.70	3.11
	Follow-up	Max	[%]	76.12	10.30
		Median	[%]	51.85	3.54
		Min	[%]	37.30	3.33
Δ Plaque Burden	Delta (T)	Max	[%]	+ 0.69	5.75
		Median	[%]	+ 2.60	2.39
		Min	[%]	+ 0.60	1.64
Calcium	Baseline		[mm^3]	55.72	55.14
	Follow-up		[mm^3]	68.64	65.90
Δ Calcium	Δ C (T)		[mm^3]	+ 12.91	12.50

Progression

From the global morphometrical change over time a form of plaque development can be indicated. Figure 4.12 shows the maximum Δ WT, Δ PB and Δ Calcium in relation to each other to track the maximum change over time. First, a relation between Δ WT and Δ PB was considered in Figure 4.12a, which yielded an R^2 of 0.08. An outlier at + 4.50 mm Δ WT and - 0.05 % Δ PB corresponds to the data of case 2R. Figure 4.12b shows the positive correlation (R^2 0.68) between Δ WT and Calcium growth. The greatest outlier at + 4.5 mm and + 40.00 mm^3 here also corresponds to case 2R. Finally, a weak correlation was posted between Δ PB and Δ Calcium with an R^2 of 0.05. Here, an outlier is observed at - 3.00 % PB and 40.00 mm^3 Calcium (case 2R) and + 15.00 % PB and + 2.00 mm^3 (case 1L).

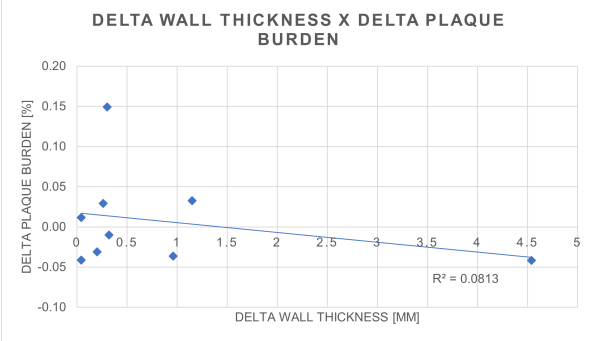

(a)

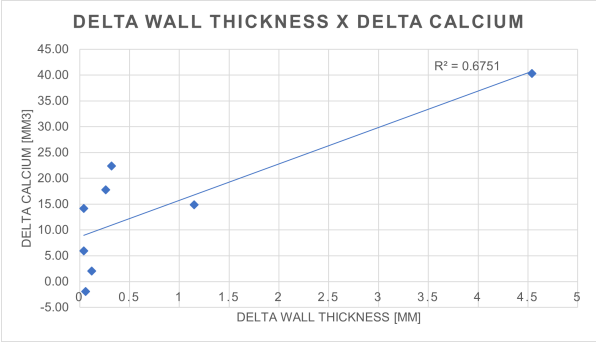

(b)

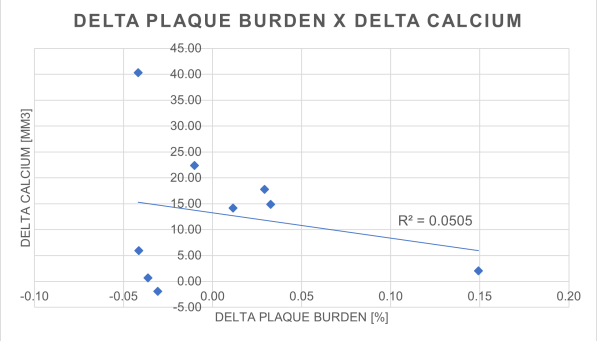

(c)

Figure 4.12: Scatterplots of the morphometrical change parameters in relation to each other. 4.12a: Scatterplot for the maximum wall thickness change against the maximum plaque burden over time. The linear correlation revealed an R-squared of 0.08. 4.12b: Scatterplot of the change in wall thickness against the change in calcium volume over time. Linear correlation revealed an R-squared of 0.68. 4.12c: Scatterplot of the change in plaque burden over time against the change in calcium. This relation resulted in an R-squared of 0.05.

4.3.2. Baseline biomechanics and morphometrical change

All in all, these nine carotid arteries demonstrated an average increase in WT, PB and calcium volume and interrelations have been shown in Figure 4.12. Consequently, the question is raised on the role of structural biomechanics in these progressive parameters. Figure 4.13 presents the relations between median stress, strain and morphometrical change. The median value was expressed as this best represents the condition of the whole vessel, including both healthy and diseased vessel parts.

First, Figures 4.13a and 4.13b shows the nearly flat linear relationship between the Δ WT and median stress (R^2 = 0.001). Figures 4.13c and 4.13d presents a slightly higher positive linear relation for Δ WT against strain (R^2 = 0.05). Second, the Δ PB shows a similar nearly flat (R^2 = 0.00) and positive (R^2 = 0.06) relation to stress and strain respectively. Finally, a change in calcium volume presented a negative linear relation with stress (R^2 = 0.33) and a positive relation with strain (R^2 = 0.02) in Figures 4.13e and 4.13f.

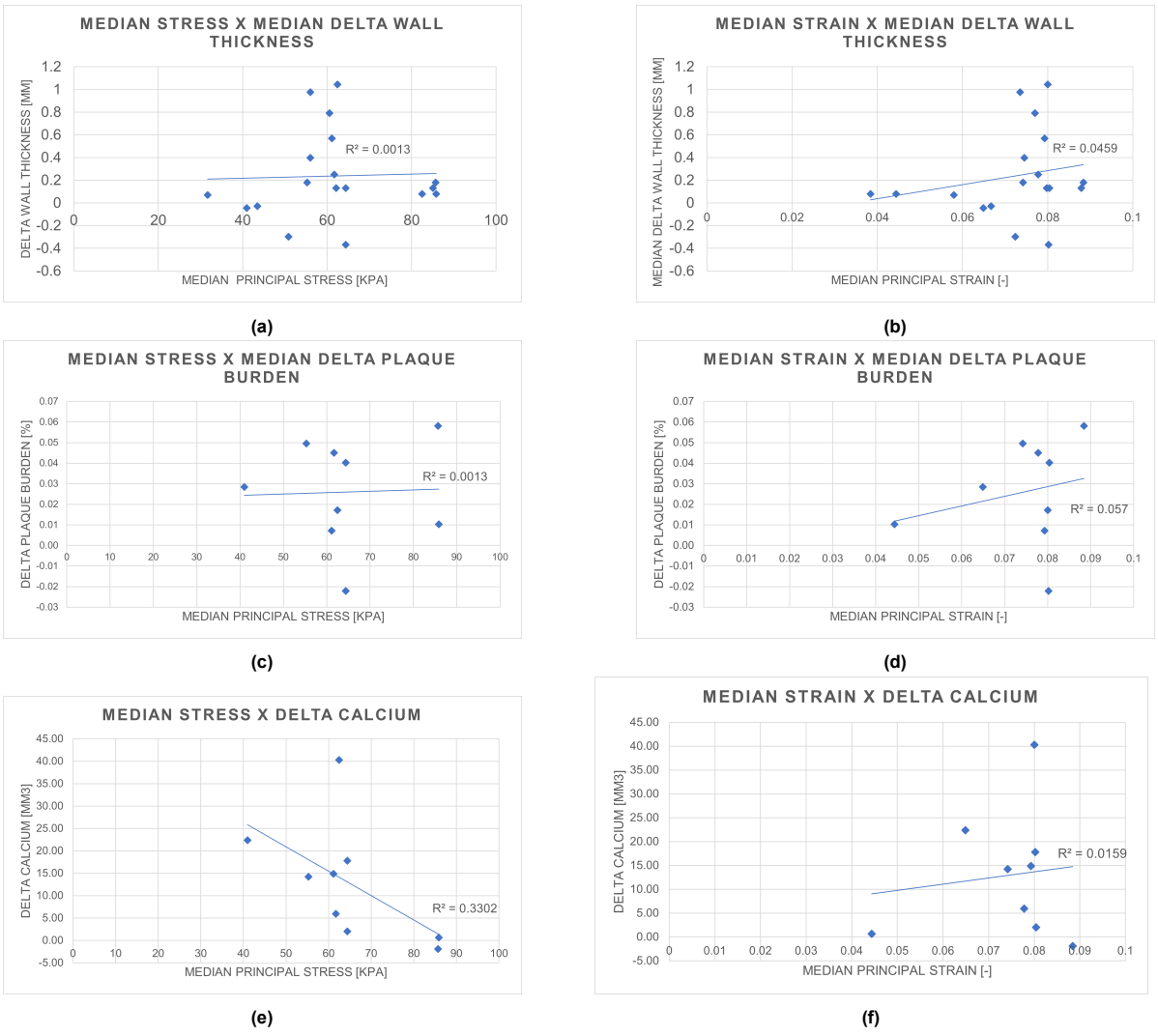

Figure 4.13: Scatterplots of the median biomechanical parameters against the median morphometrical change measurements. 4.13a: Scatterplot for the wall thickness change against principal stress shows a nearly flat linear relation with an R-squared of 0.00. 4.13b: Relation between median principal strain and change in wall thickness over time. A positive slope corresponding to an R-squared of 0.05 was computed. 4.13c: The correlation between principal stress and median change in plaque burden shows a nearly flat line with an R-squared of 0.00. 4.13d: A positive correlation between change in plaque burden and principal strain with an R-squared of 0.06. 4.13e: A negative correlation between principal stress and change in calcium volume with a correlation of 0.33. 4.13f: A positive slope between principal strain and change in calcium volume holds an R-squared of 0.02.

5 Discussion

This study aimed to develop the groundwork for a 3D patient-specific biomechanical modelling approach that contributes to future research insights and ultimately be implemented in clinical practice. The multi-phase approach is a 3D, semi-automatic, robust and accurate method for biomechanical modelling combined with a detailed morphometrical assessment. It has delivered preliminary results through a demonstration in nine different atherosclerotic carotid arteries.

Only recently have structural stresses gained interest in the research field. As a result, only a few pipelines have been published. Similar methods have been developed with different research goals, and hardly any prediction models have been reported [32, 45, 63, 64]. So, this framework will be compared and contrasted on dilemmas and requirements of these methods. Due to the multidisciplinary nature of the different phases, other fields have also been consulted to reflect on this study [82, 102]. Second, the demonstration delivered preliminary results on the association between biomechanics and progression. These associations will be considered in the context of well-accepted 2D and idealized model studies. Finally, limitations and recommendations are made while also considering the future perspective of this methodology.

5.1. Framework

Imaging, segmentation, reconstruction, biomechanics, morphometrics and post-processing stages make up this entire framework. Herein, five different types of software are listed, with MATLAB and Abaqus being the most important. Fundamental differences with other pipelines will be assessed. In general, Tang et al. (2008-2014) and Costopoulos et al. (2019) assessed the role of structural biomechanics in relation to plaque progression in carotid and coronary arteries, respectively [32, 51, 54, 64]. Alternatively, Buckler et al. (2022) and Warren et al. (2022) focussed on framework development for structural stresses in light of plaque rupture for carotid and coronary arteries, respectively [45, 63].

First, CTA imaging and semi-automatic segmentation are the data resources in this pipeline. Likewise, Buckler et al. (2022) used CTA with a single observer segmentation, supported by a histology-based machine learning-based (ML) algorithm [45]. Similarly, Tang et al. (2008 - 2014) performed Artificial intelligence (AI)-supported segmentation on MRI scans [32, 51, 54]. Alternatively, both coronary studies were virtual histology intravascular ultrasound (VH-IVUS)-based where no observers were mentioned [63, 64]. CTA was the primary data resource due to the routine use of CTA in clinical practice. Although it provides limited information on plaque composition, the interobserver similarity of 80 % proves that it serves as a reproducible method (Figure 4.2a). This issue on composition could be overcome by introducing ML-based histology validation, like in Buckler et al. (2022) [45]. Although MRI offers more data on plaque components, the number of contraindications and time-consuming processing prevent custom clinical implementation, thereby limiting future prospects for an MRI-based method. Furthermore, the higher resolution of CTA and rough kernel reconstruction yield more accurate reconstruction, as MRI is known to produce smoother images in the kernel reconstruction [97, 103]. So, CTA forms a reliable and reproducible source of data and segmentation could be further enhanced by the implementation of ML-based plaque recognition.

Secondly, the reconstruction formed a vital part of the foundation of the entire framework. Anatomy defines the patient-specific requirement in this pipeline as no additional (clinical) patient data was made available at the time of this study. The reconstruction of this anatomy was done by a self-developed method composed of five different software packages. Each of these introduced requirements and limitations that had to be overseen through manual inspection between the steps. Theory, principles and requirements behind accurate 3D reconstruction were self-taught from 3D-printing and Geomatics communities [83, 84]. The greatest challenges came from the 3D design, data conversion between operators and software-introduced demands. As in Warren et al. (2022), two reconstruction phases are identified. First, the surface definition of the lumen and vessel wall as outer boundaries. Contrary to the lofting approach in Warren et al. (2022), the isosurface was applied based on experience in the departments [63]. In this study, surfaces had to meet the manifold, valid and precise design requirements in the geometry descriptions, introduced by Abaqus [89]. The coordinates extracted from the segmentation analysis were oriented along the centerline orientation [82]. This challenged the reconstruction efforts as coordinates were not aligned along a central axis. Therefore, the more robust and manually-steered software VMTK and MeshMixer had to be used. The reconstruction similarity of 0.87 in Figure 4.5a proves that, despite the manual control in this software, the anatomical accuracy was preserved and the geometry had become meshable. No other framework had reported an evaluation of the reconstruction accuracy. The second phase of reconstruction was the conversion to a solid entity through tetrahedralization, which is often done in the FE software itself [45, 63]. This was achieved through an Abaqus plug-in that creates a geometry from an orphan mesh [90]. No inaccuracies were detected from this plug-in.

In general, the 3D reconstruction of patient-specific anatomy is a challenging geometry. Other pipelines introduce idealized models, 2D slice-based simulations or construction of the 3D geometry through lofting of a limited number of 2D slices [32, 51, 54, 64, 97]. Some disadvantages are loss of patient-specific anatomy in idealized models and thus cannot represent realistic plaque progression. For 2D simulations, the longitudinal stress effects are not measured. The 2D-lofted 3D models often lose the accuracy of plaque description due to increased slice thickness. So, a 3D geometry reconstruction appears to be the most accurate but also the most challenging and computationally demanding. Not one method is recommended for the 3D definition of surfaces. Buckler et al. (2022) describe the use of the iso2mesh package in their segmentation [45]. Whereas Auricchio et al (2012) reconstruct a 3D stented carotid through direct quadrangulation of the surface [102]. All pipelines show a similar trend to first defining the surfaces, transferring these as explicitly defined STL to the FE software, where the surface is converted to a volumetric mesh. Compared to other pipelines, this study's method introduces manual inspection and is reliant on the manual transfer of surfaces between software packages. One way to improve the latter would be to integrate surface adjustment functions in Rhino directly with Abaqus through a user subroutine application, as described by Lai et al. (2016, 2017) [83, 104]. Although this could be for the far future, it would allow for a more automated reconstruction.

Third, the biomechanical FE simulation was determined to represent a 3D systolic pressure application on the carotid arteries. As mentioned, no patient-specific data was available at the time of this study, so the FE model in this study represents a robust foundation that leaves room for personification. This can be achieved through patient-based load application and material assignment like other research presents [32, 45, 51, 54, 63, 64]. However, as the stresses are directly related to the pressure applied, a cyclic application would be an overcomplication that would not improve accuracy [49]. Furthermore, material models assigned to the calcified and non-calcified tissue are both assumed homogeneous and isotropic. For arterial and plaque tissue, the isotropic assumption is common [32, 45, 51, 54, 63, 64]. Although the HGO model allows for the introduction of local anisotropic properties [70], no such data was available. Isotropy, homogeneity and longitudinal orientation of the fibres was assumed for the one-fibre family. According to Akyildiz et al (2017) and Holzapfel and Ogden (2018), this could be considered a simplification of the main load-bearing adventitia layer [105, 106]. However, implementation of local anisotropic properties is also absent in any of the aforementioned frameworks. The assumption of homogeneity has been countered by Warren et al. (2022) and Buckler et al. (2022). Although, both methods reported great increases in computational complexity with the introduction of inhomogeneous material functions [45, 63]. For now, this option was neglected in this study. Additionally, the accuracy could be improved by implementing a backward incremental method to obtain the no-load geometry for the initial loading conditions. Tang et al. (2014) report the preference for an incremental method over their own developed trial-and-error shrinkage method [32]. As in vivo

carotid arteries are under tension, the reconstructed geometry based on in vivo imaging represents the arteries under pre-stress. This tethering can be eliminated by defining the no-load geometry using a backward incremental method [33, 107]. Finally, component-specific mesh generation, definition of multicomponent plaques and more detailed phenomenological material models can be considered to improve modelling accuracy, but should always be weighed against computational cost. The cost of 3D anatomical modelling is already substantial, so extensions will only further burden this.

Fourth, a multiparameter morphometrical assessment of the carotid arteries at baseline and follow-up was performed. Buckler et al. (2022) and Warren et al. (2022) were rupture-oriented and limited morphometry to fibrous cap thickness and volumetric differences at one timepoint only, respectively [45, 63]. Tang et al. (2008-2014) defined progression as WT change over time using the same pointwise minimum distance measurement as is used here [51]. Costopoulos et al. (2019) performed a more elaborate interpretation of plaque progression composed of plaque components and plaque size [64], which is more comparable to the definition applied here. The starting point in this morphometrical analysis was to use the same geometries as in FE-modeling, to achieve a locally comparable format. Next, the morphometry described the arteries through dimensions (wall thickness, plaque burden), surface (curvature) and assembly (calcium). Originally, it was thought that the global change in time would represent plaque progression sufficiently. In reality, the global interpretation gave in no distinct observations. In clinical practice the intima-media thickness is used for surgery indications [96]. As such, Ghasemi et al. (2020) successfully used this definition to further define local curvature as a predictor for progression [100]. Moreover, clinical studies present a new point of view, where plaque composition is considered more predictive than geometrical measurements [108, 109]. This shows that these primary measurements can be further advanced to become significant factors that can predict plaque growth. Thus, this study has presented a detailed description of carotid morphometry which had no direct relation to progression hypotheses. However, it raises a discussion on what progression is exactly and that clinical practice and research context should confer to unanimously narrow down this definition. All in all, this should aid in comparing methods and results in future studies.

Finally, this study aimed to achieve the results in a format for full comprehension of local associations. As such, a final conversion was added to create contour maps of the biomechanical and morphometrical output. Based on the methodology presented by Hartman et al. (2022) and Antiga et al. (2004) [42, 110], this is the first study to present contour maps for local associations of structural stresses. Other frameworks opt for the slice-based and sector analyses from their 3D models [32, 45, 63, 64]. The advantage of this 2D contour mapping method is the simultaneous analysis of circumferential slices and longitudinal observations. Moreover, the slice-based analysis often reduces slices to larger sectors rather than assessing the local behaviour. High-resolution contour maps were presented in this approach, but this can be altered to bigger pixels by increasing the pixel dimensions of the bins. By subjecting each geometry to both the morphometrical and FE simulations, an accurate local association was computed without the need for additional interventions. The next step would be to derive the relative translation and rotation between baseline and follow-up geometries so that co-localized progression metrics can be obtained. As mentioned, this is the first PSS study that uses 2D-conversion of the results for an easier interpretation of parameter associations.

5.2. Preliminary results

Successful application of this pipeline in nine carotid arteries has delivered preliminary results on morphometric parameters that affect stress and strain distribution on a local and global level. One overall observation was the easy localization of the flow divider point (FDP) in the bifurcation in all cases. Stress and strain exhibited maximum values in this region. According to Thubrikar (2007) this is explained by the geometrical characteristics in a bifurcation [34]. Other observations are discussed per parameters.

First, the overall mean stress ranged between 2.31 kPa and 269.07 kPa and strain was between 0.03 and 0.14 (Table 4.1). Stress reports much lower than the 426 kPa reported by Tang et al. (2008) for their 3D models [51]. These models describe carotid arteries through fibrous tissue, lipid pools and calcified tissue. Global stress results are likely an underestimation as lipids are known to (locally) increase the structural stresses [47]. No literature was found that reported on strain magnitudes in relation to composition. Further local observations have demonstrated great similarity in stress and strain behaviour in each of the plots. Strain in nearly all cases demonstrates a circumferential direction.

Therefore, the relevance of the strain computations could be improved by calculating the radial strain metric, as opposed to the axial strain demonstrated here.

Second, wall thickness exhibited an overall increase in all patients. All patients labelled diseased WT areas at follow-up. The local DWT regions often corresponded with decreased stress and strain. This supports the idealized tube theory introduced by Thubrikar (2007) [34]. However, it is unclear whether this decrease in mechanics is only caused by DWT, as all DWT corresponded with calcified tissue localization. Globally, maximum WT change exhibited much more variety than the median did. This shows that plaque progression can be considered a vessel-specific process. Moreover, the number of negative minimum WT values has indicated that this is the result of a measurement error so these were excluded in further detailed analysis. Finally, no global relation was found between median stress, strain and wall thickness. As WT locally decreases the stress and strain, it is possible that this is not reflected in the median of the entire surface.

Third, curvature was used to interpret the lumen mathematical shape and observe local relations with biomechanics. Local correspondence was observed with changing curvature magnitude adjacent to increased WT and to an increased stress and strain magnitude. In literature, the curvature can be employed for the detection of surface irregularities, thereby exposing the weaker shoulder regions on the plaque surface. As such, these regions exhibit a higher stress response [97, 111]. Although this metric is not often used on 3D geometries, it could potentially be used as an indication of vessel wall remodelling direction.

Fourth, an increase in high-density calcium volume in plaque progression is believed to have a stabilizing effect over time [14, 15]. These preliminary results show a local stress-lowering outcome in multiple patients. The high stiffness of the calcified material creates a high load-bearing function for the lumen which ultimately strengthens the lumen [11]. The load-bearing function was confirmed by Figure 4.13e, where a weak negative correlation of 0.33 was found. A detailed local assessment confirmed this behaviour when the calcium was close enough to the lumen. No research was found that could confirm the principle of calcium localization with regard to the lumen. When considering the global change of calcium volume over time, a strong positive correlation of 0.68 was found for calcium growth and maximum wall thickness increase. This shows that calcium could be used as an indicator for stenosis localization and growth.

Finally, overall plaque burden was obtained from segmentation analysis and compared to progression and biomechanical parameters. No relations were found for either of the questions. Regardless, all patients exhibited an increase in plaque burden over time, as opposed to the global WT metric. This rephrases the aforementioned question on the definition of progression. How should progression be defined and what parameters can be implemented in clinical practice easily? Other pipelines and clinical research show no unanimous agreement on how to define this. Some researchers focus on a simple description such as wall thickness measurements [45, 54], whereas others introduce more extensive definition that includes a detailed composition characterisation [15, 64, 88]. In order to achieve the ultimate prediction model the morphometrical parameters should be depicted that can accurately describe plaque growth, related to (surgical) intervention benefits.

5.3. Limitations

The development and demonstration of this pipeline have exposed three limitations to this study. First is the absence of available patient data. The patient-specific requirement of this framework has been reduced to an anatomical basis due to the lack of patient characteristics, medication use and clinical data. Although this framework is now designed to be tailored in numerous ways, this has also constrained the interpretation of these initial results. For instance, statin use is known to promote calcium growth [112, 113], a relation that could not be considered in this data analysis. Moreover, it is also known that atherosclerotic processes exhibit different outcomes in different ethnicities and gender across patient populations [114, 115]. In the overall search for a morphometrical description of plaque growth, patient data is needed to categorize population-specific or universal metrics.

Second, is the number of manual interventions in the pipeline. Ideally, a fully automated pipeline is developed with low computational demands. This semi-automated approach greatly increases labour intensity when applied to a bigger cohort. However, as this study laid the foundation for a new pipeline, the manual steps and visual inspection served as validation for the correct establishment of geometries and analysis output. Further developments could aim to advance automation and reduce labour

intensity.

Finally, the CTA-based segmentation software limited plaque definition to calcified tissue only. Although CTA most accurately detects calcium, plaques are composed of softer tissues as well. The inclusion of softer components can change local stress and strain behaviour, and produce more accurate results. Additionally, more plaque components would mean more plaque parameters that can be used for defining plaque development. Overall, a more complete definition of plaque is expected to improve the overall outcome. However, basing this framework on only CTA allows for the direct implementation of research findings in the future. So, although this limited definition of plaque restricts research accuracy, it is a vital requirement for the overall goal in this research field.

5.4. Recommendations and future outlook

Overall, the successful demonstration of this pipeline in nine distinctly different arteries has proven its robustness (Figures 4.3 and 4.4). As mentioned, this pipeline forms the basis for future additions. Although there are numerous suggestions, three of the most important topics for recommendations are listed.

The first would be to co-register the baseline and follow-up geometries. This will allow for a full local assessment of morphometrical changes over time. In the current results, the global approach demonstrated too inaccurate description of plaque growth or reduction. In coronary arteries, this is often done by matching the side branches [42]. However, this carotid structure only contains one bifurcation, so accurate co-registration is more challenging. Additionally, it is recommended to elongate the segmentation path in the artery, as the co-registration will reduce the total segment length.

Second is the expansion of the FE model. Currently, this is a basic model that assumes only calcified plaque material and the average systolic blood pressure. Introducing case-specific blood pressure will further characterize the model response. Identification of softer plaque tissue in the assembly will change the stress behaviour locally. This will yield more realistic results that can better depict the dynamic plaque behaviour. Also, accuracy can be further improved by the implementation of the aforementioned incremental method, to define initial loading conditions. Furthermore, similar stress and strain behaviour can be differentiated by computing the radial strain component rather than the axial strain, as outlined before.

Finally, the successful nine-fold demonstration has presented a certain robustness. For more conclusive results on the hypothesis, a larger cohort study can be performed using this method. The inclusion of more cases with balanced-out characteristics could potentially lead to more conclusive results on the global and local assessment of structural biomechanics in plaque progression.

6

Conclusion

This study aimed to develop a research pipeline to research in vivo plaque progression in carotid arteries in relation to structural biomechanical parameters. Ultimately, the prediction of progression through stress analyses would enable the development of prevention plans to improve disease management for atherosclerosis in carotid arteries. This framework shows a successful integration of local analyses of in vivo reconstructed anatomy, Finite Element modelling and morphometry. Most challenges arose from the 3D reconstruction, as it laid the ground for the subsequent phases. Patient-specific geometries were achieved with a 0.80 similarity compared to the in vivo segmented anatomy. The biomechanical simulations, performed with Finite Element modelling, resulted in the basis for a future model. Patient personalization can easily be implemented following the recommendations. The morphometrical analysis was defined in multiple parameters that each exposed local relations to structural stress and strain. This emphasizes that plaque development cannot be reduced to one parameter, and that progression can be traced in many ways. Preliminary results proposed a weak negative linear correlation between calcium progression and structural stresses, indicating that calcium is not the only plaque component related to the lumen structural stress response. A strong positive correlation between the maximum wall thickness increase in relation to calcium growth implies that calcium can be used to define plaque growth. Additional local observations of biomechanical behaviour in relation to calcium indicate that further research should be more extensive on the volume, density and location of this tissue. Finally, the role of plaque structural stresses in global plaque progression remains unanswered. A consensus on a plaque progression definition, larger patient cohorts and expected computational developments in the 3D modelling field provide a hopeful prospect that this question can be answered in the future.

References

[1] M. Truijman, M. E. Kooi, A. Van Dijk, A. De Rotte, A. van der Kolk, M. Liem, F. Schreuder, E. Boersma, W. Mess, R. J. van Oostenbrugge, *et al.*, "Plaque at risk (parisk): Prospective multicenter study to improve diagnosis of high-risk carotid plaques," *International Journal of Stroke*, vol. 9, no. 6, pp. 747–754, 2014.

[2] D. Mozaffarian, E. J. Benjamin, A. S. Go, D. K. Arnett, M. J. Blaha, M. Cushman, S. R. Das, S. De Ferranti, J.-P. Després, H. J. Fullerton, *et al.*, "Heart disease and stroke statistics—2016 update: A report from the american heart association," *circulation*, vol. 133, no. 4, e38–e360, 2016.

[3] S. A. Randolph, "Ischemic stroke," *Workplace Health & Safety*, vol. 64, no. 9, pp. 444–444, Sep. 2016. DOI: 10.1177/2165079916665400. [Online]. Available: https://doi.org/10.1177/2165079916665400.

[4] C. Yuan, S.-x. Zhang, N. L. Polissar, D. Echelard, G. Ortiz, J. W. Davis, E. Ellington, M. S. Ferguson, and T. S. Hatsukami, "Identification of fibrous cap rupture with magnetic resonance imaging is highly associated with recent transient ischemic attack or stroke," *Circulation*, vol. 105, no. 2, pp. 181–185, Jan. 2002. DOI: 10.1161/hc0202.102121. [Online]. Available: https://doi.org/10.1161/hc0202.102121.

[5] P. Song, Z. Fang, H. Wang, Y. Cai, K. Rahimi, Y. Zhu, F. G. R. Fowkes, F. J. Fowkes, and I. Rudan, "Global and regional prevalence, burden, and risk factors for carotid atherosclerosis: A systematic review, meta-analysis, and modelling study," *The Lancet Global Health*, vol. 8, no. 5, e721–e729, 2020.

[6] A. J. Brown, Z. Teng, P. C. Evans, J. H. Gillard, H. Samady, and M. R. Bennett, "Role of biomechanical forces in the natural history of coronary atherosclerosis," *Nature reviews cardiology*, vol. 13, no. 4, pp. 210–220, 2016.

[7] T. E. of Encyclopaedia. "Brittanica encyclopedia." (2020), [Online]. Available: https://www.britannica.com/science/atherosclerosis.

[8] H. C. Stary, A. B. Chandler, S. Glagov, J. R. Guyton, W. Insull, M. E. Rosenfeld, S. A. Schaffer, C. J. Schwartz, W. D. Wagner, and R. W. Wissler, "A definition of initial, fatty streak, and intermediate lesions of atherosclerosis. a report from the committee on vascular lesions of the council on arteriosclerosis, american heart association.," *Circulation*, vol. 89, no. 5, pp. 2462–2478, May 1994. DOI: 10.1161/01.cir.89.5.2462. [Online]. Available: https://doi.org/10.1161/01.cir.89.5.2462.

[9] H. C. Stary, A. B. Chandler, R. E. Dinsmore, V. Fuster, S. Glagov, W. Insull, M. E. Rosenfeld, C. J. Schwartz, W. D. Wagner, and R. W. Wissler, "A definition of advanced types of atherosclerotic lesions and a histological classification of atherosclerosis," *Circulation*, vol. 92, no. 5, pp. 1355–1374, Sep. 1995. DOI: 10.1161/01.cir.92.5.1355. [Online]. Available: https://doi.org/10.1161/01.cir.92.5.1355.

[10] J.-M. Cai, T. S. Hatsukami, M. S. Ferguson, R. Small, N. L. Polissar, and C. Yuan, "Classification of human carotid atherosclerotic lesions with in vivo multicontrast magnetic resonance imaging," *Circulation*, vol. 106, no. 11, pp. 1368–1373, Sep. 2002. DOI: 10.1161/01.cir.0000028591.44554.f9. [Online]. Available: https://doi.org/10.1161/01.cir.0000028591.44554.f9.

[11] T. Asanuma, Y. Higashikuni, H. Yamashita, R. Nagai, T. Hisada, and S. Sugiura, "Discordance of the areas of peak wall shear stress and tissue stress in coronary artery plaques as revealed by fluid-structure interaction finite element analysis," *International Heart Journal*, vol. 54, no. 1, pp. 54–58, 2013. DOI: 10.1536/ihj.54.54. [Online]. Available: https://doi.org/10.1536/ihj.54.54.

[12] G. Pugliese, C. Iacobini, C. B. Fantauzzi, and S. Menini, “The dark and bright side of atherosclerotic calcification,” *Atherosclerosis*, vol. 238, no. 2, pp. 220–230, 2015.

[13] Q. Zhao, Z. Cai, J. Cai, X. Zhao, F. Li, and C. Yuan, “Correlation of coronary plaque phenotype and carotid atherosclerotic plaque composition,” *The American Journal of the Medical Sciences*, vol. 342, no. 6, pp. 480–485, Dec. 2011. DOI: 10.1097/maj.0b013e31821caa88. [Online]. Available: https://doi.org/10.1097/maj.0b013e31821caa88.

[14] M. Miralles, J. Merino, M. Busto, X. Perich, C. Barranco, and F. Vidal-Barraquer, “Quantification and characterization of carotid calcium with multi-detector CT-angiography,” *European Journal of Vascular and Endovascular Surgery*, vol. 32, no. 5, pp. 561–567, Nov. 2006. DOI: 10.1016/j.ejvs.2006.02.019. [Online]. Available: https://doi.org/10.1016/j.ejvs.2006.02.019.

[15] A. C. Razavi, A. S. Agatston, L. J. Shaw, C. N. D. Cecco, M. van Assen, L. S. Sperling, M. S. Bittencourt, M. A. Daubert, K. Nasir, R. S. Blumenthal, M. B. Mortensen, S. P. Whelton, M. J. Blaha, and O. Dzaye, “Evolving role of calcium density in coronary artery calcium scoring and atherosclerotic cardiovascular disease risk,” *JACC: Cardiovascular Imaging*, vol. 15, no. 9, pp. 1648–1662, Sep. 2022. DOI: 10.1016/j.jcmg.2022.02.026. [Online]. Available: https://doi.org/10.1016/j.jcmg.2022.02.026.

[16] H. E. Barrett, J. J. Mulvihill, E. M. Cunnane, and M. T. Walsh, “Characterising human atherosclerotic carotid plaque tissue composition and morphology using combined spectroscopic and imaging modalities,” *BioMedical Engineering OnLine*, vol. 14, no. S1, Jan. 2015. DOI: 10.1186/1475-925x-14-s1-s5. [Online]. Available: https://doi.org/10.1186/1475-925x-14-s1-s5.

[17] T. Seime, M. van Wanrooij, E. Karlöf, M. Kronqvist, S. Johansson, L. Matic, T. C. Gasser, and U. Hedin, “Biomechanical assessment of macro-calcification in human carotid atherosclerosis and its impact on smooth muscle cell phenotype,” *Cells*, vol. 11, no. 20, p. 3279, Oct. 2022. DOI: 10.3390/cells11203279. [Online]. Available: https://doi.org/10.3390/cells11203279.

[18] A. E. Odink, A. van der Lugt, A. Hofman, M. G. Hunink, M. M. Breteler, G. P. Krestin, and J. C. Witteman, “Association between calcification in the coronary arteries, aortic arch and carotid arteries: The rotterdam study,” *Atherosclerosis*, vol. 193, no. 2, pp. 408–413, Aug. 2007. DOI: 10.1016/j.atherosclerosis.2006.07.007. [Online]. Available: https://doi.org/10.1016/j.atherosclerosis.2006.07.007.

[19] S. Dossabhoy and S. Arya, “Epidemiology of atherosclerotic carotid artery disease,” in *Seminars in Vascular Surgery*, Elsevier, vol. 34, 2021, pp. 3–9.

[20] K. L. Moore, A. M. Agur, A. F. Dalley, *et al.*, *Essential clinical anatomy*, 5th ed. Wolters Kluwer Health Baltimore, MD, 2015, ch. 8.

[21] A. Lo, M. Oehley, A. Bartlett, D. Adams, P. Blyth, and S. Al-Ali, “ANATOMICAL VARIATIONS OF THE COMMON CAROTID ARTERY BIFURCATION,” *ANZ Journal of Surgery*, vol. 76, no. 11, pp. 970–972, Nov. 2006. DOI: 10.1111/j.1445-2197.2006.03913.x. [Online]. Available: https://doi.org/10.1111/j.1445-2197.2006.03913.x.

[22] D. Anangwe, H. Saidi, J. Ogeng’o, and K. Awori, “Anatomical variations of the carotid arteries in adult kenyans,” *East African Medical Journal*, vol. 85, no. 5, Aug. 2008. DOI: 10.4314/eamj.v85i5.9619. [Online]. Available: https://doi.org/10.4314/eamj.v85i5.9619.

[23] Ö. Zümre, A. Salbacak, A. E. Çiçekcibaşi, I. Tuncer, and M. Seker, “Investigation of the bifurcation level of the common carotid artery and variations of the branches of the external carotid artery in human fetuses,” *Annals of Anatomy - Anatomischer Anzeiger*, vol. 187, no. 4, pp. 361–369, Sep. 2005. DOI: 10.1016/j.aanat.2005.03.007. [Online]. Available: https://doi.org/10.1016/j.aanat.2005.03.007.

[24] M. Markl, F. Wegent, T. Zech, S. Bauer, C. Strecker, M. Schumacher, C. Weiller, J. Hennig, and A. Harloff, “In vivo wall shear stress distribution in the carotid artery,” *Circulation: Cardiovascular Imaging*, vol. 3, no. 6, pp. 647–655, Nov. 2010. DOI: 10.1161/circimaging.110.958504. [Online]. Available: https://doi.org/10.1161/circimaging.110.958504.

[25] M. Sitzer, D. Puac, A. Buehler, D. A. Steckel, S. von Kegler, H. S. Markus, and H. Steinmetz, "Internal carotid artery angle of origin," *Stroke*, vol. 34, no. 4, pp. 950–955, Apr. 2003. DOI: 10.1161/01.str.0000060895.38298.c4. [Online]. Available: https://doi.org/10.1161/01.str.0000060895.38298.c4.

[26] J. M. Wardlaw, M. D. Stevenson, F. Chappell, P. M. Rothwell, J. Gillard, G. Young, S. M. Thomas, G. Roditi, and M. J. Gough, "Carotid artery imaging for secondary stroke prevention," *Stroke*, vol. 40, no. 11, pp. 3511–3517, Nov. 2009. DOI: 10.1161/strokeaha.109.557017. [Online]. Available: https://doi.org/10.1161/strokeaha.109.557017.

[27] V. Baliyan, K. Shaqdan, S. Hedgire, and B. Ghoshhajra, "Vascular computed tomography angiography technique and indications," *Cardiovascular Diagnosis and Therapy*, vol. 9, no. S1, S14–S27, Aug. 2019. DOI: 10.21037/cdt.2019.07.04. [Online]. Available: https://doi.org/10.21037/cdt.2019.07.04.

[28] M. Wintermark, S. Jawadi, J. Rapp, T. Tihan, E. Tong, D. Glidden, S. Abedin, S. Schaeffer, G. Acevedo-Bolton, B. Boudignon, B. Orwoll, X. Pan, and D. Saloner, "High-resolution CT imaging of carotid artery atherosclerotic plaques," *American Journal of Neuroradiology*, vol. 29, no. 5, pp. 875–882, Feb. 2008. DOI: 10.3174/ajnr.a0950. [Online]. Available: https://doi.org/10.3174/ajnr.a0950.

[29] T. T. de Weert, M. Ouhlous, E. Meijering, P. E. Zondervan, J. M. Hendriks, M. R. van Sambeek, D. W. Dippel, and A. van der Lugt, "In vivo characterization and quantification of atherosclerotic carotid plaque components with multidetector computed tomography and histopathological correlation," *Arteriosclerosis, Thrombosis, and Vascular Biology*, vol. 26, no. 10, pp. 2366–2372, Oct. 2006. DOI: 10.1161/01.atv.0000240518.90124.57. [Online]. Available: https://doi.org/10.1161/01.atv.0000240518.90124.57.

[30] O. Shafaat and H. Sotoudeh, "Stroke imaging," 2019.

[31] A. C. van Dijk, S. Fonville, T. Zadi, A. M. van Hattem, G. Saiedie, P. J. Koudstaal, and A. van der Lugt, "Association between arterial calcifications and nonlacunar and lacunar ischemic strokes," *Stroke*, vol. 45, no. 3, pp. 728–733, Mar. 2014. DOI: 10.1161/strokeaha.113.003197. [Online]. Available: https://doi.org/10.1161/strokeaha.113.003197.

[32] D. Tang, R. D. Kamm, C. Yang, J. Zheng, G. Canton, R. Bach, X. Huang, T. S. Hatsukami, J. Zhu, G. Ma, A. Maehara, G. S. Mintz, and C. Yuan, "Image-based modeling for better understanding and assessment of atherosclerotic plaque progression and vulnerability: Data, modeling, validation, uncertainty and predictions," *Journal of Biomechanics*, vol. 47, no. 4, pp. 834–846, Mar. 2014. DOI: 10.1016/j.jbiomech.2014.01.012. [Online]. Available: https://doi.org/10.1016/j.jbiomech.2014.01.012.

[33] D. Camasão and D. Mantovani, "The mechanical characterization of blood vessels and their substitutes in the continuous quest for physiological-relevant performances. a critical review," *Materials Today Bio*, vol. 10, p. 100 106, Mar. 2021. DOI: 10.1016/j.mtbio.2021.100106. [Online]. Available: https://doi.org/10.1016/j.mtbio.2021.100106.

[34] M. J. Thubrikar, *Vascular mechanics and pathology*. Springer, 2007, vol. 494.

[35] D. J. PATEL, D. L. FRY, and J. S. Janicki, "Longitudinal tethering of arteries in dogs," *Circulation Research*, vol. 19, no. 6, pp. 1011–1021, Dec. 1966. DOI: 10.1161/01.res.19.6.1011. [Online]. Available: https://doi.org/10.1161/01.res.19.6.1011.

[36] S. Hodis and M. Zamir, "Arterial wall tethering as a distant boundary condition," *Physical Review E*, vol. 80, no. 5, Nov. 2009. DOI: 10.1103/physreve.80.051913. [Online]. Available: https://doi.org/10.1103/physreve.80.051913.

[37] A. Das, A. Paul, M. D. Taylor, and R. K. Banerjee, "Pulsatile arterial wall-blood flow interaction with wall pre-stress computed using an inverse algorithm," *BioMedical Engineering OnLine*, vol. 14, no. S1, Jan. 2015. DOI: 10.1186/1475-925x-14-s1-s18. [Online]. Available: https://doi.org/10.1186/1475-925x-14-s1-s18.

[38] W. F. Boron and E. L. Boulpaep, *Medical physiology: A cellular and molecular approach*, en. W.B. Saunders Company, 2012, ch. Section IV.

[39] M. H. Ross and W. Pawlina, *Histology*, 6th ed. Philadelphia, PA: Lippincott Williams and Wilkins, Oct. 2010, ch. 13.

[40] J. J. Wentzel, Y. S. Chatzizisis, F. J. Gijsen, G. D. Giannoglou, C. L. Feldman, and P. H. Stone, "Endothelial shear stress in the evolution of coronary atherosclerotic plaque and vascular remodelling: Current understanding and remaining questions," *Cardiovascular research*, vol. 96, no. 2, pp. 234–243, 2012.

[41] D. Katritsis, L. Kaiktsis, A. Chaniotis, J. Pantos, E. P. Efstathopoulos, and V. Marmarelis, "Wall shear stress: Theoretical considerations and methods of measurement," *Progress in cardiovascular diseases*, vol. 49, no. 5, pp. 307–329, 2007.

[42] E. M. J. Hartman, G. D. Nisco, A. M. Kok, M. Tomaniak, F. M. A. Nous, S.-A. Korteland, F. J. H. Gijsen, W. K. den Dekker, R. Diletti, N. M. D. A. van Mieghem, J. M. Wilschut, F. Zijlstra, A. F. W. van der Steen, R. P. J. Budde, J. Daemen, and J. J. Wentzel, "Wall shear stress–related plaque growth of lipid-rich plaques in human coronary arteries: An near-infrared spectroscopy and optical coherence tomography study," *Cardiovascular Research*, Dec. 2022. DOI: 10.1093/cvr/cvac178. [Online]. Available: https://doi.org/10.1093/cvr/cvac178.

[43] P. Eshtehardi, A. J. Brown, A. Bhargava, C. Costopoulos, O. Y. Hung, M. T. Corban, H. Hosseini, B. D. Gogas, D. P. Giddens, and H. Samady, "High wall shear stress and high-risk plaque: An emerging concept," *The international journal of cardiovascular imaging*, vol. 33, no. 7, pp. 1089–1099, 2017.

[44] F. Helderman, D. Segers, R. de Crom, B. P. Hierck, R. E. Poelmann, P. C. Evans, and R. Krams, "Effect of shear stress on vascular inflammation and plaque development," *Current opinion in lipidology*, vol. 18, no. 5, pp. 527–533, 2007.

[45] A. J. Buckler, M. van Wanrooij, M. Andersson, E. Karlöf, L. P. Matic, U. Hedin, and T. C. Gasser, "Patient-specific biomechanical analysis of atherosclerotic plaques enabled by histologically validated tissue characterization from computed tomography angiography: A case study," en, *J. Mech. Behav. Biomed. Mater.*, vol. 134, no. 105403, p. 105 403, Oct. 2022.

[46] C. Yang, G. Canton, C. Yuan, M. Ferguson, T. S. Hatsukami, and D. Tang, "Advanced human carotid plaque progression correlates positively with flow shear stress using follow-up scan data: An in vivo MRI multi-patient 3d FSI study," *Journal of Biomechanics*, vol. 43, no. 13, pp. 2530–2538, Sep. 2010. DOI: 10.1016/j.jbiomech.2010.05.018. [Online]. Available: https://doi.org/10.1016/j.jbiomech.2010.05.018.

[47] X. Huang, Z. Teng, G. Canton, M. Ferguson, C. Yuan, and D. Tang, "Intraplaque hemorrhage is associated with higher structural stresses in human atherosclerotic plaques: An in vivo mri-based 3d fluid-structure interaction study," *Biomedical engineering online*, vol. 9, no. 1, pp. 1–12, 2010.

[48] C. Yang, G. Canton, C. Yuan, M. Ferguson, T. S. Hatsukami, and D. Tang, "Advanced human carotid plaque progression correlates positively with flow shear stress using follow-up scan data: An in vivo mri multi-patient 3d fsi study," *Journal of biomechanics*, vol. 43, no. 13, pp. 2530–2538, 2010.

[49] C. Yang, G. Canton, C. Yuan, M. Ferguson, T. S. Hatsukami, and D. Tang, "Impact of flow rates in a cardiac cycle on correlations between advanced human carotid plaque progression and mechanical flow shear stress and plaque wall stress," *BioMedical Engineering OnLine*, vol. 10, no. 1, pp. 1–11, 2011.

[50] X. Huang, C. Yang, G. Canton, M. Ferguson, C. Yuan, and D. Tang, "Quantifying effect of intraplaque hemorrhage on critical plaque wall stress in human atherosclerotic plaques using three-dimensional fluid-structure interaction models," *Journal of biomechanical engineering*, vol. 134, no. 12, p. 121 004, 2012.

[51] D. Tang, C. Yang, S. Mondal, F. Liu, G. Canton, T. S. Hatsukami, and C. Yuan, "A negative correlation between human carotid atherosclerotic plaque progression and plaque wall stress: In vivo mri-based 2d/3d fsi models," *Journal of biomechanics*, vol. 41, no. 4, pp. 727–736, 2008.

[52] R. Fan, D. Tang, C. Yang, J. Zheng, R. Bach, L. Wang, D. Muccigrosso, K. Billiar, J. Zhu, and G. Ma, "Human coronary plaque wall thickness correlated positively with flow shear stress and negatively with plaque wall stress: An ivus-based fluid-structure interaction multi-patient study," *Biomedical engineering online*, vol. 13, no. 1, pp. 1–14, 2014.

[53] D. Tang, C. Yang, J. Zheng, P. K. Woodard, G. A. Sicard, J. E. Saffitz, and C. Yuan, "3d mri-based multicomponent fsi models for atherosclerotic plaques," *Annals of biomedical engineering*, vol. 32, no. 7, pp. 947–960, 2004.

[54] D. Tang, C. Yang, G. Canton, Z. Wu, T. Hatsukami, and C. Yuan, "Correlations between carotid plaque progression and mechanical stresses change sign over time: A patient follow up study using mri and 3d fsi models," *BioMedical Engineering OnLine*, vol. 12, no. 1, pp. 1–12, 2013.

[55] L. Wang, Z. Wu, C. Yang, J. Zheng, R. Bach, D. Muccigrosso, K. Billiar, A. Maehara, G. S. Mintz, and D. Tang, "Ivus-based fsi models for human coronary plaque progression study: Components, correlation and predictive analysis," *Annals of biomedical engineering*, vol. 43, no. 1, pp. 107–121, 2015.

[56] L. Wang, D. Tang, A. Maehara, Z. Wu, C. Yang, D. Muccigrosso, J. Zheng, R. Bach, K. L. Billiar, and G. S. Mintz, "Fluid-structure interaction models based on patient-specific ivus at baseline and follow-up for prediction of coronary plaque progression by morphological and biomechanical factors: A preliminary study," *Journal of biomechanics*, vol. 68, pp. 43–50, 2018.

[57] L. Wang, D. Tang, A. Maehara, D. Molony, J. Zheng, H. Samady, Z. Wu, W. Lu, J. Zhu, G. Ma, D. P. Giddens, G. W. Stone, and G. S. Mintz, "Multi-factor decision-making strategy for better coronary plaque burden increase prediction: A patient-specific 3d fsi study using ivus follow-up data," *Biomechanics and modeling in mechanobiology*, vol. 18, no. 5, pp. 1269–1280, 2019.

[58] X. Liu, G. Wu, C. Xu, Y. He, L. Shu, Y. Liu, N. Zhang, and C. Lin, "Prediction of coronary plaque progression using biomechanical factors and vascular characteristics based on computed tomography angiography," *Computer Assisted Surgery*, vol. 22, no. sup1, pp. 286–294, 2017.

[59] D. H. van Dam-Nolen, A. C. van Dijk, G. A. Crombag, C. Lucci, M. E. Kooi, J. Hendrikse, P. J. Nederkoorn, M. J. Daemen, A. F. van der Steen, P. J. Koudstaal, F. Kronenberg, J. E. R. van Lennep, M. T. Mulder, and A. van der Lugt, "Lipoprotein(a) levels and atherosclerotic plaque characteristics in the carotid artery: The plaque at RISK (PARISK) study," *Atherosclerosis*, vol. 329, pp. 22–29, Jul. 2021. DOI: 10.1016/j.atherosclerosis.2021.06.004. [Online]. Available: https://doi.org/10.1016/j.atherosclerosis.2021.06.004.

[60] H. Underhill, C. Yuan, V. Yarnykh, B. Chu, M. Oikawa, L. Dong, N. Polissar, G. Garden, S. Cramer, and T. Hatsukami, "Predictors of surface disruption with MR imaging in asymptomatic carotid artery stenosis," *American Journal of Neuroradiology*, vol. 31, no. 3, pp. 487–493, Oct. 2009. DOI: 10.3174/ajnr.a1842. [Online]. Available: https://doi.org/10.3174/ajnr.a1842.

[61] A. Gupta, H. Baradaran, A. D. Schweitzer, H. Kamel, A. Pandya, D. Delgado, A. Dunning, A. I. Mushlin, and P. C. Sanelli, "Carotid plaque MRI and stroke risk," *Stroke*, vol. 44, no. 11, pp. 3071–3077, Nov. 2013. DOI: 10.1161/strokeaha.113.002551. [Online]. Available: https://doi.org/10.1161/strokeaha.113.002551.

[62] K. R. Nandalur, E. Baskurt, K. D. Hagspiel, M. Finch, C. D. Phillips, S. R. Bollampally, and C. M. Kramer, "Carotid artery calcification on CT may independently predict stroke risk," *American Journal of Roentgenology*, vol. 186, no. 2, pp. 547–552, Feb. 2006. DOI: 10.2214/ajr.04.1216. [Online]. Available: https://doi.org/10.2214/ajr.04.1216.

[63] J. L. Warren, J. E. Yoo, C. A. Meyer, D. S. Molony, H. Samady, and H. N. Hayenga, "Automated finite element approach to generate anatomical patient-specific biomechanical models of atherosclerotic arteries from virtual histology-intravascular ultrasound," *Frontiers in Medical Technology*, vol. 4, Nov. 2022. DOI: 10.3389/fmedt.2022.1008540. [Online]. Available: https://doi.org/10.3389/fmedt.2022.1008540.

[64] C. Costopoulos, L. H. Timmins, Y. Huang, O. Y. Hung, D. S. Molony, A. J. Brown, E. L. Davis, Z. Teng, J. H. Gillard, H. Samady, and M. R. Bennett, "Impact of combined plaque structural stress and wall shear stress on coronary plaque progression, regression, and changes in composition," *European heart journal*, vol. 40, no. 18, pp. 1411–1422, 2019.

[65] A. Paini, P. Boutouyrie, D. Calvet, M. Zidi, E. Agabiti-Rosei, and S. Laurent, “Multiaxial mechanical characteristics of carotid plaque,” *Stroke*, vol. 38, no. 1, pp. 117–123, Jan. 2007. DOI: 10.1161/01.str.0000251796.38954.b2. [Online]. Available: https://doi.org/10.1161/01.str.0000251796.38954.b2.

[66] N. S. Gokhale, *Practical finite element analysis*. Finite to infinite, 2008.

[67] G. A. Holzapfel, T. C. Gasser, and R. W. Ogden, *Journal of Elasticity*, vol. 61, no. 1/3, pp. 1–48, 2000. DOI: 10.1023/a:1010835316564. [Online]. Available: https://doi.org/10.1023/a:1010835316564.

[68] M. Marino, “Constitutive modeling of soft tissues,” in *Encyclopedia of Biomedical Engineering*, Elsevier, 2019, pp. 81–110. DOI: 10.1016/b978-0-12-801238-3.99926-4. [Online]. Available: https://doi.org/10.1016/b978-0-12-801238-3.99926-4.

[69] B. Suki, “Selected examples of tissue-level collagen suprastructures: Tendon, bone, and skin,” in *Structure and Function of the Extracellular Matrix*, Elsevier, 2022, pp. 113–142. DOI: 10.1016/b978-0-12-819716-5.00004-6. [Online]. Available: https://doi.org/10.1016/b978-0-12-819716-5.00004-6.

[70] G. A. Holzapfel, J. J. Mulvihill, E. M. Cunnane, and M. T. Walsh, “Computational approaches for analyzing the mechanics of atherosclerotic plaques: A review,” *Journal of Biomechanics*, vol. 47, no. 4, pp. 859–869, Mar. 2014. DOI: 10.1016/j.jbiomech.2014.01.011. [Online]. Available: https://doi.org/10.1016/j.jbiomech.2014.01.011.

[71] K. Takamizawa and K. Hayashi, “Strain energy density function and uniform strain hypothesis for arterial mechanics,” *Journal of Biomechanics*, vol. 20, no. 1, pp. 7–17, Jan. 1987. DOI: 10.1016/0021-9290(87)90262-4. [Online]. Available: https://doi.org/10.1016/0021-9290(87)90262-4.

[72] T. C. Gasser, R. W. Ogden, and G. A. Holzapfel, “Hyperelastic modelling of arterial layers with distributed collagen fibre orientations,” *Journal of The Royal Society Interface*, vol. 3, no. 6, pp. 15–35, Sep. 2005. DOI: 10.1098/rsif.2005.0073. [Online]. Available: https://doi.org/10.1098/rsif.2005.0073.

[73] D. Nolan, A. Gower, M. Destrade, R. Ogden, and J. McGarry, “A robust anisotropic hyperelastic formulation for the modelling of soft tissue,” *Journal of the Mechanical Behavior of Biomedical Materials*, vol. 39, pp. 48–60, Nov. 2014. DOI: 10.1016/j.jmbbm.2014.06.016. [Online]. Available: https://doi.org/10.1016/j.jmbbm.2014.06.016.

[74] K. Dilba, H. Barrett, H. Bassiouny, S.-A. Korteland, K. van Gaalen, P. J. Nederkoorn, T. J. van Velzen, J. Hendrikse, M. Kassem, M. E. Kooi, A. F. W. van der Steen, A. van der Lugt, D. Bos, J. J. Wentzel, and A. C. Akyildiz, “In-depth calcium geometry assessment of atherosclerotic carotid arteries using ct angiography: A plaque at risk study (parisk) sub-study,” Unpublished manuscript, 2022.

[75] P. Sprawls, *Magnetic resonance imaging: principles, methods, and techniques*. Medical Physics Publishing Madison, 2000, ch. 10.

[76] D. STALLING, M. WESTERHOFF, and H.-C. HEGE, “Amira: A highly interactive system for visual data analysis,” in *Visualization Handbook*, Elsevier, 2005, pp. 749–767. DOI: 10.1016/b978-012387582-2/50040-x. [Online]. Available: https://doi.org/10.1016/b978-012387582-2/50040-x.

[77] E. A. Hulten, S. Carbonaro, S. P. Petrillo, J. D. Mitchell, and T. C. Villines, “Prognostic value of cardiac computed tomography angiography: A systematic review and meta-analysis,” *Journal of the American College of Cardiology*, vol. 57, no. 10, pp. 1237–1247, 2011.

[78] T. Eelbode, J. Bertels, M. Berman, D. Vandermeulen, F. Maes, R. Bisschops, and M. B. Blaschko, “Optimization for medical image segmentation: Theory and practice when evaluating with dice score or jaccard index,” *IEEE Transactions on Medical Imaging*, vol. 39, no. 11, pp. 3679–3690, Nov. 2020. DOI: 10.1109/tmi.2020.3002417. [Online]. Available: https://doi.org/10.1109/tmi.2020.3002417.

[79] M. Bardis, R. Houshyar, C. Chantaduly, K. Tran-Harding, A. Ushinsky, C. Chahine, M. Rupasinghe, D. Chow, and P. Chang, "Segmentation of the prostate transition zone and peripheral zone on MR images with deep learning," en, *Radiol Imaging Cancer*, vol. 3, no. 3, e200024, May 2021.

[80] C. Pinter, A. Lasso, A. Wang, D. Jaffray, and G. Fichtinger, "SlicerRT: Radiation therapy research toolkit for 3d slicer," *Medical Physics*, vol. 39, no. 10, pp. 6332–6338, Sep. 2012. DOI: 10.1118/1.4754659. [Online]. Available: https://doi.org/10.1118/1.4754659.

[81] M. Alidoost, V. Ghodrati, A. Ahmadian, A. Shafiee, C. H. Hassani, A. Bedayat, and J. L. Wilson, "Model utility of a deep learning-based segmentation is not dice coefficient dependent: A case study in volumetric brain blood vessel segmentation," *Intelligence-Based Medicine*, vol. 7, p. 100 092, 2023. DOI: 10.1016/j.ibmed.2023.100092. [Online]. Available: https://doi.org/10.1016/j.ibmed.2023.100092.

[82] P. H. Kitslaar, R. van't Klooster, M. Staring, B. P. F. Lelieveldt, and R. J. van der Geest, "Segmentation of branching vascular structures using adaptive subdivision surface fitting," in *SPIE Proceedings*, S. Ourselin and M. A. Styner, Eds., SPIE, Mar. 2015. DOI: 10.1117/12.2082222. [Online]. Available: https://doi.org/10.1117/12.2082222.

[83] Y. Lai, L. Liu, Y. J. Zhang, J. Chen, E. Fang, and J. Lua, "Rhino 3d to abaqus: A t-spline based isogeometric analysis software framework," in *Advances in Computational Fluid-Structure Interaction and Flow Simulation*, Springer International Publishing, 2016, pp. 271–281. DOI: 10.1007/978-3-319-40827-9_21. [Online]. Available: https://doi.org/10.1007/978-3-319-40827-9_21.

[84] K. A. Ohori, H. Ledoux, and R. Peters, *3d modelling of the built environment*, Publicly available for the course: 3D modelling of the built environment, 2022. [Online]. Available: https://github.com/tudelft3d/3dbook/releases.

[85] K. Sommer, R. L. Izzo, L. Shepard, A. R. Podgorsak, S. Rudin, A. H. Siddiqui, M. F. Wilson, E. Angel, Z. Said, M. Springer, and C. N. Ionita, "Design optimization for accurate flow simulations in 3D printed vascular phantoms derived from computed tomography angiography," en, *Proc. SPIE*, vol. 10138, Feb. 2017.

[86] W. E. Lorensen and H. E. Cline, "Marching cubes: A high resolution 3d surface construction algorithm," *ACM siggraph computer graphics*, vol. 21, no. 4, pp. 163–169, 1987.

[87] T. B. Oliver, G. A. Lammie, A. R. Wright, J. Wardlaw, S. G. Patel, R. Peek, C. V. Ruckley, and D. A. Collie, "Atherosclerotic plaque at the carotid bifurcation: CT angiographic appearance with histopathologic correlation," en, *AJNR Am. J. Neuroradiol.*, vol. 20, no. 5, pp. 897–901, May 1999.

[88] D. Bos, M. A. Ikram, S. E. Elias-Smale, G. P. Krestin, A. Hofman, J. C. Witteman, A. van der Lugt, and M. W. Vernooij, "Calcification in major vessel beds relates to vascular brain disease," *Arteriosclerosis, Thrombosis, and Vascular Biology*, vol. 31, no. 10, pp. 2331–2337, Oct. 2011. DOI: 10.1161/atvbaha.111.232728. [Online]. Available: https://doi.org/10.1161/atvbaha.111.232728.

[89] M. Smith, *ABAQUS/Standard User's Manual, Version 6.9*, English. United States: Dassault Systèmes Simulia Corp, 2009.

[90] C. Obbink-Huizer, *Two ways to get geometry from an orphan mesh in abaqus - simuleon*, Feb. 2022. [Online]. Available: https://info.simuleon.com/blog/two-ways-to-get-geometry-from-an-orphan-mesh-in-abaqus.

[91] L. Heller and et al., "What are the biomechanical differences due to the presence of calcification and the specific morphology in carotid atherosclerosis plaques?" Internship report, Mar. 2019.

[92] S. Barrett, M. Sutcliffe, S. Howarth, Z. Li, and J. Gillard, "Experimental measurement of the mechanical properties of carotid atherothrombotic plaque fibrous cap," *Journal of Biomechanics*, vol. 42, no. 11, pp. 1650–1655, Aug. 2009. DOI: 10.1016/j.jbiomech.2009.04.025. [Online]. Available: https://doi.org/10.1016/j.jbiomech.2009.04.025.

[93] D. M. Ebenstein, D. Coughlin, J. Chapman, C. Li, and L. A. Pruitt, “Nanomechanical properties of calcification, fibrous tissue, and hematoma from atherosclerotic plaques,” *Journal of Biomedical Materials Research Part A*, vol. 91A, no. 4, pp. 1028–1037, Dec. 2009. DOI: 10.1002/jbm.a.32321. [Online]. Available: https://doi.org/10.1002/jbm.a.32321.

[94] M. Swaab and et al., “The effects of local fibre organization on the elastic and rupture behaviour of tissue engineered fibrous cap models,” Delft University of Technology, Aug. 2021. [Online]. Available: https://repository.tudelft.nl/islandora/object/uuid%5C%3A74882c32-bfef-4dc8-8586-ebf732f6aad8.

[95] S. A. Maas, B. J. Ellis, G. A. Ateshian, and J. A. Weiss, “FEBio: Finite elements for biomechanics,” *Journal of Biomechanical Engineering*, vol. 134, no. 1, Jan. 2012. DOI: 10.1115/1.4005694. [Online]. Available: https://doi.org/10.1115/1.4005694.

[96] P. Poredos, “Intima-media thickness: Indicator of cardiovascular risk and measure of the extent of atherosclerosis,” *Vascular Medicine*, vol. 9, no. 1, pp. 46–54, Feb. 2004. DOI: 10.1191/1358863x04vm514ra. [Online]. Available: https://doi.org/10.1191/1358863x04vm514ra.

[97] A. C. Akyildiz, L. Speelman, H. A. Nieuwstadt, H. van Brummelen, R. Virmani, A. van der Lugt, A. F. van der Steen, J. J. Wentzel, and F. J. Gijsen, “The effects of plaque morphology and material properties on peak cap stress in human coronary arteries,” *Computer Methods in Biomechanics and Biomedical Engineering*, vol. 19, no. 7, pp. 771–779, Aug. 2015. DOI: 10.1080/10255842.2015.1062091. [Online]. Available: https://doi.org/10.1080/10255842.2015.1062091.

[98] A. Murgia, M. Erta, J. S. Suri, A. Gupta, M. Wintermark, and L. Saba, “Ct imaging features of carotid artery plaque vulnerability,” *Annals of Translational Medicine*, vol. 8, no. 19, 2020, ISSN: 2305-5847. [Online]. Available: https://atm.amegroups.com/article/view/45347.

[99] B. López-Melgar, L. Fernández-Friera, B. Oliva, J. M. García-Ruiz, J. L. Peñalvo, S. Gómez-Talavera, J. Sánchez-González, J. M. Mendiguren, B. Ibáñez, A. Fernández-Ortiz, J. Sanz, and V. Fuster, “Subclinical atherosclerosis burden by 3d ultrasound in mid-life,” *Journal of the American College of Cardiology*, vol. 70, no. 3, pp. 301–313, Jul. 2017. DOI: 10.1016/j.jacc.2017.05.033. [Online]. Available: https://doi.org/10.1016/j.jacc.2017.05.033.

[100] M. Ghasemi, D. R. Nolan, and C. Lally, “Assessment of mechanical indicators of carotid plaque vulnerability: Geometrical curvature metric, plaque stresses and damage in tissue fibres,” *Journal of the Mechanical Behavior of Biomedical Materials*, vol. 103, p. 103 573, Mar. 2020. DOI: 10.1016/j.jmbbm.2019.103573. [Online]. Available: https://doi.org/10.1016/j.jmbbm.2019.103573.

[101] L. Antiga, M. Piccinelli, L. Botti, B. Ene-Iordache, A. Remuzzi, and D. A. Steinman, “An image-based modeling framework for patient-specific computational hemodynamics,” *Medical &amp Biological Engineering &amp Computing*, vol. 46, no. 11, Nov. 2008. DOI: 10.1007/s11517-008-0420-1. [Online]. Available: https://doi.org/10.1007/s11517-008-0420-1.

[102] F. Auricchio, M. Conti, A. Ferrara, S. Morganti, and A. Reali, “Patient-specific finite element analysis of carotid artery stenting: A focus on vessel modeling,” *International Journal for Numerical Methods in Biomedical Engineering*, vol. 29, no. 6, pp. 645–664, Sep. 2012. DOI: 10.1002/cnm.2511. [Online]. Available: https://doi.org/10.1002/cnm.2511.

[103] J. Kim, W. Dillon, C. Glastonbury, J. Provenzale, and M. Wintermark, “Sixty-four-section multidetector CT angiography of carotid arteries: A systematic analysis of image quality and artifacts,” *American Journal of Neuroradiology*, vol. 31, no. 1, pp. 91–99, Sep. 2009. DOI: 10.3174/ajnr.a1768. [Online]. Available: https://doi.org/10.3174/ajnr.a1768.

[104] Y. Lai, Y. J. Zhang, L. Liu, X. Wei, E. Fang, and J. Lua, “Integrating CAD with abaqus: A practical isogeometric analysis software platform for industrial applications,” *Computers &amp Mathematics with Applications*, vol. 74, no. 7, pp. 1648–1660, Oct. 2017. DOI: 10.1016/j.camwa.2017.03.032. [Online]. Available: https://doi.org/10.1016/j.camwa.2017.03.032.

[105] A. C. Akyildiz, C.-K. Chai, C. W. Oomens, A. van der Lugt, F. P. Baaijens, G. J. Strijkers, and F. J. Gijsen, “3d fiber orientation in atherosclerotic carotid plaques,” *Journal of Structural Biology*, vol. 200, no. 1, pp. 28–35, Oct. 2017. DOI: 10.1016/j.jsb.2017.08.003. [Online]. Available: https://doi.org/10.1016/j.jsb.2017.08.003.

[106] G. A. Holzapfel and R. W. Ogden, “Biomechanical relevance of the microstructure in artery walls with a focus on passive and active components,” *American Journal of Physiology-Heart and Circulatory Physiology*, vol. 315, no. 3, H540–H549, 2018.

[107] J. Bols, J. Degroote, B. Trachet, B. Verhegghe, P. Segers, and J. Vierendeels, “A computational method to assess the in vivo stresses and unloaded configuration of patient-specific blood vessels,” *Journal of Computational and Applied Mathematics*, vol. 246, pp. 10–17, Jul. 2013. DOI: 10.1016/j.cam.2012.10.034. [Online]. Available: https://doi.org/10.1016/j.cam.2012.10.034.

[108] B. Mujaj, D. Bos, M. Selwaness, M. J. Leening, M. Kavousi, J. J. Wentzel, A. van der Lugt, A. Hofman, B. H. Stricker, M. W. Vernooij, and O. H. Franco, “Statin use is associated with carotid plaque composition: The rotterdam study,” *International Journal of Cardiology*, vol. 260, pp. 213–218, Jun. 2018. DOI: 10.1016/j.ijcard.2018.02.111. [Online]. Available: https://doi.org/10.1016/j.ijcard.2018.02.111.

[109] D. Bos, B. Arshi, Q. J. van den Bouwhuijsen, M. K. Ikram, M. Selwaness, M. W. Vernooij, M. Kavousi, and A. van der Lugt, “Atherosclerotic carotid plaque composition and incident stroke and coronary events,” *Journal of the American College of Cardiology*, vol. 77, no. 11, pp. 1426–1435, Mar. 2021. DOI: 10.1016/j.jacc.2021.01.038. [Online]. Available: https://doi.org/10.1016/j.jacc.2021.01.038.

[110] L. Antiga and D. Steinman, “Robust and objective decomposition and mapping of bifurcating vessels,” *IEEE Transactions on Medical Imaging*, vol. 23, no. 6, pp. 704–713, Jun. 2004. DOI: 10.1109/tmi.2004.826946. [Online]. Available: https://doi.org/10.1109/tmi.2004.826946.

[111] Z. Teng, U. Sadat, Z. Li, X. Huang, C. Zhu, V. E. Young, M. J. Graves, and J. H. Gillard, “Arterial luminal curvature and fibrous-cap thickness affect critical stress conditions within atherosclerotic plaque: An in vivo MRI-based 2d finite-element study,” *Annals of Biomedical Engineering*, vol. 38, no. 10, pp. 3096–3101, May 2010. DOI: 10.1007/s10439-010-0078-3. [Online]. Available: https://doi.org/10.1007/s10439-010-0078-3.

[112] B. Mujaj, D. Bos, T. Muka, A. van der Lugt, M. A. Ikram, M. W. Vernooij, B. H. Stricker, and O. H. Franco, “Antithrombotic treatment is associated with intraplaque haemorrhage in the atherosclerotic carotid artery: A cross-sectional analysis of the rotterdam study,” *European Heart Journal*, vol. 39, no. 36, pp. 3369–3376, Jul. 2018. DOI: 10.1093/eurheartj/ehy433. [Online]. Available: https://doi.org/10.1093/eurheartj/ehy433.

[113] R. M. Kwee, R. J. van Oostenbrugge, M. H. Prins, J. W. ter Berg, C. L. Franke, A. G. C. Korten, B. J. Meems, J. M. van Engelshoven, J. E. Wildberger, W. H. Mess, and M. E. Kooi, “Symptomatic patients with mild and moderate carotid stenosis,” *Stroke*, vol. 41, no. 7, pp. 1389–1393, Jul. 2010. DOI: 10.1161/strokeaha.109.575670. [Online]. Available: https://doi.org/10.1161/strokeaha.109.575670.

[114] S. Pfohl, B. Marafino, A. Coulet, F. Rodriguez, L. Palaniappan, and N. H. Shah, “Creating fair models of atherosclerotic cardiovascular disease risk,” in *Proceedings of the 2019 AAAI/ACM Conference on AI, Ethics, and Society*, ACM, Jan. 2019. DOI: 10.1145/3306618.3314278. [Online]. Available: https://doi.org/10.1145/3306618.3314278.

[115] W. E. Hellings, G. Pasterkamp, B. A. Verhoeven, D. P. D. Kleijn, J.-P. P. D. Vries, K. A. Seldenrijk, T. van den Broek, and F. L. Moll, “Gender-associated differences in plaque phenotype of patients undergoing carotid endarterectomy,” *Journal of Vascular Surgery*, vol. 45, no. 2, pp. 289–296, Feb. 2007. DOI: 10.1016/j.jvs.2006.09.051. [Online]. Available: https://doi.org/10.1016/j.jvs.2006.09.051.

A

Geometry reconstruction

This appendix contains additional data for Chapter 2. Dice scores on observers and reconstruction are illustrated in more detail here. Additionally, the surface reconstruction method and considerations are explained in detail.

A.1. Image segmentation

Here, detailed results on the calculation of the Dice scores for each segment is shown in Figure A.1. For each segmented vessel, the similarity between two observers is shown for the lumen and vessel wall delineations on a scale of 0 to 1.

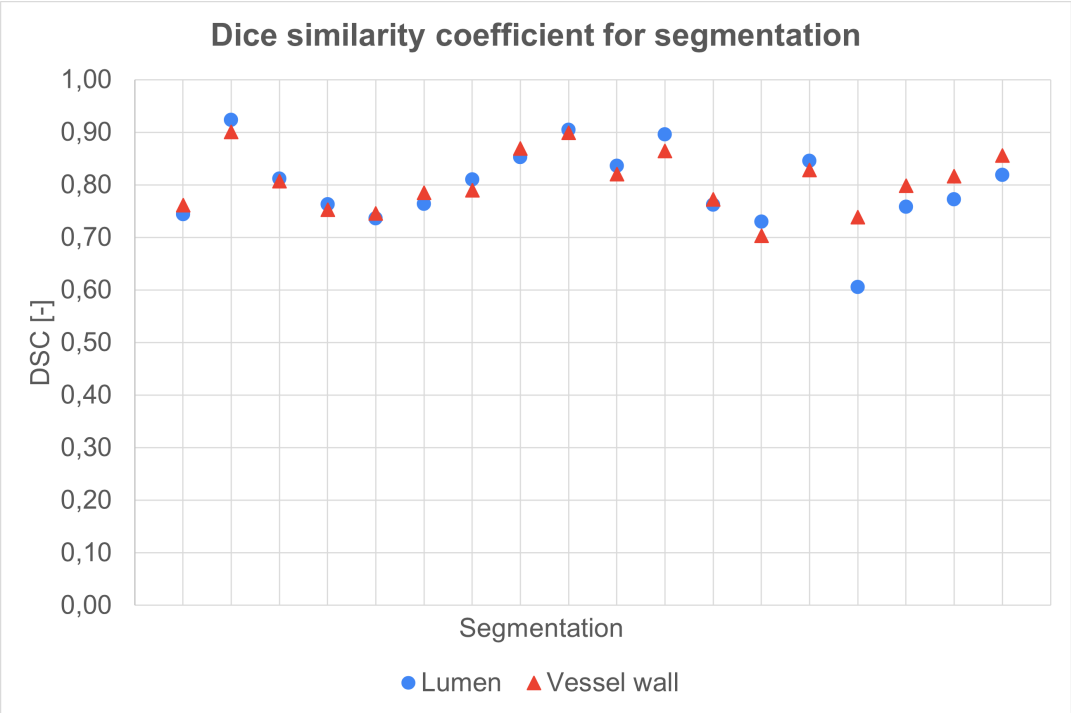

Figure A.1: Scatterplot of the Dice similarity coefficient per comparison for lumen and vessel wall contours, per segmentation.

A.2. 3D reconstruction

A.2.1. Reconstruction similarity

For quantification of the reconstruction steps the similarity was computed between the initial surface and the final segment. For lumen, vessel wall, baseline and follow-up this was calculated per segment. Figure A.2 shows the detailed similarity scores per segment.

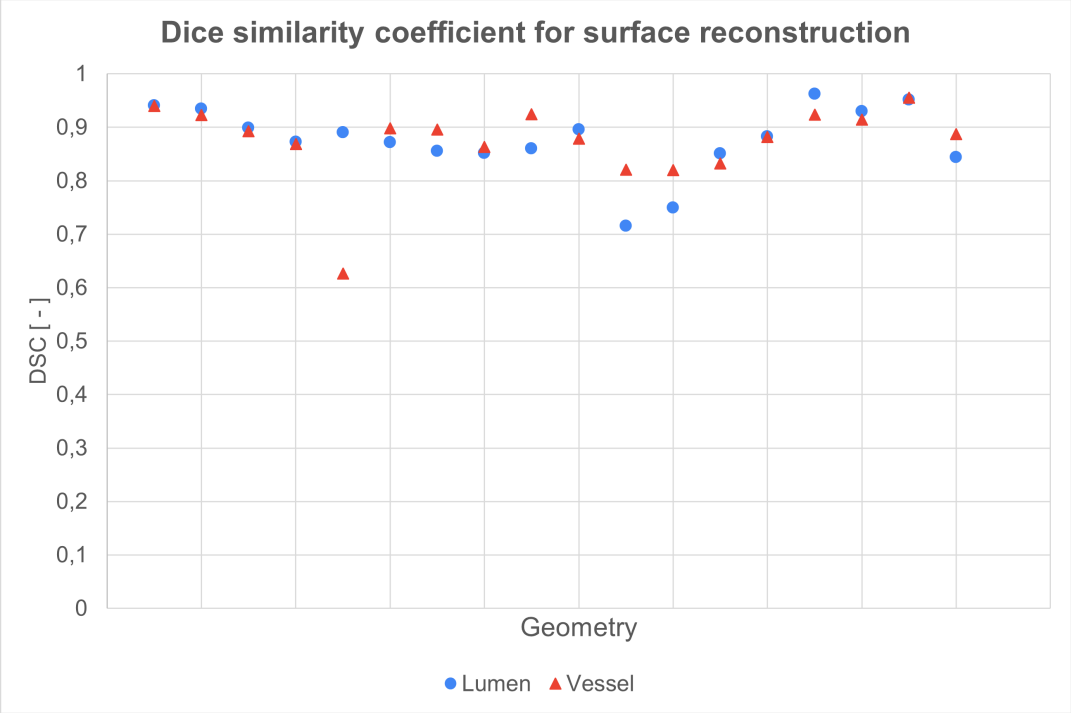

Figure A.2: Scatterplot of the Dice similarity coefficient per comparison for lumen and vessel wall contours for each reconstructed surface, baseline and follow-up.

A.2.2. Surface reconstruction method

The complete reconstruction method is visualized in Figure 2.2, Chapter 2. A detailed outline of the steps, codes and requirements are illustrated in Figure A.3. Per phase of the reconstruction the visual inspection requirements are shown. After, the motivations for each software are explained, based on the requirements.

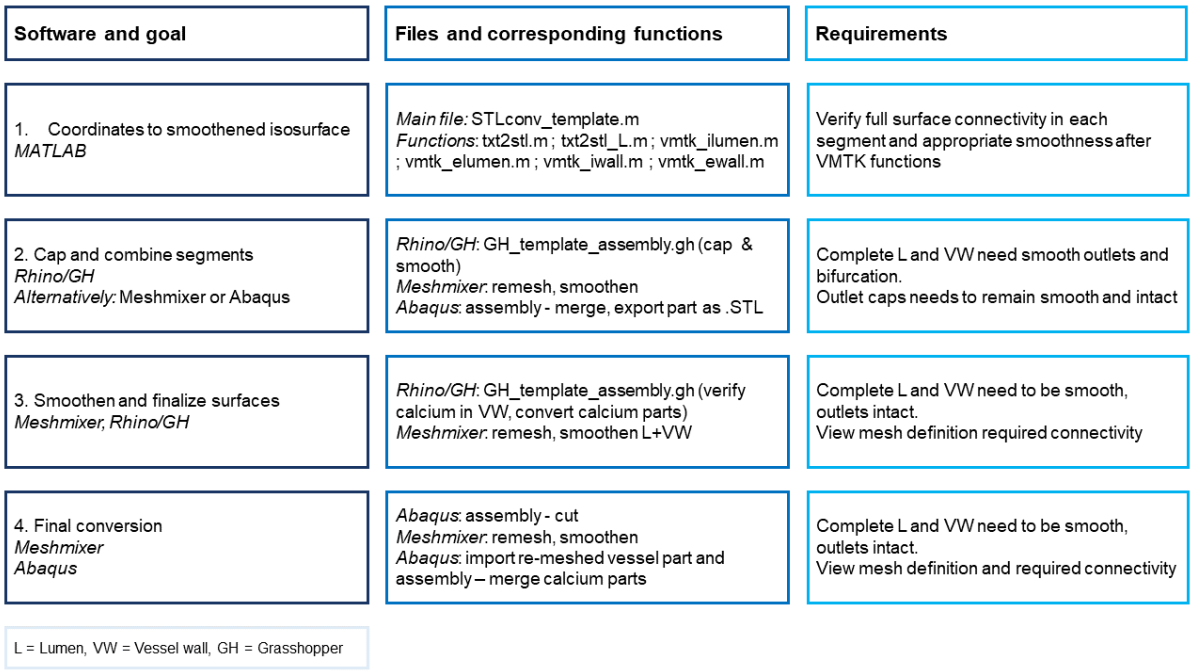

Figure A.3: Overview of the reconstruction phases, corresponding files and requirements. Verifications were based on visual inspection.

Matlab

By importing the coordinate .TXT-files a multidimensional array was built. Based on the maximum number of coordinates of all slices, each slice of coordinates was interpolated using the curvspace function. The coordinates were then structured to a page for each slice to contain all the X, Y and Z-coordinates.

From all pages, a meshgrid was determined to form a bounding box, in which all the coordinates fit. For each slice, the griddata was determined. This meant that coordinates within the closed outline, were assigned a value. The locations that fell outside this area, received a NaN. Using the isnan, a binary multidimensional array was built. Ones would indicate the outside, zeros the inside. Based on this binary data, and the meshgrid, an isosurface could be computed. In this isosurface, the boundary was set between the one and zero positions, for each slice. This left a, open pipe-like structure, the vessel segment.

Vascular Modeling Toolkit

The Vascular Modeling ToolKit (VMTK) is an extension of the image analysis software 3DSlicer. This software can be used to analyze and evaluate imaged vessels. This application is programmed to receive a Python-C++ coding input, calling upon pre-described functions. This programme can mesh, re-mesh and adapt STL-files, even open surfaces. It uses PypePad as input programme and communicates through python. The software can be called upon from a Matlab script, and run through Python in the system [101]. Here, it was used to smoothen open surfaces and rewrite the .STL-files.

Rhino - Grasshopper

Rhinoceros® is another software that can create and adapt geometries through parametric design. Its sub-application, Grasshopper 3D, offers the ability to build a scheme with a flow of reconstruction steps, that will create the same steps for each patient. Here, Grasshopper was used to verify and validate the mesh. The surfaces were closed through capping, and the internal and external branches were combined for the lumen and vessel wall, through the boolean union. The lumen and vessel wall were exported as STL files again.

MeshMixer

Meshmixer is a software by Autodesk. This programme offered the function to remesh an existing mesh. Here, this was useful to smoothen the surface, after the boolean union in Rhino. Moreover, the remesh function created a smoother surface that also contained fewer triangles, thereby reducing the computational costs in later mesh pre-processing steps.

Abaqus

In Abaqus, the final steps were completed. The files from MeshMixer were imported and converted to a solid entity through the STL2geometry plugin. This plugin converted orphan meshes from STL files to solid or shell entities, depending on their validity. Once the solids were obtained, the lumen was cut from the vessel wall in the Assembly module, leaving the final vessel geometry. This was further processed in the pre-processing for FE-analysis (Chapter 3).

A.2.3. Software considerations

The final workflow consisted of five software packages. In theory, VMTK and Rhino were capable of overtaking this entire workflow. However, practical bottlenecks interfered with this plan, which is outlined here.

Vascular Modeling Toolkit

Vascular Modeling Toolkit functions have been used in the final methods. However, this software offers many more options. Currently, this coding only applied the taubin surface smoothing. Overall, VMTK has the capacity and functions to fully cap, merge and transform the vessels to a near-manifold structure. However, in the final conversion to create the explicit definition of the surface, the STL files became corrupted. Therefore, a full VMTK-based reconstruction would result in STL files that were not accepted by Abaqus and could not be used for FE-modeling. So the role of VMTK was reduced to its ability to smoothen all kinds of surfaces, even open ones.

Rhino - Grasshopper

A more extensive approach to perform the entire data conversion in Grasshopper was also researched. Before importing the coordinates, a dedicated Matlab script would split the TXT file containing all coordinates, into separate files, containing all coordinates per slice. Here, ICA and ECA were processed separately as well.

In Grasshopper, the coordinates were connected through Non-uniform rational basis spline (NURBS) curves. This type of polyline is known to transition smoother between points, and can still connect all the points. This way, the contours from the segmentation were reconstructed. The NURBS curves were lofted along the length of the vessel to mimic the outer surface of the vessel. Like in the surface computation of the Matlab code, this yields an open surface vessel-like structure. This was capped and smoothed, for all four segments of a vessel. Then, to compute the proper bifurcation, the contours were re-calculated along the z-axis. Lofting along these contours, yielded the closed surface, bifurcated vessel structure.

This method seemed feasible, but the final recomputation of the contours would deviate too much from the original contours from QAngio CT. It became evident that these contours are placed perpendicular to the seed orientation in the centerline. This caused overlapping and tilted contours, relative to each other. By using this Grasshopper method, this could be filtered out by clearing out nonadjacent NURB curves. However, it would also create confusion in where the actual surface would be, causing an underestimation of the luminal or vessel wall volume. Eventually, this affects the wall thickness, thereby the structural analysis as well. So, although this method reduced the workflow to one software, the inaccuracies led to the decision to not implement this method in this project.

B

Finite Element Analysis

B.1. Mesh sensitivity analysis

A mesh sensitivity analysis was performed using case 1R. By comparing the maximum stress and maximum strain response in the lumen, seed sizes were explored. The sensitivity analysis was performed with a minimum increment size of 0.005 s for a duration of 1.00 seconds. Full convergence was achieved in all seed sizes. Table B.1 shows that a seed size below 0.4 reached a stress and strain difference below 2 %. So the seed size was set at 0.4 for all cases.

Table B.1: Mesh sensitivity analysis results. All seed sizes were run with a fixed increment size. The outcome of this analysis determined the mesh settings for the FE-analysis in Chapter 3.

Seed size [–]	**Nodes** [#]	**Elements** [#]	**Max(S)** [kPa]	**Δ S** [%]	**Max(Sn)** [–]	**Δ Sn** [%]
2.0	1921	7598	226.822		.141	
1.0	4237	16919	225.808	-0.002	0.148	0.025
0.5	18628	84164	241.751	0.034	0.152	0.011
0.4	33472	158341	236.735	**-0.010**	0.147	**-0.016**
0.39	35327	167624	231.739	**-0.011**	0.147	**-0.001**
0.38	37932	180605	228.120	**-0.008**	0.153	**0.017**

B.2. Patient-specific meshing

Based on the mesh sensitivity, the number of nodes was collected for each case. An overview of the number of nodes and the number of elements per simulation, is shown in Table B.2.

Table B.2: Mesh settings per simulation. For each patient, only the baseline was simulated.

Patient	**Side**	**Mesh**	
		Nodes	*Elements*
	[L/R]	[#]	[#]
1L	Left	28845	137953
1R	Right	33472	158341
2L	Left	57048	307179
2R	Right	55601	296365
3L	Left	45208	230165
3R	Right	75102	404630
4R	Right	81804	444136
5L	Left	67390	345597
6R	Right	25289	116475

C

Morphometrics

This appendix contains the patient-specific morphometrical results.

C.1. Calcium

Raw data for calcium analysis was obtained from QAngio ReportWizard and files from QAngio 3DWorkbench. This data was used to consider the progression as a function of calcium. Both parameters, volume and number of bodies, should provide insight into atherosclerotic vessels' progressive behaviour (Table C.1).

Table C.1: Calcium data per vessel. Calcium volume and the number of bodies has been computed for baseline and follow-up. Δ has been calculated by subtracting baseline data from follow-up points. Based on that, progression, regression or constant has been concluded.

Patient no.	**Vessel no.**	**Timepoint**	**Calcium** *Volume [mm^3]*	**Δ C** *Volume [mm^3]*	**Calcium** *Bodies [#]*	**Δ Bodies** *Bodies [#]*
1	1L	Baseline	1.66		1	
1	1L	Follow-up	3.69	2.04	1	0
1	1R	Baseline	8.08		1	
1	1R	Follow-up	6.14	- 1.94	1	0
2	2L	Baseline	118.88		1	
2	2L	Follow-up	136.66	17.78	1	0
2	2R	Baseline	131.73		1	
2	2R	Follow-up	172.02	40.29	2	1
3	3L	Baseline	18.38		2	
3	3L	Follow-up	24.34	5.97	3	1
3	3R	Baseline	98.78		5	
3	3R	Follow-up	112.97	14.19	2	-3
4	4R	Baseline	116.63		1	
4	4R	Follow-up	139.00	22.37	1	0
5	5L	Baseline	7.36		2	
5	5L	Follow-up	22.25	14.89	5	3
6	6R	Baseline	0.00		2	
6	6R	Follow-up	0.66	0.66	1	-1

C.2. Global analysis results

C.2.1. Segment based: Stress, Strain, Curvature and Wall thickness

Table C.2: Case-specific global results per segment for the first five cases. For each segment the principal stress, strain, curvature (curv) and wall thickness have been calculated. T(0) = Baseline, T(1) = Follow-up, ΔWT (T) = wall thickness change over time.

			1L		1R		2L		2R		4R	
			CCA-ICA	CCA-ECA	CCA-ICA	CCA-ECA	CCA-ICA	CCA-ECA	CCA-ICA	CCA-ECA	CCA-ICA	CCA-ECA
Stress	T(0)Max	[kPa]	177.46	145.48	151.91	156.78	234.24	276.02	273.96	299.80	104.74	113.74
	T(0)Median	[kPa]	64.39	62.13	85.70	85.06	64.39	50.83	62.47	56.00	31.71	40.99
	T(0)Min	[kPa]	-6.59	23.63	15.34	14.99	10.84	5.01	7.01	2.72	-11.20	3.39
Strain	T(0)Max	[-]	0.12	0.12	0.12	0.12	0.15	0.15	0.15	0.17	0.10	0.11
	T(0)Median	[-]	0.08	0.08	0.09	0.09	0.08	0.07	0.08	0.07	0.06	0.06
	T(0)Min	[-]	0.03	0.04	0.04	0.04	0.03	0.03	0.03	0.02	0.02	0.02
Max Curv	T(0)Max	[m^{-1}]	1.04	0.87	0.87	1.70	3.71	1.15	0.62	0.91	3.62	1.56
	T(0)Median	[m^{-1}]	0.38	0.38	0.30	0.33	0.39	0.44	0.33	0.38	0.65	0.62
	T(0)Min	[m^{-1}]	0.04	-0.01	0.01	0.03	-0.01	0.04	0.17	0.13	0.16	0.11
	T(1)Max	[m^{-1}]	1.60	1.49	1.58	1.58	27.13	27.13	0.38	1.03	17.85	26.66
	T(1)Median	[m^{-1}]	0.48	0.41	0.00	0.00	0.36	0.40	0.00	0.00	0.73	0.49
	T(1)Min	[m^{-1}]	-0.22	-0.29	0.00	0.00	-0.15	0.00	-0.01	0.00	-408.78	-408.78
Min Curv	T(0)Max	[m^{-1}]	0.43	0.43	0.32	0.32	0.24	0.61	0.16	0.15	0.38	0.26
	T(0)Median	[m^{-1}]	-0.03	-0.02	0.00	0.00	-0.02	-0.04	-0.01	-0.01	0.00	0.00
	T(0)Min	[m^{-1}]	-1.32	-1.67	-0.66	-2.05	-1.83	-1.49	-1.33	-1.52	-2.04	-1.84
	T(1)Max	[m^{-1}]	0.47	0.47	0.00	0.00	0.45	0.45	12.45	6.48	0.00	0.00
	T(1)Median	[m^{-1}]	-0.02	-0.01	0.00	0.00	0.00	-0.01	-0.01	-0.02	0.00	0.00
	T(1)Min	[m^{-1}]	-2.66	-2.62	-7.17	-7.17	-12.37	-12.37	-86.50	-37.19	-1.76	-1.76
Wall thickness	T(0)Max	[mm]	3.58	3.37	3.34	3.20	4.51	4.61	0.29	0.51	4.47	4.47
	T(0)Median	[mm]	1.11	1.04	1.06	1.01	1.47	1.69	0.08	0.11	2.02	1.65
	T(0)Min	[mm]	0.74	0.63	0.79	0.38	0.75	0.76	0.00	0.00	0.85	0.56
	T(1)Max	[mm]	3.70	3.67	3.40	3.40	4.77	4.77	4.83	4.83	4.79	4.79
	T(1)Median	[mm]	1.24	1.17	1.24	1.14	1.10	1.39	1.13	1.09	2.09	1.60
	T(1)Min	[mm]	0.35	0.35	0.46	0.67	-0.03	0.19	-0.65	0.53	-0.01	0.45
Δ WT (T)	Max	[mm]	0.10	0.03	-0.30	-0.33	-0.03	-0.04	-0.33	-0.38	0.08	-0.13
	Median	[mm]	-0.26	-0.28	-0.01	-0.03	-0.14	-0.04	-0.18	-0.14	-408.94	-408.89
	Min	[mm]	-1.17	-1.06	-1.27	-1.27	-26.89	-26.52	-0.21	-0.88	-17.46	-26.40

Table C.3: Case-specific global results per segment for the final four cases. For each segment the principal stress, strain, curvature (Curv) and wall thickness have been calculated. T(0) = Baseline, T(1) = Follow-up, ΔWT (T) = wall thickness change over time.

				3L		3R		5L		6R	
				CCA-ICA	CCA-ECA	CCA-ICA	CCA-ECA	CCA-ICA	CCA-ECA	CCA-ICA	CCA-ECA
Stress	T(0)	Max	[kPa]	269.48	270.14	118.17	111.53	744.31	839.66	276.11	279.66
	T(0)	Median	[kPa]	56.05	61.68	43.47	55.27	61.14	60.55	85.85	82.52
	T(0)	Min	[kPa]	7.34	-9.30	-33.03	10.12	-24.31	-13.98	19.90	19.88
Strain	T(0)	Max	[-]	0.15	0.15	0.11	0.11	0.22	0.22	0.14	0.15
	T(0)	Median	[-]	0.07	0.08	0.07	0.07	0.08	0.08	0.04	0.04
	T(0)	Min	[-]	0.02	0.04	0.02	0.03	0.03	0.03	-0.14	0.15
Max Curv	T(0)	Max	[m^{-1}]	139.10	139.10	1.15	1.30	17.09	17.09	0.73	0.85
	T(0)	Median	[m^{-1}]	0.32	0.33	0.49	0.45	0.30	0.35	0.32	0.35
	T(0)	Min	[m^{-1}]	-6.22	-6.22	0.02	0.02	-0.10	-0.10	-0.03	0.00
	T(1)	Max	[m^{-1}]	3.16	3.16	2.73	6.07	1.71	2.26	1.47	0.79
	T(1)	Median	[m^{-1}]	0.00	0.00	0.40	0.45	0.31	0.35	0.38	0.32
	T(1)	Min	[m^{-1}]	0.00	0.00	-0.23	-0.59	-0.04	0.00	-0.04	-0.04
Min Curv	T(0)	Max	[m^{-1}]	139.10	139.10	0.30	0.14	1.74	1.74	0.33	0.33
	T(0)	Median	[m^{-1}]	0.32	0.33	-0.01	-0.01	-0.01	-0.01	-0.01	-0.02
	T(0)	Min	[m^{-1}]	-6.22	-6.22	-1.20	-1.27	-24.18	-24.18	-1.26	-1.47
	T(1)	Max	[m^{-1}]	22.27	22.27	0.83	0.73	0.41	0.47	0.33	0.24
	T(1)	Median	[m^{-1}]	-0.01	-0.01	-0.04	-0.03	-0.01	-0.03	-0.02	-0.01
	T(1)	Min	[m^{-1}]	-11.61	-11.61	-2.74	-5.76	-0.77	-1.21	-10.91	-10.91
Wall thickness	T(0)	Max	[mm]	3.63	3.63	4.44	4.44	2.81	2.87	1.67	1.67
	T(0)	Median	[mm]	1.23	1.17	1.58	1.35	1.44	1.47	1.06	1.06
	T(0)	Min	[mm]	0.34	0.30	0.84	0.84	0.83	0.89	0.20	0.20
	T(1)	Max	[mm]	3.67	3.67	39.11	4.48	3.96	3.46	2.63	2.39
	T(1)	Median	[mm]	1.62	1.42	1.55	1.53	2.00	2.26	1.14	1.14
	T(1)	Min	[mm]	0.02	0.02	0.17	0.21	0.70	0.70	0.58	0.54
Δ WT (T)		Max	[mm]	-0.32	-0.33	-0.09	0.00	0.01	0.00	0.05	-0.03
		Median	[mm]	6.22	6.22	-0.25	-0.61	0.06	0.10	-0.01	-0.04
		Min	[mm]	135.94	135.94	-2.43	-5.93	0.02	-0.53	-1.14	-0.45

C.2.2. Full vessel: Plaque burden and Calcium

Table C.4: Case-specific global results for all patients from a full vessel analysis. For each case the plaque burden, change in plaque burden (△PB (T)), calcium volume and change in calcium volume over time (△ C(T)) are calculated. T(0) = Baseline, T(1) = Follow-up.

				1L	1R	2L	2R	3L	3R	4R	5L	6R
Plaque burden *	T(0)	Max	[%]	73.44	72.85	72.25	80.67	75.84	79.44	95.76	67.62	61.04
	T(0)	Median	[%]	48.43	40.63	53.28	51.21	47.65	51.68	53.95	51.48	45.00
	T(0)	Min	[%]	33.73	34.07	43.19	35.29	34.28	35.68	41.06	35.72	37.25
	T(1)	Max	[%]	88.37	69.76	75.16	76.49	71.70	80.60	94.74	70.88	57.41
	T(1)	Median	[%]	52.45	46.45	51.07	52.92	52.15	56.63	56.80	52.20	46.02
	T(1)	Min	[%]	33.59	35.28	43.78	32.96	37.19	37.57	41.55	38.07	35.71
△ PB (T)		Max	[%]	14.93	-3.09	2.91	-4.18	-4.14	1.15	-1.02	3.26	-3.63
		Median	[%]	4.02	5.81	-2.21	1.71	4.50	4.96	2.84	0.72	1.03
		Min	[%]	-0.14	1.21	0.59	-2.34	2.91	1.88	0.49	2.35	-1.53
Calcium volume *	T(0)		[mm^3]	1.66	8.08	118.88	131.73	18.38	98.78	116.63	7.36	0.00
	T(1)		[mm^3]	3.69	6.14	136.66	172.02	24.34	112.97	139.00	22.25	0.66
△ C (T)			[mm^3]	2.03	-1.94	17.78	40.29	5.96	14.19	22.37	14.89	0.66

D

Results

This appendix includes all results per vessel. The first page is the 3D FE-modeling output in terms of stress and strain. The second page is the 3D morphometry. The third page shows the metrics to convert 3D structures to 2D heatmaps shown on the fourth and fifth pages. These show the output for the CCA-ICA and CCA-ECA segments, respectively. The final page shows metrics for the analyses for each vessel specifically. All vessels are printed here.

Patient 1L – 3D Metrics

Biomechanical analysis

Stress – Luminal surface

Medial

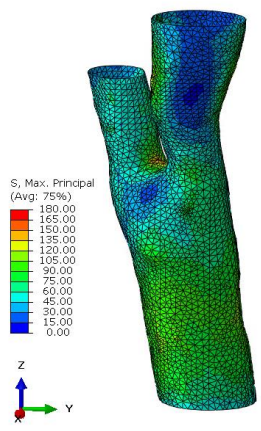

Anterior

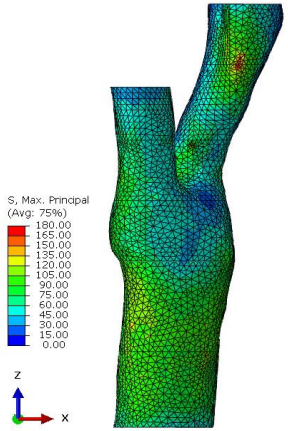

Lateral

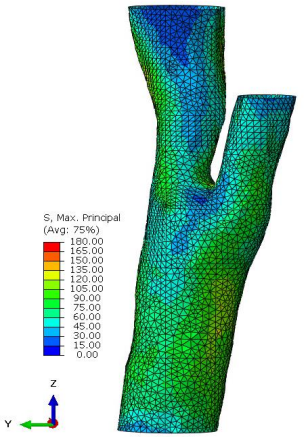

Posterior

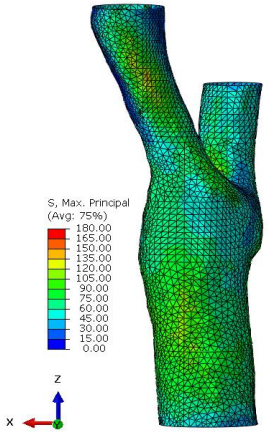

Strain – Luminal surface

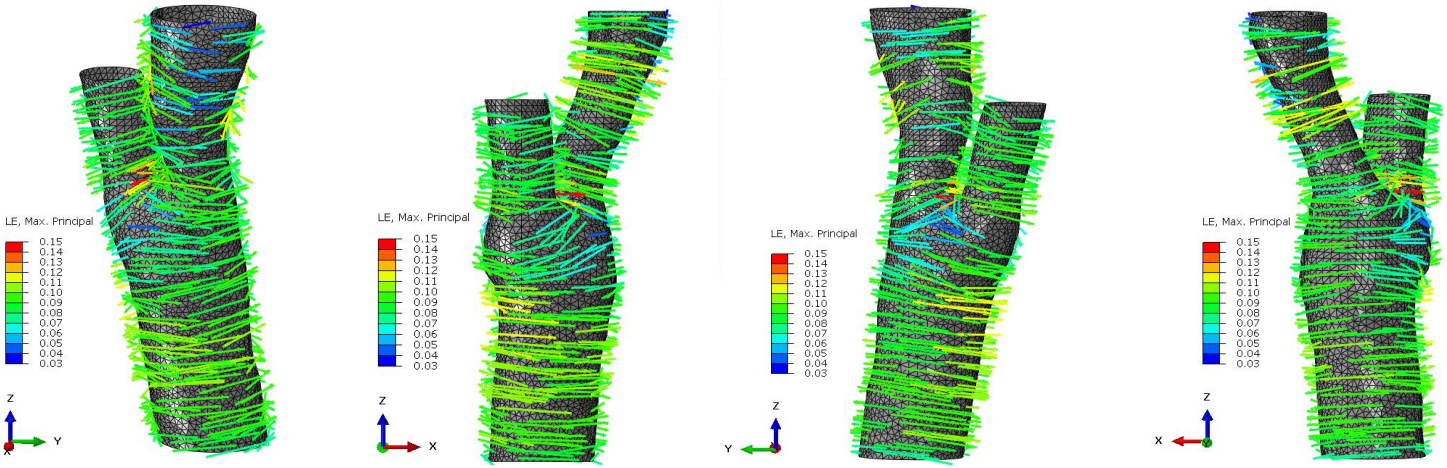

Strain – Lumen + Calcium

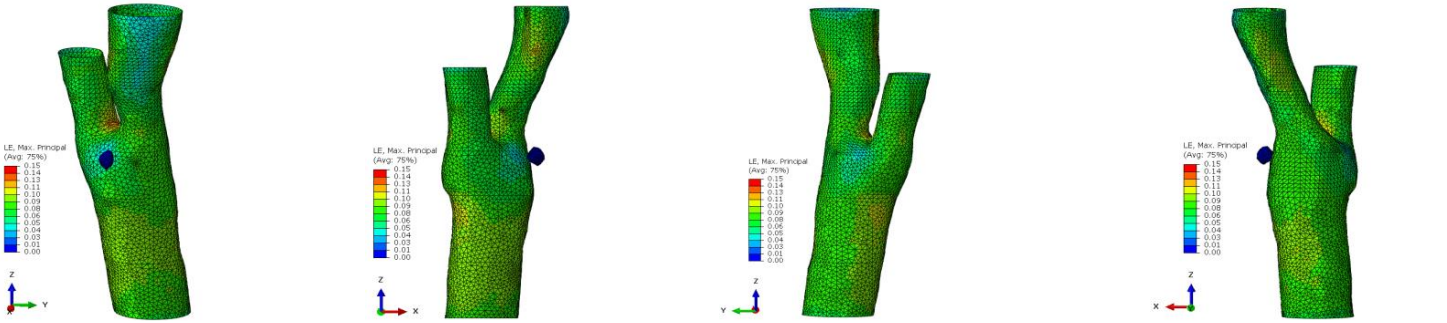

Patient 1L – 3D Morphometry

Morphometrical analysis

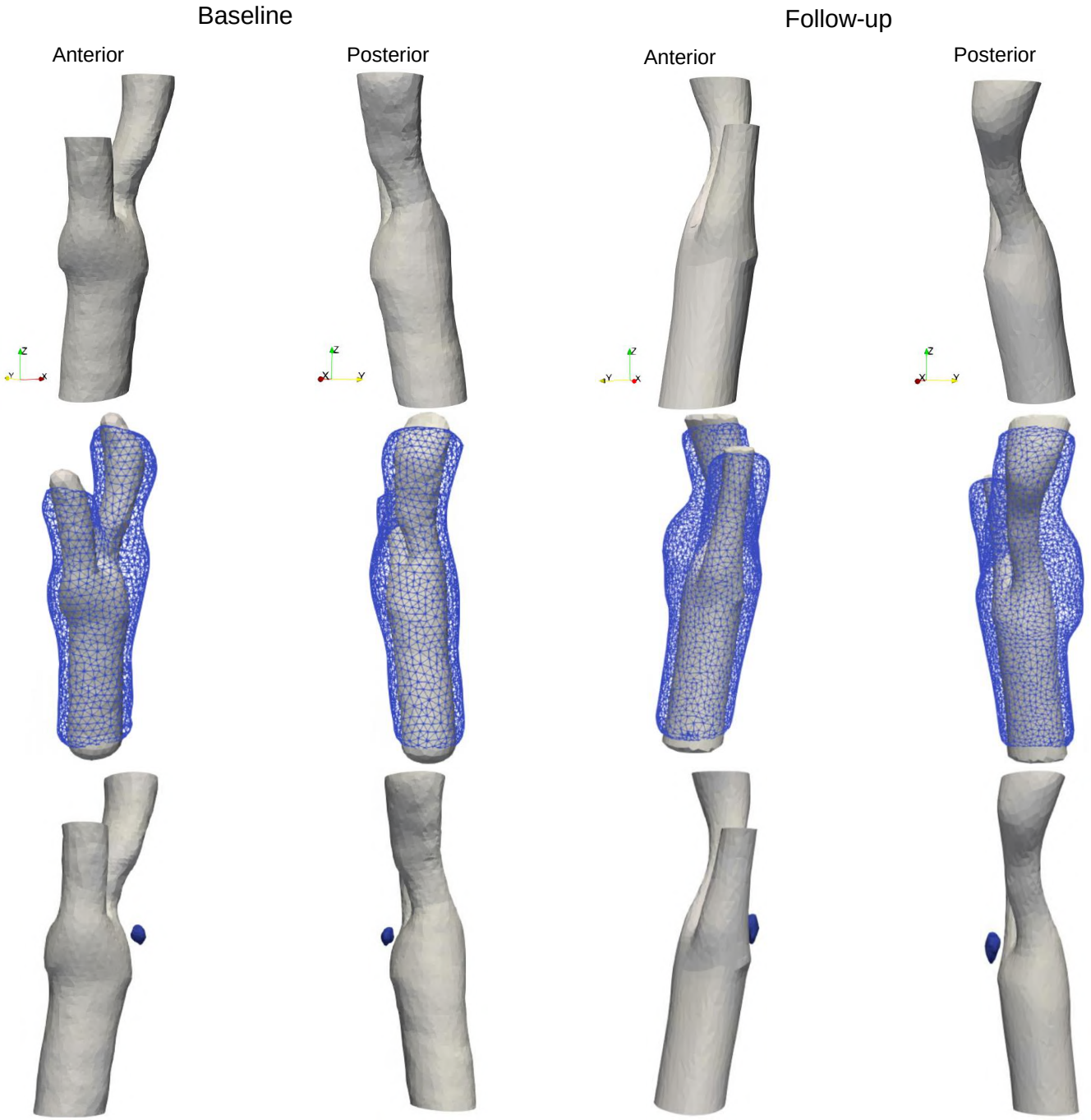

Patient 1L – 2D Metrics

2D Plot metrics
Lateral view

	Centerline	Segment identification	Abcissa metric	Angular metric
Baseline	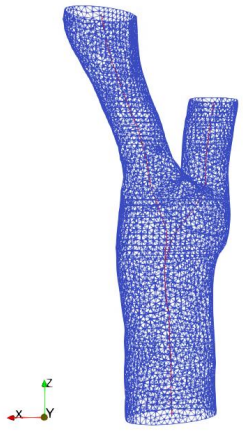	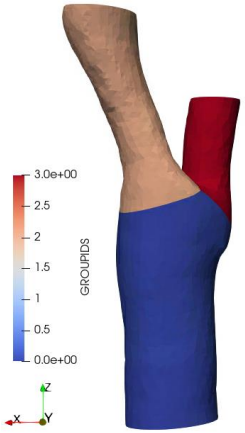	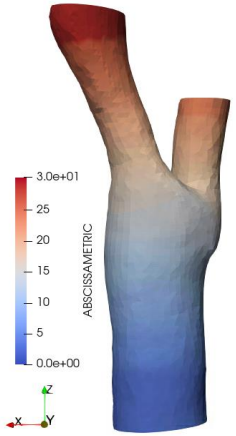	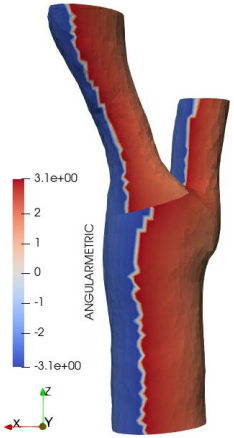
Follow-up	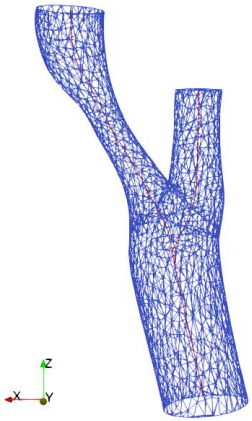	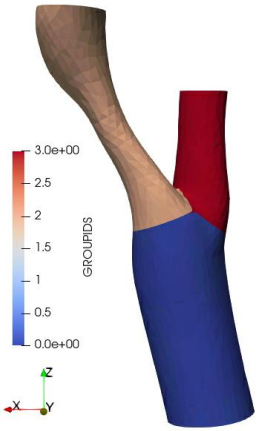	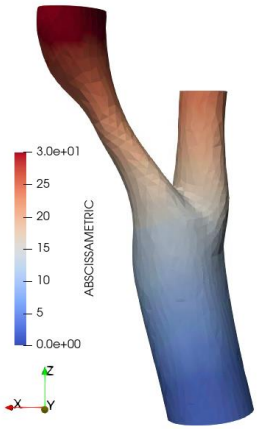	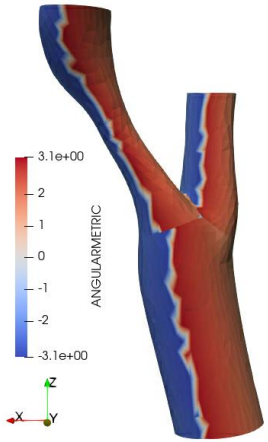

Patient 1L – 2D CCA-ICA

Biomechanical analysis

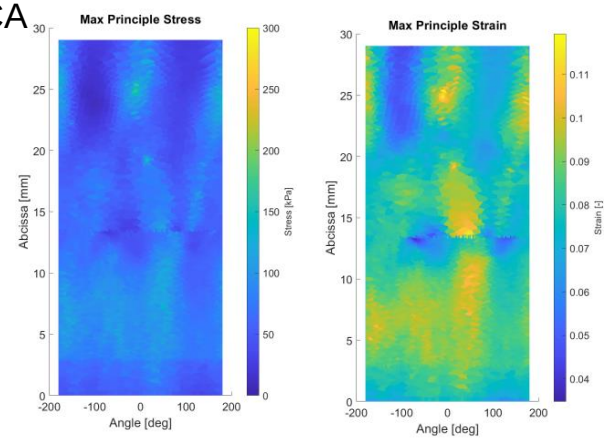

	Stress	Strain	Wall thickness		Max Curvature		Min Curvature	
			Base	*Foll*	*Base*	*Foll*	*Base*	*Foll*
	[kPa]	[-]	[mm]	[mm]	[m^{-1}]	[m^{-1}]	[m^{-1}]	[m^{-1}]
Max	117.46	0.12	3.58	3.70	1.04	1.60	0.43	0.47
Median	64.39	0.08	1.11	1.24	0.38	0.48	-0.03	-0.02
Min	-6.59	0.03	0.74	0.35	0.04	-0.22	-1.32	-2.66

Morphometrical analysis

Baseline

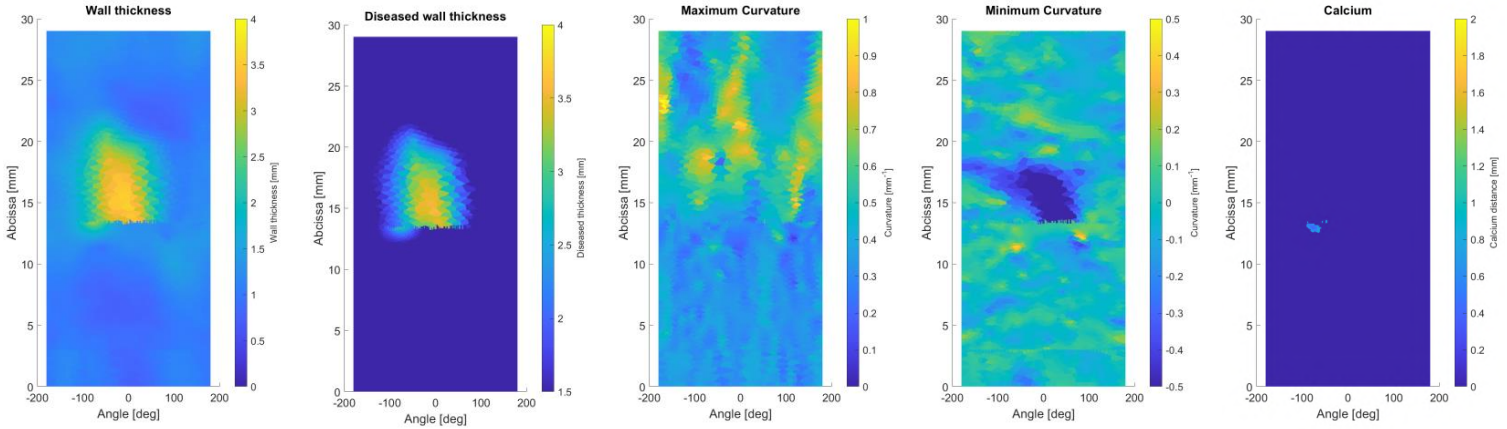

Follow-up

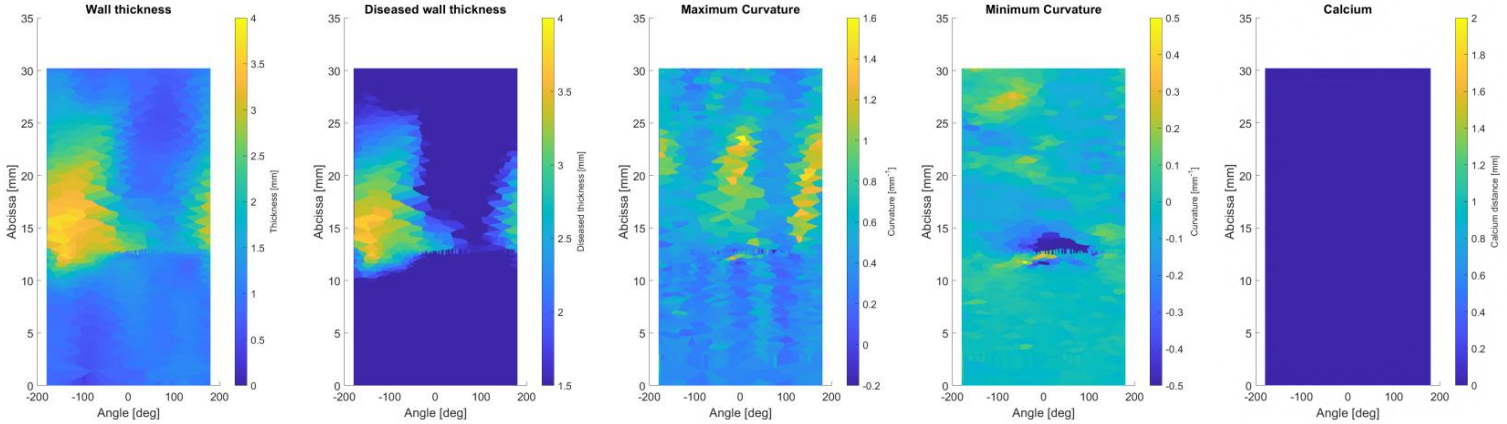

Patient 1L – 2D CCA-ECA

Biomechanical analysis

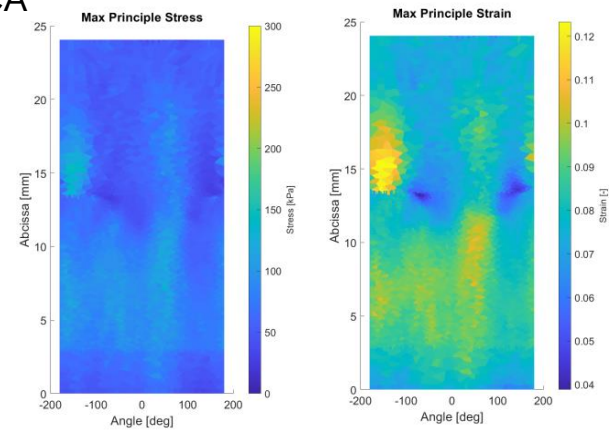

	Stress	Strain	Wall thickness		Max Curvature		Min Curvature	
			Base	*Foll*	*Base*	*Foll*	*Base*	*Foll*
	[kPa]	[-]	[mm]	[mm]	[m^{-1}]	[m^{-1}]	[m^{-1}]	[m^{-1}]
Max	145.48	0.12	3.58	3.7	1.04	1.60	0.43	0.47
Median	62.13	0.08	1.11	1.24	0.38	0.48	-0.03	-0.02
Min	23.63	0.04	0.74	0.35	0.04	-0.22	-1.32	-2.66

Morphometrical analysis

Baseline

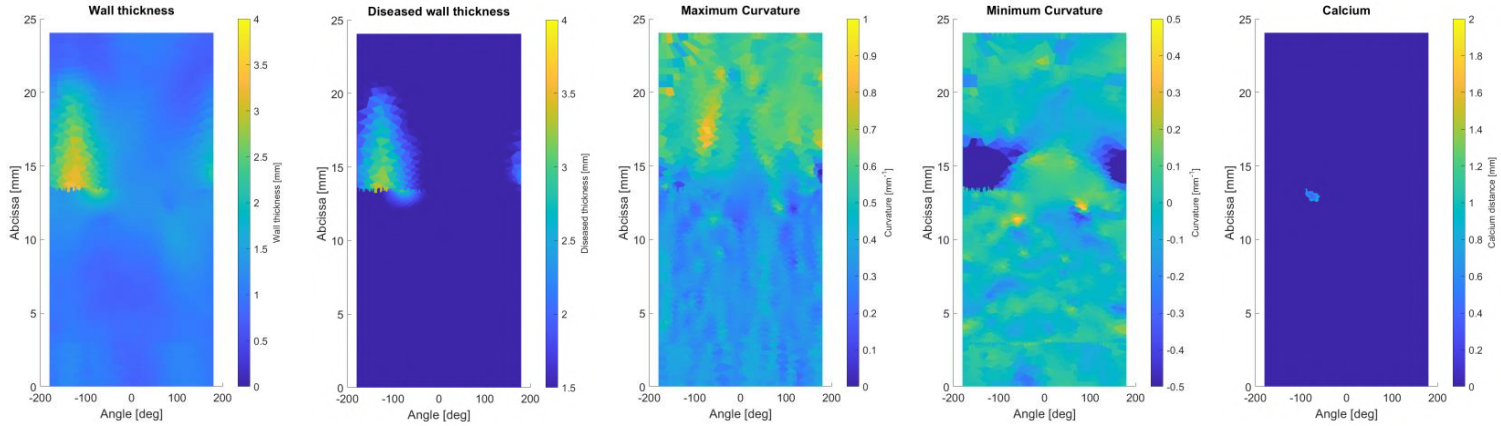

Follow-up

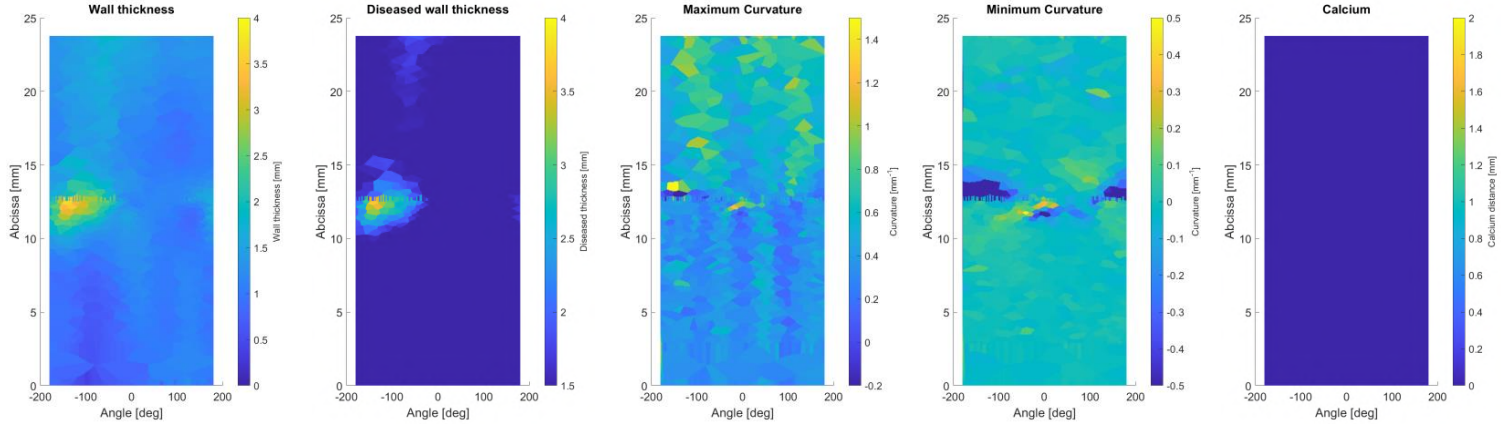

Patient 1L – Metrics

Post-processing metrics			Unit	CCA - ICA	CCA - ECA
Stress	Baseline	Max	[kPa]	145.48	145.48
		Median	[kPa]	62.13	62.13
		Min	[kPa]	23.63	23.63
Strain	Baseline	Max	[-]	0.12	0.12
		Median	[-]	0.08	0.08
		Min	[-]	0.04	0.04
Wall thickness	Baseline	Max	[mm]	3.58	3.37
	Baseline	Median	[mm]	1.11	1.04
	Baseline	Min	[mm]	0.74	0.63
	Follow-up	Max	[mm]	3.70	3.67
	Follow-up	Median	[mm]	1.24	1.17
	Follow-up	Min	[mm]	0.35	0.35
Plaque burden *	Baseline	Max	[%]	73.44	
	Baseline	Median	[%]	48.43	
	Baseline	Min	[%]	33.73	
	Follow-up	Max	[%]	88.37	
	Follow-up	Median	[%]	52.45	
	Follow-up	Min	[%]	33.59	
Calcium *	Baseline		[mm^3]	1.66	
	Follow-up		[mm^3]	3.69	

Patient 1R – 3D Metrics

Biomechanical analysis

Medial | Anterior | Lateral | Posterior

Stress – Luminal surface

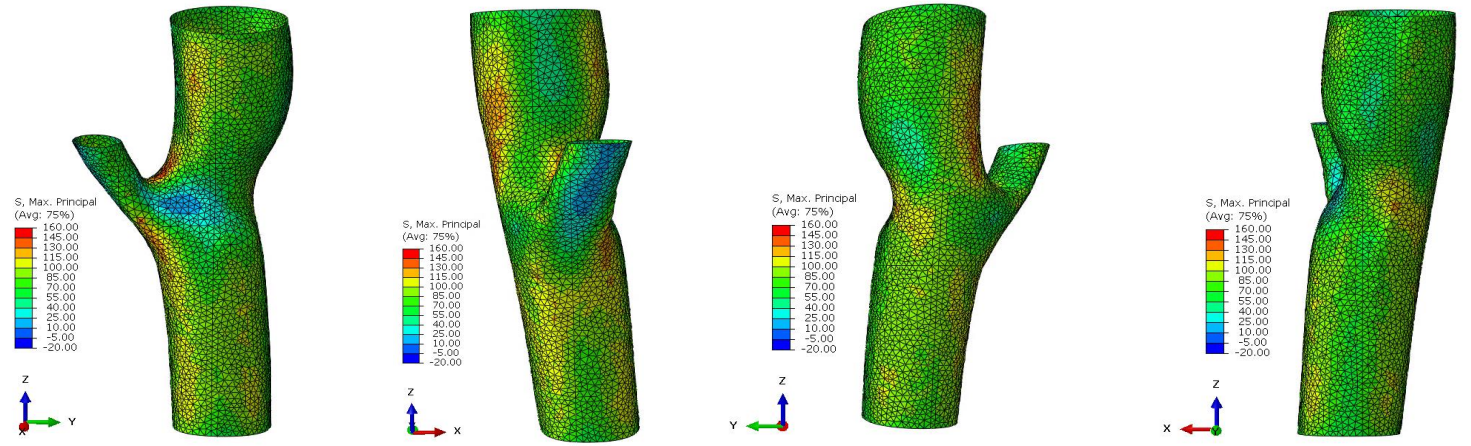

Strain – Luminal surface

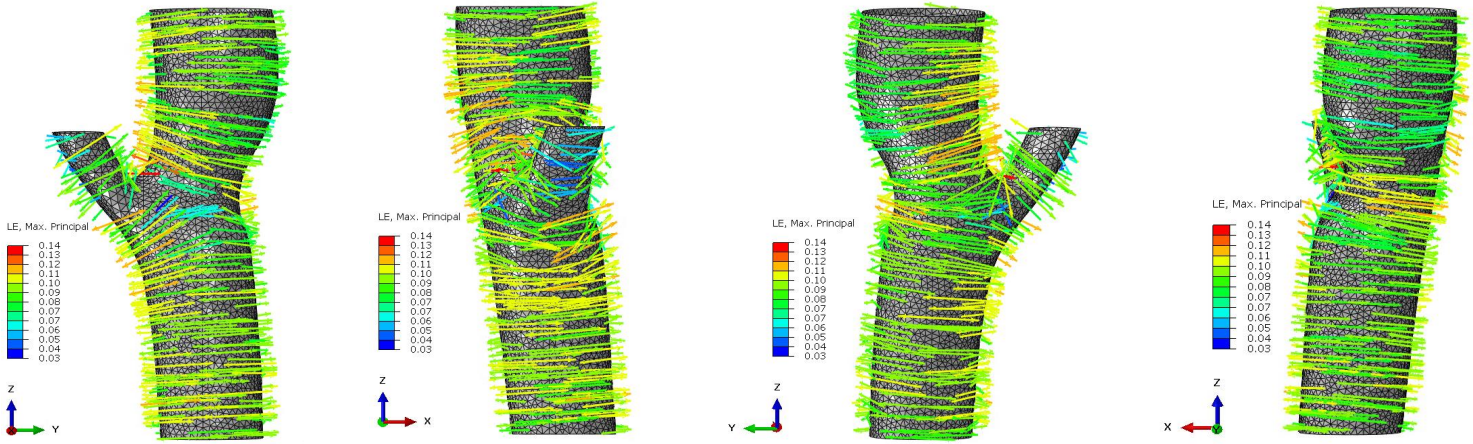

Strain – Lumen + Calcium

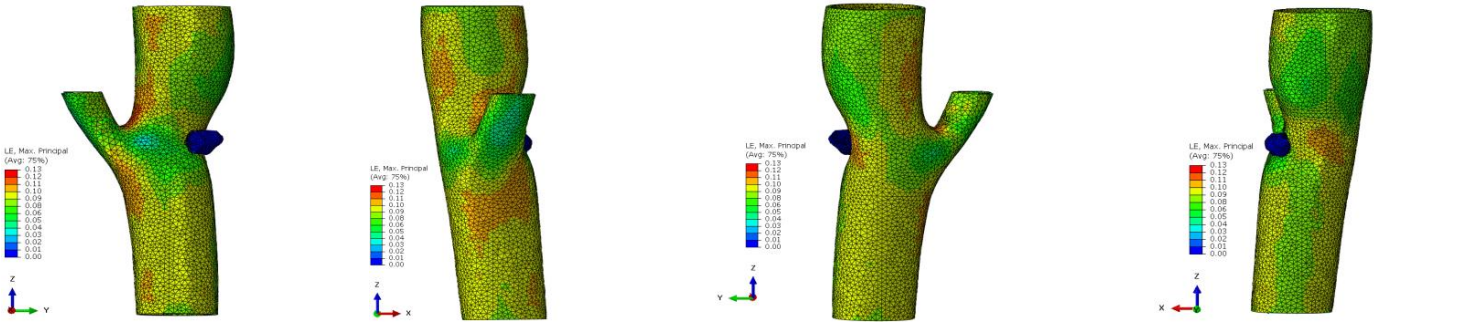

Patient 1R – 3D Morphometry

Morphometrical analysis

Baseline

Follow-up

Anterior

Posterior

Anterior

Posterior

Lumen Geometry

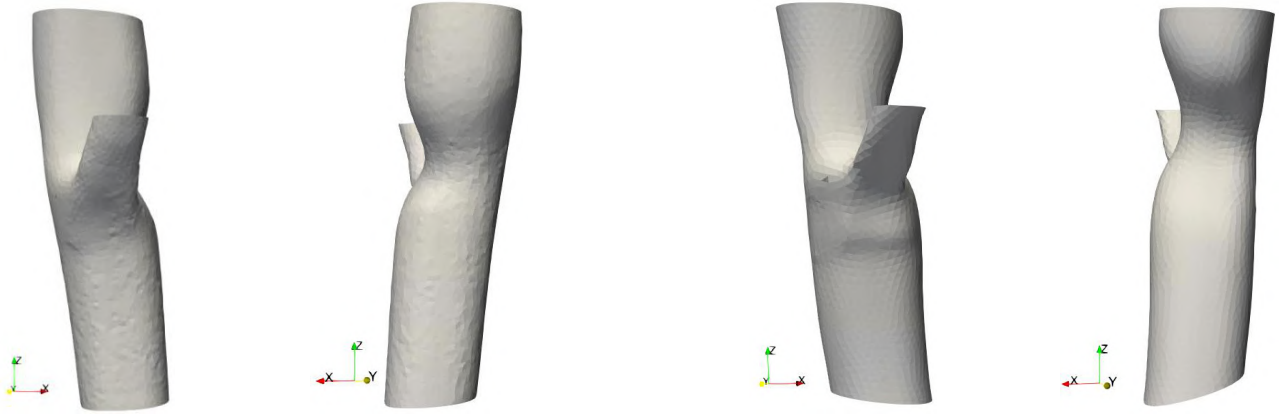

Wall thickness

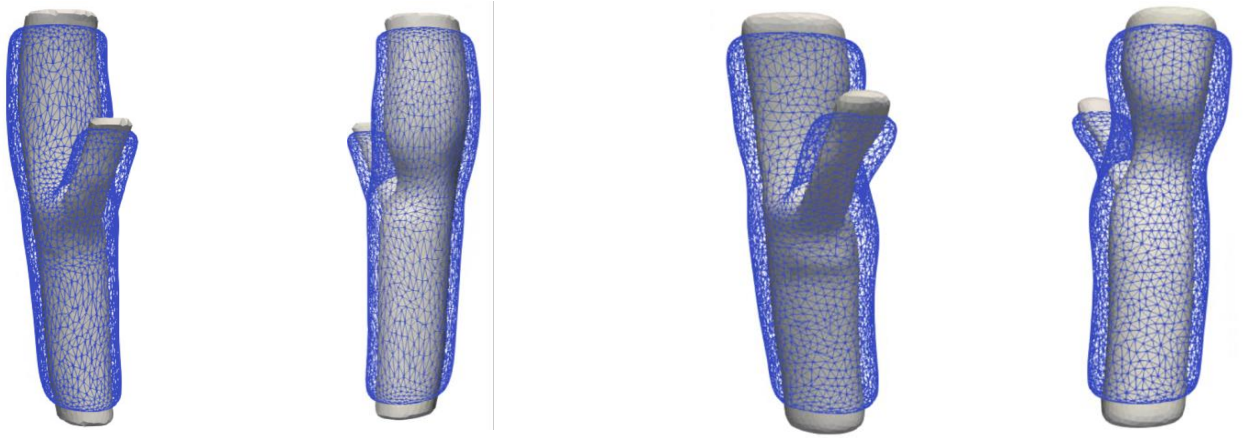

Calcium

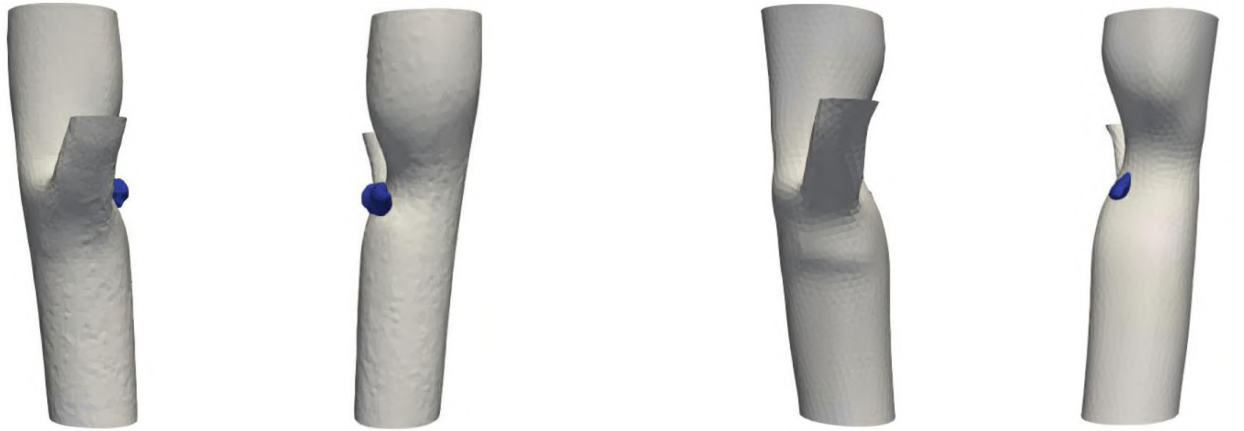

Patient 1R – 2D Metrics

2D Plot metrics
Medial view

	Centerline	Segment identification	Abcissa metric	Angular metric
Baseline	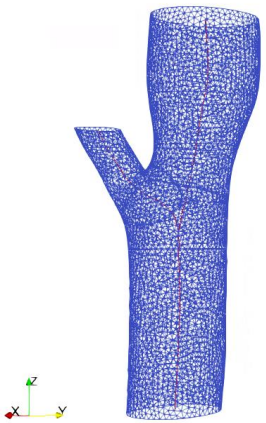	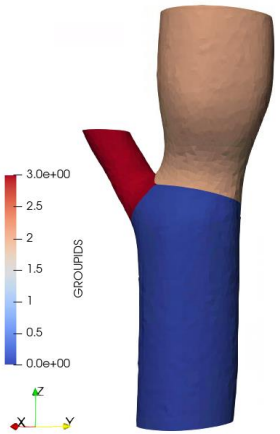	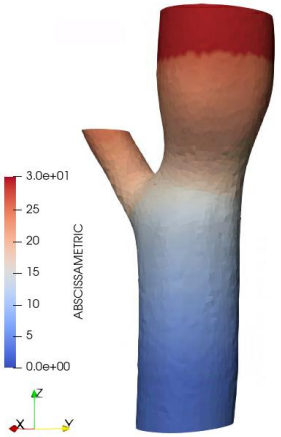	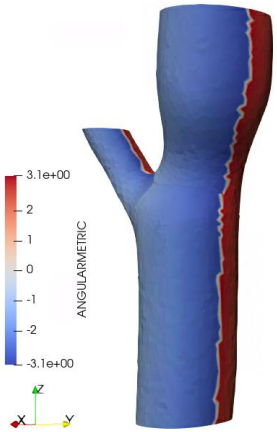
Follow-up	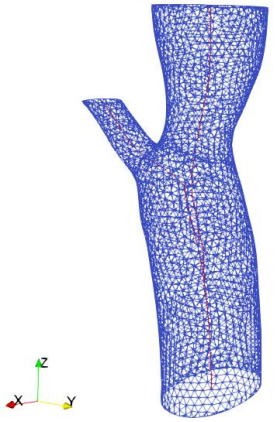	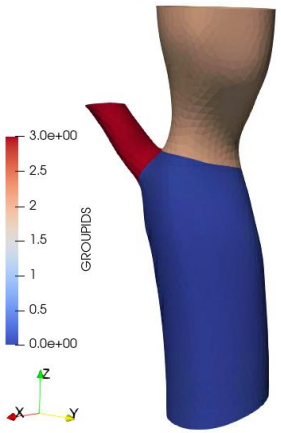	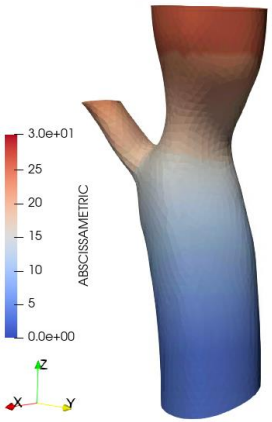	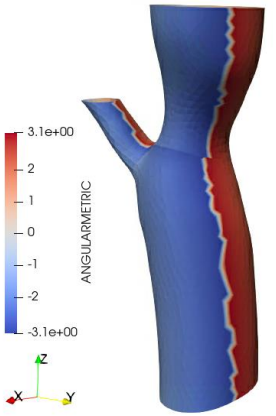

Patient 1R – 2D CCA-ICA

Biomechanical analysis

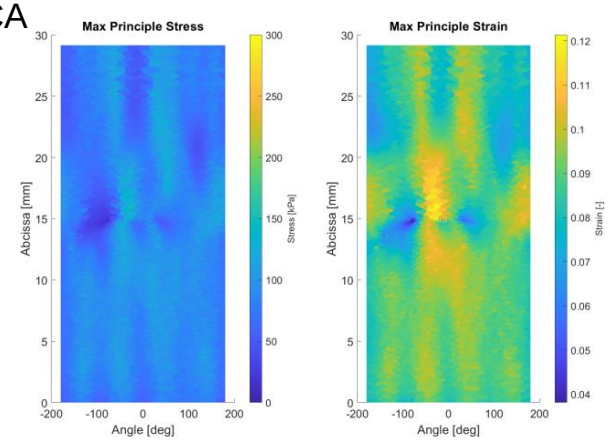

	Stress	Strain	Wall thickness		Max Curvature		Min Curvature	
			Base	*Foll*	*Base*	*Foll*	*Base*	*Foll*
	[kPa]	[-]	[mm]	[mm]	[m^{-1}]	[m^{-1}]	[m^{-1}]	[m^{-1}]
Max	151.91	0.12	3.34	3.40	0.87	0.32	1.58	0.00
Median	85.7	0.09	1.06	1.24	0.30	0.00	0.00	0.00
Min	15.34	0.04	0.79	0.46	0.01	-0.66	0.00	-7.17

Morphometrical analysis

Baseline

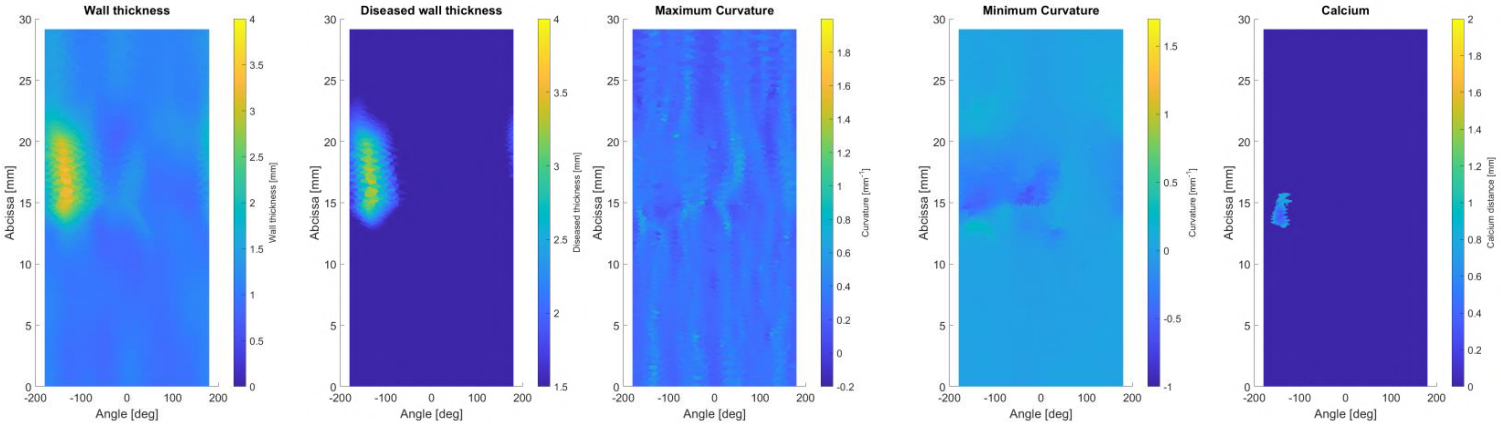

Follow-up

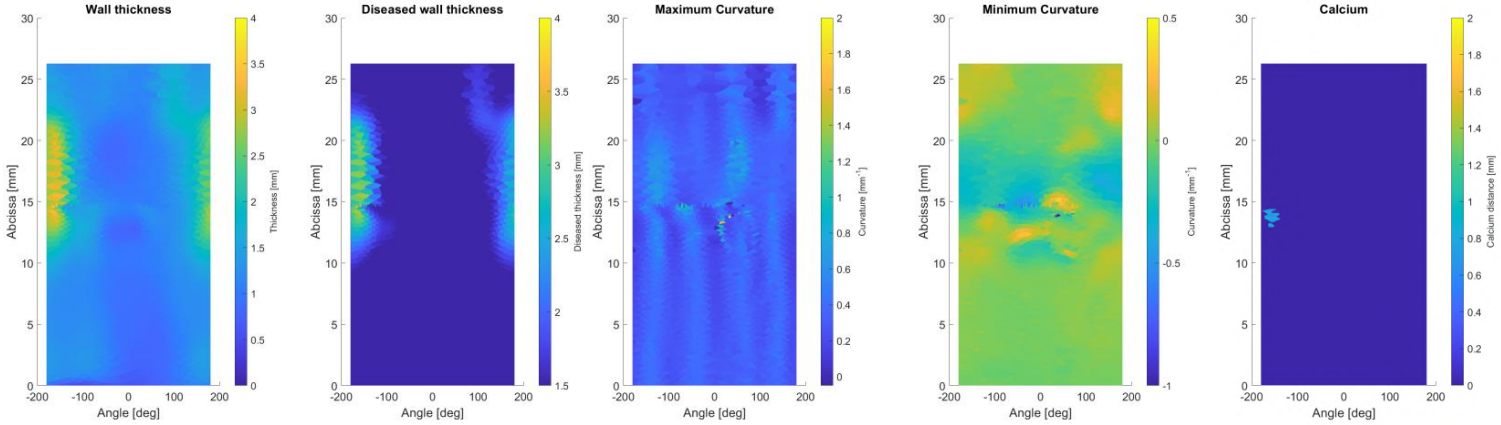

Patient 1R – 2D CCA-ECA

Biomechanical analysis

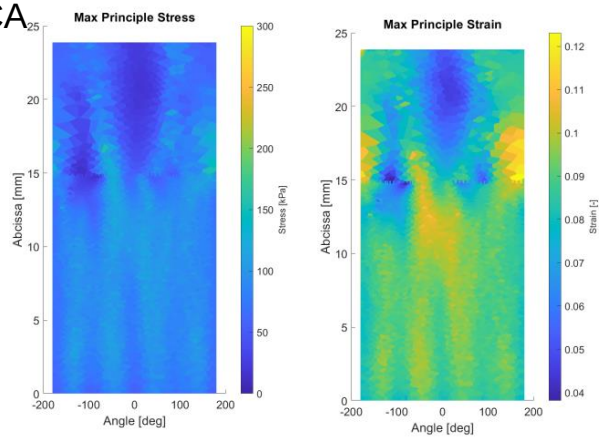

	Stress	Strain	Wall thickness		Max Curvature		Min Curvature	
			Base	*Foll*	*Base*	*Foll*	*Base*	*Foll*
	[kPa]	[-]	[mm]	[mm]	[m^{-1}]	[m^{-1}]	[m^{-1}]	[m^{-1}]
Max	156.78	0.12	3.20	3.40	1.70	1.58	0.32	0.00
Median	85.06	0.09	1.01	1.14	0.33	0.00	0.00	0.00
Min	14.99	0.04	0.38	0.67	0.03	0.00	-2.05	-7.17

Morphometrical analysis

Baseline

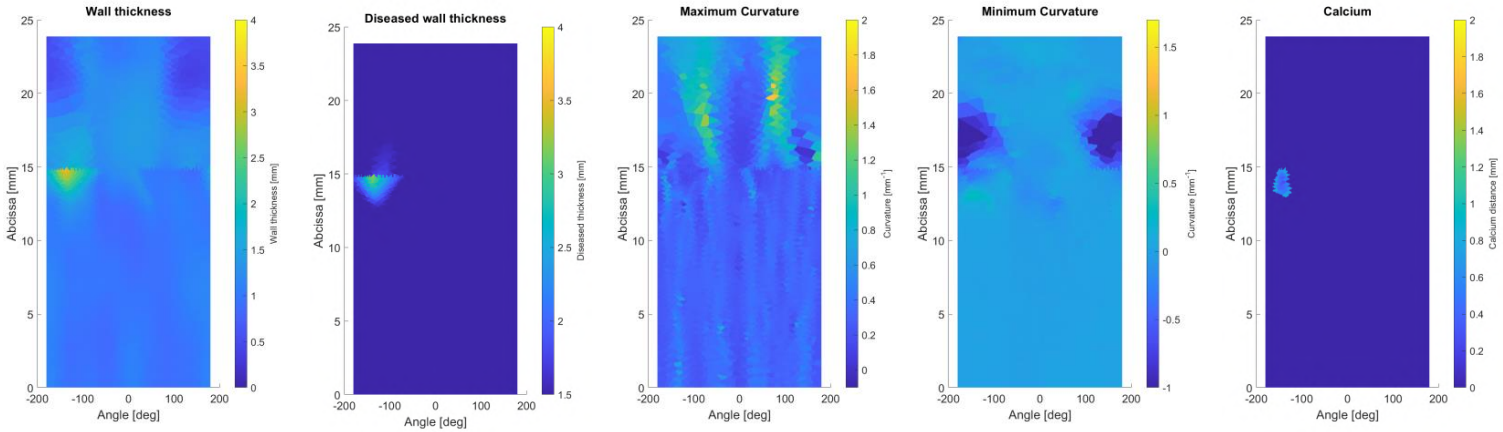

Follow-up

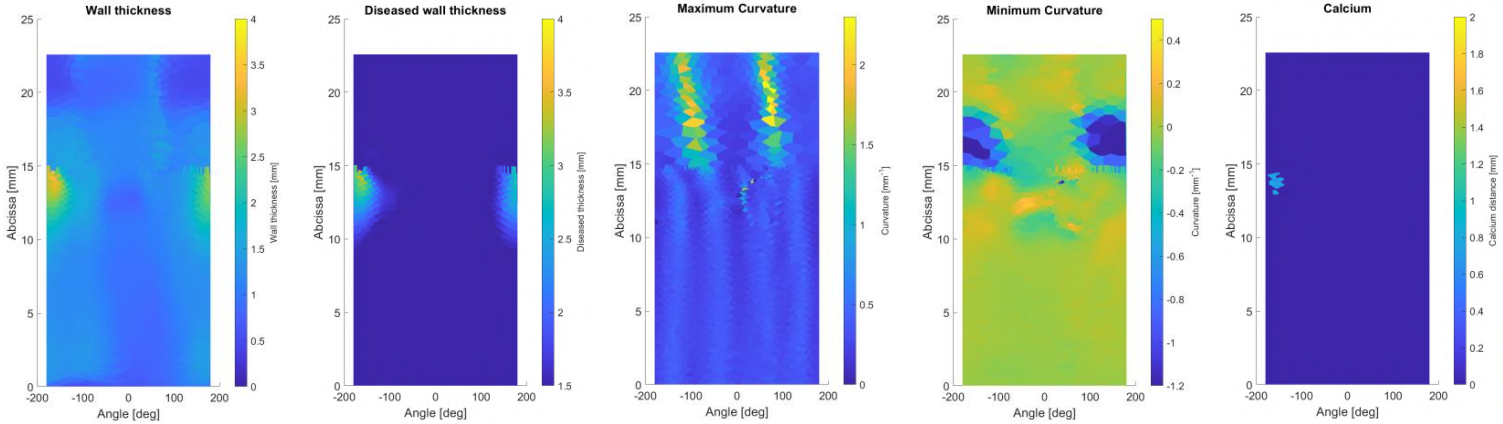

Patient 1R – Metrics

Post-processing metrics			Unit	CCA - ICA	CCA - ECA
Stress	Baseline	Max	[kPa]	151.91	156.78
		Median	[kPa]	85.70	85.06
		Min	[kPa]	15.34	14.99
Strain	Baseline	Max	[-]	0.12	0.12
		Median	[-]	0.09	0.09
		Min	[-]	0.04	0.04
Wall thickness	Baseline	Max	[mm]	5.25	5.25
	Baseline	Median	[mm]	0.98	0.96
	Baseline	Min	[mm]	0.59	0.59
	Follow-up	Max	[mm]	4.96	4.96
	Follow-up	Median	[mm]	1.04	1.04
	Follow-up	Min	[mm]	0.66	0.72
Plaque burden *	Baseline	Max	[%]	72.85	
	Baseline	Median	[%]	40.63	
	Baseline	Min	[%]	34.07	
	Follow-up	Max	[%]	69.76	
	Follow-up	Median	[%]	46.45	
	Follow-up	Min	[%]	35.28	
Calcium *	Baseline		[mm^3]	8.08	
	Follow-up		[mm^3]	6.14	

Patient 2L – 3D Metrics

Biomechanical analysis

Posterior | Medial | Anterior | Lateral

Stress – Luminal surface

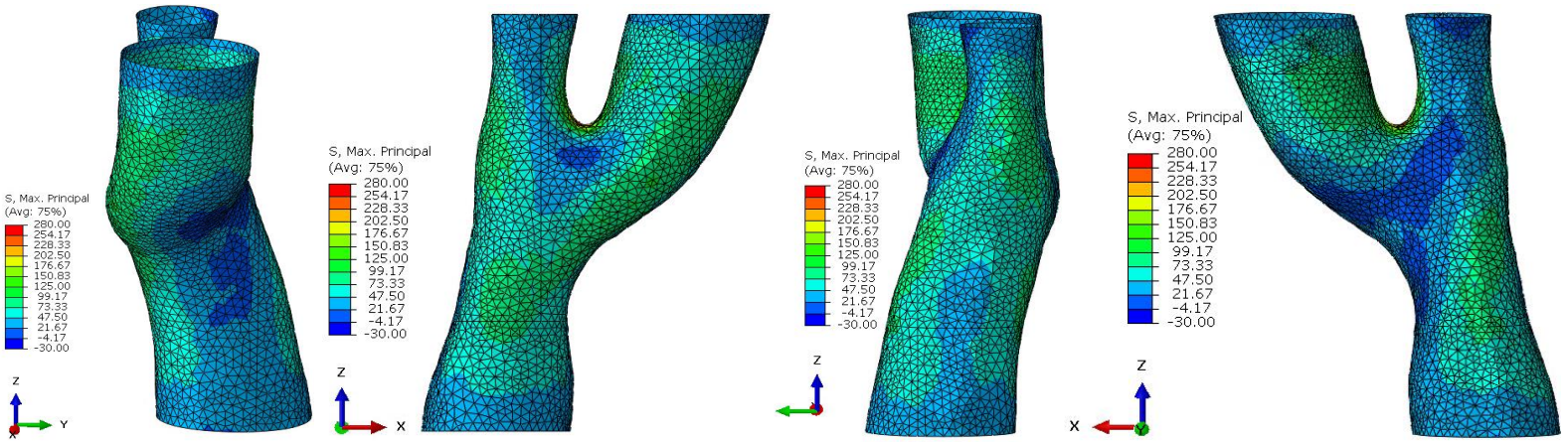

Strain – Luminal surface

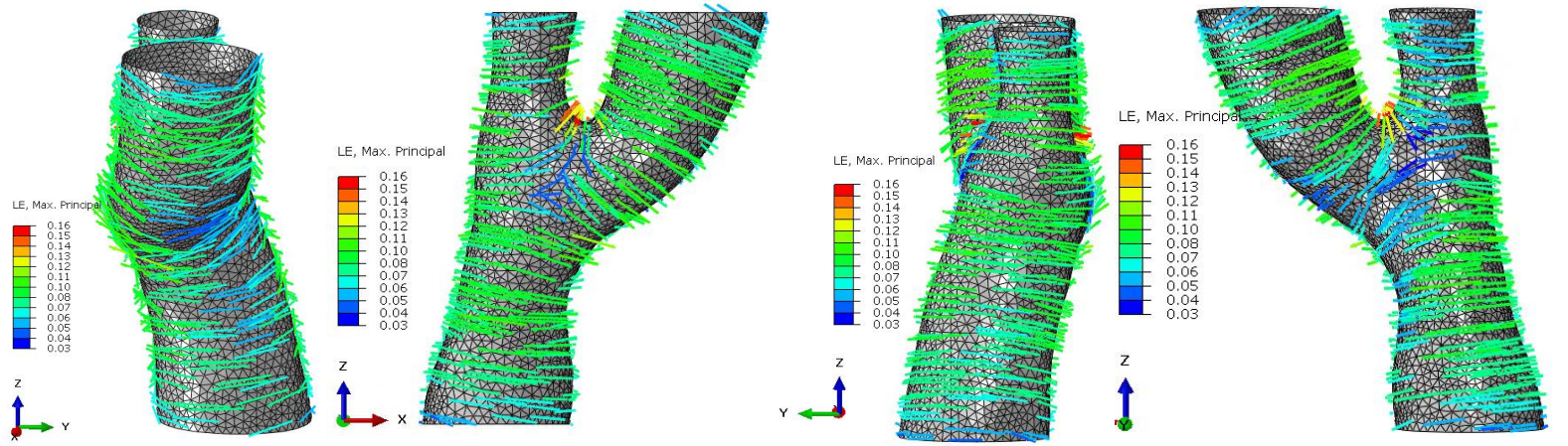

Strain – Lumen + Calcium

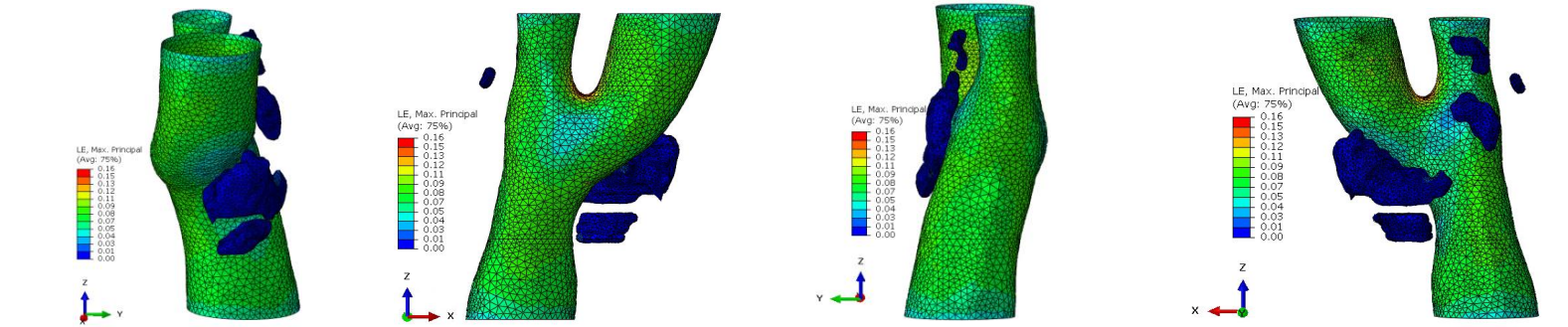

Patient 2L – 3D Morphometry

Morphometrical analysis

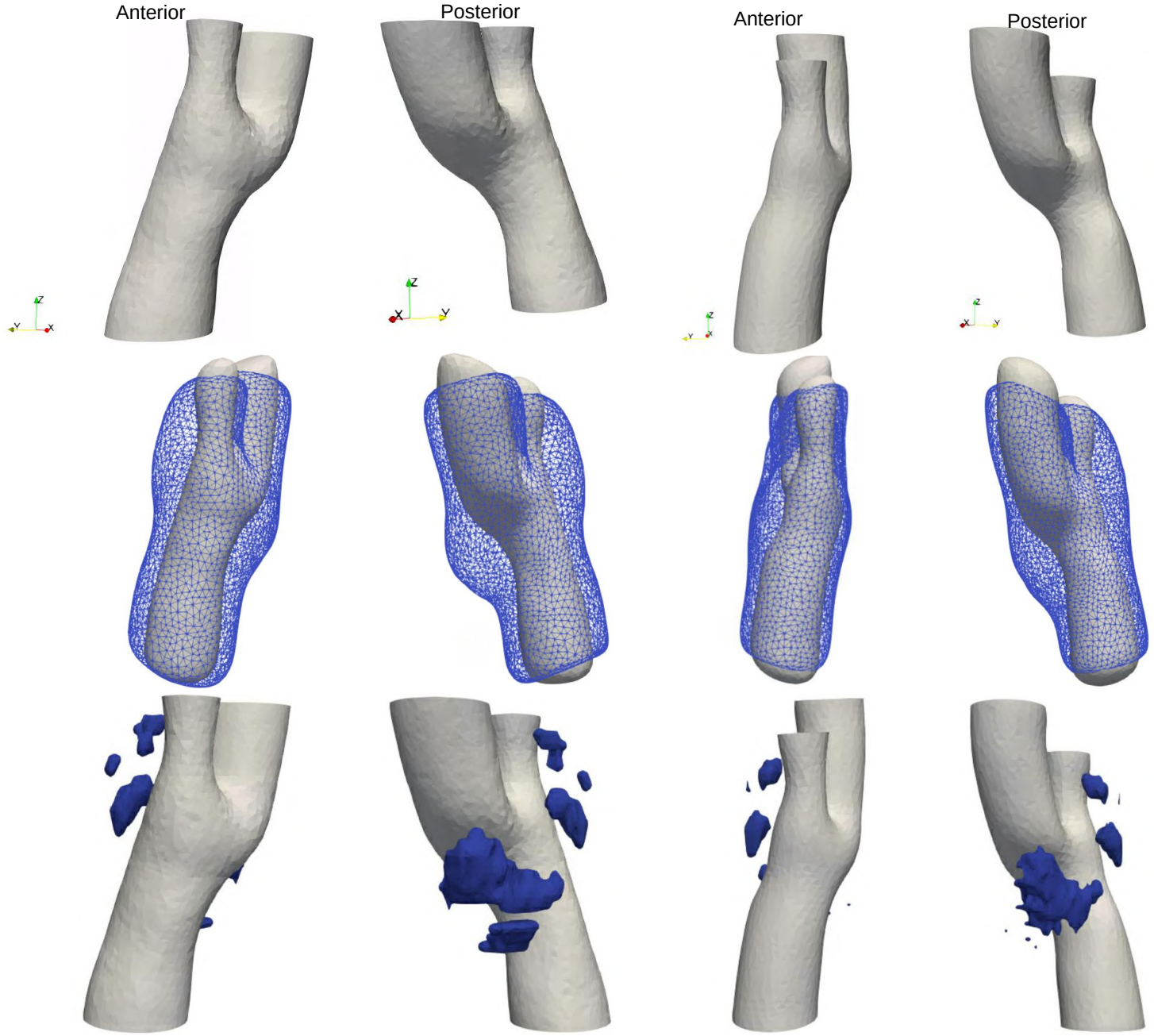

Patient 2L – 2D Metrics

2D Plot metrics
Lateral view

Centerline | Segment identification | Abcissa metric | Angular metric

Baseline

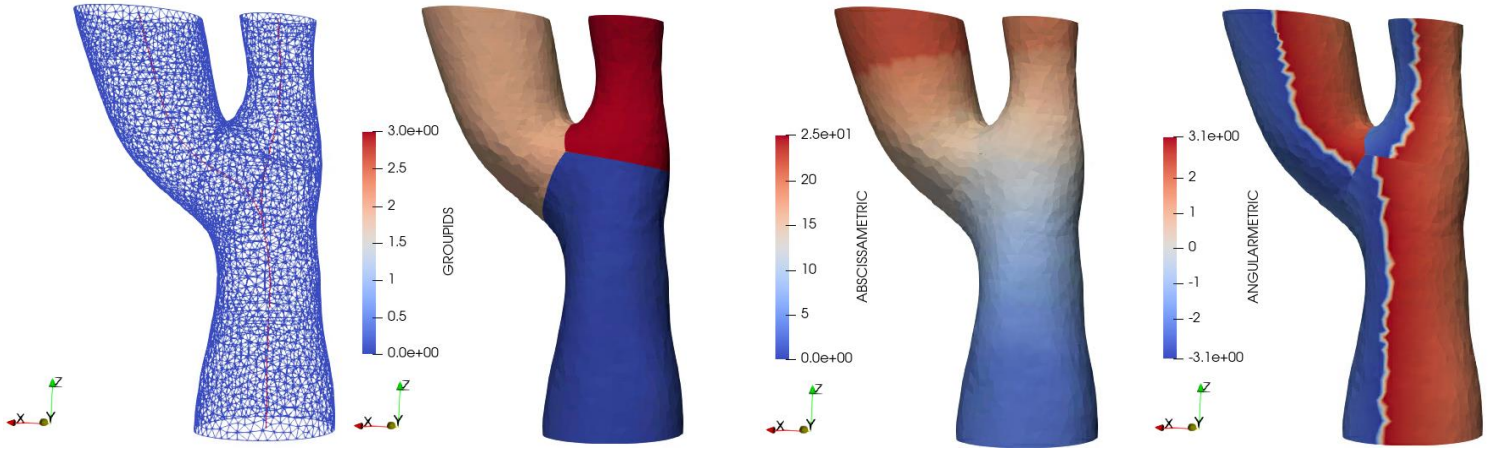

Follow-up

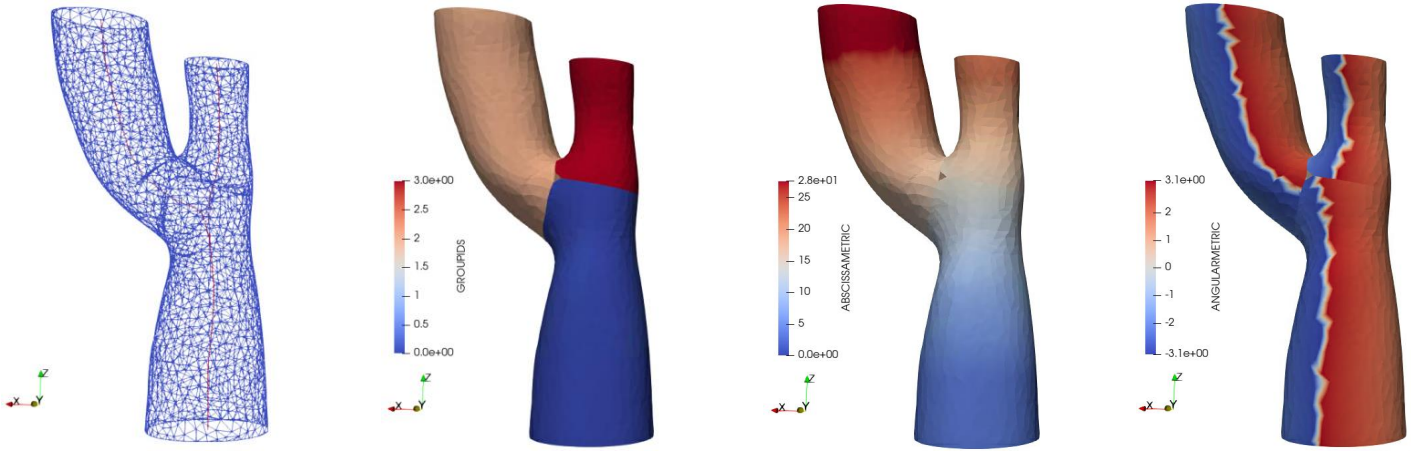

Patient 2L – 2D CCA-ICA

Biomechanical analysis

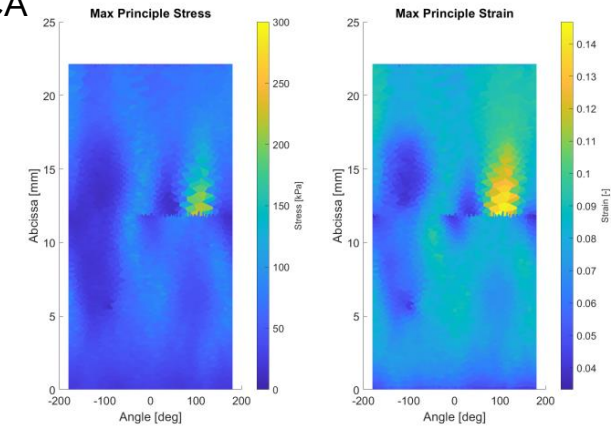

	Stress	Strain	Wall thickness		Max Curvature		Min Curvature	
			Base	*Foll*	*Base*	*Foll*	*Base*	*Foll*
	[kPa]	[-]	[mm]	[mm]	[m^{-1}]	[m^{-1}]	[m^{-1}]	[m^{-1}]
Max	234.24	0.15	4.51	4.77	3.71	27.13	0.24	0.45
Median	64.39	0.08	1.47	1.10	0.39	0.36	-0.02	0.00
Min	10.84	0.03	0.75	-0.03	-0.01	-0.15	-1.83	-12.37

Morphometrical analysis

Baseline

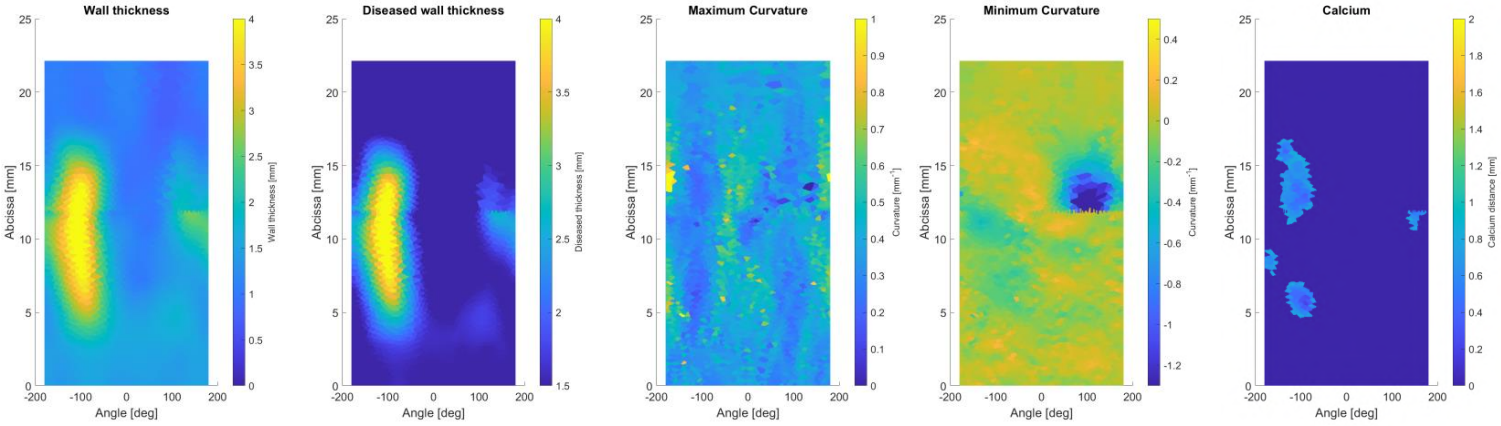

Follow-up

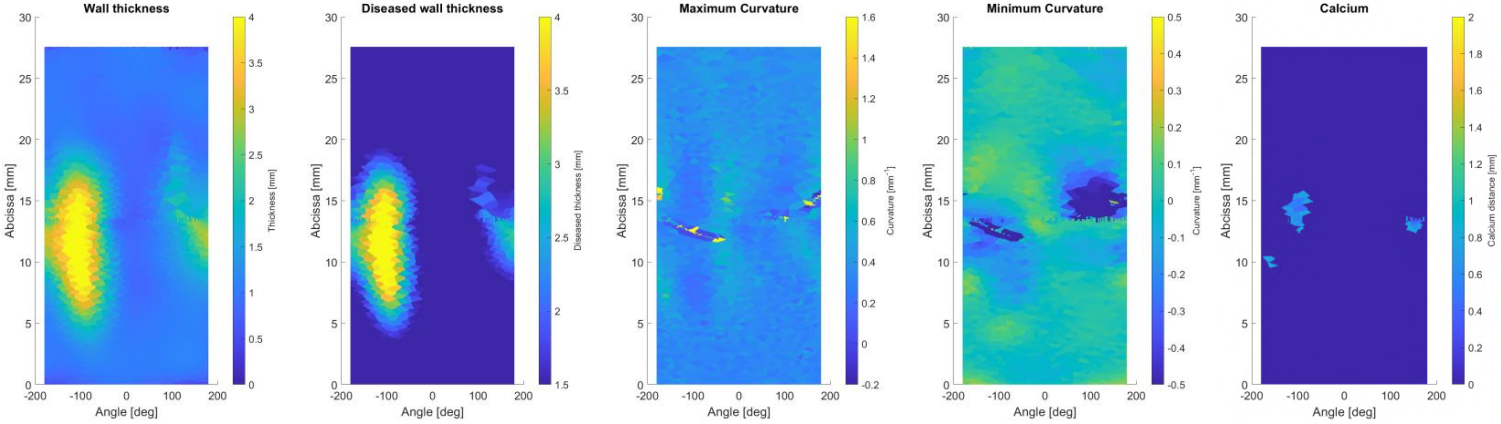

Patient 2L – 2D CCA-ECA

Biomechanical analysis

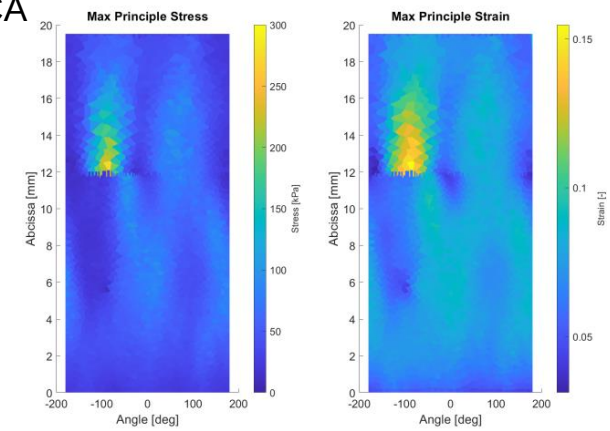

	Stress	Strain	Wall thickness		Max Curvature		Min Curvature	
			Base	*Foll*	*Base*	*Foll*	*Base*	*Foll*
	[kPa]	[-]	[mm]	[mm]	[m^{-1}]	[m^{-1}]	[m^{-1}]	[m^{-1}]
Max	276.02	0.15	4.77	3.4	1.15	27.13	0.61	0.45
Median	50.83	0.07	1.39	1.14	0.44	0.40	-0.04	-0.01
Min	5.01	0.03	0.19	0.67	0.04	0.00	-1.49	-12.37

Morphometrical analysis

Baseline

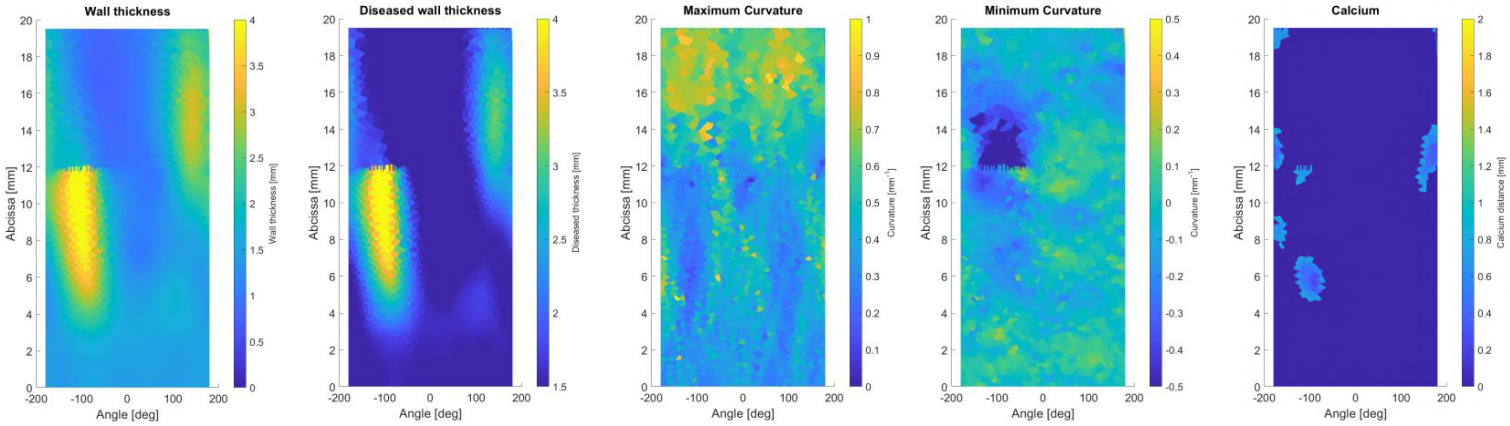

Follow-up

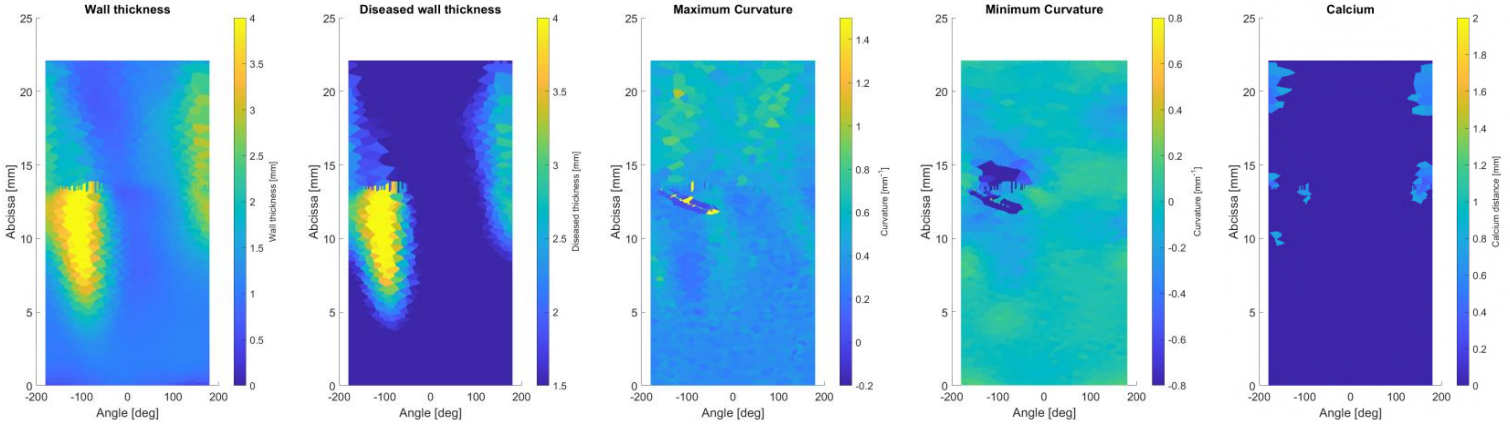

Patient 2L – Metrics

Post-processing metrics			Unit	CCA - ICA	CCA - ECA
Stress	Baseline	Max	[kPa]	234.24	276.02
		Median	[kPa]	64.39	50.83
		Min	[kPa]	10.84	5.01
Strain	Baseline	Max	[-]	0.15	0.15
		Median	[-]	0.08	0.07
		Min	[-]	0.03	0.03
Wall thickness	Baseline	Max	[mm]	4.51	4.77
	Baseline	Median	[mm]	1.47	1.39
	Baseline	Min	[mm]	0.75	0.19
	Follow-up	Max	[mm]	4.77	3.4
	Follow-up	Median	[mm]	1.10	1.14
	Follow-up	Min	[mm]	-0.03	0.67
Plaque burden *	Baseline	Max	[%]	72.25	
	Baseline	Median	[%]	53.28	
	Baseline	Min	[%]	43.19	
	Follow-up	Max	[%]	75.16	
	Follow-up	Median	[%]	51.07	
	Follow-up	Min	[%]	43.78	
Calcium *	Baseline		[mm^3]	118.88	
	Follow-up		[mm^3]	136.66	

Patient 2R – 3D Metrics

Biomechanical analysis

Medial | Anterior | Lateral | Posterior

Stress – Luminal surface

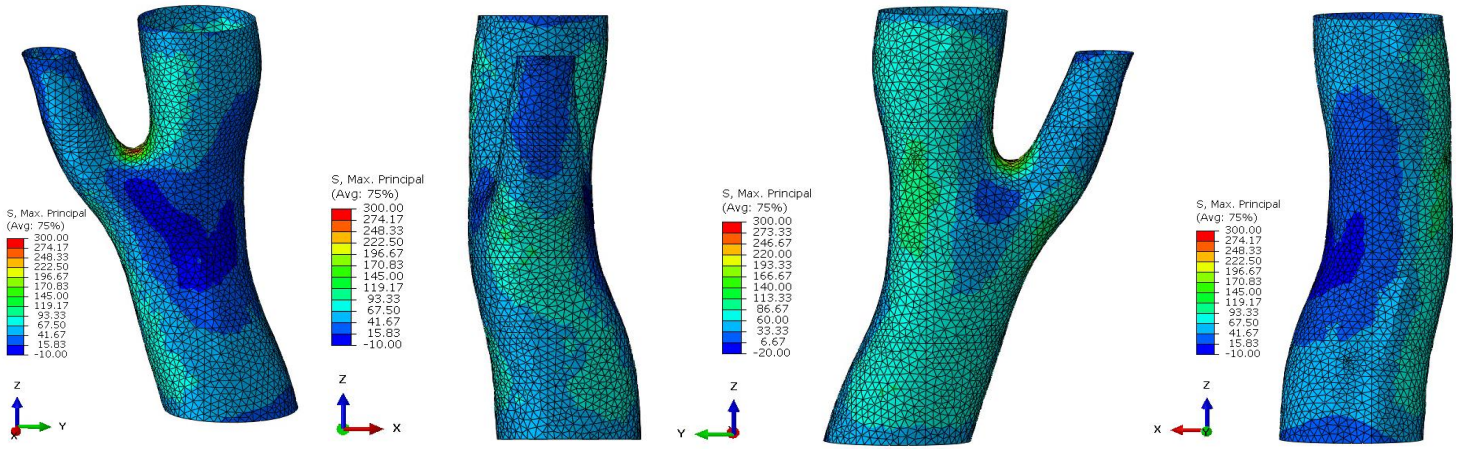

Strain – Luminal surface

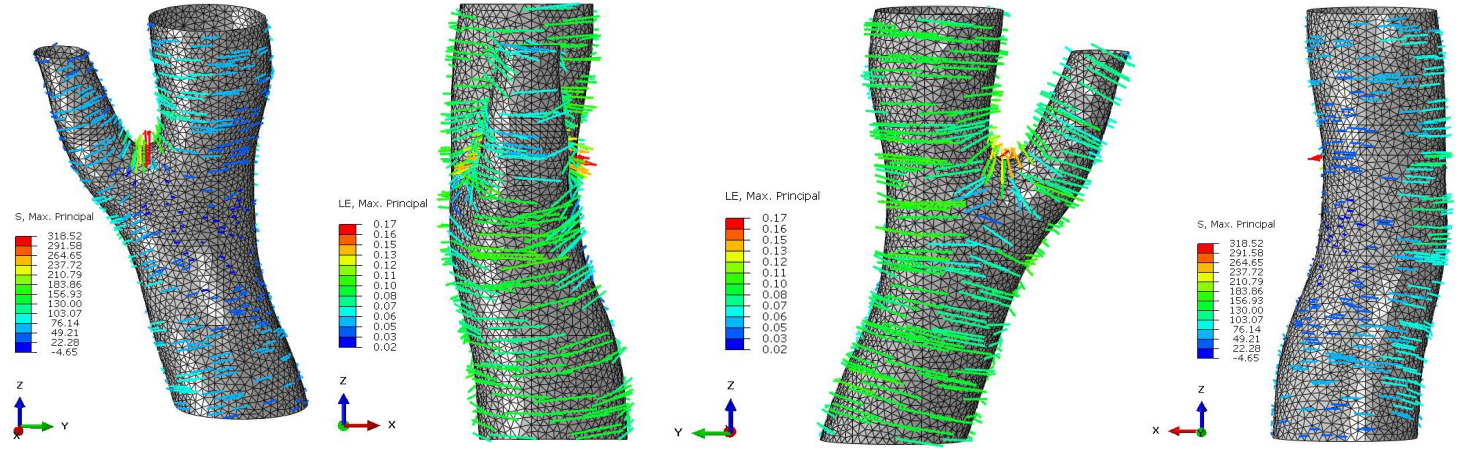

Strain – Lumen + Calcium

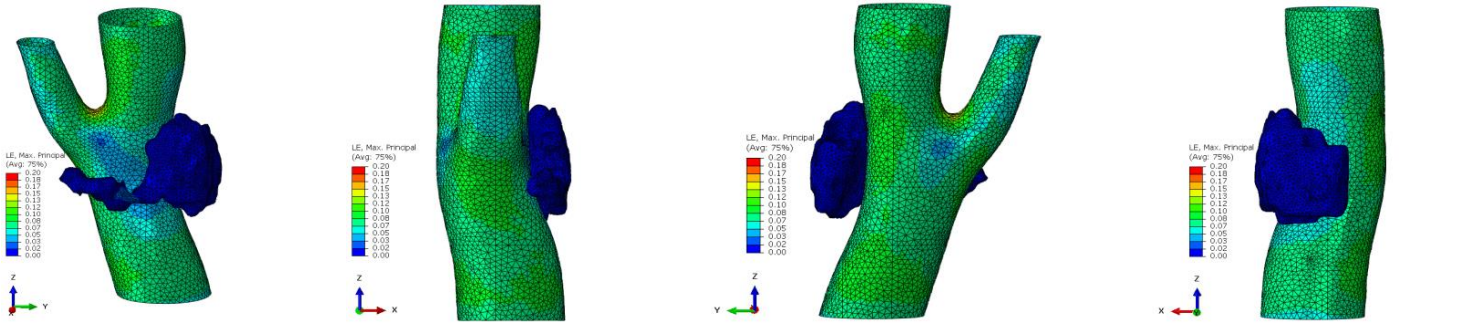

Patient 2R – 3D Morphometry

Morphometrical analysis

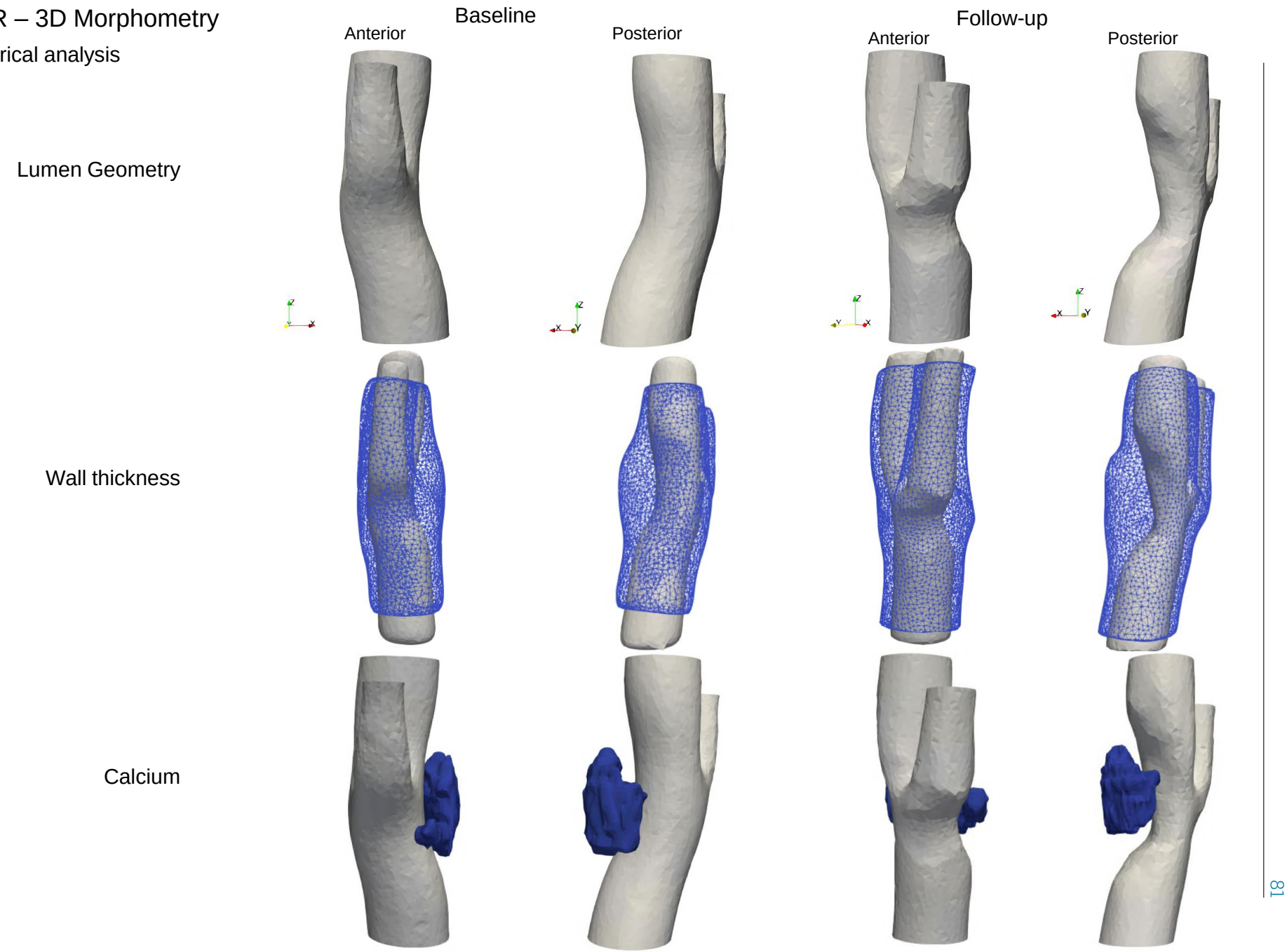

Patient 2R – 2D Metrics

2D Plot metrics
Medial view

	Centerline	Segment identification	Abcissa metric	Angular metric
Baseline	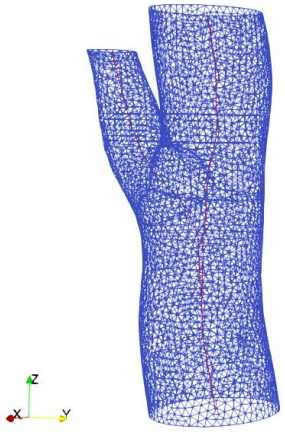	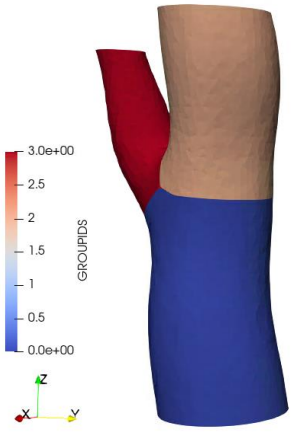	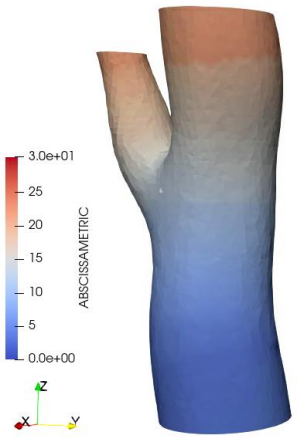	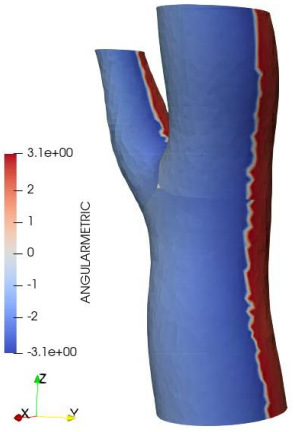
Follow-up	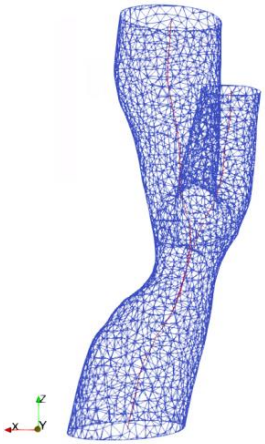	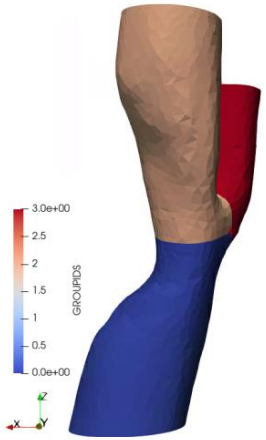	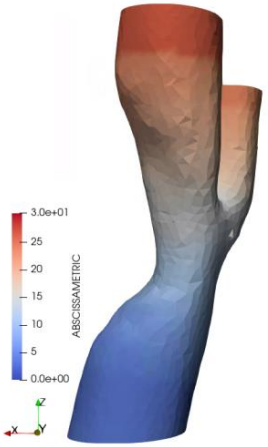	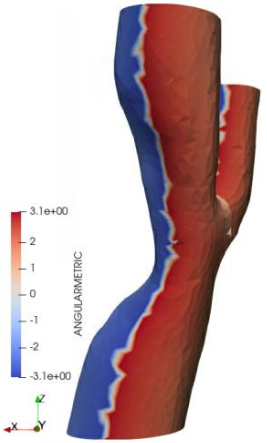

Patient 2R – 2D CCA-ICA

Biomechanical analysis

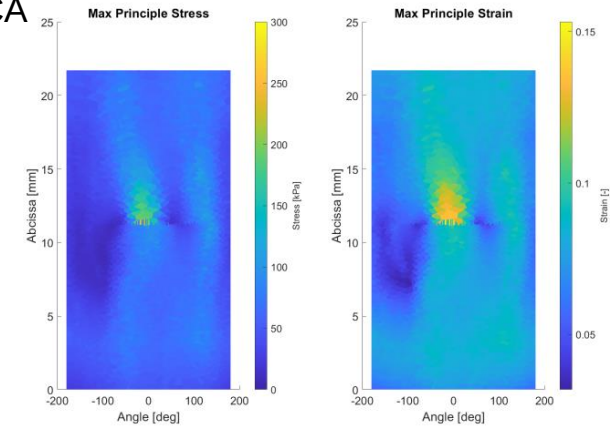

	Stress	Strain	Wall thickness		Max Curvature		Min Curvature	
			Base	*Foll*	*Base*	*Foll*	*Base*	*Foll*
	[kPa]	[-]	[mm]	[mm]	[m^{-1}]	[m^{-1}]	[m^{-1}]	[m^{-1}]
Max	273.96	0.15	0.29	4.83	0.62	0.38	0.16	12.45
Median	62.47	0.08	0.08	1.13	0.33	0.00	-0.01	-0.01
Min	7.01	0.03	0.00	-0.65	0.17	-0.01	-1.33	-86.50

Morphometrical analysis

Baseline

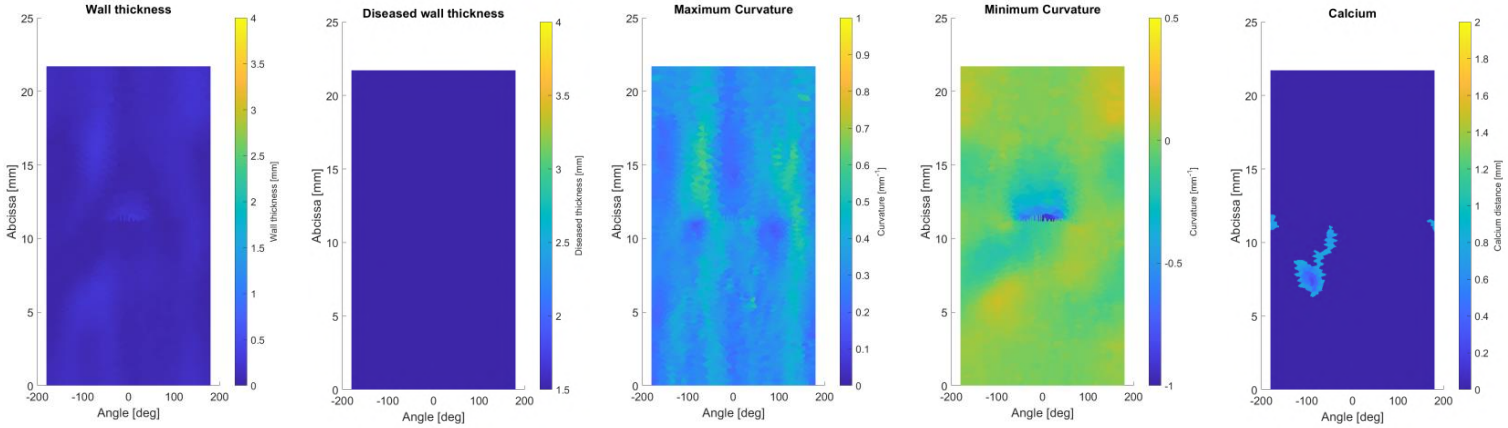

Follow-up

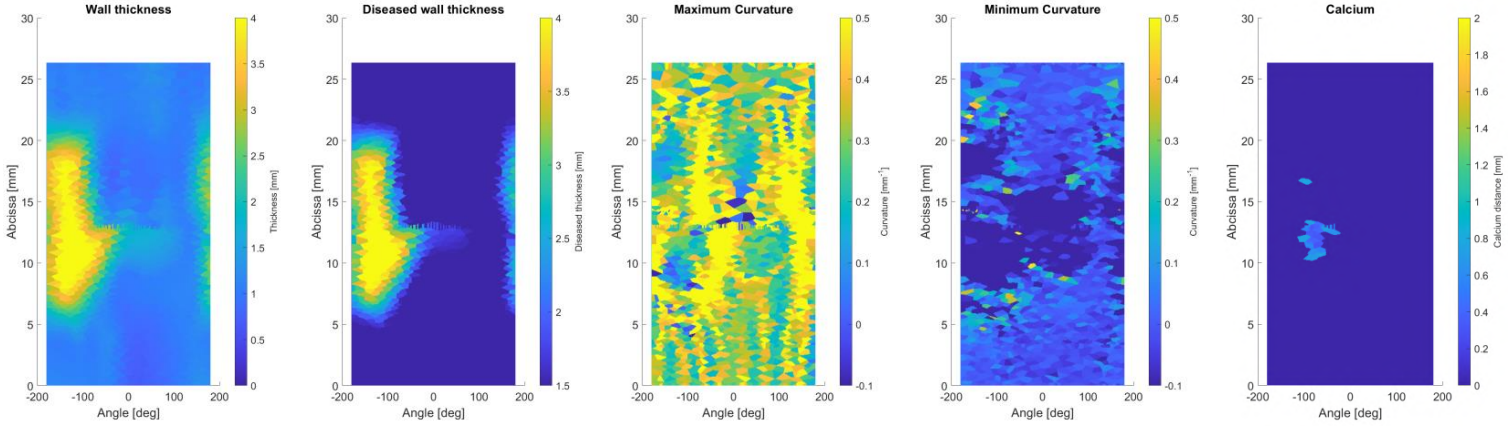

Patient 2R – 2D CCA-ECA

Biomechanical analysis

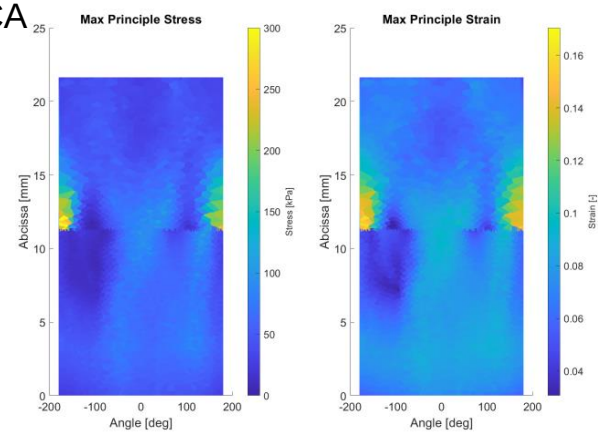

	Stress	Strain	Wall thickness		Max Curvature		Min Curvature	
			Base	*Foll*	*Base*	*Foll*	*Base*	*Foll*
	[kPa]	[-]	[mm]	[mm]	[m^{-1}]	[m^{-1}]	[m^{-1}]	[m^{-1}]
Max	299.80	0.17	0.51	4.83	0.91	1.03	0.15	6.48
Median	56.00	0.07	0.11	1.09	0.38	0.00	-0.01	-0.02
Min	2.72	0.03	0.00	0.53	0.13	0.00	-1.52	-37.19

Morphometrical analysis

Baseline

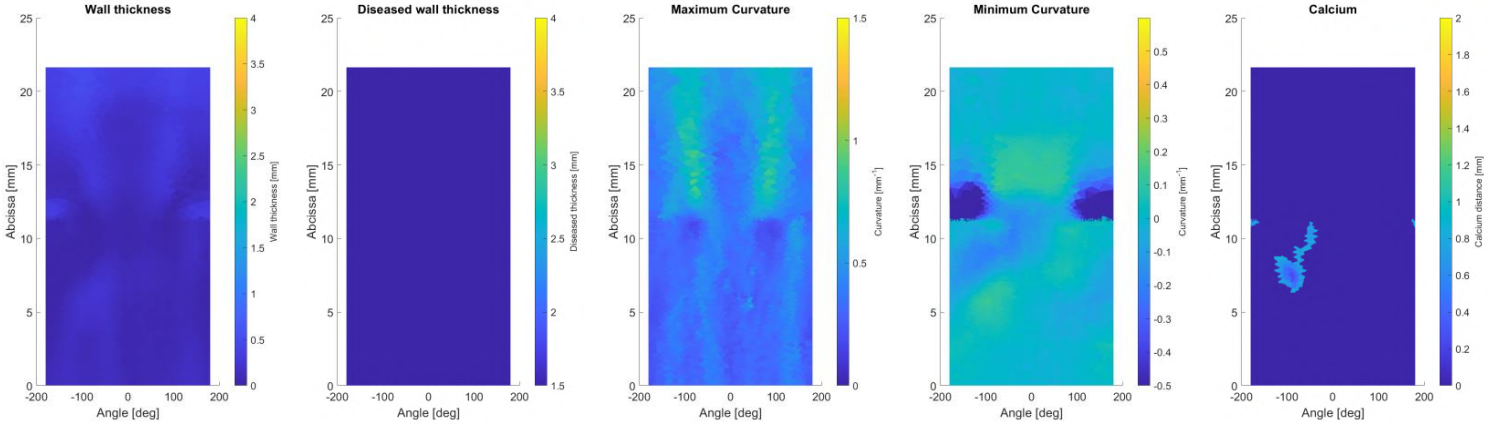

Follow-up

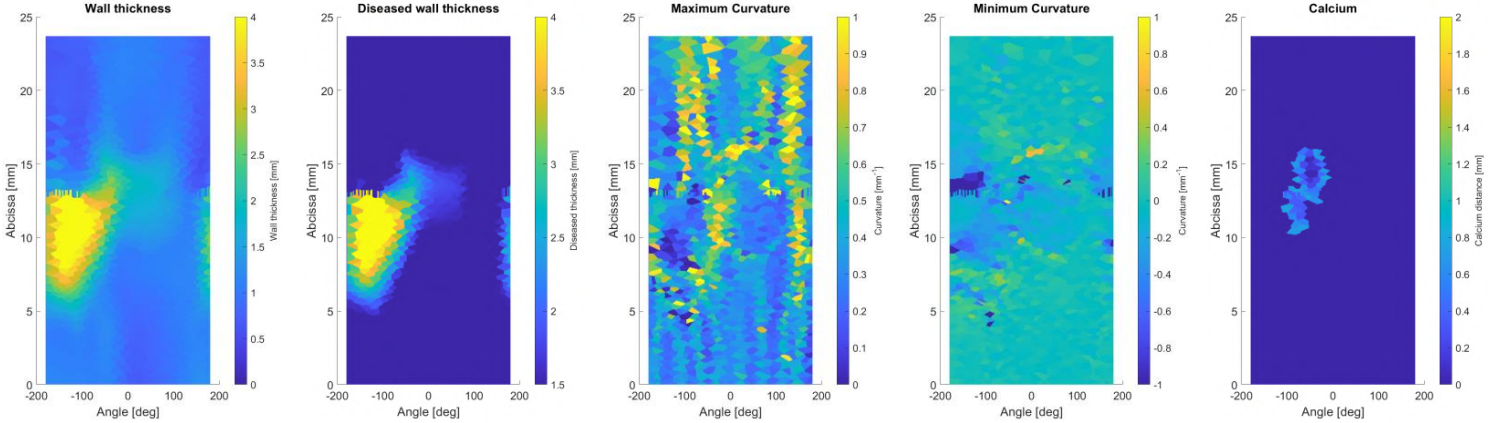

Patient 2R – Metrics

Post-processing metrics			Unit	CCA - ICA	CCA - ECA
Stress	Baseline	Max	[kPa]	273.96	299.80
		Median	[kPa]	62.47	56.00
		Min	[kPa]	7.01	2.72
Strain	Baseline	Max	[-]	0.15	0.17
		Median	[-]	0.08	0.07
		Min	[-]	0.03	0.03
Wall thickness	Baseline	Max	[mm]	0.29	0.51
	Baseline	Median	[mm]	0.08	0.11
	Baseline	Min	[mm]	0.00	0.00
	Follow-up	Max	[mm]	4.83	4.83
	Follow-up	Median	[mm]	1.13	1.09
	Follow-up	Min	[mm]	-0.65	0.53
Plaque burden *	Baseline	Max	[%]	80.67	
	Baseline	Median	[%]	51.21	
	Baseline	Min	[%]	35.29	
	Follow-up	Max	[%]	76.49	
	Follow-up	Median	[%]	52.92	
	Follow-up	Min	[%]	32.96	
Calcium *	Baseline		[mm^3]	131.73	
	Follow-up		[mm^3]	172.02	

Patient 3L – 3D Metrics

Biomechanical analysis

Lateral | Anterior | Medial | Posterior

Stress – Luminal surface

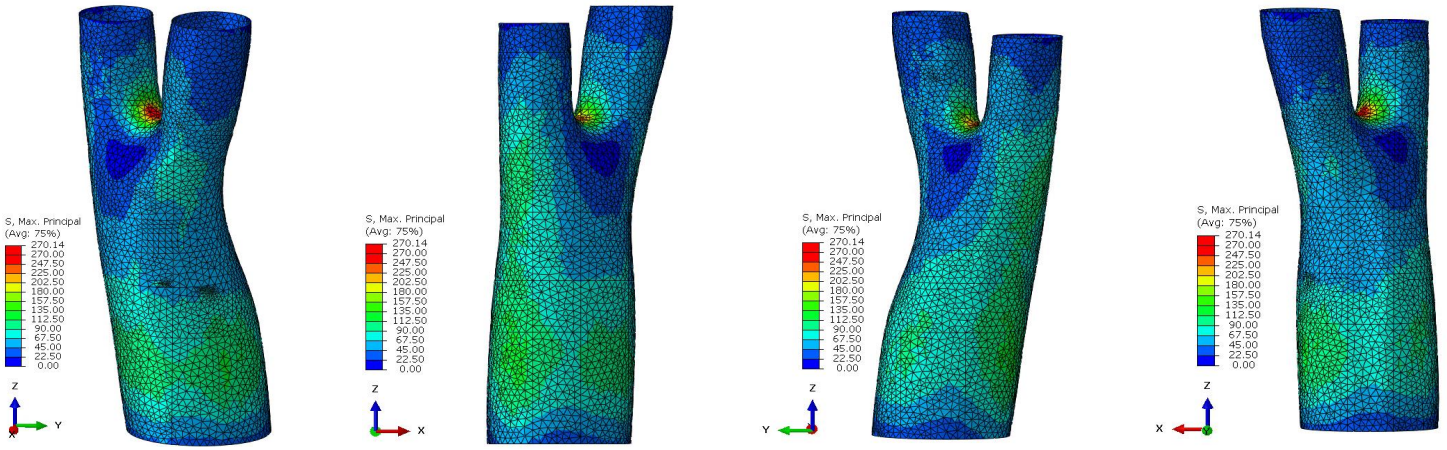

Strain – Luminal surface

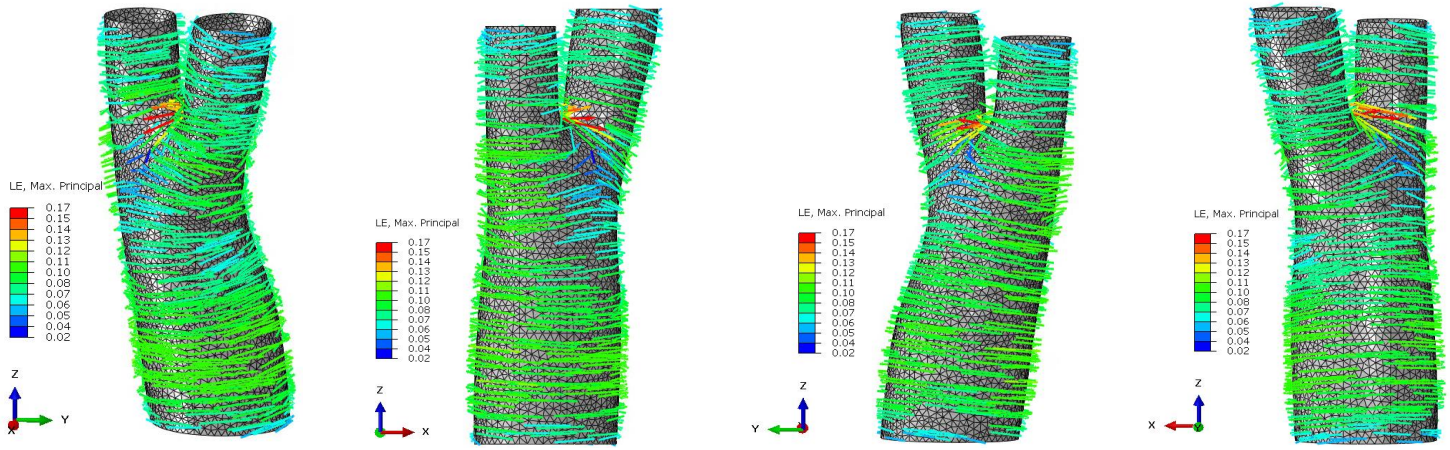

Strain – Lumen + Calcium

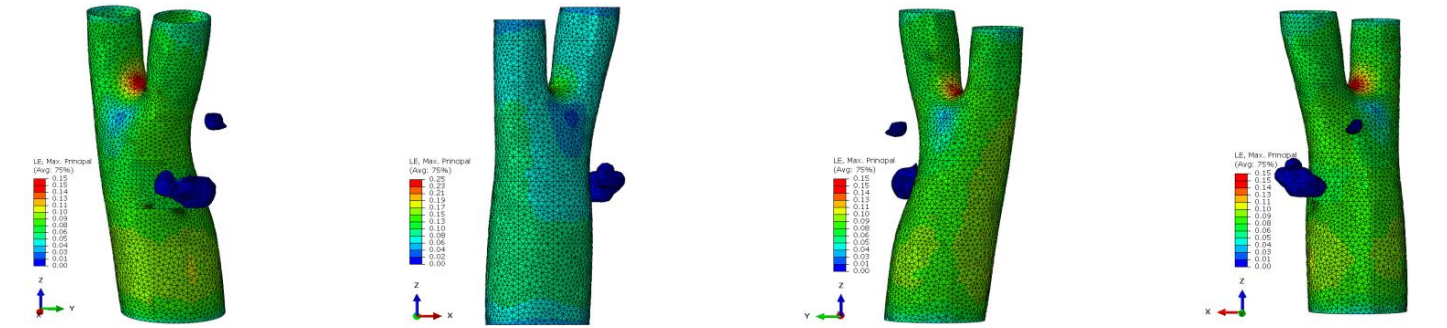

Patient 3L – 3D Morphometry

Morphometrical analysis

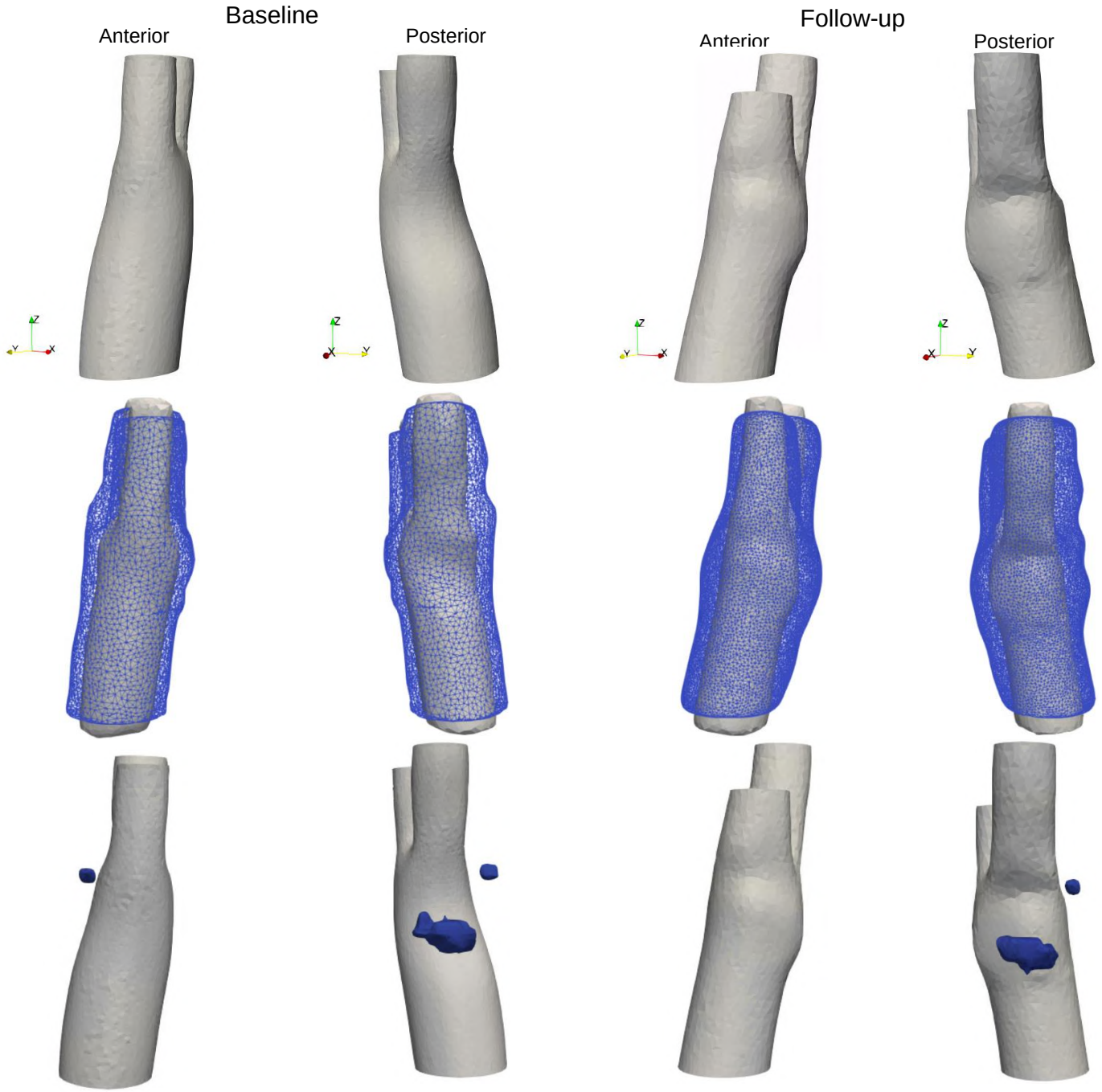

Patient 3L – 2D Metrics

2D Plot metrics
Medial view

	Centerline	Segment identification	Abcissa metric	Angular metric
Baseline	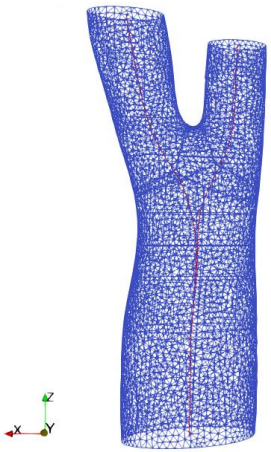	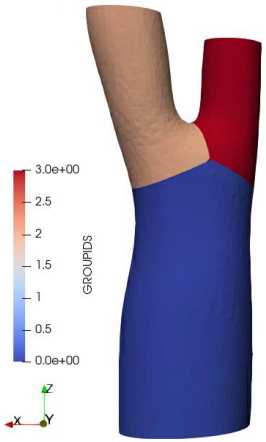	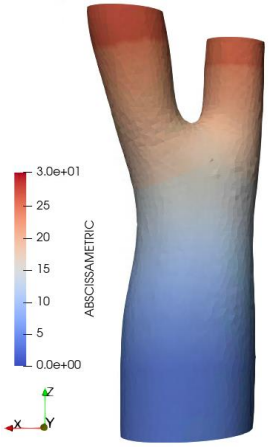	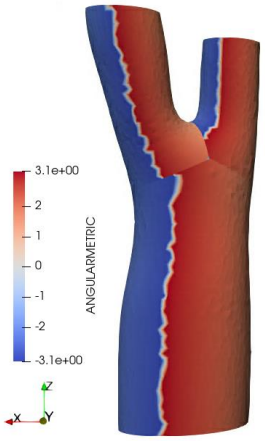
Follow-up	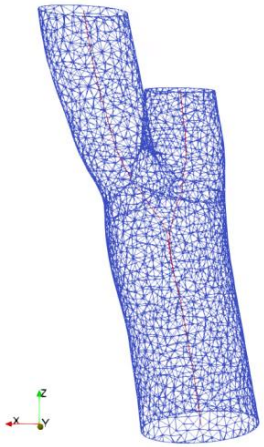	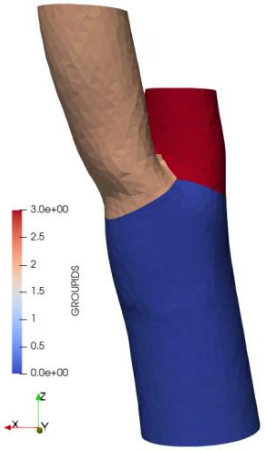	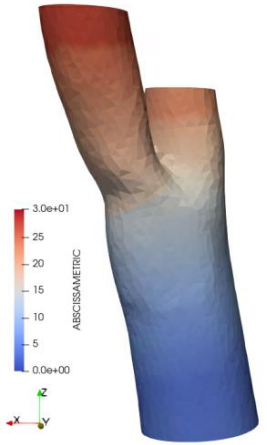	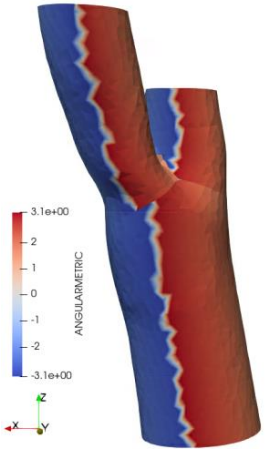

Patient 3L – 2D CCA-ICA

Biomechanical analysis

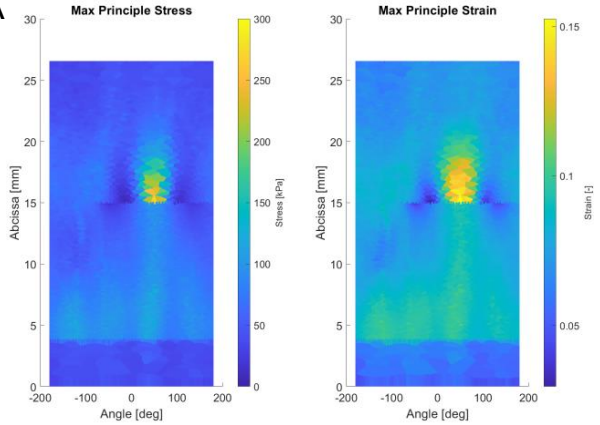

	Stress	Strain	Wall thickness		Max Curvature		Min Curvature	
			Base	*Foll*	*Base*	*Foll*	*Base*	*Foll*
	[kPa]	[-]	[mm]	[mm]	[m^{-1}]	[m^{-1}]	[m^{-1}]	[m^{-1}]
Max	269.48	0.15	3.63	3.67	139.10	3.16	139.10	22.27
Median	56.05	0.07	1.23	1.62	0.32	0.00	0.32	-0.01
Min	7.34	0.03	0.34	0.02	-6.22	0.00	-6.22	-11.61

Morphometrical analysis

Baseline

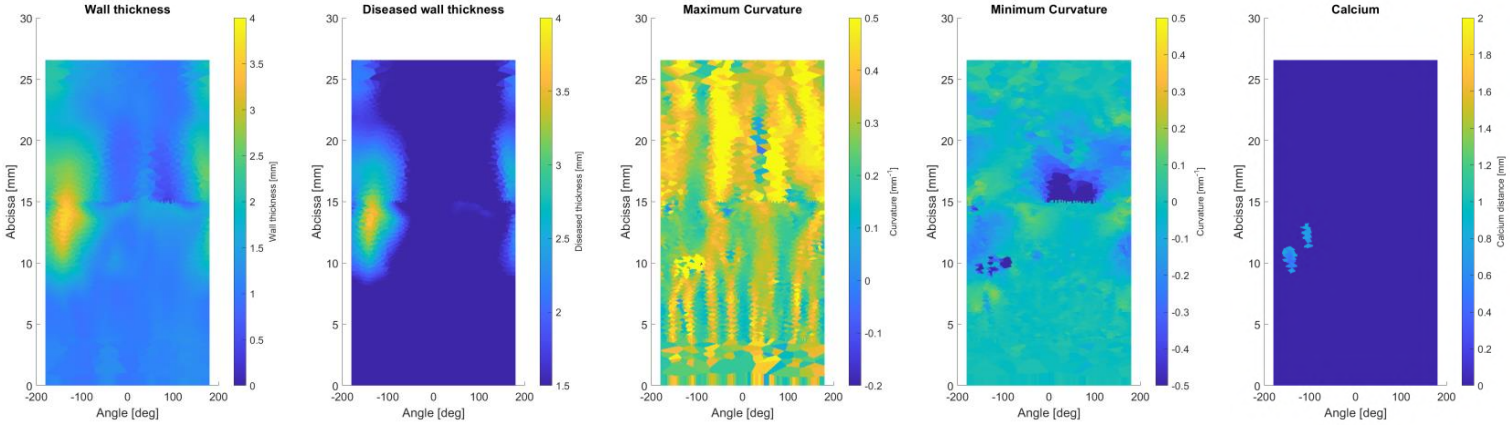

Follow-up

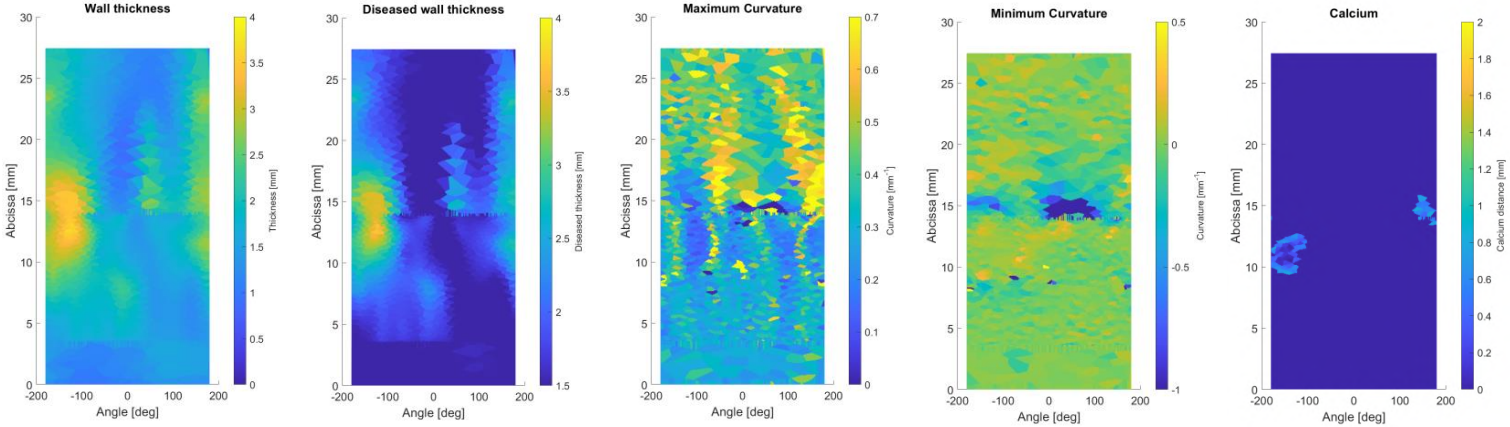

Patient 3L – 2D CCA-ECA

Biomechanical analysis

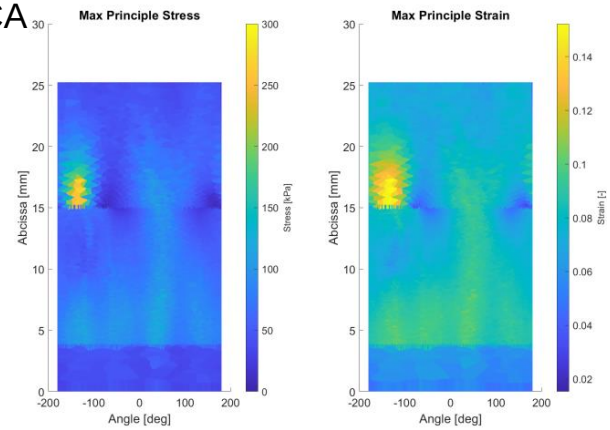

	Stress	Strain	Wall thickness		Max Curvature		Min Curvature	
			Base	*Foll*	*Base*	*Foll*	*Base*	*Foll*
	[kPa]	[-]	[mm]	[mm]	[m^{-1}]	[m^{-1}]	[m^{-1}]	[m^{-1}]
Max	270.14	0.15	3.63	3.67	139.10	3.16	139.10	22.27
Median	61.68	0.08	1.17	1.42	0.33	0.00	0.33	-0.01
Min	-9.30	0.02	0.30	0.02	-6.22	0.00	-6.22	-11.61

Morphometrical analysis

Baseline

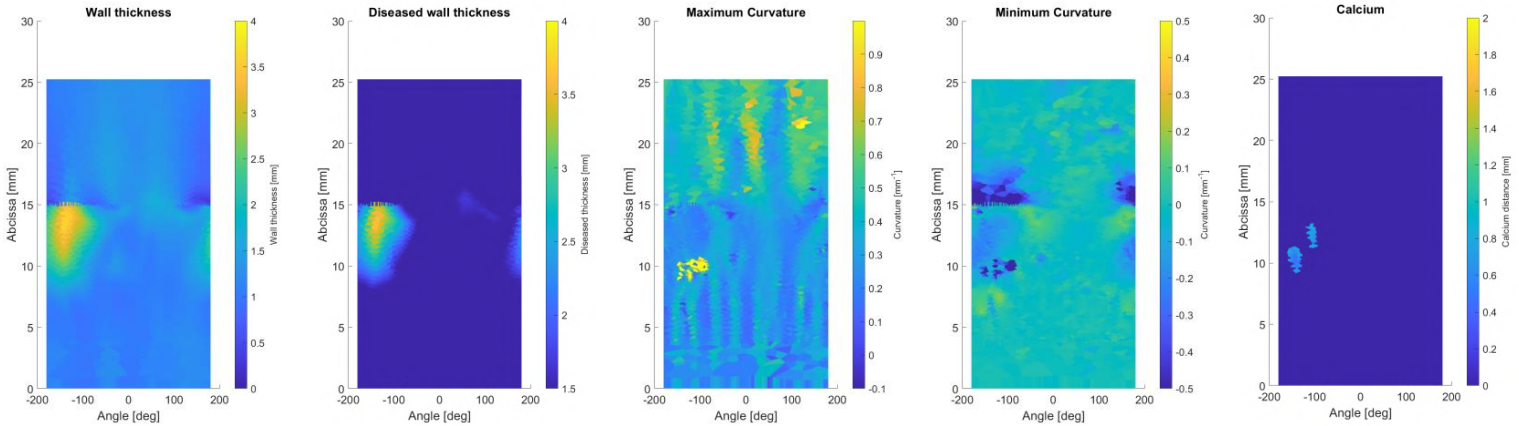

Follow-up

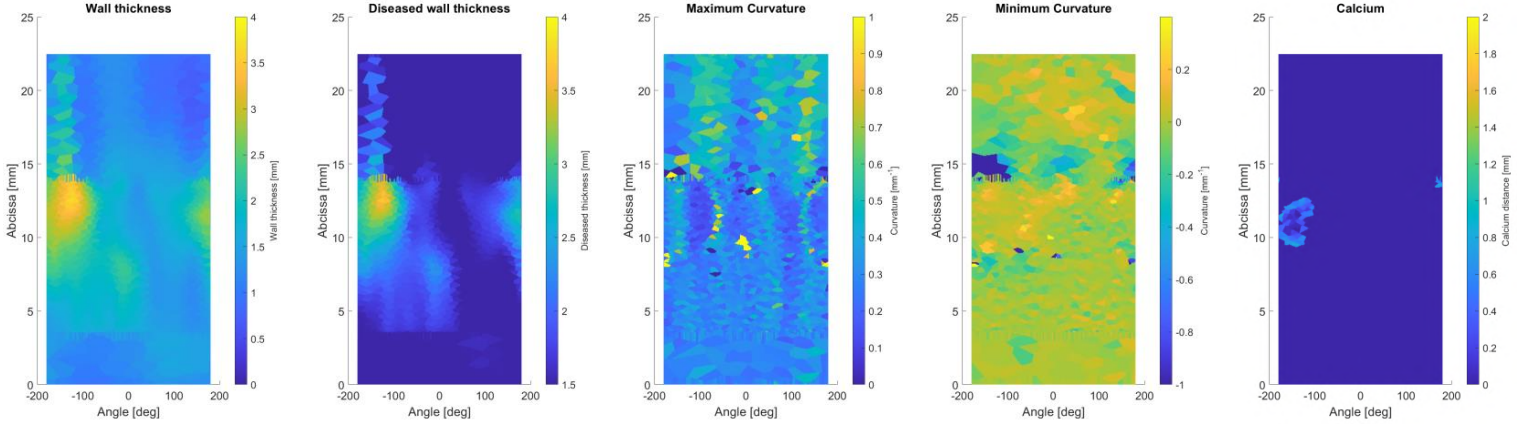

Patient 3L – Metrics

Post-processing metrics			Unit	CCA - ICA	CCA - ECA
Stress	Baseline	Max	[kPa]	269.48	270.14
		Median	[kPa]	56.05	61.68
		Min	[kPa]	7.34	-9.30
Strain	Baseline	Max	[-]	0.15	0.15
		Median	[-]	0.07	0.08
		Min	[-]	0.03	0.02
Wall thickness	Baseline	Max	[mm]	3.63	3.63
	Baseline	Median	[mm]	1.23	1.17
	Baseline	Min	[mm]	0.34	0.30
	Follow-up	Max	[mm]	3.67	3.67
	Follow-up	Median	[mm]	1.62	1.42
	Follow-up	Min	[mm]	0.02	0.02
Plaque burden *	Baseline	Max	[%]	75.84	
	Baseline	Median	[%]	47.65	
	Baseline	Min	[%]	34.28	
	Follow-up	Max	[%]	71.70	
	Follow-up	Median	[%]	52.15	
	Follow-up	Min	[%]	37.19	
Calcium *	Baseline		[mm^3]	18.38	
	Follow-up		[mm^3]	24.34	

Patient 3R – 3D Metrics

Biomechanical analysis

Medial | Anterior | Lateral | Posterior

Stress – Luminal surface

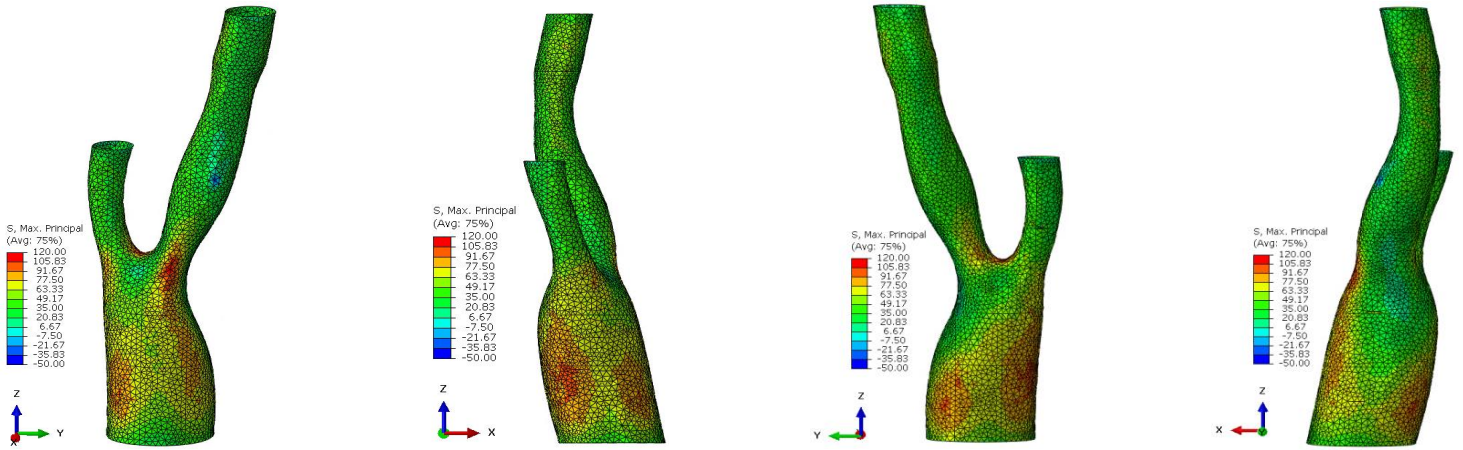

Strain – Luminal surface

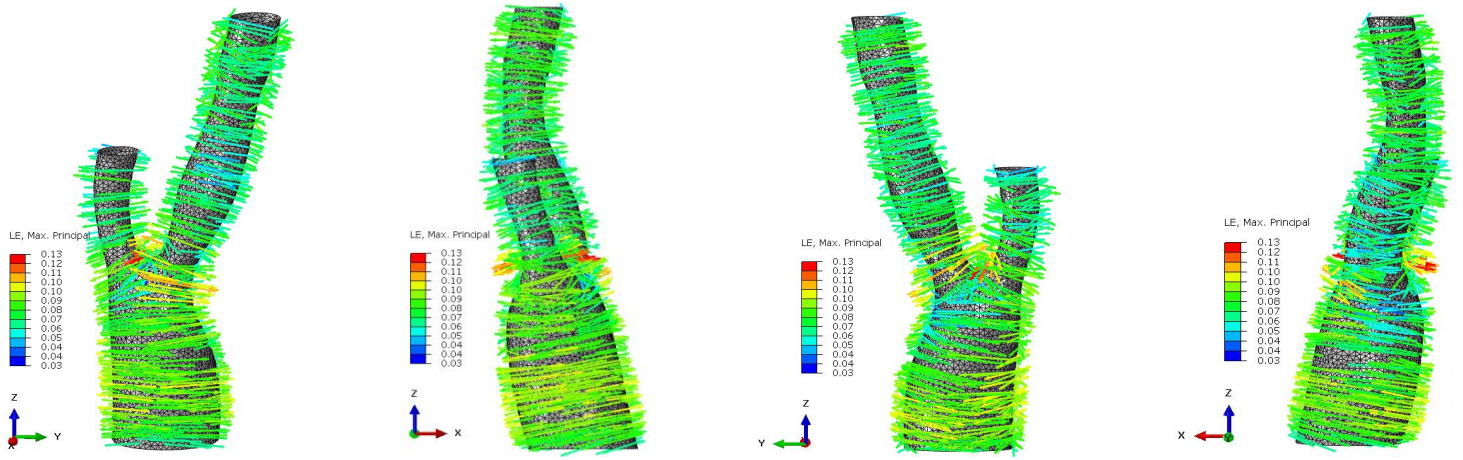

Strain – Lumen + Calcium

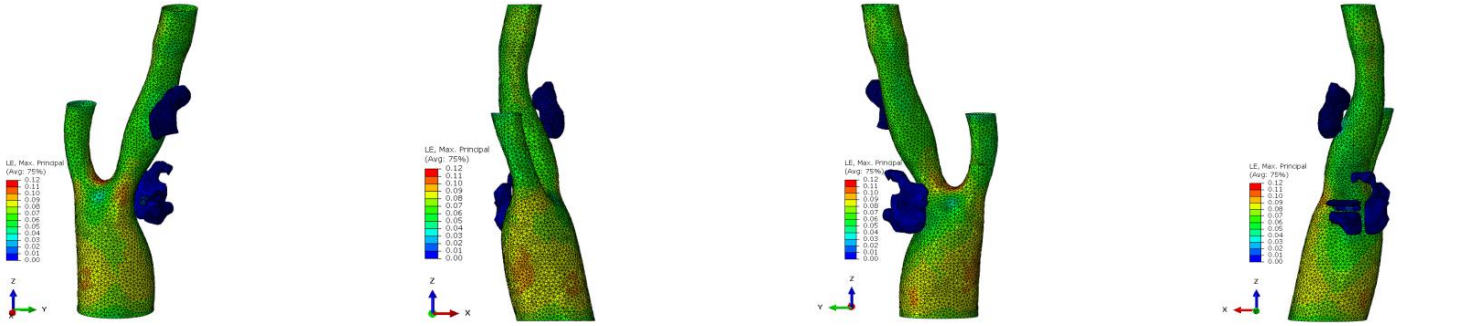

Patient 3R – 3D Morphometry

Morphometrical analysis

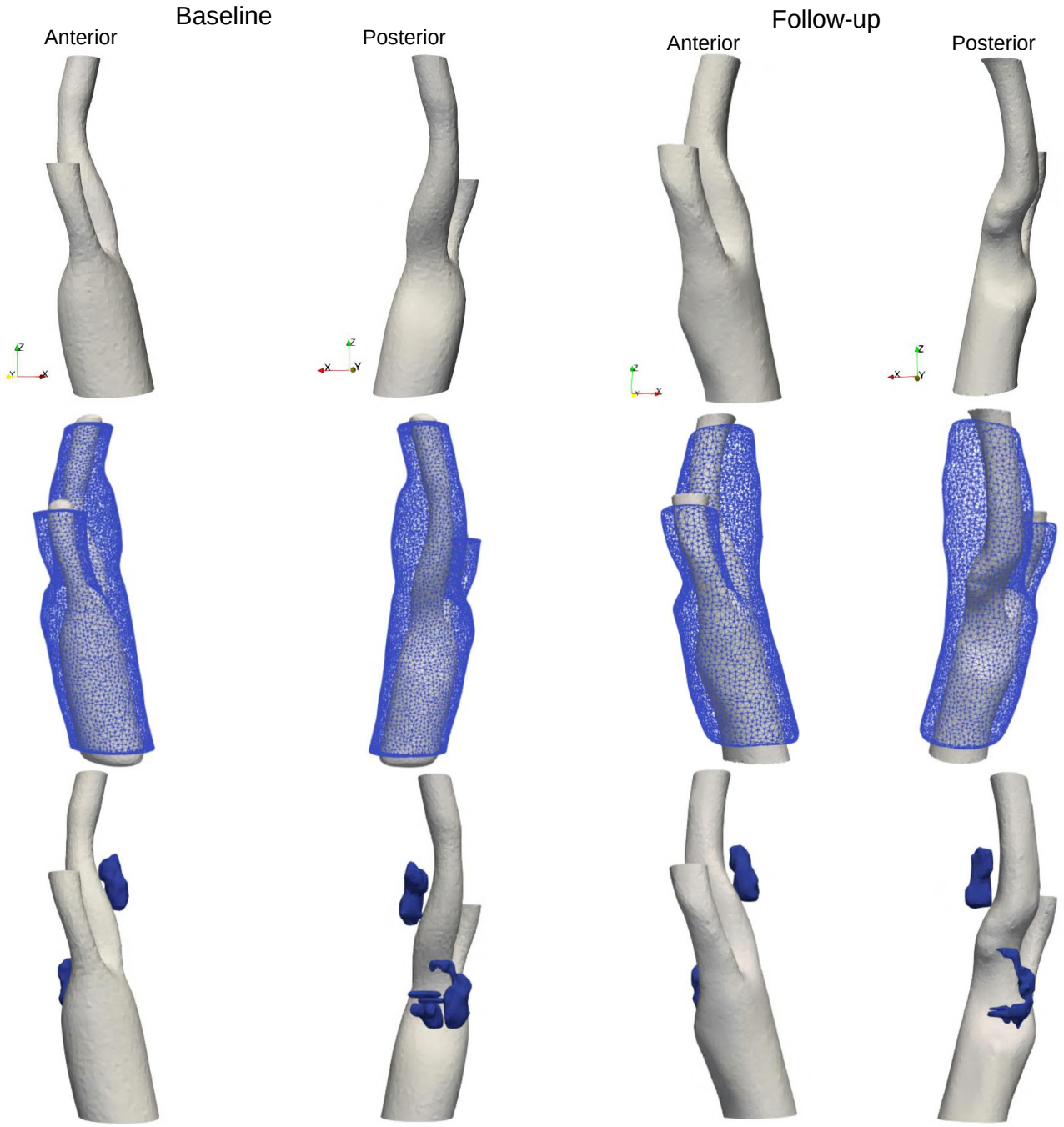

Patient 3R – 2D Metrics

2D Plot metrics
Medial view

	Centerline	Segment identification	Abcissa metric	Angular metric
Baseline	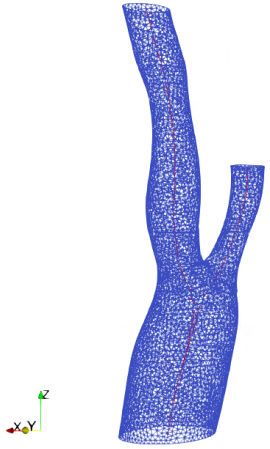	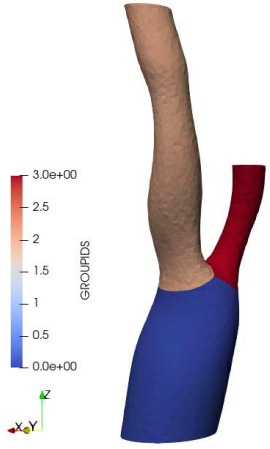	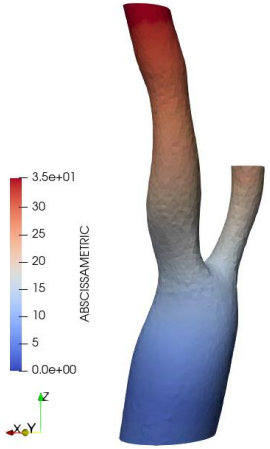	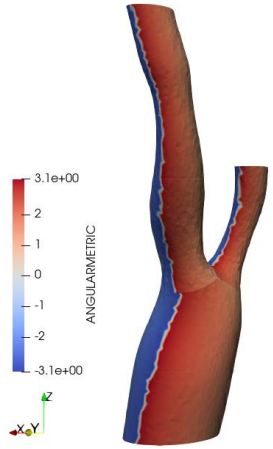
Follow-up	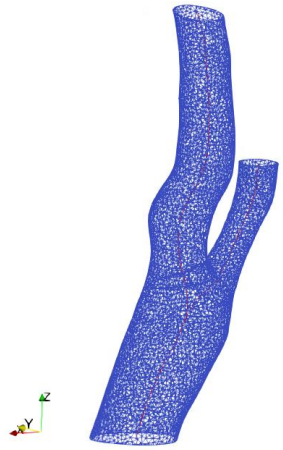	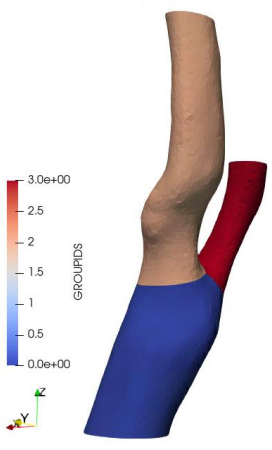	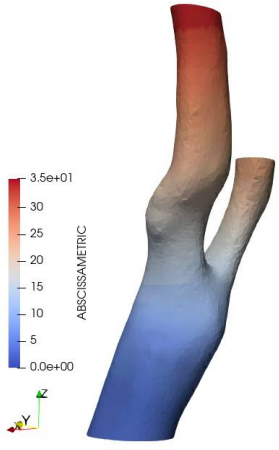	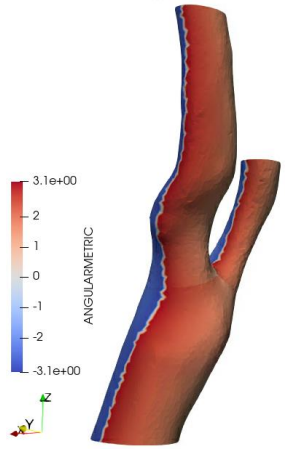

Patient 3R – 2D CCA-ICA

Biomechanical analysis

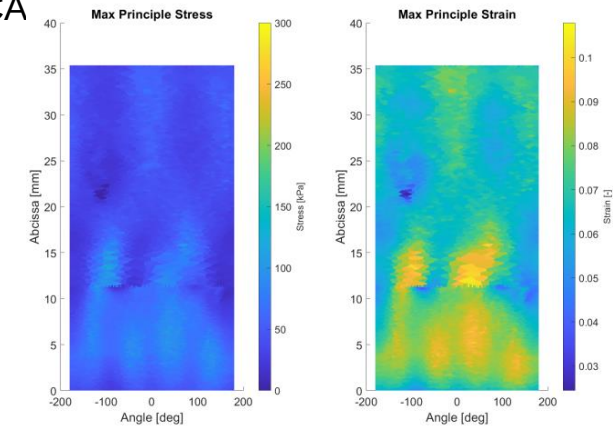

	Stress	Strain	Wall thickness		Max Curvature		Min Curvature	
			Base	*Foll*	*Base*	*Foll*	*Base*	*Foll*
	[kPa]	[-]	[mm]	[mm]	[m^{-1}]	[m^{-1}]	[m^{-1}]	[m^{-1}]
Max	118.17	0.11	4.44	39.11	1.15	2.73	0.30	0.83
Median	43.47	0.07	1.58	1.55	0.49	0.40	-0.01	-0.04
Min	-33.03	0.02	0.84	0.17	0.02	-0.23	-1.20	-2.74

Morphometrical analysis

Baseline

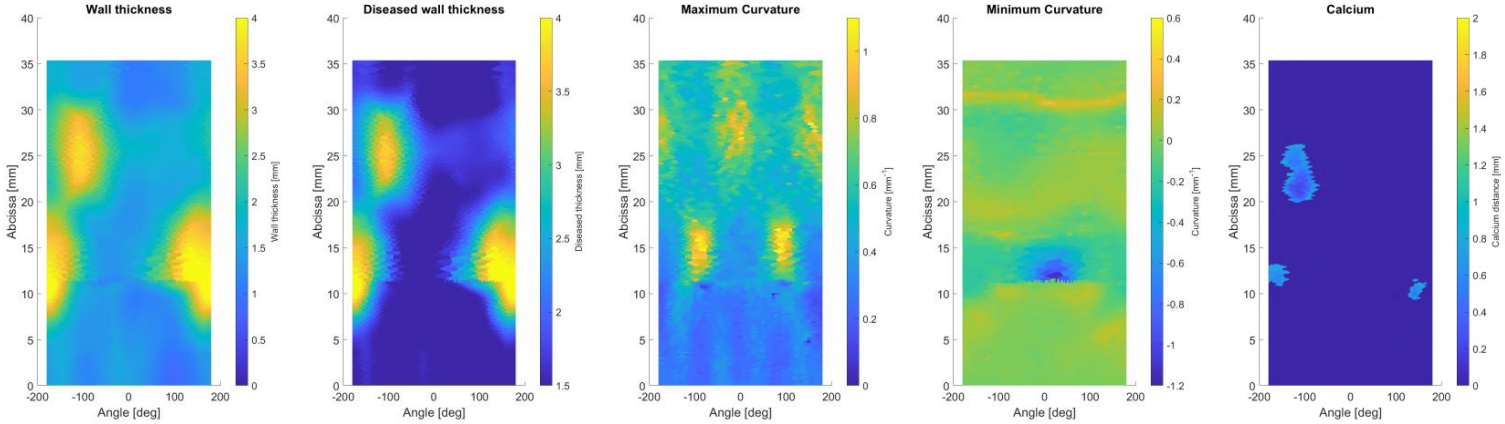

Follow-up

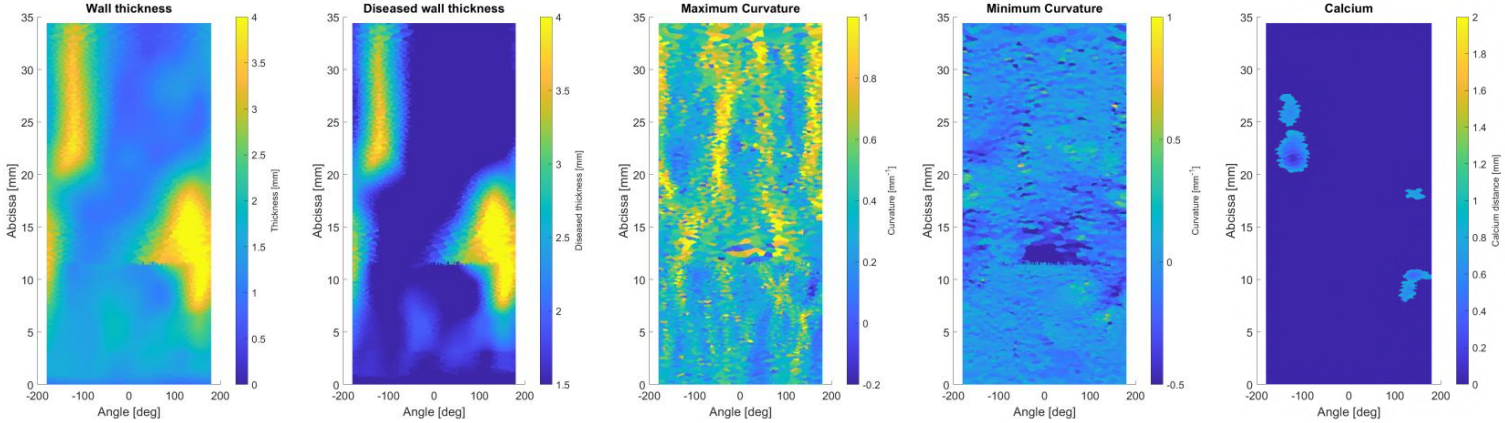

Patient 3R – 2D CCA-ECA

Biomechanical analysis

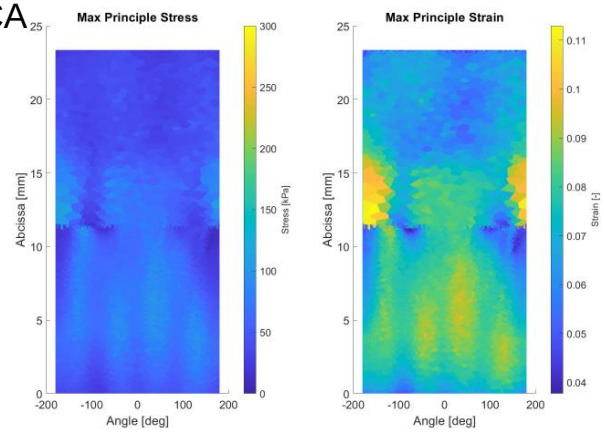

	Stress	Strain	Wall thickness		Max Curvature		Min Curvature	
			Base	*Foll*	*Base*	*Foll*	*Base*	*Foll*
	[kPa]	[-]	[mm]	[mm]	[m^{-1}]	[m^{-1}]	[m^{-1}]	[m^{-1}]
Max	111.53	0.11	4.44	4.48	1.30	6.07	0.14	0.73
Median	55.27	0.07	1.35	1.53	0.45	0.45	-0.01	-0.03
Min	10.12	0.04	0.84	0.21	0.02	-0.59	-1.27	-5.76

Morphometrical analysis

Baseline

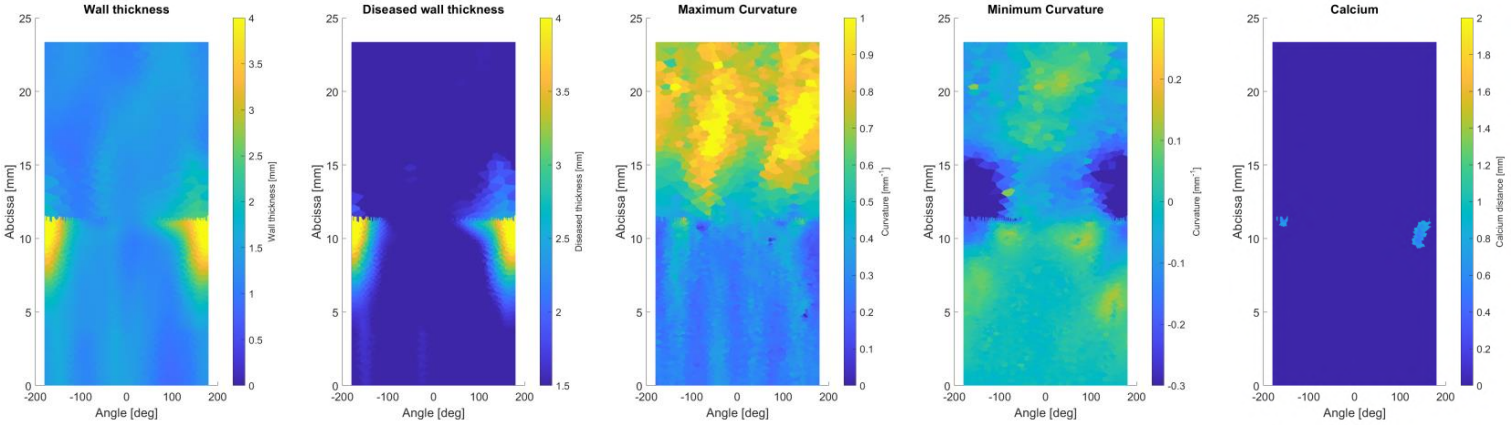

Follow-up

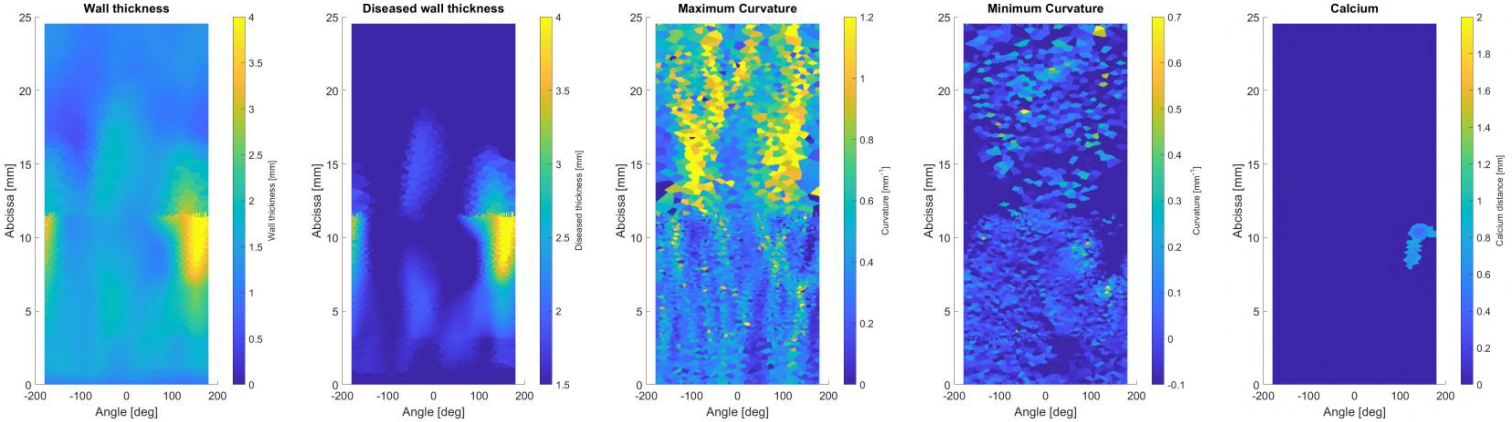

Patient 3R – Metrics

Post-processing metrics			Unit	CCA - ICA	CCA - ECA
Stress	Baseline	Max	[kPa]	118.17	111.53
		Median	[kPa]	43.47	55.27
		Min	[kPa]	-33.03	10.12
Strain	Baseline	Max	[-]	0.11	0.11
		Median	[-]	0.07	0.07
		Min	[-]	0.02	0.04
Wall thickness	Baseline	Max	[mm]	4.44	4.44
	Baseline	Median	[mm]	1.58	1.35
	Baseline	Min	[mm]	0.84	0.84
	Follow-up	Max	[mm]	39.11	4.48
	Follow-up	Median	[mm]	1.55	1.53
	Follow-up	Min	[mm]	0.17	0.21
Plaque burden *	Baseline	Max	[%]	79.44	
	Baseline	Median	[%]	51.68	
	Baseline	Min	[%]	35.68	
	Follow-up	Max	[%]	80.60	
	Follow-up	Median	[%]	56.63	
	Follow-up	Min	[%]	37.57	
Calcium *	Baseline		[mm^3]	98.78	
	Follow-up		[mm^3]	112.97	

Patient 4R – 3D Metrics

Biomechanical analysis

Lateral | Anterior | Medial | Posterior

Stress – Luminal surface

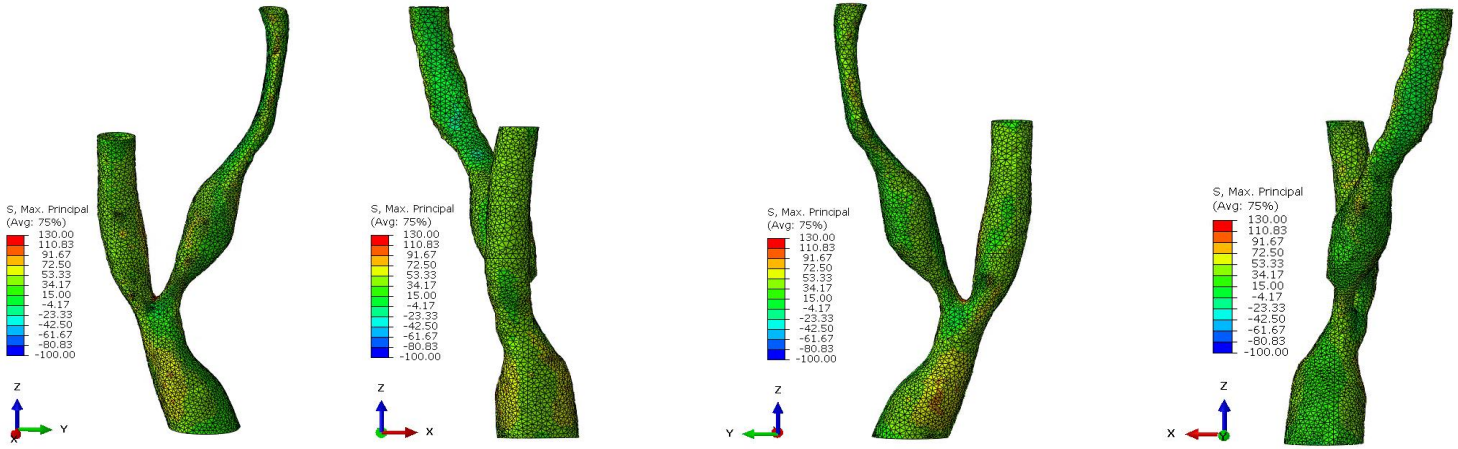

Strain – Luminal surface

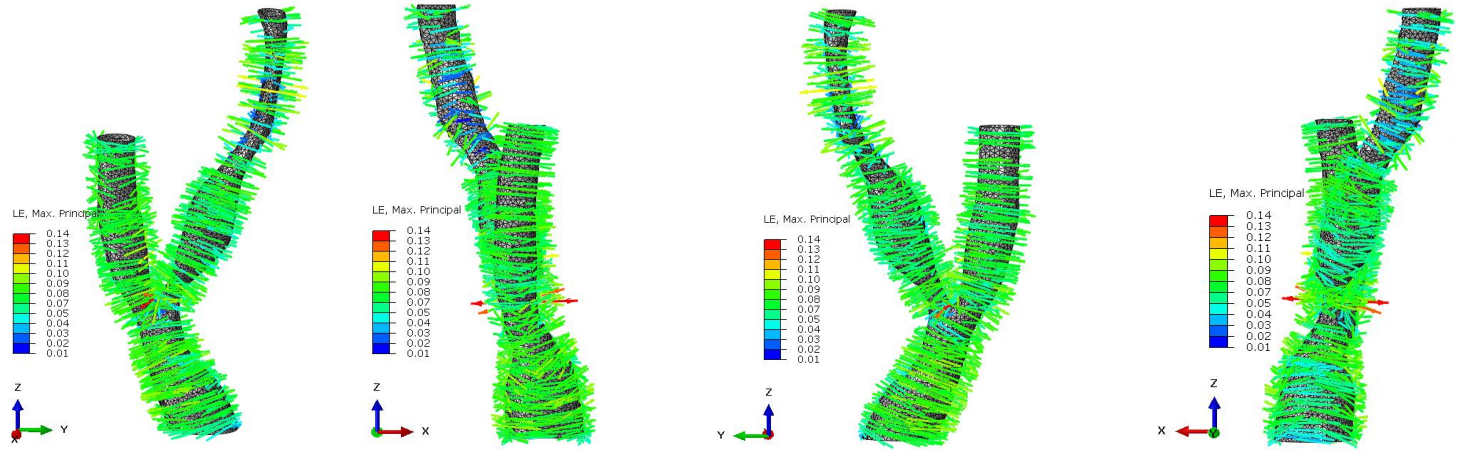

Strain – Lumen + Calcium

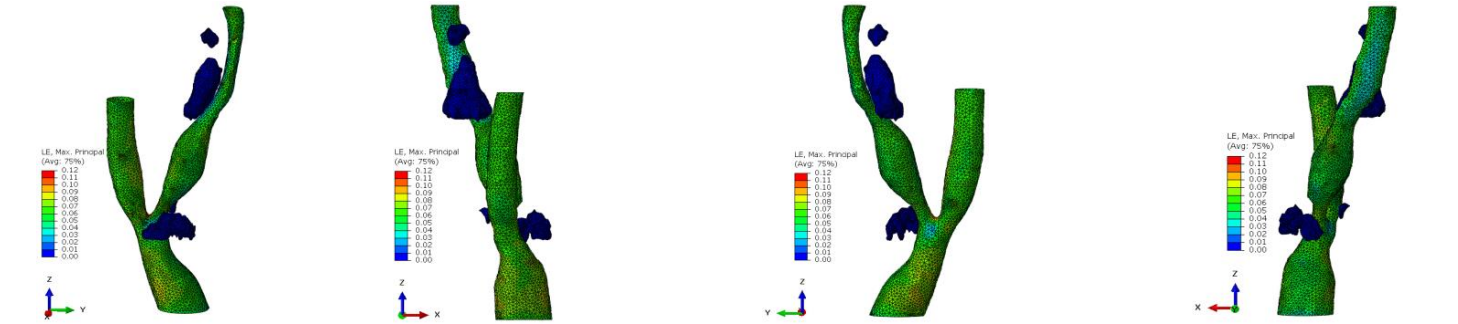

Patient 4R – 3D Morphometry

Morphometrical analysis

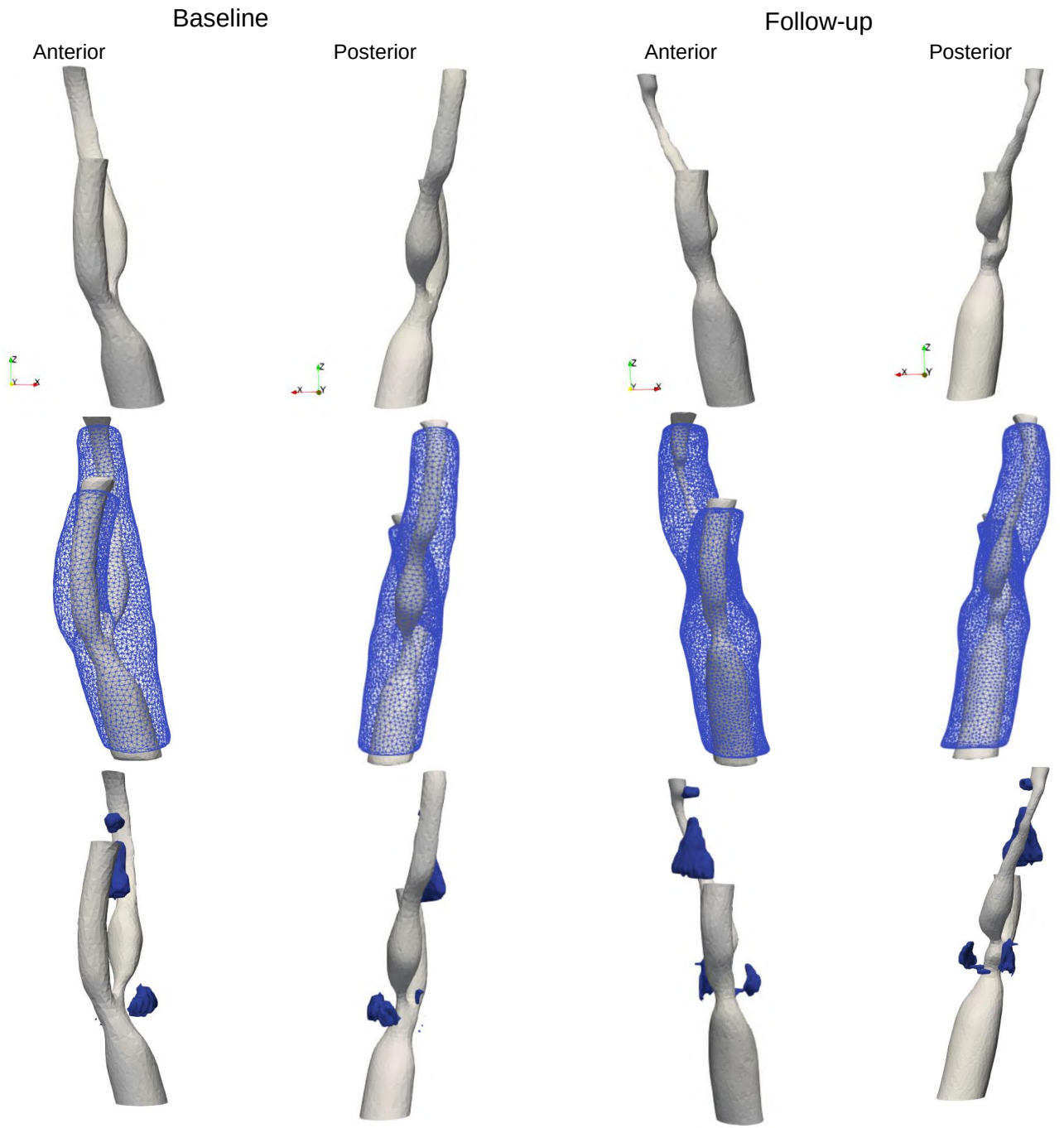

Patient 4R – 2D Metrics

2D Plot metrics
Medial view

	Centerline	Segment identification	Abcissa metric	Angular metric
Baseline		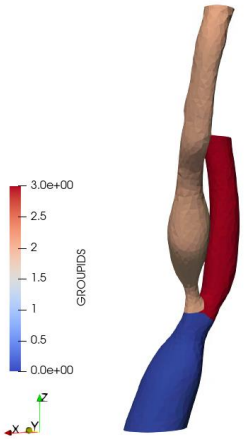	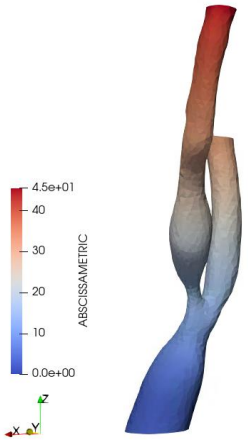	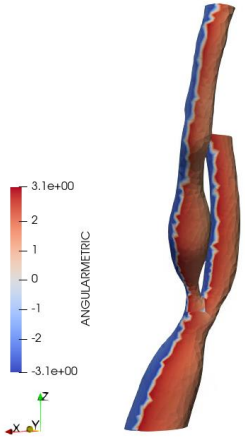
Follow-up	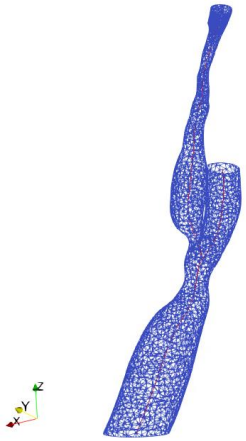	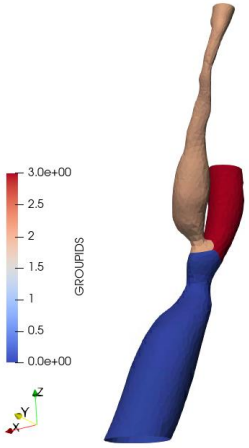	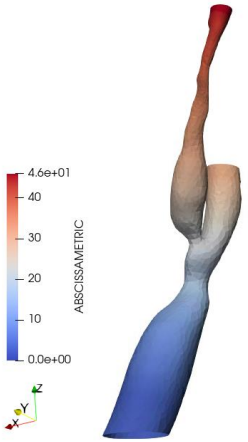	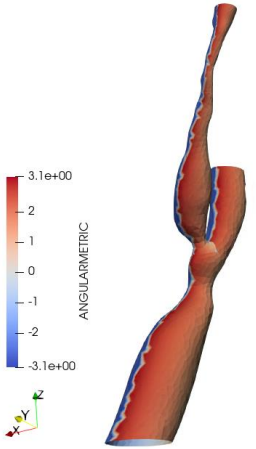

Patient 4R – 2D CCA-ICA

Biomechanical analysis

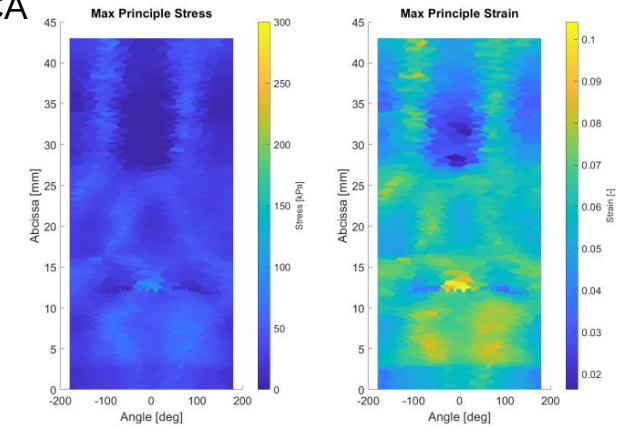

	Stress	Strain	Wall thickness		Max Curvature		Min Curvature	
			Base	*Foll*	*Base*	*Foll*	*Base*	*Foll*
	[kPa]	[-]	[mm]	[mm]	[m^{-1}]	[m^{-1}]	[m^{-1}]	[m^{-1}]
Max	104.74	0.10	4.47	4.79	3.62	17.85	0.38	0.00
Median	31.71	0.06	2.02	2.09	0.65	0.73	0.00	0.00
Min	-11.2	0.02	0.85	-0.01	0.16	-408.78	-2.04	-1.76

Morphometrical analysis

Baseline

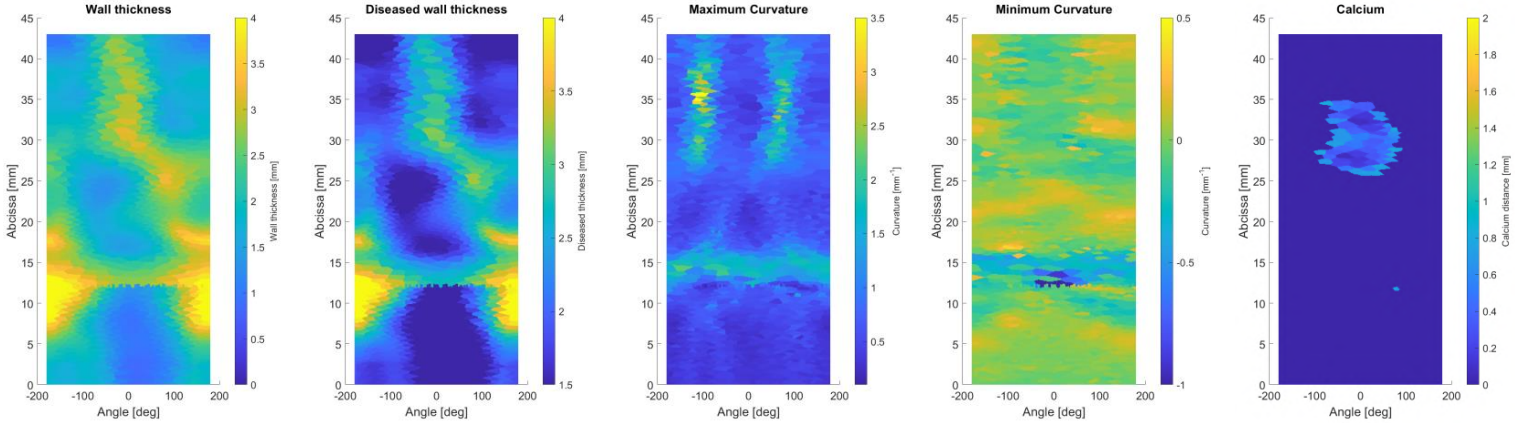

Follow-up

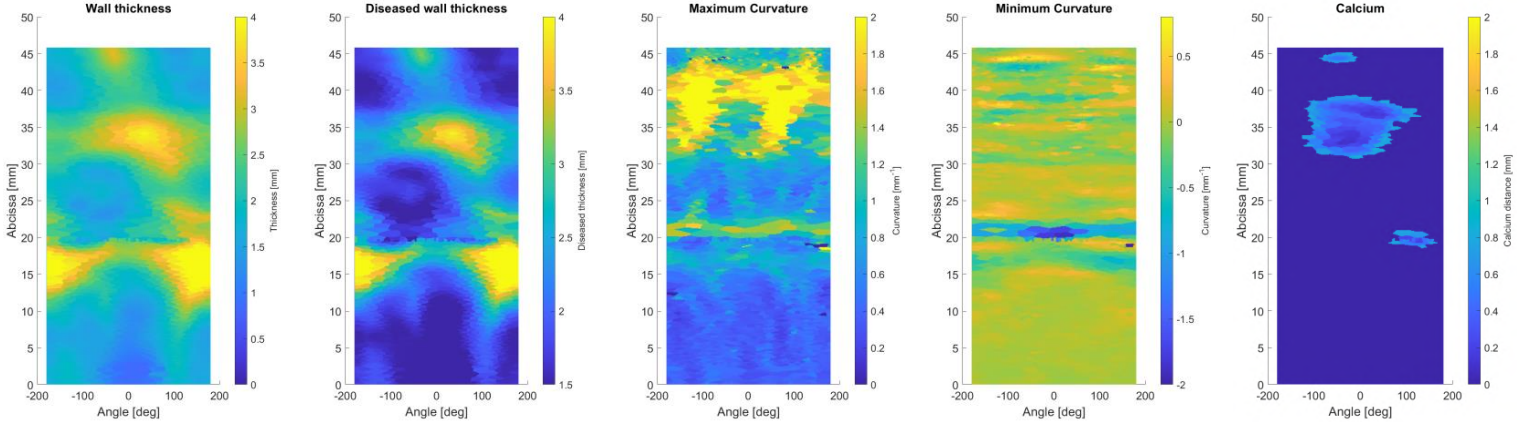

Patient 4R – 2D CCA-ECA

Biomechanical analysis

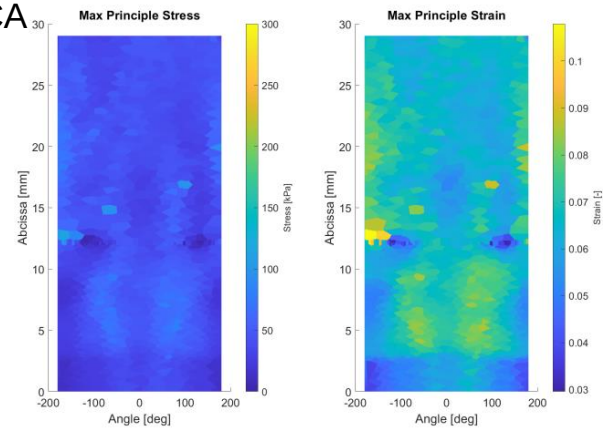

	Stress	Strain	Wall thickness		Max Curvature		Min Curvature	
			Base	*Foll*	*Base*	*Foll*	*Base*	*Foll*
	[kPa]	[-]	[mm]	[mm]	[m^{-1}]	[m^{-1}]	[m^{-1}]	[m^{-1}]
Max	113.74	0.11	4.47	4.79	1.56	26.66	0.26	0.00
Median	40.99	0.06	1.65	1.60	0.62	0.49	0.00	0.00
Min	3.39	0.03	0.56	0.45	0.11	-408.78	-1.84	-1.76

Morphometrical analysis

Baseline

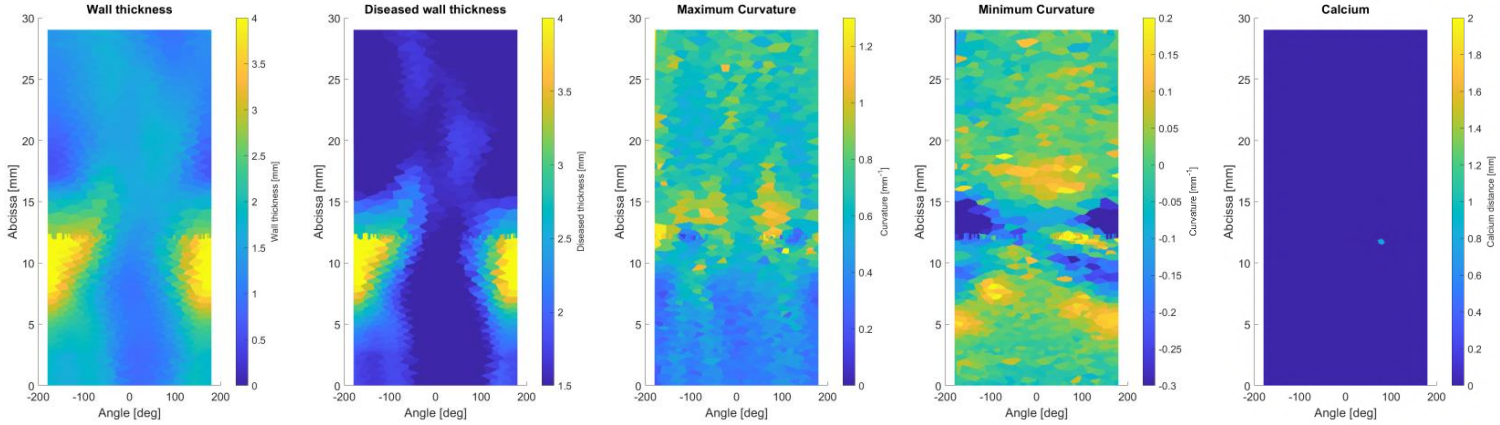

Follow-up

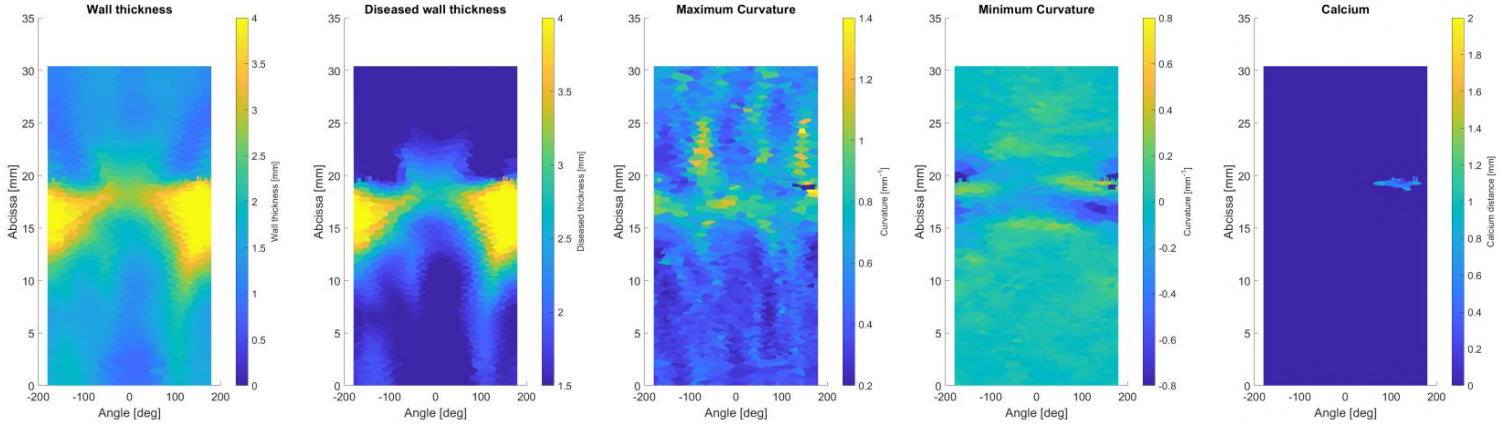

Patient 4R – Metrics

Post-processing metrics			Unit	CCA - ICA	CCA - ECA
Stress	Baseline	Max	[kPa]	104.74	113.74
		Median	[kPa]	31.71	40.99
		Min	[kPa]	-11.2	3.39
Strain	Baseline	Max	[-]	0.10	0.11
		Median	[-]	0.06	0.06
		Min	[-]	0.02	0.03
Wall thickness	Baseline	Max	[mm]	4.47	4.47
	Baseline	Median	[mm]	2.02	1.65
	Baseline	Min	[mm]	0.85	0.56
	Follow-up	Max	[mm]	4.79	4.79
	Follow-up	Median	[mm]	2.09	1.60
	Follow-up	Min	[mm]	-0.01	0.45
Plaque burden *	Baseline	Max	[%]	95.76	
	Baseline	Median	[%]	53.95	
	Baseline	Min	[%]	41.06	
	Follow-up	Max	[%]	94.74	
	Follow-up	Median	[%]	56.80	
	Follow-up	Min	[%]	41.55	
Calcium *	Baseline		[mm^3]	116.63	
	Follow-up		[mm^3]	139.00	

Patient 5L – 3D Metrics

Biomechanical analysis

Medial Anterior Lateral Posterior

Stress – Luminal surface

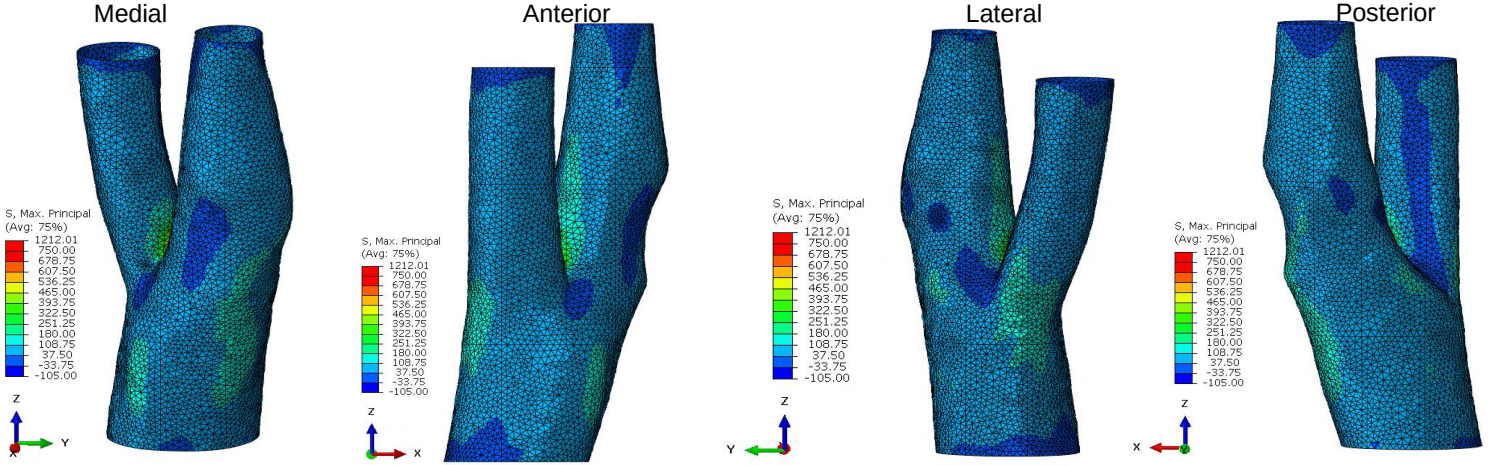

Strain – Luminal surface

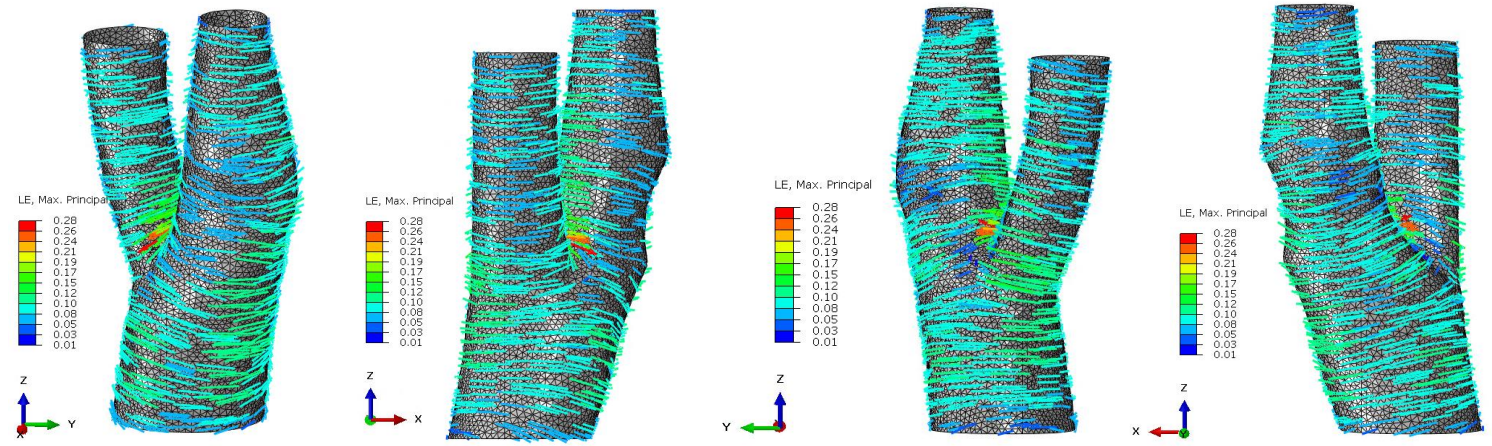

Strain – Lumen + Calcium

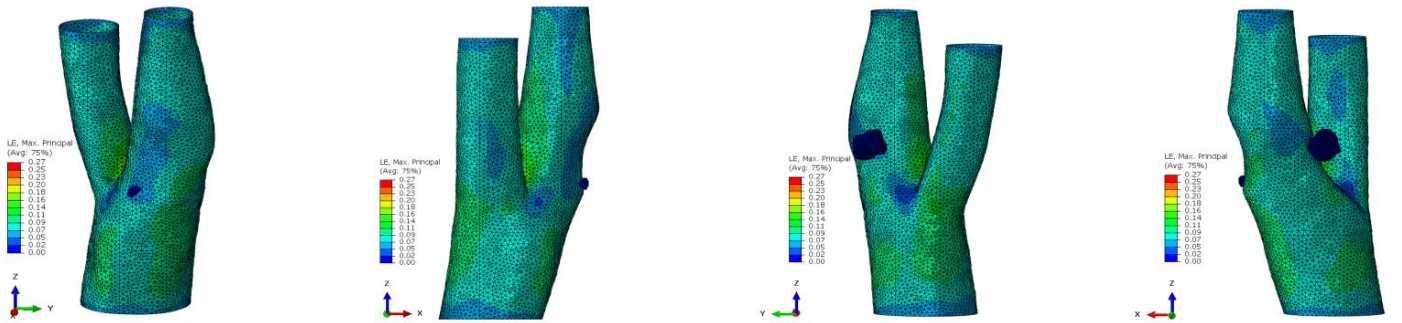

Patient 5L – 3D Morphometry

Morphometrical analysis

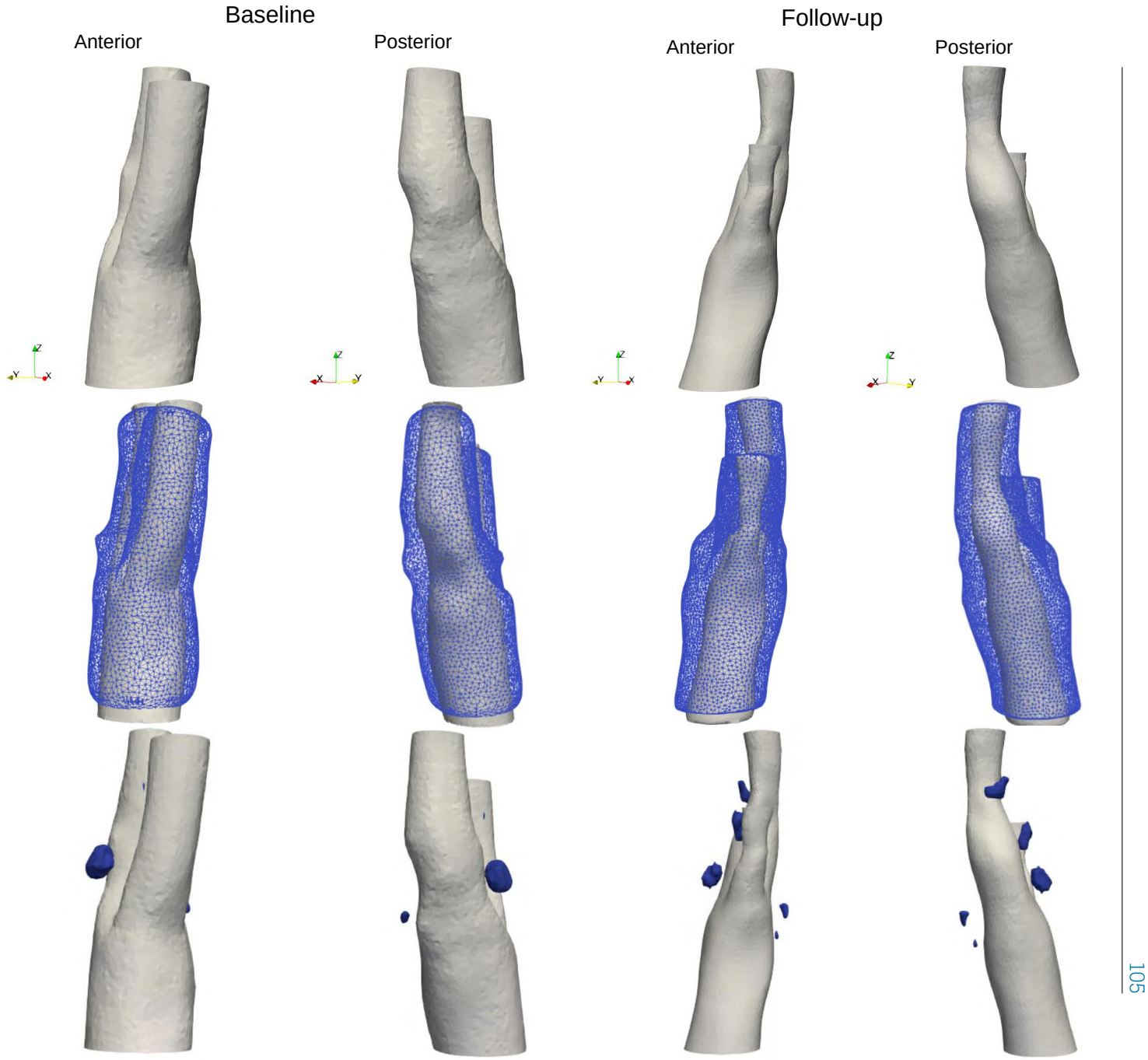

Patient 5L – 2D Metrics

2D Plot metrics
Lateral view

	Centerline	Segment identification	Abcissa metric	Angular metric
Baseline	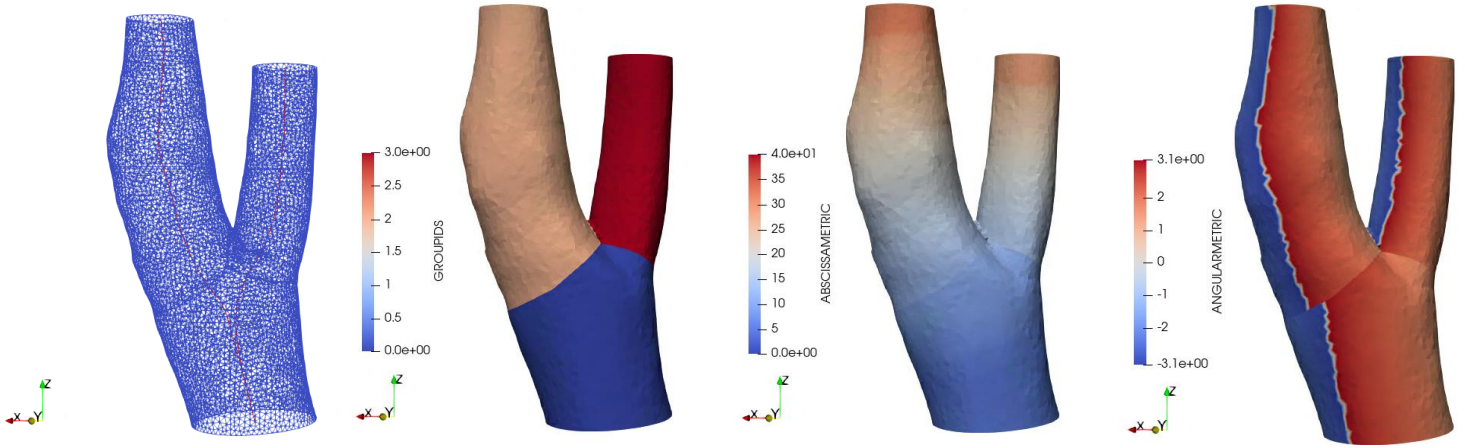			
Follow-up	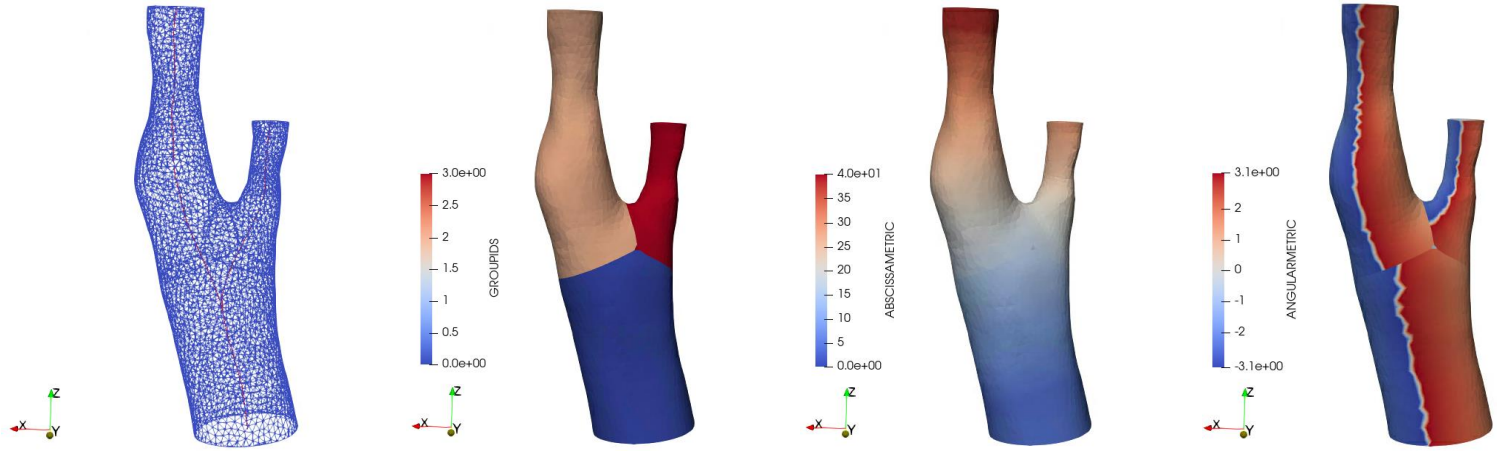			

Patient 5L – 2D CCA-ICA

Biomechanical analysis

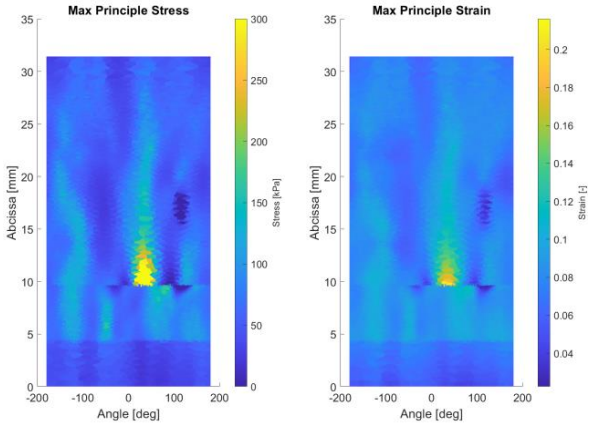

	Stress	Strain	Wall thickness		Max Curvature		Min Curvature	
			Base	*Foll*	*Base*	*Foll*	*Base*	*Foll*
	[kPa]	[-]	[mm]	[mm]	[m^{-1}]	[m^{-1}]	[m^{-1}]	[m^{-1}]
Max	744.31	0.22	2.81	3.96	17.09	1.71	1.74	0.41
Median	61.14	0.08	1.44	2.00	0.30	0.31	-0.01	-0.01
Min	-24.31	0.02	0.83	0.70	-0.10	-0.04	-24.18	-0.77

Morphometrical analysis

Baseline

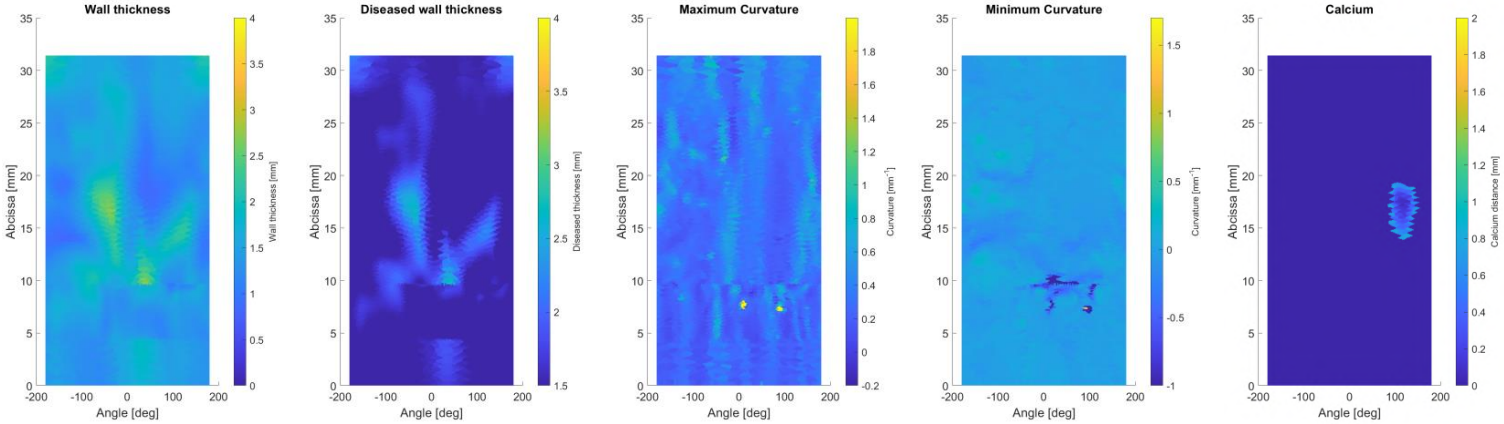

Follow-up

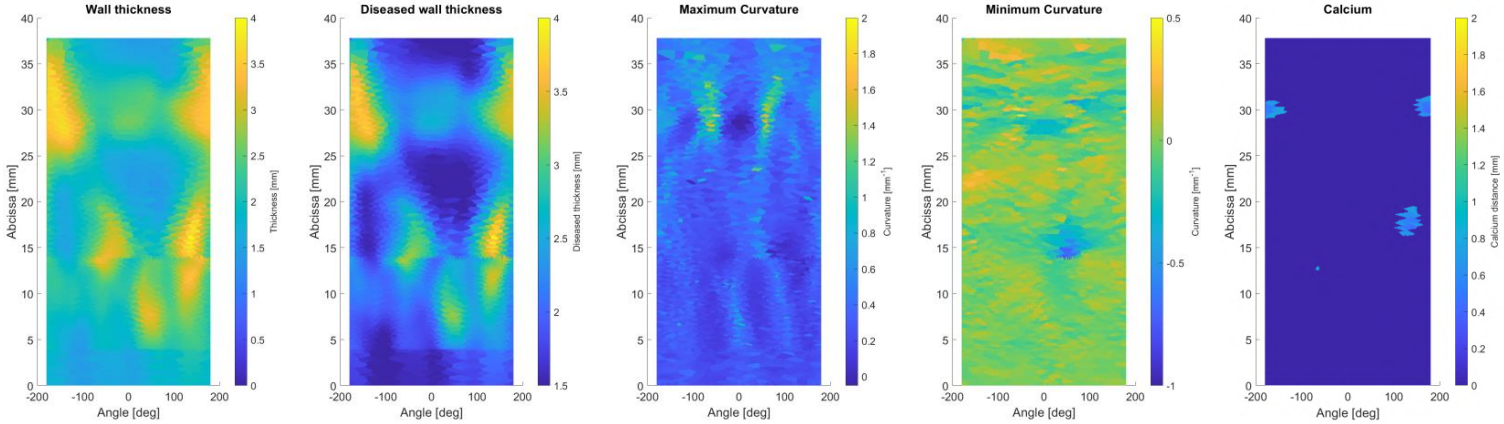

Patient 5L – 2D CCA-ECA

Biomechanical analysis

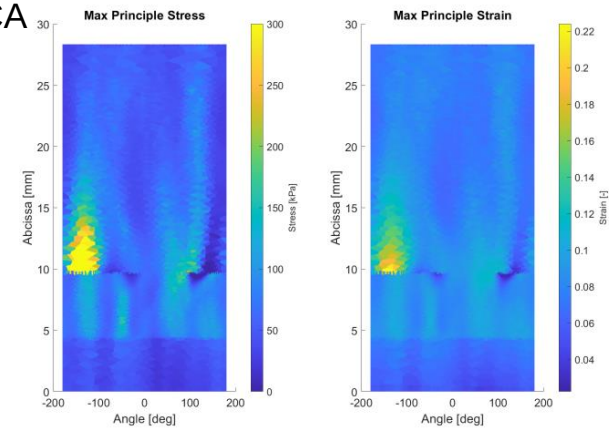

	Stress	Strain	Wall thickness		Max Curvature		Min Curvature	
			Base	*Foll*	*Base*	*Foll*	*Base*	*Foll*
	[kPa]	[-]	[mm]	[mm]	[m^{-1}]	[m^{-1}]	[m^{-1}]	[m^{-1}]
Max	839.66	0.22	2.87	3.46	17.09	2.26	1.74	0.47
Median	60.55	0.08	1.47	2.26	0.35	0.35	-0.01	-0.03
Min	-13.98	0.02	0.89	0.70	-0.10	0.00	-24.18	-1.21

Morphometrical analysis

Baseline

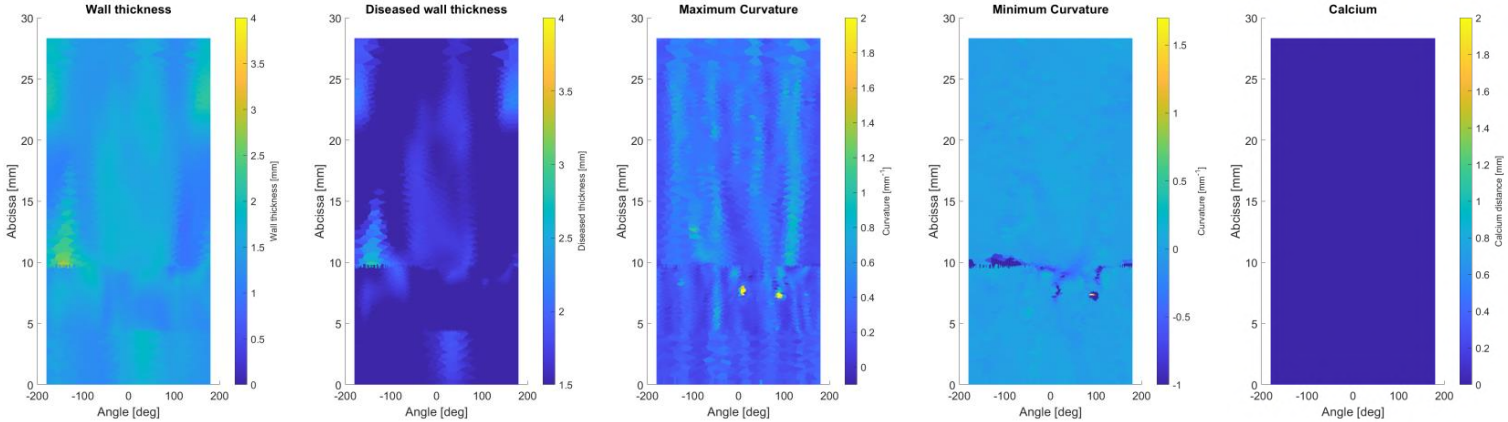

Follow-up

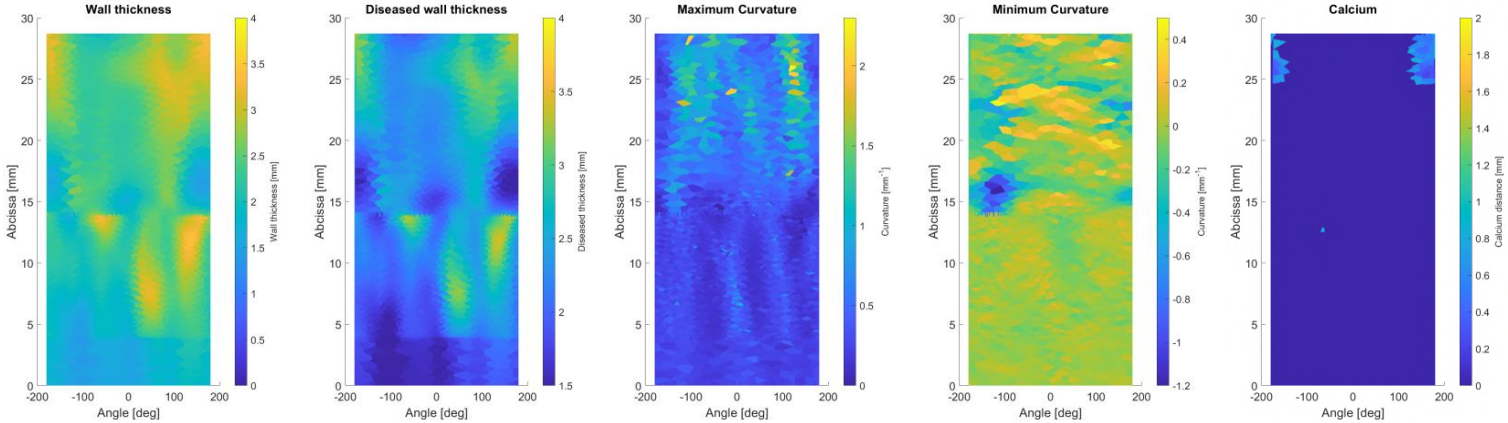

Patient 5L – Metrics

Post-processing metrics			Unit	CCA - ICA	CCA - ECA
Stress	Baseline	Max	[kPa]	744.31	839.66
		Median	[kPa]	61.14	60.55
		Min	[kPa]	-24.31	-13.98
Strain	Baseline	Max	[-]	0.22	0.22
		Median	[-]	0.08	0.08
		Min	[-]	0.02	0.02
Wall thickness	Baseline	Max	[mm]	2.81	2.87
	Baseline	Median	[mm]	1.44	1.47
	Baseline	Min	[mm]	0.83	0.89
	Follow-up	Max	[mm]	3.96	3.46
	Follow-up	Median	[mm]	2.00	2.26
	Follow-up	Min	[mm]	0.7	0.70
Plaque burden *	Baseline	Max	[%]	67.62	
	Baseline	Median	[%]	51.48	
	Baseline	Min	[%]	35.72	
	Follow-up	Max	[%]	70.88	
	Follow-up	Median	[%]	52.20	
	Follow-up	Min	[%]	38.07	
Calcium *	Baseline		[mm^3]	7.35	
	Follow-up		[mm^3]	22.25	

Patient 6R – 3D Metrics

Biomechanical analysis

Posterior | Lateral | Anterior | Medial

Stress – Luminal surface

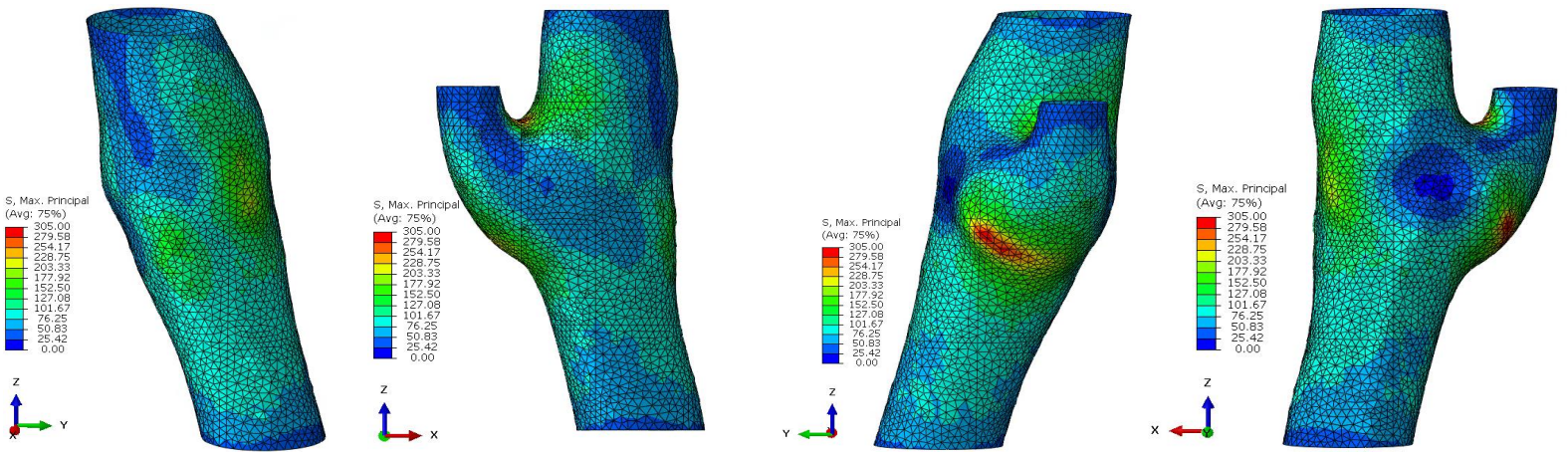

Strain – Luminal surface

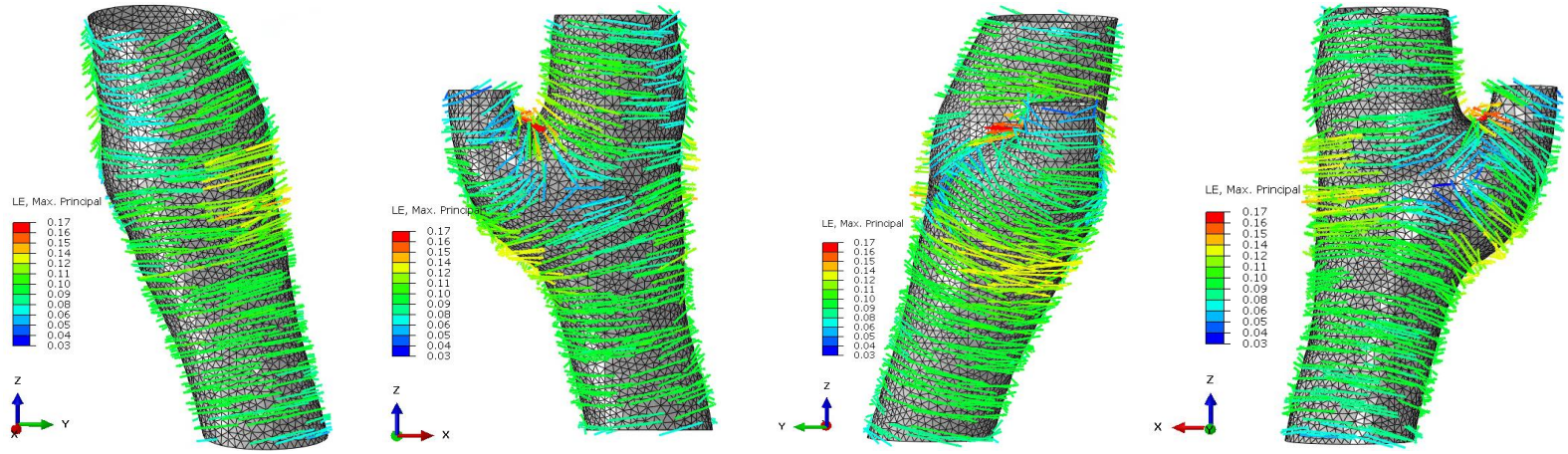

Strain – Lumen

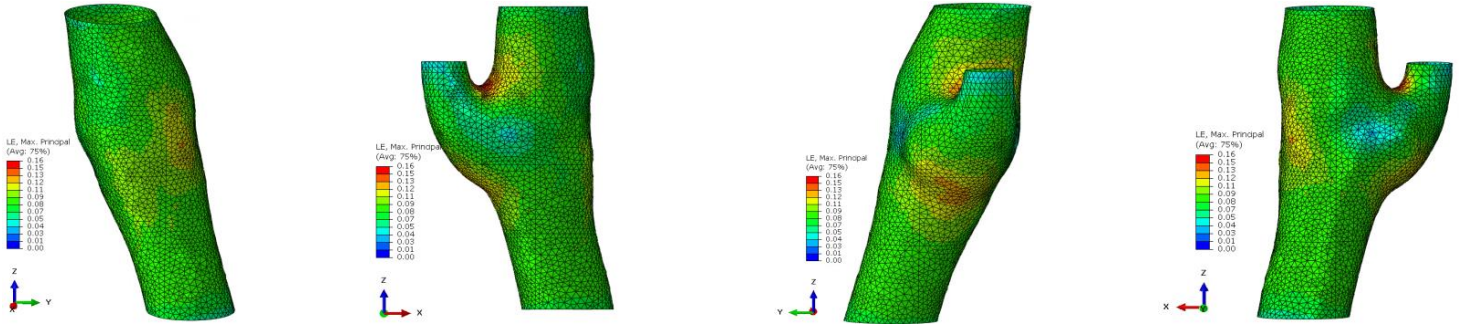

Patient 6R – 3D Morphometry

Morphometrical analysis

	Baseline		Follow-up	
	Anterior	Posterior	Anterior	Posterior
Lumen Geometry				
Wall thickness	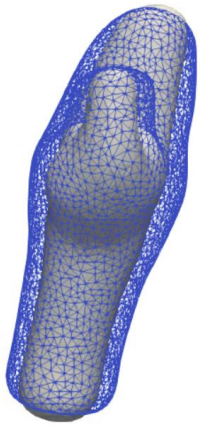	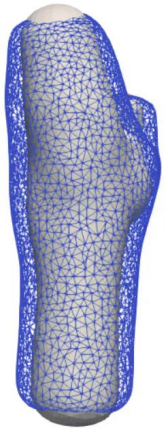	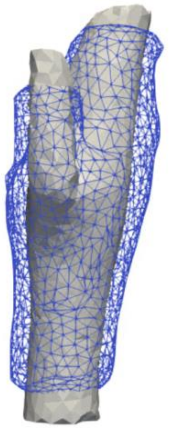	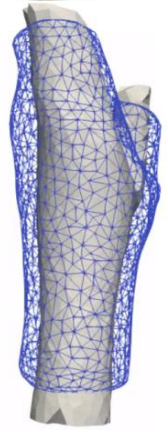
Calcium	NA	NA		

Patient 6R – 2D Metrics

2D Plot metrics
Medial view

	Centerline	Segment identification	Abcissa metric	Angular metric
Baseline	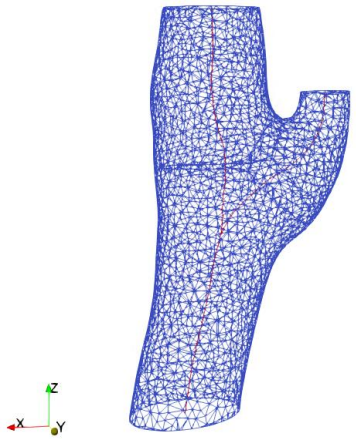	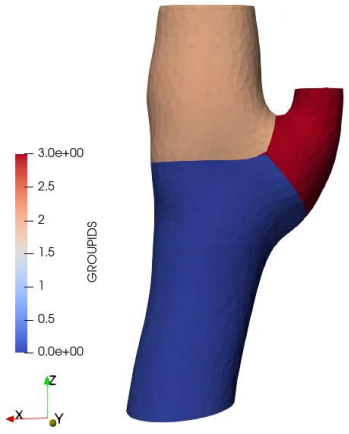	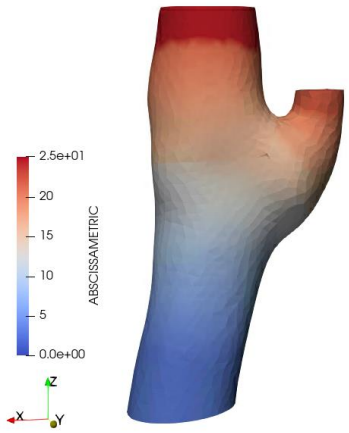	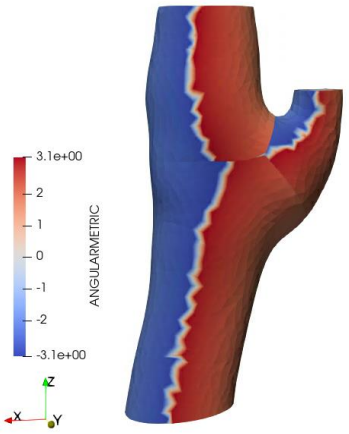
Follow-up	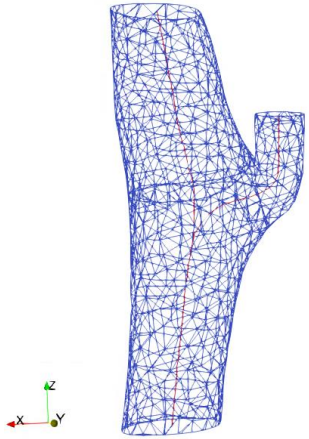	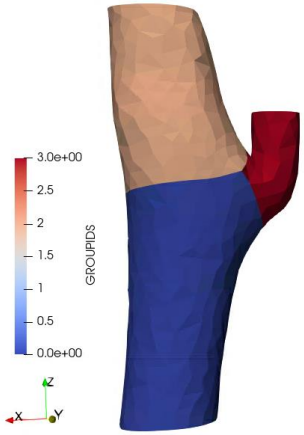	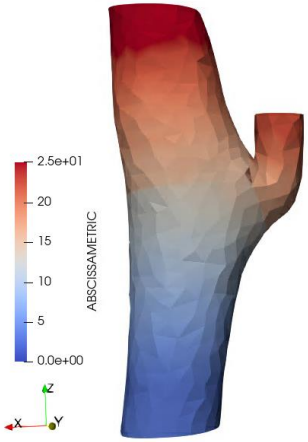	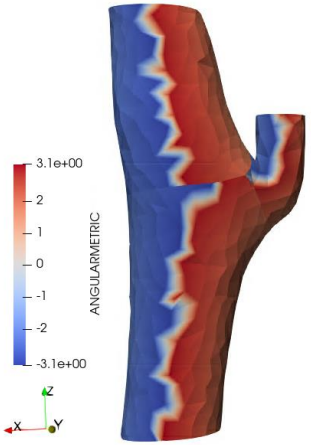

Patient 6R – 2D CCA-ICA

Biomechanical analysis

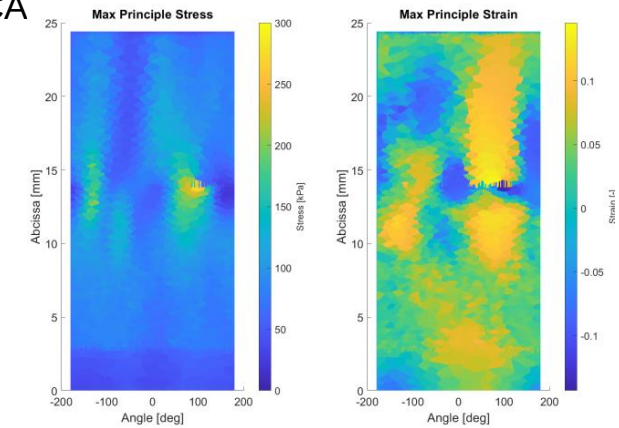

	Stress	Strain	Wall thickness		Max Curvature		Min Curvature	
			Base	*Foll*	*Base*	*Foll*	*Base*	*Foll*
	[kPa]	[-]	[mm]	[mm]	[m^{-1}]	[m^{-1}]	[m^{-1}]	[m^{-1}]
Max	276.11	0.14	1.67	2.63	0.73	1.47	0.33	0.33
Median	85.85	0.04	1.06	1.14	0.32	0.38	-0.01	-0.02
Min	19.9	-0.14	0.20	0.04	-0.03	-0.04	-1.26	-10.91

Morphometrical analysis

Baseline

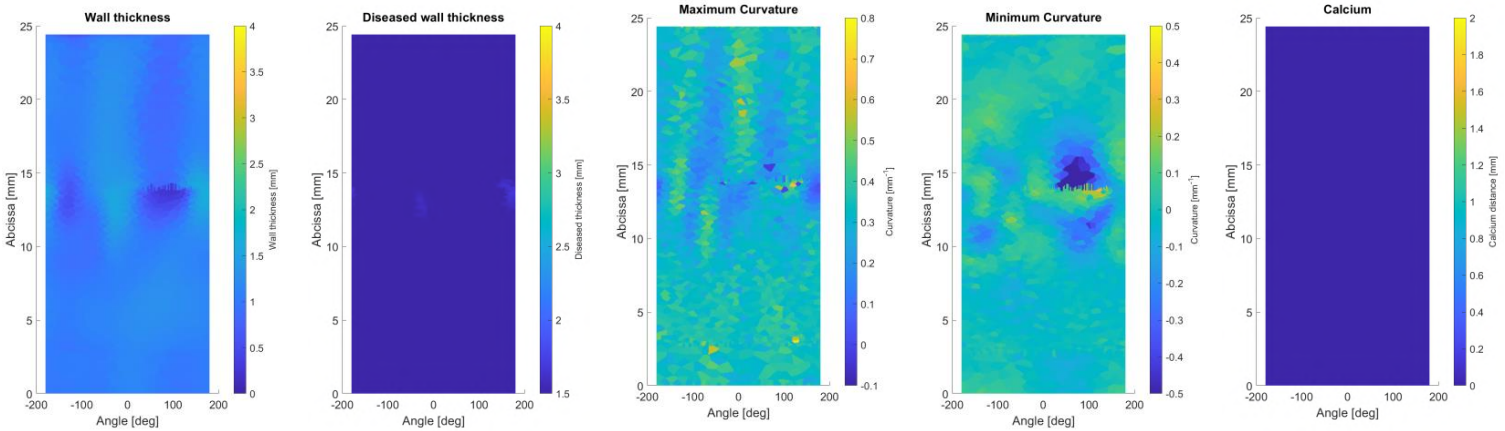

Follow-up

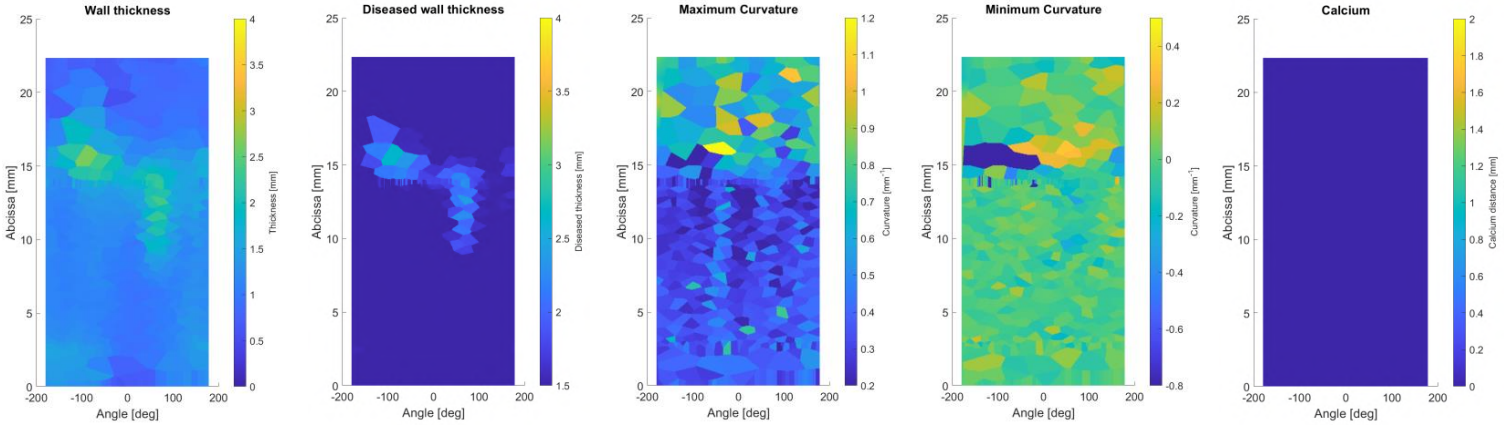

Patient 6R – 2D CCA-ECA

Biomechanical analysis

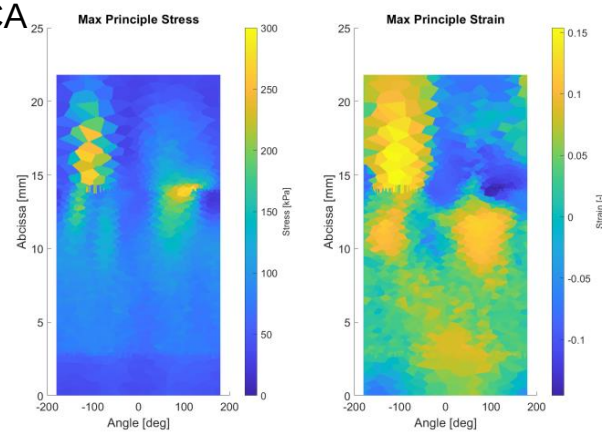

	Stress	Strain	Wall thickness		Max Curvature		Min Curvature	
			Base	*Foll*	*Base*	*Foll*	*Base*	*Foll*
	[kPa]	[-]	[mm]	[mm]	[m^{-1}]	[m^{-1}]	[m^{-1}]	[m^{-1}]
Max	279.66	0.15	1.67	2.39	0.85	0.79	0.33	0.24
Median	82.52	0.04	1.06	1.14	0.35	0.32	-0.02	-0.01
Min	19.88	0.15	0.20	0.04	0.00	-0.04	-1.47	-10.91

Morphometrical analysis

Baseline

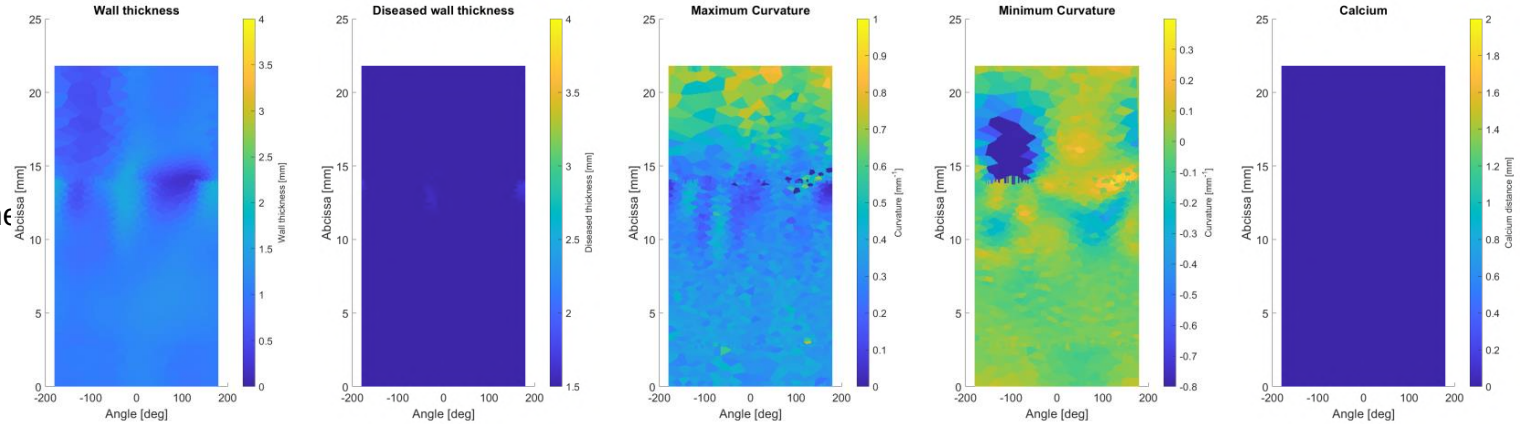

Follow-up

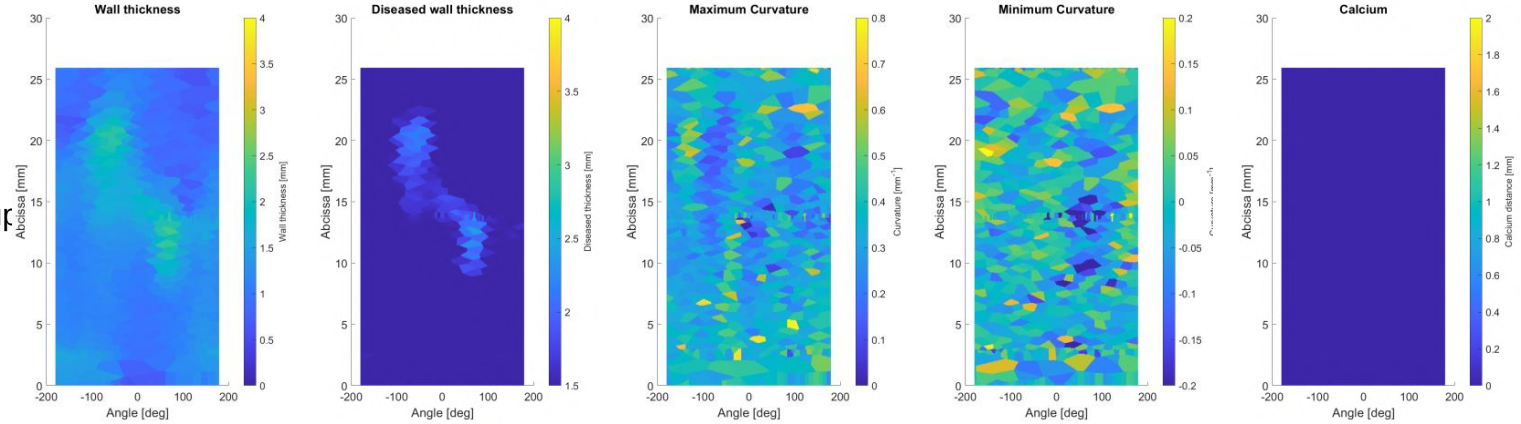

Patient 6R – Data

Post-processing metrics			Unit	CCA - ICA	CCA - ECA
Stress	Baseline	Max	[kPa]	276.11	279.66
		Median	[kPa]	85.85	82.52
		Min	[kPa]	19.9	19.88
Strain	Baseline	Max	[-]	0.14	0.15
		Median	[-]	0.04	0.04
		Min	[-]	-0.14	0.15
Wall thickness	Baseline	Max	[mm]	1.67	1.67
	Baseline	Median	[mm]	1.06	1.06
	Baseline	Min	[mm]	0.20	0.20
	Follow-up	Max	[mm]	2.63	2.39
	Follow-up	Median	[mm]	1.14	1.14
	Follow-up	Min	[mm]	0.04	0.04
Plaque burden *	Baseline	Max	[%]	61.04	
	Baseline	Median	[%]	45.00	
	Baseline	Min	[%]	37.25	
	Follow-up	Max	[%]	57.41	
	Follow-up	Median	[%]	46.02	
	Follow-up	Min	[%]	35.71	
Calcium *	Baseline		[mm^3]	0.00	
	Follow-up		[mm^3]	0.66	